Clay characterization using spectral induced polarization

Aída Mendieta Tenorio

Sorbonne Université

École doctorale Géosciences, Ressources Naturelles et Environnement (ED 398)

UMR 7619 METIS

Clay characterization using spectral induced polarization

Par Aída MENDIETA

Thèse de doctorat en Géophysique

Dirigée par Damien JOUGNOT et Alexis MAINEULT

Co-encadrée par Philippe LEROY

Soutenance prévue le 25 juin 2021

Devant le jury composé de :

M. Konstantin TITOV	Professeur, Université de St. Pétersbourg, Russie	Rapporteur
Mme Chi ZHANG	Professeure associée, Université de Vienne, Autriche	Rapportrice
M. Philippe COSENZA	Professeur des Universités, Université de Poitiers	Examinateur
M. Ahmad GHORBANI	Professeur associé, Université de Yazd, Iran	Examinateur
M. Roger GUÉRIN	Professeur des Universités, Sorbonne Université, Paris	Examinateur
Mme Pauline KESSOURI	Chercheuse, BRGM, Orléans	Examinatrice
M. Damien JOUGNOT	Chargé de recherche CNRS, Sorbonne Université, Paris	Directeur de thèse
M. Alexis MAINEULT	Chargé de recherche CNRS, Sorbonne Université, Paris	Directeur de thèse
M. Philippe LEROY	Chercheur, BRGM, Orléans	Invité
Mme Sabine KRUSCHWITZ	Professeure Junior, TU Berlin, Allemagne	Invitée

A mi familia (dónde sea que estén en el mundo...)

“Non mais laissez-moi manger ma banane.”

Philippe Katerine

“¡Qué felicidad! Porque arena, porque amigos siempre hay en el mar.”

Gary González - 31 minutos

“So many questions remain unanswered. Perhaps we are poorer for having lost a possible explanation or richer for having gained a mystery. But aren’t both possibilities equally intriguing?”

Peter Wohlleben

Acknowledgments

D'abord je voudrais remercier mes trois encadrants, la team EXCITING WP-4. Je vous remercierai pour toujours votre patience et la qualité humaine que vous avez. Surtout pendant la période du COVID. Damien, Alexis et Philippe LEROY, merci!

I would also like to thank the jury for all their precious comments that will certainly help me improve this particular research project but my approach to science in my career as well. I would like to thank: Chi ZHANG, Konstantin TITOV, Ahmad GHORBANI, and Sabine KRUSCHWITZ. Pour les français du jury, j'ai aussi à vous remercier pour tous vos commentaires et pour être un soutien pendant ma thèse. Merci Pauline, Roger, et Philippe COSENZA.

Je voudrais aussi remercier les membres du laboratoire METIS qui ont aidé à que cette thèse arrive à son bout. Valérie, Bénédicte, vous êtes impréscindibles. Jean-Marie MOUCHEL, merci pour le bon humour et les chansons boliviennes. Julien THIESSON, tes travaux en archéologie, bon ça place est dans un musée (et la tienne aussi). Je tiens à remercier le groupe international de la banane pour les bons moments et souvenirs pendant la thèse, c'est à dire: Larita, Angie, Cécile, Flore, Kawtar et Karim.

I would like to thank those friends (from El Salvador, the US and France) who have been a great support during this thesis, thanks to: Rivita, Konsti, Megancita, Cheche, Marlon, Spyros, Amaita, Guadalupe and many others. Thaaaanks (read in Ida's voice)!

Por supuesto debo agradecer el enorme apoyo de mi familia en El Salvador y fuera: Tío Tavo, Tía Any, Priscy, Aru, Tía Mita, Tía Aída, Madre, Yaya, Natalita, Julito, Tío Chico y demás que han estado ahí para mi durante todas mis aventuras académicas y de la vida.

I am certainly forgetting names but know that I will be forever thankful to those kind souls who have helped me through these thesis times, specially during COVID.

Résumé

Les argiles sont répandues dans la proche surface de la Terre, et ont un fort impact sur la perméabilité des formations géologiques. Leur très faible perméabilité fait des formations argileuses des "pièges géologiques" d'intérêt dans divers domaines d'étude des géosciences (notamment pour le pétrole et le gaz, la géothermie, le stockage des déchets nucléaires, entre autres). Les minéraux argileux présentent une charge de surface et une surface spécifique très importantes, ce qui génère le développement d'une double couche électrique particulièrement importante. La polarisation provoquée spectrale (PPS) est une méthode géoélectrique active qui permet d'obtenir de manière non-invasive la conductivité électrique complexe en fonction de la fréquence d'un géo-matériau du mHz au kHz. La conductivité complexe informe sur la capacité du matériau sondé à conduire un courant électrique et sur sa capacité à se polariser (à mobiliser de manière réversible des charges électriques). Cette thèse présente un protocole de laboratoire détaillé pour obtenir des mesures de PPS sur différents types d'argiles à des salinités variables, ainsi que des mélanges hétérogènes artificiels d'illite et de montmorillonite. Les résultats de la première étude montrent que la partie réelle de la conductivité électrique augmente avec la salinité, mais la partie imaginaire augmente jusqu'à un maximum et puis diminue. Cette diminution est due à la coagulation des argiles à hautes salinités. Cette coagulation potentielle des argiles altérerait l'espace poral puis modifierait les mécanismes de polarisation en jeu. Par ailleurs, en comparant le rapport de la conductivité de surface (imaginaire versus réelle) et d'autres données de la littérature, on remarque que ce rapport diminue avec la teneur en argile. Pour la deuxième étude, on observe que la montmorillonite domine la polarisation par rapport à l'illite. Cependant, les deux argiles ont un effet sur la conduction des mélanges. Les lois de mélanges sont une approche efficace pour modéliser ce type de mélange hétérogène d'argiles. Les modèles de réseaux de conductance complexes sont également utiles pour prédire la forme des spectres de polarisa-

tion. Les résultats de ce travail de thèse ouvrent de nouvelles perspectives pour la caractérisation des matériaux argileux avec la PPS.

Mots clés polarisation provoquée spectrale, argiles, variation avec la salinité, mélanges hétérogènes, lois de mélanges, réseaux de conductance complexe

Contents

List of Figures

List of Tables

List of Tables

Introduction

This PhD thesis was conducted in the framework of the ANR EXCITING (French National Research Funding Agency - EXploring geological resourCes and reservoirs Integrity by geophysical prospecTING of clays properties from nano to field scale") project. The EXCITING project is a partnership of three universities, a French "EPIC" (public industrial and commercial establishment), and a private company: Sorbonne Université (Paris), Université de Strasbourg, Université de Poitiers, BRGM (French geological survey), and IRIS instruments. The goal of this project is to characterize the properties of clay materials through the measurement of their complex electrical conductivity, at different scales (from the nm to pluri-m) and at different frequencies (from the mHz to the kHz). The research I have carried out in this thesis focuses on the characterization using spectral induced polarization (SIP) from the mHz to the kHz, of different types of clay minerals and at different pore water salinities at the laboratory scale (cm).

Background and problematic

According to Hillier (2003) clay minerals are typical of Earth's near surface environments. Tournassat et al. (2015) mention that illite and smectite, two main clay minerals, make up to 30% of all sedimentary rocks. Clay minerals can be formed under weathering, sedimentation, diagenesis, and hydrothermal processes (Hillier 2003). In other words, clay minerals are ubiquitous in the Earth's near surface (the first 10 km). Figure 0.1 shows the overall content of clay minerals in the Earth's upper crust.

Additionally, clay minerals have a high impact on fluid permeability thus their study is of importance for many applications, such as: critical zone research (Chorover et al. 2007), hydrogeology (Parker et al. 2008), civil engineering (Islam et al. 2020), nuclear waste storage

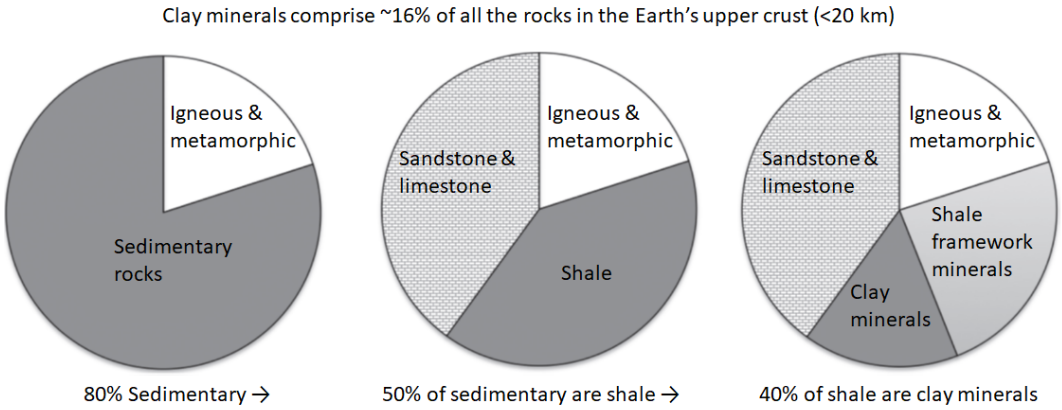

Figure 0.1: Distribution of types of rocks in the Earth's upper crust (Schroeder 2018)

(Wenk et al. 2008), oil and gas (Morsy and Sheng 2014), geothermal energy exploration and production (Corrado et al. 2014), among others. Low permeability clay formations can act as cap rocks on reservoirs and thus act as geological storage formations (see figure 0.2 for a sketch on clay formations as cap rocks). They can act as natural storage for natural resources (as oil and gas), but can also act as artificial (human-made storage) for various elements (such as nuclear waste or CO_2 sequestration). It is therefore of utmost importance to be able to understand these materials, characterize and monitor them with different physical and chemical conditions (e.g., varying pore water salinity, pressure, temperature, among others).

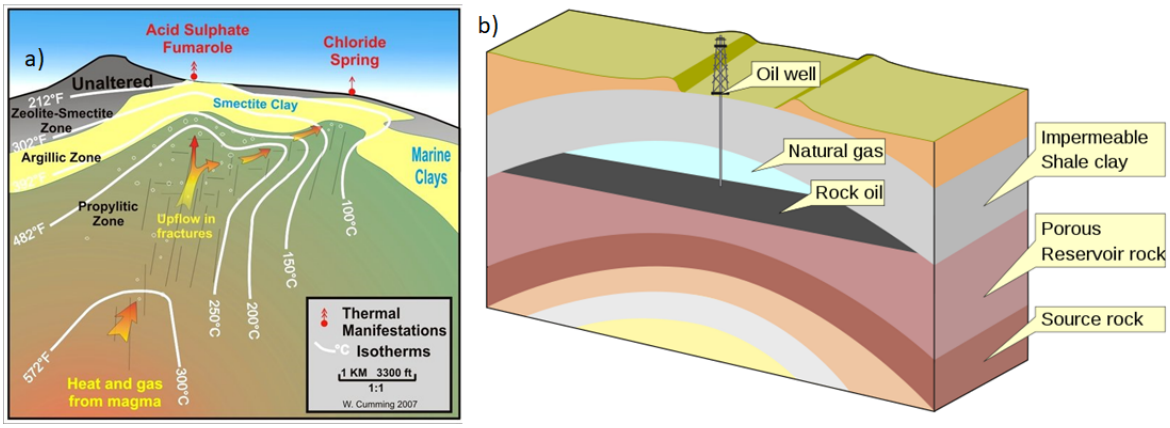

Figure 0.2: Sketch of a clay formation acting as a cap rock for: a) geothermal reservoir (Cumming and Mackie 2010), and b) oil and gas reservoir (credit: https://www.wikiwand.com/en/Petroleum_trap).

Traditionally, clay systems can be characterized through sampling, with punctual and invasive methods. Obtaining clay samples is costly, time consuming, and represents a single data point in a system. Geophysical methods offer a more integrative way to characterize geological systems in 2D or even 3D profiles and result less costly, and non-invasive. If one would like to use geophysics for the characterization of a geological system with clay minerals, elec-

tric and/or electromagnetic methods are often used. The most used geo-electric method in the field is the electrical resistivity method, this method however only yields information on the electrical resistivity of the system at one single frequency. Important information is lost when not taking into account the polarization in addition to the conduction. Clays have a very complex electrical signal, thus the importance its study using multi-frequency geo-electrical tools.

Important advances have been made for the characterization of clays using geo-electrical methods, both experimentally and with models. Notably, clayrocks that are candidates for nuclear waste storage (e.g., Callovo-Oxfordian clay, Boom clay, Opalinus clay) have been intensely studied (e.g., Kruschwitz and Yaramanci 2004; Cosenza et al. 2008; Wenk et al. 2008; Jougnot et al. 2010). Furthermore, clayrocks in geothermal systems have been studied by many others (see for instance, Lévy et al. 2018, 2019a,b). These clayrocks, however, have mixed mineralogy so it is not possible to determine the electrical signature of a particular clay mineral. For this purpose, studies such as Breede et al. (2012) or Okay et al. (2014) investigate individual clay types in mixtures of quartz sand and clay. Leroy et al. (2017) study the electrical signal of Na-montmorillonites but in dilution. There is therefore a lack of studies that have individual types of clays in mind with smaller porosity than a dilute clay suspension, and not a mixture of clay and sand.

Furthermore, clays present in the Earth's subsurface are often times saturated in an aqueous solution (i.e. water and dissolved salts such as NaCl). Clays can be present in different types of environments with different salinities and their electrical signature can thus change dramatically. Therefore, understanding how the electrical signature of clays evolves with different concentrations of salts is important and more studies with this in mind are needed. Additionally, most times clay formations are made of mixed-layer minerals (illite and smectite, see for example Bergaya and Lagaly 2006), thus understanding the electrical signal of these anisotropic systems is important.

Outline of this thesis

This thesis is divided into five chapters. The first chapter gives a background on the structures of the clays and an explanation of the SIP phenomenon. In the same fashion, it presents the most common physical and phenomenological models used in SIP for clay characterization in specific.

This thesis is mostly experimental, and therefore in chapter 2, I present a thorough expla-

nation of the laboratory experiments I pursued, related to SIP experiments and more. I also present the path I followed in order to attain a particular laboratory protocol.

In chapter 3, I present the results of the SIP characterization of different types of clays at varying salinities, and an interpretation of these results. I present these results in the form of a scientific article (published in *Journal of Geophysical Research*) together with the supplementary material of the article.

In chapter 4, I present the SIP results of synthetic heterogeneous clay mixtures of illite and red montmorillonite with different geometrical arrangements. I also present models used to try to predict the SIP response of these mixtures that is, mixing laws and complex conductance networks. I present these results in the form of a draft version of an article. This article is in preparation, and the co-authors and I would like to submit it to *Geophysical Journal International*. I also present further analysis on the different types of meshing with the complex conductance network models.

In Chapter 5, I present the perspectives of this work. Some perspectives correspond to future work I believe would be most interesting for the SIP-geophysics community, following the work presented in this thesis. Additionally, I present work in progress that is not mature enough to be added to the main body of this thesis.

CHAPTER

1 Theoretical background

This chapter attempts to establish the theoretical background needed to understand the work I have done in my thesis. First, I present a background on clay structures, then I introduce a background on the electromagnetic laws that govern the geo-electric methods. Then, I delve into the geo-electric methods, and later into the spectral induced polarization (SIP) method. I present the basic mechanisms that are attributed as the cause of polarization in clay minerals. I mention the most commonly used SIP models (physical and phenomenological). Finally, I introduce some upscaling techniques used for SIP.

1.1 Background on clay structures

The term "clay" has different meanings in different disciplines within the geosciences (Bergaya and Lagaly 2006). For sedimentology, for example, "clay" refers only to small grain sizes. Engineers use the term "clay" to refer to a plastic geo-material (Wagner 2013). I, however, refer to clay minerals as clays in this manuscript. Clay minerals are phyllosilicates (phyllo=sheets) and are characterized as such due to their cristallography. All clay minerals have as very basic building blocks SiO_4 tetrahedrons (see figure 1.1) and octahedrons (see figure 1.1) with Al^{3+}, Mg^{2+}, or Fe^{3+} centers and a base of oxygen atoms or hydroxyls (see Hillier 2003).

Comparon (2005) explains that the overall negative surface charge of clays can be explained because:

- Tetrahedrons have a Si^{4+} cation in the center and 4 O^{2-} atoms, so there is an overall negative charge for each tetrahedron. Tetrahedrons can connect with each other and share up to 3 oxygens (Hillier 2003; Leroy 2005), but there still is an overall negative surface charge for the tetrahedral sheet (T sheet). This overall negative surface charge

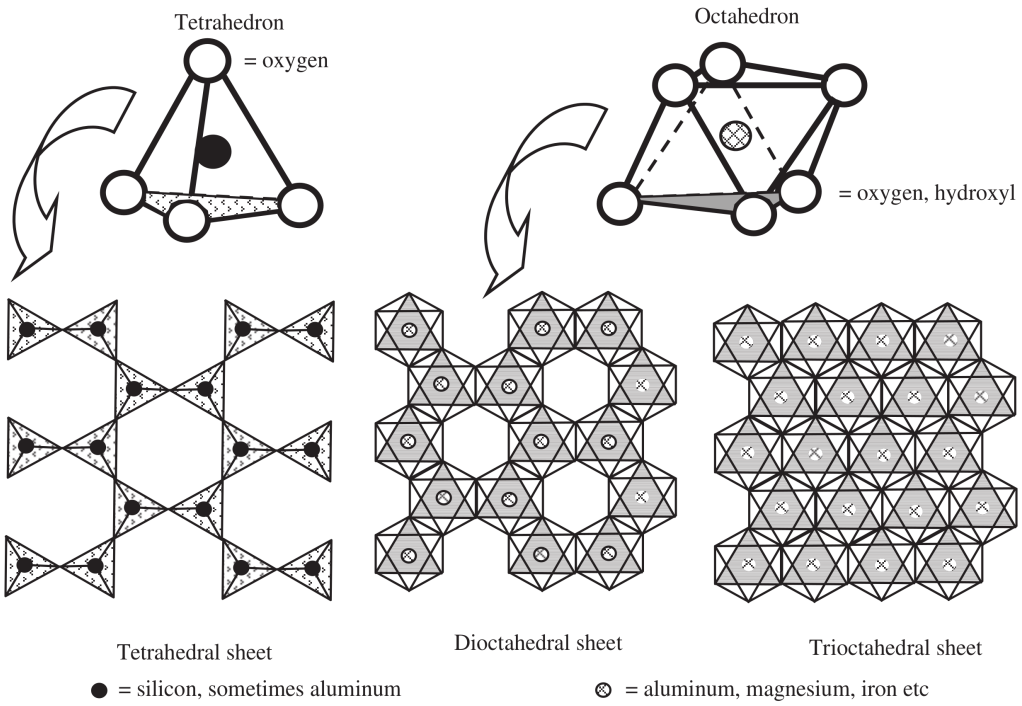

Figure 1.1: Sketch of tetrahedrons and octahedrons, as well as their corresponding sheets (modified from Hillier 2003).

compensates with the ions in contact with the oxygen base of the T sheet. The tetrahedron centers are usually Si^{+4}, Al^{+3}, or Fe^{+3} (Brigatti et al. 2006).

- For an oxygen based octahedron, there is an Al^{3+} cation and 6 O^{2-} atoms, leaving an overall negative surface charge per octahedron. For OH^{-}, there is similarly an overall negative charge per octahedron. However, in octahedral sheets (O sheets) up to 3 cations can share an OH^{-} (Hillier 2003; Leroy 2005). The octahedron centers are usually Al^{+3}, Fe^{+3}, Mg^{+2}, or Fe^{+2} (Brigatti et al. 2006).

In order to obtain electroneutrality in the O sheets, 2 out of 3 octahedral sites are occupied by a Al^{3+} cation (dioctahedral sheet). When all sites are occupied by Mg^{2+}, there is a trioctahedral sheet. Smectite, illite, and kaolinite all have as main cation Al^{3+} in their octahedral sheets, and these are the most common clay minerals in the majority of sedimentary environments (Tournassat and Steefel 2015).

The T and O sheets are the main building blocks for all clays. Clays form layers of TO (1:1 clay) or TOT (2:1 clay) sheets. Although there are many types of clay minerals, I will focus mostly in kaolinite, illite, and montmorillonite (from the smectite family), because they are the most common. In figure 1.2 we can see that kaolinite is a 1:1 clay mineral, and both illite and smectite are 2:1 clay minerals. As shown in figure 1.2, the height of a TO layer is

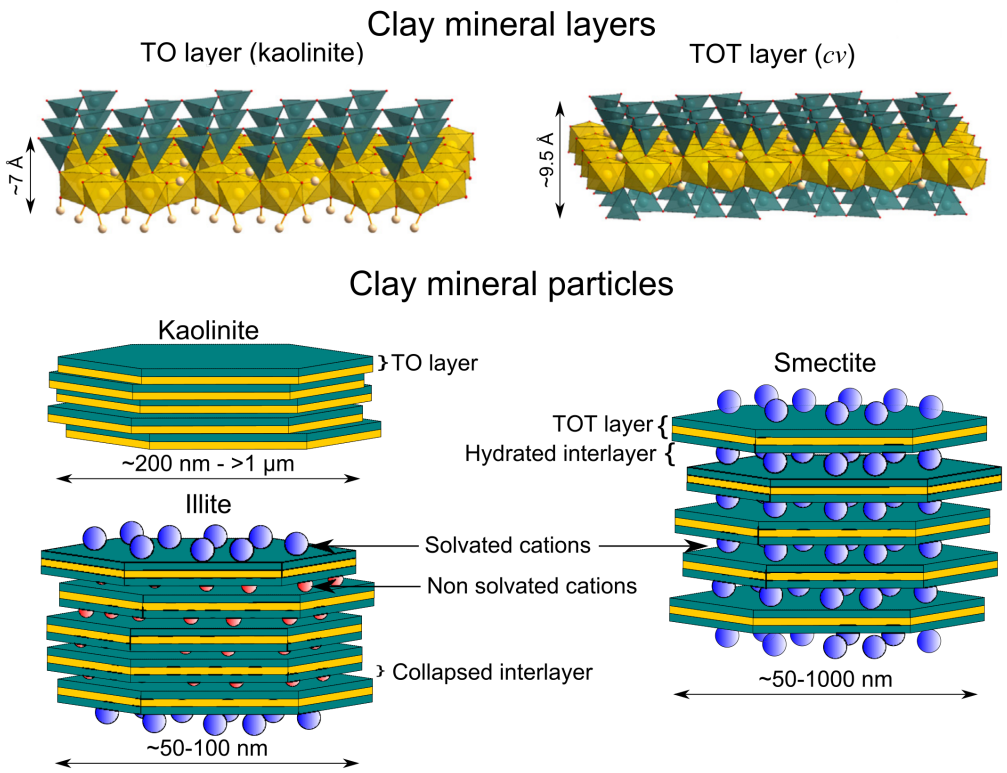

Figure 1.2: Structure of kaolinite, illite, and smectite from their T and O sheets (modified from Tournassat and Steefel 2015).

around 7 Å and for the TOT layer it is around 9.5 Å. The length of a kaolinite particle (stack of TO sheets) is in the range of 200 nm to 1 μm, an illite particle (stack of TOT layers) is in the range of 50 to 100 nm, and for smectites the range is from 50 to 1000 nm (Tournassat and Steefel 2015). A kaolinite particle can be made of stacks from 10 to more than 200, but there are stacks of 1 and 2, 6 and 10, or 5 and 20 for Na-montmorillonite, Ca-montmorillonite and illite, respectively (Tournassat et al. 2015; Tournassat and Steefel 2015; Leroy et al. 2017). In addition, the total specific surface area of a kaolinite particle, typically 10-20 $m^2\ g^{-1}$, is considerably smaller than the total specific surface area of an illite and montmorillonite particle (typically 100-200 $m^2\ g^{-1}$ for illite and 750-800 $m^2\ g^{-1}$ for Na-montmorillonite).

A particularity of clays is their high negative surface charge. The layer charge has a relation to the cationic exchange capacity (CEC)(Leroy et al. 2007; Okay et al. 2014). According to Bergaya et al. (2013), the CEC in clays happens due to two phenomena:

- Isomorphic (iso=same, morphic=shape) substitutions in the T and/or O sheets. According to Tournassat and Steefel (2015), the most common substitution are from Si^{4+} to Al^{3+} in the tetrahedral sheets, and from Fe^{3+} to Fe^{2+}, or Al^{3+} to Mg^{2+}, in the octahedral sheets, for dioctahedral clays.

- pH-dependent reactions between edge cations (such as Si^{4+}, Al^{3+}, or Mg^{2+}) and H_3O^+, H_2O, or OH^-. As kaolinites have higher layer stacking, this phenomena is of more importance to their CEC.

1.2 Background on geo-electrical methods

In this section, I present the physics principles for geo-electrical research, as well as a brief introduction to geo-electrical methods.

1.2.1 Maxwell's laws for induced polarization

The basis of geo-electrical methods in geophysics come from the fundamental laws of electromagnetism that is Maxwell laws (Maxwell 1865). We are only interested in only two of these equations. Faraday's law can be written as follows:

$$\nabla \times \mathbf{H} = \mathbf{J_c} + \frac{\partial \mathbf{D}}{\partial t}, \tag{1.1}$$

where, $\mathbf{H}$ is the magnetic field strength [A m^{-1}], $\mathbf{J_c}$ is the conduction displacement current [A m^{-2}], and $\mathbf{D}$ is the electrical displacement field [C m^{-2}]. Therefore, $\partial \mathbf{D}/\partial t$ is the electrical displacement current density. Gauss' law for electricity can be written as:

$$\nabla \cdot \mathbf{D} = \rho_v, \tag{1.2}$$

where, ρ_v represents the electrical charge density [C m^{-3}]. Two more constitutive equations that are pertinent to geo-electrical studies are:

$$\mathbf{D} = \epsilon_0 \mathbf{E} + \mathbf{P} = \epsilon \mathbf{E}, \tag{1.3}$$

and Ohm's law:

$$\mathbf{J_c} = \sigma \mathbf{E}, \tag{1.4}$$

where, $\mathbf{P} = \epsilon_0(\epsilon_r - 1)\mathbf{E}$. Also, ϵ [F m^{-1}] represents the dielectric permittivity, and is an intrinsic property of each material, and ϵ_0 is the dielectric permittivity of vacuum, $\mathbf{E}$ is the electric field [V m^{-1}], $\mathbf{P}$ is the electric polarization density [C m^{-2}], σ is the electrical conductivity and also

is an intrinsic property of each material [S m^{-1}]. When combining equations 1.3 and 1.4 into equation 1.1, we obtain:

$$\mathbf{J} = \sigma \mathbf{E} + \epsilon \frac{\partial \mathbf{E}}{\partial t}. \tag{1.5}$$

If we assume that the electrical field is of the form $\mathbf{E} = \mathbf{E_0} e^{i\omega t}$, the derivative of the field will always introduce an imaginary term ($\partial \mathbf{E}/\partial t = i\omega \mathbf{E}$), that is:

$$\mathbf{J} = \sigma^*(\omega)\mathbf{E} = \sigma \mathbf{E} + i\omega\epsilon \mathbf{E}. \tag{1.6}$$

We can then express the frequency dependent and complex electrical conductivity as:

$$\sigma^*(\omega) = \sigma + i\omega\epsilon. \tag{1.7}$$

It is worth noting that I have used i as the imaginary unit, and ω represents the angular frequency that is related to the linear frequency by $\omega = 2\pi f$. Equation 1.7 is the basis for SIP mathematical expressions. Note that this equation is expressed for homogeneous media.

1.2.2 Active electrical methods in geophysics

The electrical methods in geophysics are one of the first geophysical methods to be developed, notably by the Schlumberger brothers. Conrad Schlumberger published the seminal work of geo-electrical methods in 1920 (Schlumberger 1920). According to Zonge et al. (2005) within the active geo-electrical methods (i.e., an active source is provided for the electrical current) we can distinguish three: the electrical resistivity at one single frequency (mostly used for near-surface fieldwork), the time-domain induced polarization (TDIP, mostly used for near surface fieldwork), and the SIP (until today mostly used at the laboratory scale). All of these methods require at least a pair of current injecting electrodes and a pair of voltage measuring electrodes.

In the field, an electrical resistivity survey can be conducted in 1D (electrical sounding) (see Ward 1988), 2D (electrical resistivity tomography, ERT), 3D (3D ERT) (Robinson et al. 2008), or even 4D (3D time-lapse monitoring)(Karaoulis et al. 2014). For a 2D ERT array multiple co-linear electrode quadripoles are set up, and for the 3D ERT multiple co-linear electrode quadripoles with several electrode lines perpendicular to each other are set up (usually perpendicular for simplicity). For the TDIP, after the injecting current has been shut-off, the

measuring electrodes measure the decay of the electrical potential difference with respect to time (Zonge et al. 2005). Finally, in SIP a phase-lag between the injected current and the measured voltage, at multiple finite frequencies, usually from the mHz to the kHz is measured (see figure 1.3)(Revil 2012). According to Ohm's law, from the injected electrical current, and the measured electric potential difference of a rock sample, we can deduce the complex impedance of the sample in a straightforward way

$$U^*(\omega) = I(\omega)Z^*(\omega), \tag{1.8}$$

where I is the electrical current [A], U is the electric potential difference [V], and Z is the impedance [Ω]. If we know the geometrical disposition of the measurement, we can calculate the complex electrical resistivity (ρ^*, in Ω m) or conductivity (σ^*, in S m^{-1}) of the sample, that is:

$$\rho^*(\omega) = K\frac{U^*(\omega)}{I(\omega)}, \tag{1.9}$$

where K [m] is the geometric factor related to the position of the electrodes, and $\rho^*(\omega) = [\sigma^*(\omega)]^{-1}$.

Another way to represent the complex electrical conductivity (σ^*) or resistivity (ρ^*) is:

$$\frac{1}{\rho^*(\omega)} = \sigma^*(\omega) = \sigma' + i\sigma'' = |\sigma|e^{(i\varphi)}, \tag{1.10}$$

where σ' [S m^{-1}] is the real part of the electrical conductivity, σ'' [S m^{-1}] is the imaginary part, $|\sigma|$ [S m^{-1}] is the amplitude of the conductivity, and φ [rad] represents the phase-lag. In a way, σ' can be thought of as a representation of the conduction in the sample and σ'' as the polarization of the sample. Conduction refers to the electrical charge transportation and polarization refers to the electrical separation of charges (Kemna et al. 2012).

1.3 Background on SIP

The geo-electrical method I use in my research is SIP. It is therefore necessary to devote a section to understand the physical processes that affect the SIP signal. Additionally, I introduce the most important models used in SIP (physical and phenomenological).

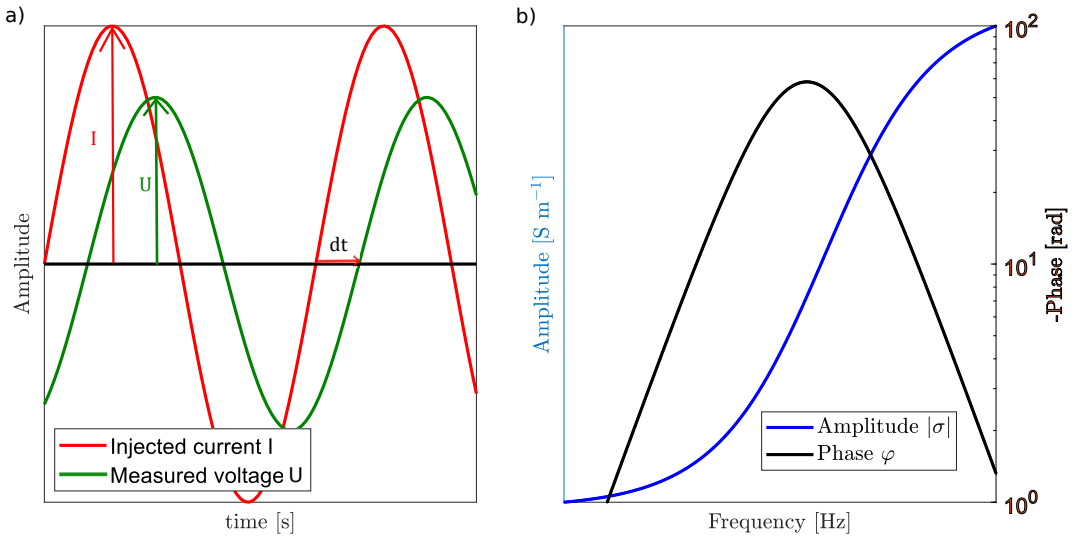

Figure 1.3: Sketch of (a) the phase-lag between the injected electrical current (I) and the measured voltage (U) at one single frequency and (b) the resulting complex conductivity measurement ($|\sigma|$ and φ) at multiple frequencies.

1.3.1 The electrical double layer

When a mineral is in contact with water, an electrical charge (negative for clays) builds up on the surface of the mineral creating an electrical double layer (EDL). The EDL is composed by the Stern and diffuse layers (see figure 1.4).

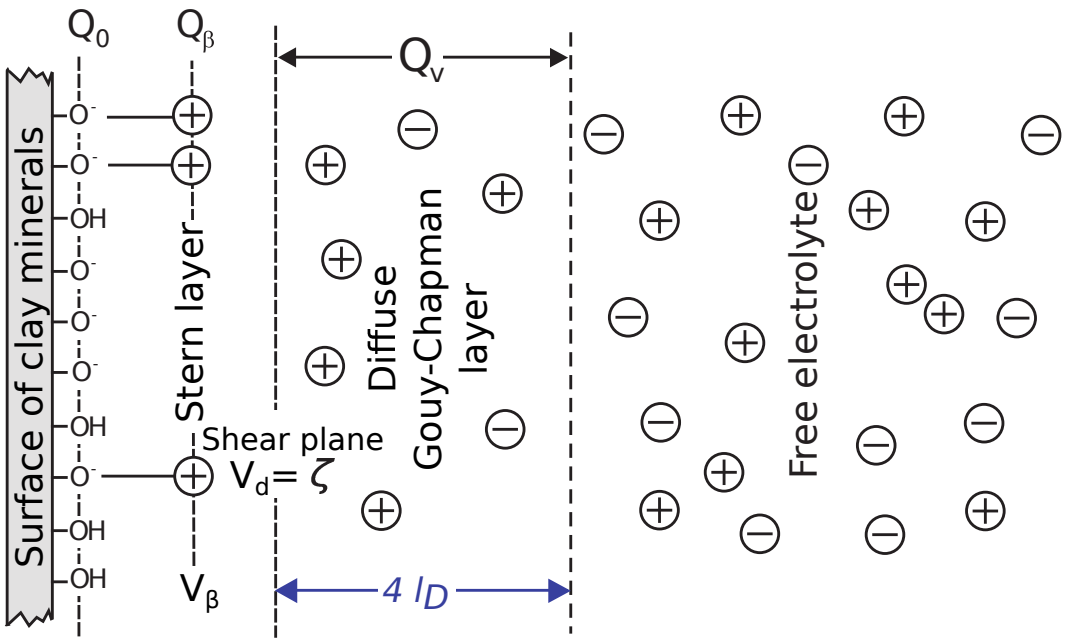

Figure 1.4: Sketch of the EDL for a clay mineral (modified from Jougnot et al. 2019).

As we see in figure 1.4, the surface charge of the clay mineral (Q_0, in C m^{-2}) (this sketch may represent the electrochemical properties of the edge surface, Leroy and Revil 2009) is negative, therefore a build-up of positive charges in the Stern layer is created in contact with

the clay surface (Q_β, in C m^{-2}), and finally a positive electric charge build-up is created in the pore space in the diffuse layer (Q_V, in C m^{-3}). The electric potential at the Stern layer is then labeled V_β [V], and the electric potential in the shear plane is called Zeta-potential: ζ [V]. The Stern layer is strongly bound to the surface of the mineral. Ions located in the Stern layer are only able to move tangentially to the surface of the mineral when subjected to an external electrical field and have low mobility compared to the bulk electrolyte (Tournassat and Steefel 2015). The diffuse layer is composed mostly of counter-ions that are still affected by the charge build-up of the mineral's surface, but are more mobile than the ions located in the Stern layer (Rasmusson et al. 1997). When the ions in a solution are thought to no longer be affected by the electrical potential from the pore wall, they are considered to be part of the bulk electrolyte and are considered free ions. Some authors (as Leroy and Revil 2009) consider that the EDL is as large as 2 Debye-lengths (l_D) [m], and others go as far as 4 l_D (e.g., Jougnot et al. 2019). For a 1:1 electrolyte such as NaCl electrolyte the l_D can be calculated using:

$$l_D = \sqrt{\frac{\epsilon_w k_B T}{2 e_0^2 C_w N_A}}, \tag{1.11}$$

where, ϵ_w is the electric permittivity of the pore water [F m^{-1}], $k_B = 1.381 \times 10^{-23}$ J K^{-1} is the Boltzmann constant, T is the absolute temperature [K], $e_0 = 1.602 \times 10^{-19}$ C is the elementary charge, C_w is the ionic bulk concentration [mol m^{-3}], and $N_A = 6.022 \times 10^{23}$ mol^{-1} is the Avogadro number. The classic way to derive the potential decrease in the pore space is through the Debye-Hückel approximation (Leroy and Maineult 2018; Guarracino and Jougnot 2018; Soldi et al. 2019). However, this approximation is not accurate for ζ potentials larger than 25.7 mV in magnitude (Jougnot et al. 2019). Therefore, a more accurate way to determine the decrease of the electrical potential through the pore space is to numerically solve the Poisson-Boltzmann equation. Leroy and Maineult (2018) propose a solution to this equation valid for multivalent electrolytes.

The Self-Potential method is a passive geo-electrical method and consists on measuring the naturally occurring electric current induced phenomena in the subsurface (Revil et al. 2003). Several physical and chemical processes can induce an electrical current. The one related to water-flux (electro-kinetic contribution) is called streaming potential (Voytek et al. 2019). Numerous streaming potential models depend on a correct quantification of the potential distribution in the pore space (e.g., Guarracino and Jougnot 2018; Soldi et al. 2019). Jougnot et al. (2019) explore the effect the pore size distribution on the streaming potential genera-

tion from pore network modeling in a saturated medium, and they compare both ways to solve the potential distribution in the pore space. They assume the pore geometry is cylindrical. See Appendix 2 for this article that I co-authored. It is worth mentioning that clays have an important ζ potential, that ranges at least from -5 to -40 mV (depending on clay mineral, salinity and pH) according to Sondi et al. (1996). Furthermore, Sondi et al. (1996) reported apparent ζ potentials not corrected of surface conductivity effects decreasing electrophoretic mobility measurements. Therefore, they probably underestimate clay ζ potentials (Leroy et al. 2015). Thus solving for the Poisson-Boltzmann equation is a more accurate way to determine the electrical potential length of the diffuse layer.

1.3.2 Polarization mechanisms

When subjecting a geo-material saturated in an aqueous solution to a time-varying electrical field (in the low frequency range from the mHz to the kHz), charges within the EDL (Stern and diffuse layer) and the bulk water will move according to the electrical field. Following the Nernst-Planck equation at the pore scale, in the stationary state and neglecting advective flow:

$$\begin{aligned} \mathbf{J} &= \mathbf{J}_{\pm}^{\mathbf{d}} + \mathbf{J}_{\pm}^{\mathbf{e}} \\ &= -DN_A\nabla C_{\pm} - z_{\pm}\mu N_A C_{\pm}\nabla V, \end{aligned} \tag{1.12}$$

where $\mathbf{J}$ is the total current density [A m^{-2}], $\mathbf{J}_{\pm}^{\mathbf{d}}$ represents the contribution from the diffusion term, $\mathbf{J}_{\pm}^{\mathbf{e}}$ represents the contribution from electro-migration. D is the mean diffusion coefficient of electrolyte ions [m^2 s^{-1}] and can be related to the mean ionic mobility of the electrolyte (μ, in m^2 s^{-1} V^{-1}) through the Einstein relation $D = \mu k_B T / z e_0$. The $\pm$ parameter is merely used to describe if the ion is positive or negative. The rest of the parameters that describe the electrolyte are the ionic concentration (C, in mol m^{-3}), and the valence of the ion species (z).

The movement of the electrical charges happens then at different scales and are related to different types of polarization mechanisms that have different associated frequencies ranges. The Maxwell-Wagner polarization mechanism happens due to a charge build-up in the interfaces of different phases (see figure 1.5a). Meaning, different rock components have different electric properties, and thus when subjected to an external electrical field there is a separation of electrical charges at certain frequencies (Chelidze and Gueguen 1999). This

polarization mechanism is thought to happen at high frequencies > 1 kHz and <100 MHz (Chen and Or 2006).

The EDL polarization mechanism happens due to electrical charges moving around a particle within the EDL due to the applied external electric field (see figure 1.5b) This phenomenon is thought to happen at mid-frequencies (for SIP), that is from Hz to kHz (Ishida et al. 2000; Loewer et al. 2017). Schwarz (1962) introduced a model of the EDL polarization for spherical particles submerged in an electrolyte. He was trying to interpret dielectric measurements of a dispersion of colloidal particles. The important elements for EDL polarization are the surface properties of the mineral subjected to the external electric field (Chelidze and Gueguen 1999). Clays have a strong EDL (important surface charge) (Leroy and Revil 2004) and thus the EDL polarization mechanism (especially the Stern layer contribution) is particularly important for clays as specified by Leroy and Revil (2009).

Finally, the membrane polarization mechanism happens at the lowest frequencies, from the mHz to the lower kHz (Loewer et al. 2017), and arises due to a blockage of electrical charges in the pore throats of geo-materials (see figure 1.5c). Marshall and Madden (1959) studied the causes of polarization and listed the membrane polarization as an important contribution to the overall polarization of a geo-material. When an electrical field is applied to a geo-material and there is an ion-selective zone (Titov et al. 2002), only some electrical charges are able to move so there is a charge build-up (either cation or anion build up), therefore there is polarization. Pore throats are thought to cause this polarization mechanism (Bücker et al. 2017).

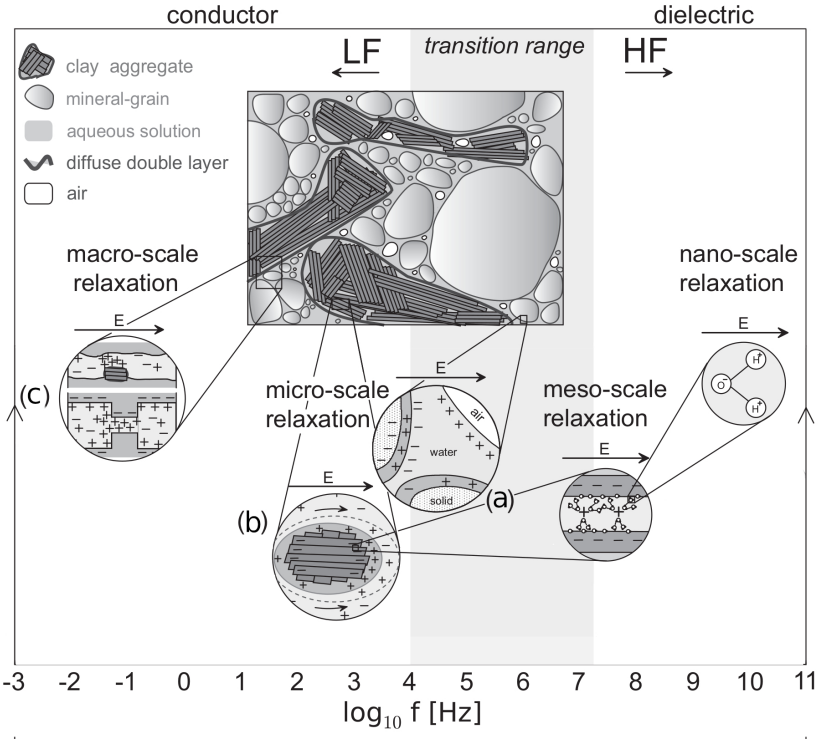

Figure 1.5: Sketch of the main polarization mechanisms within the SIP range (modified from Loewer et al. 2017): a) Maxwell-Wagner polarization, b) EDL polarization, and c) membrane polarization.

1.3.3 SIP models

There are different types of models that help us recreate an SIP signal: phenomenological and physical models. Phenomenological models are able to relate few parameters to a SIP signal, they are often times simple in comparison to physical models and require less parameters as well. Physical models are often quite complex, depend on a plethora of physical and chemical parameters (e.g., pH, CEC, μ, among others). These models have the benefit that they are able to relate a physico-chemical process to an SIP signal. In this sections I will describe the most used phenomenological models for clays, as well as the best known physical models for SIP.

1.3.3.1 Phenomenological models

A commonly used way to model the SIP signal is through mathematical relations that have been proven to fit SIP data correctly, called phenomenological models. These models depend on fewer parameters than physical models and are widely used in geophysics (e.g. Florsch et al. 2012; Tarasov and Titov 2013; Weigand and Kemna 2016, among others).

Pelton models

Some of the most commonly used phenomenological models are the Pelton type models, the basis is the Debye model (Debye 1929) and can be written as:

$$\epsilon^*(\omega) = \epsilon_\infty + \frac{\epsilon_0 - \epsilon_\infty}{1 + i\omega\tau}, \tag{1.13}$$

where $\epsilon^*(\omega)$ is the complex dielectric permittivity of a material, ϵ_∞ is the permittivity at highest frequency, and ϵ_0 is the permittivity at the lowest frequency. Note that the relation between $\epsilon^*(\omega)$ and $\sigma^*(\omega)$ is:

$$\epsilon^*(\omega) = \frac{\sigma^*(\omega)}{i\omega}. \tag{1.14}$$

That means that the relations between individual components are: $\epsilon' = \sigma''/\omega$, $\epsilon'' = \sigma'/\omega$, or $\sigma' = \omega\epsilon''$, and $\sigma'' = \omega\epsilon'$. For a more thorough explanation of these relations see Knight and Endres (2005). Later, the Debye model was modified by Cole and Cole (1941) and a new parameter was introduced (α):

$$\epsilon^*(\omega) = \epsilon_\infty + \frac{\epsilon_0 - \epsilon_\infty}{1 + (i\omega\tau)^{1-\alpha}}. \tag{1.15}$$

This Cole-Cole model can be written in terms of the conductivity:

$$\sigma^*(\omega) = \sigma_\infty + \frac{\sigma_0 - \sigma_\infty}{1 + (i\omega\tau)^c}, \tag{1.16}$$

where c is called the Cole-Cole exponent or parameter. This expression, presented in terms of the electrical resistivity is called the Pelton model (Pelton et al. 1978) and is:

$$\rho^*(\omega) = \rho_\infty + \frac{\rho_0 - \rho_\infty}{1 + (i\omega\tau)^c}, \tag{1.17}$$

and can thus be expressed with a chargeability term. It is worth noting that although the Cole-Cole and Pelton models are similar, they are not equivalent. According to Tarasov and Titov (2013), especially at high chargeability values both models differ. The chargeability term can be expressed as:

$$m_k = \frac{\sigma_\infty - \sigma_0}{\sigma_\infty}$$

and can be introduced in equation 1.16 (or its equivalent for resistivity) and thus be expressed with a chargeabilitiy term (m_k, in mV/V). This is the definition of chargeability proposed by Seigel (1959). Furthermore, for the particular case of $c = 0.5$ in equation 1.17, we obtain a Warburg model (Warburg 1899). Additionally, all of these models describe a single polarization peak (see figure 1.6), but not all measured SIP signals have a single peak. Thus we can expand this model for a double-Pelton (see figure 1.6), or even a triple-Pelton model, by adding or multiplying individual Pelton models. For example, a double-Pelton by addition is:

$$\rho^*(\omega) = \rho_0 \left[1 - m_1 \left(1 - \frac{1}{1 + (i\omega\tau_1)^{c_1}} \right) - m_2 \left(1 - \frac{1}{1 + (i\omega\tau_2)^{c_2}} \right) \right]. \tag{1.18}$$

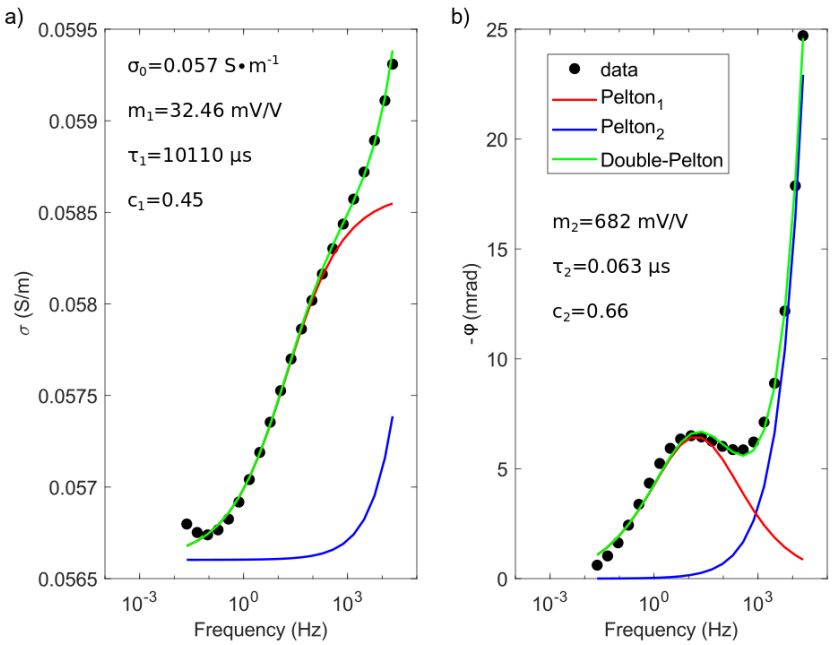

Figure 1.6: Double-Pelton model of SIP data on clays, through the (a) amplitude of the electrical conductivity and (b) the phase. The red and blue lines represent individual Pelton models, and the green line represents a double Pelton model (taken from Mendieta et al. 2021).

Another widely used model is the generalized Cole-Cole model (Vanhala and Soininen 1995):

$$\rho^*(\omega) = \rho_0 \left[1 - m_k \left(1 - \frac{1}{(1 + (i\omega\tau)^c)^a} \right) \right], \tag{1.19}$$

where, a is a Cole-Cole exponent. These Cole-Cole type models are widely used in geophysics, for forward modeling (e.g. Günther et al. 2016), in the field (Okay et al. 2013) and in the laboratory (Ghorbani et al. 2009; Schwartz and Furman 2015). Ghorbani et al. (2009)

measured the SIP signal of 3 types of clay rocks and gradually dessicated them. The authors determine that the quadrature conductivity reflects the water content in the macropores versus the micropores. They used a generalized Cole-Cole model (see equation 1.19) and a double Pelton model (via the multiplication of two individual Pelton models). They found that the generalized Cole-Cole model is better suited to model the SIP signal of an unsaturated clay rock. Later, Breede et al. (2012) characterized a set of variably saturated clay-sand mixtures. They used a Debye decomposition (Morgan and Lesmes 1994; Weigand and Kemna 2016) to better interpret their data. They found that m_k increases with clay content and has a non-monotonous behavior with saturation. Finally, Schwartz and Furman (2015) fit a double-Pelton model to SIP data of soil organic matter, they see a decrease of τ with an increase of m_k.

Various phenomenological relations used in SIP

There are other important phenomenological relationships used in SIP. Here, I will describe some of the most important relationships.

Archie's law (Archie 1942) is one of the most widely used relations within the geo-electrical methods. It is an empirical model and only valid for geo-materials not containing clay. Archie's law offers a link between the electrical conductivity of a rock (σ, S m^{-1}), the conductivity of the aqueous solution it is saturated by (σ_w, S m^{-1}) and the porosity of the rock (Φ), and it can be expressed as:

$$\sigma = F^{-1}\sigma_w, \tag{1.20}$$

$$F = \Phi^{-m}, \tag{1.21}$$

where F is formation factor of the rock and m is the cementation exponent. When measuring the electrical conductivity of a rock sample, the measurement depends on the conductivity of the rock matrix and the fluid saturating the rock sample. Waxman and Smits (1968) proposed a model where the surface conductivity (σ^*_{surf}, in Sm^{-1}) of the rock sample and the fluid conductivity (σ_w) act in parallel:

$$\sigma^* = \frac{\sigma_w}{F} + \sigma^*_{surf}. \tag{1.22}$$

Additionally, Weller et al. (2013) propose that we can calculate the real part of the surface

conductivity (σ'_{surf}, in S m^{-1}) as:

$$\sigma'_{surf}(\sigma_w) = \sigma'(\sigma_w) - \frac{\sigma_w}{F}, \tag{1.23}$$

and that the imaginary part of the surface conductivity (σ''_{surf}, in S m^{-1}) is:

$$\sigma'' = \sigma''_{surf} \tag{1.24}$$

An important relationship for polarization, was proposed by Börner (1992):

$$l = \frac{\sigma''_{surf}}{\sigma'_{surf}}, \tag{1.25}$$

Weller et al. (2013) perform an analysis with 63 datasets from the literature of sandstones and unconsolidated sediments, and find a linear relation between σ''_{surf} and σ'_{surf}. However, Lévy et al. (2019b) propose that this relation (i.e. equation 1.25) varies with smectite content.

Furthermore, Lévy et al. (2018) propose a model valid for smectites in specific, based off of an equivalent circuit. They propose that the interlayer space in smectites (see figure 1.2) offers a new pathway for electric conduction. They propose the following model:

$$\sigma_{bulk} = a_2\sigma_w + b_2 + \frac{c_2\sigma_w}{1 + \frac{c_2}{d_2}\sigma_w}, \tag{1.26}$$

where, $a_2 = F^{-1}$, $b_2 = \sigma_{EDL}$, $c_2 = X_w = F'^{-1}$, and $d_2 = X_{sol}\sigma_{sol}$. It is worth mentioning that they refer to F' as a formation factor of the interlayer space. Additionally, X_{sol} is the fraction of the solid that helps in conduction, and finally σ_{sol} represents the conductivity of the solid.

1.3.3.2 Physical models

Numerical models

Physical models are based on governing and constitutive equations in physics put in place to describe a particular physical phenomenon. For SIP, we use Maxwell's laws of electromagnetism and a set of constitutive equations, such as Ohm's law (see section 1.2.1). Some authors such as Bücker and Hördt (2013a,b), Bücker et al. (2019), and Hördt et al. (2016) use numerical models of geo-materials at the pore scale and finite-element numerical methods to solve for the SIP signal of a polarizing grain, pore space or pore constriction. This is a

promising approach, but the solution for an upscaling of multiple grains, pores and pore network proves to be too computationally expensive. Therefore, upscaling techniques should be used in order to model the SIP signal of a network of pores (e.g., Maineult et al. 2017).

Complexation models for SIP

Additionally, electro-chemical relations can be used to describe the SIP response of a geo-material. However, a thorough knowledge of physico-chemical parameters is needed in order to model the SIP signal properly. If the model was created for a single polarizing particle, an upscaling technique is also necessary, such as the differential effective medium (DEM) theory.

In particular for clays, some of the most notable advances of physical models for SIP are those of surface complexation of the EDL (e.g., Leroy and Revil 2004; Cosenza et al. 2008; Leroy and Revil 2009; Jougnot et al. 2010; Revil 2012; Okay et al. 2014; Leroy et al. 2017).

One of the most recent complexation models (Leroy et al. 2017) makes use of the electro-neutrality principle and applies it to the base of a clay particle (see Figure 1.2). The total surface charge (Q_0, in C m^{-2}) of the base and the volumetric excess charge in the EDL (Q_v, in C m^{-3}) are calculated as:

$$Q_0 = -\frac{e_0 N_A CEC}{10^3 SS_b}, \tag{1.27}$$

$$Q_v = -\rho_s \left(\frac{1-\Phi}{\Phi}\right) 10^3 SS_0 Q_0, \tag{1.28}$$

where SS_b [m^2 g^{-1}] is the total specific surface area of the base of the clay, SS_0 [m^2 g^{-1}] is the specific surface area of the outer basal surface, ρ_s [kg m^{-3}] is the volumetric mass density of the geo-material, and Φ is the porosity of the geo-material. For the surface conductivity (σ_s, in S m^{-1}), we can define:

$$\sigma_s^*(\omega) = \sigma_s(\omega) + i\omega\epsilon_s, \tag{1.29}$$

$$\sigma_s(\omega) = 2/3\Phi\mu_s f_Q Q_V f(d_k, \tau_k), \tag{1.30}$$

where, ϵ_s [F m^{-1}] is the dielectric permittivity of the clays (solid part), μ_s is the mobility of the ions in the Stern layer, and $f(d_k, \tau_k)$ denotes a convolution product for a distribution of

grains sizes (d_k), with a relaxation time distribution (τ_k). Also note that the partition coefficient (f_Q) is the fraction of the counter-charge in the Stern layer and can be calculated as (considering Q_d, the surface charge of the diffuse layer):

$$f_Q = \frac{Q_\beta}{Q_\beta + Q_d}. \tag{1.31}$$

For the water conductivity ($\sigma^*_w(\omega)$, in S m^{-1}), Leroy et al. (2017) divide it into the conductivity of the free electrolyte (σ^w_n) and of the diffuse layer (σ^w_d) as:

$$\sigma^*_w(\omega) = \sigma_w + i\omega\epsilon_w, \tag{1.32}$$

$$\sigma_w = \Omega^w_n \sigma^w_n + \Omega^w_d \sigma^w_d, \tag{1.33}$$

where, σ_w is the DC (direct current) conductivity of water. Also Ω^w_n and Ω^w_d are the volume fractions [no units] of the free electrolyte and diffuse layer, respectively. Furthermore, the individual conductivities of the free electrolyte and the diffuse layer are calculated as follows:

$$\sigma^w_n = e_0 10^3 N_A \sum_{k=1}^{N} z_k \mu^w_k C^w_k, \tag{1.34}$$

$$\sigma^w_d = e_0 10^3 N_A \sum_{k=1}^{N} z_k \mu^d_k C^w_k exp\left(-\frac{z_k e_0 V_m}{k_B T}\right), \tag{1.35}$$

where N is the different number of ions present in the aqueous solution, and k represents a particular ion species, V_m [V] is the average electric potential in the diffuse layer. Finally the complex electrical conductivity ($\sigma^*(\omega)$) of the clay sample, which is a dilute suspension, can be modeled as:

$$\sigma^*(\omega) = \sigma^*_w(\omega) + \sigma^*_s(\omega) \tag{1.36}$$

I have tried to summarize one of the most recent complexation models proposed by Leroy et al. (2017), as the previous models can be understood from this one. It is worth mentioning, that this model was created for clay dilutions, and an appropriate model for lower porosities is still needed.

Leroy and Revil (2004) present an electrical triple layer (TLM) model for clays, where they calculate a specific surface conductivity and ζ potential for salinities and pH. However, they

do not offer an expression for the complex conductivity of a clay sample. Leroy and Revil (2009) provide an expression for the complex conductivity using a DEM approach (Bruggeman 1935; Hanai 1960) for a liquid and solid phase. They also introduce a dielectric term for the Maxwell-Wagner polarization. Jougnot et al. (2010) developed a model for unsaturated conditions for Callovo-Oxfordian clay rocks, where they introduced a water saturation parameter. Revil (2012) proposes the POLARIS model, where he offers an expression for the real conductivity that depends on the fluid conductivity, μ_S (ionic mobility in the Stern layer, in $m^2\ s^{-1}\ V^{-1}$), Q_V, the formation factor (F), and the cementation exponent (m, from Archie's law). He expresses the imaginary conductivity as a function of porosity, μ_S, f_Q, and Q_V.

Furthermore, Leroy et al. (2017) used the Lyklema et al. (1983) model to explain the measured SIP relaxation times (τ). This expression can be written as:

$$\tau = \frac{r^2}{2DM}. \tag{1.37}$$

In Lyklema et al. (1983), D [$m^2\ s^{-1}$] is the mean ionic diffusion coefficient in the Stern layer and M [no units] describes the effects of the diffuse layer on the Stern polarization, which can be computed using a surface complexation model.

1.4 Upscaling techniques

Most physical models are created for a single conducting particle submerged in a conductive fluid. However, this is not representative of the electrical phenomena happening at the laboratory scale sample, thus upscaling techniques are used. Upscaling techniques take a basic and small scale electrical phenomenon and are able to calculate what the electrical response of a larger scale would be. Note that the upscaling techniques could be created for other purposes than electrical phenomena but for the sake of the discussion of this thesis, I will only mention the ones that relate to electrical phenomena.

1.4.1 Differential effective medium

The differential effective medium (DEM) approach takes an explicit physical relation for a single polarizing particle and iteratively adds more particles until a determined condition has been satisfied (for example until the amount of particles in a volume matches the one of the rock sample).

The BHS (Bruggeman-Hanai-Sen) approach refers to the theory proposed by Sen et al. (1981) but previously worked by Bruggeman (1935) and Hanai (1960). They present a self-similar model, where iteratively inclusions of a dielectric permittivity ϵ^*_m [F m^{-1}] are added onto an aqueous solution with dielectric permittivity ϵ^*_w [F m^{-1}] until the porosity Φ of the rock sample has been achieved, yielding a total resulting dielectric permittivity ϵ^* of the geo-material (for spherical particles), as in:

$$\Phi = \left(\frac{\epsilon^*_m - \epsilon^*}{\epsilon^*_m - \epsilon^*_w}\right)\left(\frac{\epsilon^*_w}{\epsilon^*}\right)^{1/3}. \tag{1.38}$$

Cosenza et al. (2008) used this approach to better understand the Maxwell-Wagner polarization of a variety of clayrocks. They conclude that micropores affect the polarization and conductivity of these samples in the 0.1 to 10^4 Hz range. Additionally, Okay et al. (2014) introduce a model for a clay-sand mixture, using a DEM approach to calculate the complex conductivity of a clay-sand mixture of a specific porosity.

1.4.2 Pore network modeling

The basic physical principle used in pore network modeling (PNM) is conservation (Bernabe 1995). This means that there are no sinks or sources inside the pore network. Meshes of pores are built with a particular geometry (e.g., rectangular, hexagonal, triangular) and are connected through a node. The size of the pore needs to be explicit (i.e. radius of the pore). The goal of PNM is to determine the response of the whole network subjected to an external gradient (for example a voltage) given a particular condition of each pore (for example particular radius).

Maineult et al. (2017) and corrected by Maineult (2018) propose a PNM to obtain the SIP response of randomly sized tubes (see figure 1.7). They randomly distribute the radius size to each pore, given a pore size distribution. They obtain the electrical response of the system using the expression:

$$\tau = \frac{r^2}{2D}. \tag{1.39}$$

Similarly to equation 1.37, τ represents the relaxation time, r the radius of the pore, and D here represents the ion diffusion coefficient in the Stern layer. Later, the SIP response is calculated through a Pelton model.

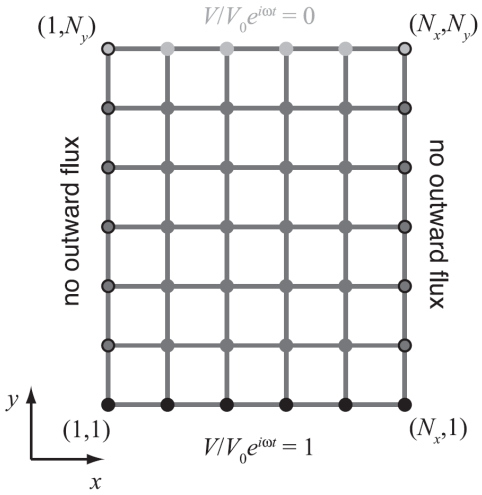

Figure 1.7: Example of a square PNM of size N_x and N_y (taken from Maineult et al. 2017).

Furthermore, PNM can become a complex conductance network model, when instead of tubes (i.e. pores in this case) we have conductances (or resistances), connected through a node and we calculate the SIP response of the whole conductance system. Note that in this case, it is not necessary to explicit a pore radius, only the individual conductance (or resistance) of each connection. In this case, we solve Ohm's law for the whole system given an external applied voltage.

CHAPTER

2 Materials and methods

This chapter gives a thorough description of the laboratory tests and logistics that were put into action in order to find the most appropriate laboratory protocol for the SIP measurements of clays. I divide this chapter in the following manner:

- Non-polarizable electrodes. In this study, I used Cu-$CuSO_4$ non-polarizable electrodes. Several tests were carried out to determine a suitable protocol for Cu-$CuSO_4$ non-polarizable electrodes. Furthermore, I propose other available approaches to non-polarizable electrodes.
- Water content tests in clays. I created a laboratory protocol to make the clay samples that I measured the SIP signal in. This involves a list of steps to go from clay powder and water (at a specific salinity) to a clay sample with a specific plasticity. This allows for repeatable SIP measurements.
- Sample holder and its structure. I created a sample holder and an external structure that would allow for repeatable SIP measurements.
- Outside of the steps involving the preparation of the SIP laboratory experiments, I did further chemical analyses on an aqueous solution that had reacted to different clays.

2.1 Non-polarizable electrodes

All SIP measurements require a pair of injecting electrodes, and a pair of voltage measuring electrodes. The pair of measuring electrodes is particularly important in SIP, as they must not polarize in order to not contaminate the SIP signal. Meaning, if the electrodes polarize then the measured polarization signal comes from both the electrode polarization and from the probed sample. To avoid this, non-polarizable electrodes are used in SIP measurements.

There are two types of electrodes, electrodes of the first and second kind. Electrodes of the first kind need to have an equilibrium between the ions in the solution and the metal element (e.g. Cu-$CuSO_4$ electrodes)(Maineult et al. 2004). Electrodes of the second kind need to have an equilibrium between the metal element, a salt covering the metal element and the solution into which all of this is imbibed (e.g. Ag-AgCl electrodes)(Jougnot and Linde 2013). The electrodes used in this thesis are Cu-$CuSO_4$ electrodes, following the work of Maineult et al. (2004) and Kremer (2015) and Kremer et al. (2016). The exact protocol that I used to build my Cu-$CuSO_4$ electrodes is presented in Appendix 1. In figure 2.1 I present a diagram of the Cu-$CuSO_4$ electrodes I used for this thesis. These electrodes consist of a tube filled with a $CuSO_4$ and gelatine solution, plugged on one end with a rubber plug with an inserted copper wire, and on the other end the tube is plugged by a ceramic porous cap. Threaded bulkhead connectors are used to place the electrode in a fixed position in the sample holder.

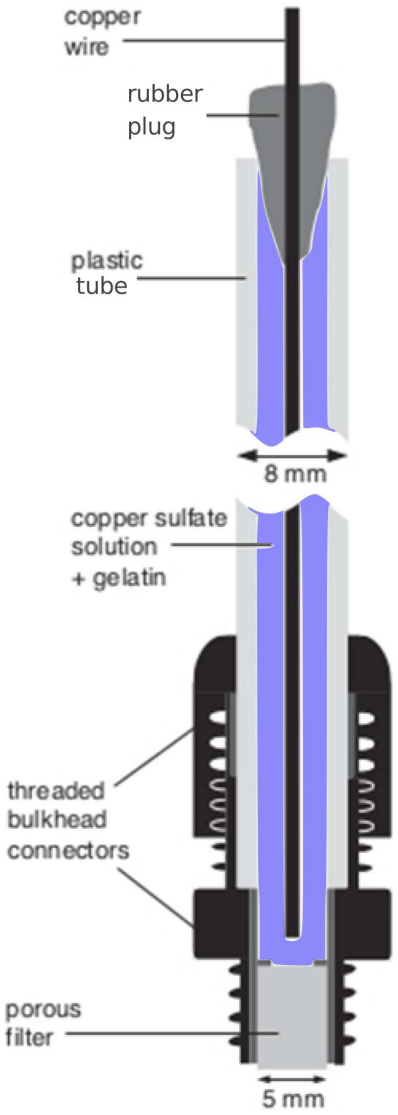

Figure 2.1: Sketch of the Cu-$CuSO_4$ electrodes I built for this thesis (modified from Kremer et al. 2016).

2.1.1 Electrode testing

In order to measure the polarization of the electrodes (or lack thereof) an SIP measurement is done. To do so, I fill a recipient with very saline water (around 36.8 mS cm^{-1}), I locate two current injecting electrodes made of stainless steel at opposing sides of the recipient, with the two potential electrodes to be tested in the middle (all located in a straight line, see figure 2.2). All four electrodes barely touch the water (see figure 2.2). This is a way to test the electrode polarization as very saline water should ideally have a very small phase. Knowing that phase can be represented as:

$$\varphi = -arctan\left(\frac{\sigma''}{\sigma'}\right), \tag{2.1}$$

where in very saline water $\sigma' >> \sigma''$, therefore the phase of very saline water should be close to zero. If the measured phase is not close to zero, that means that the measured polarization does not come from the very saline water but from the electrodes themselves. It is worth mentioning that it is normal to have a small polarization signal at high frequencies (>100 Hz), coming from impedance effects of the electrodes (see Huisman et al. 2016; Wang and Slater 2019). The idea is to build electrodes with the least amount of internal polarization possible. All the electrodes batches used in this study were tested in this same manner.

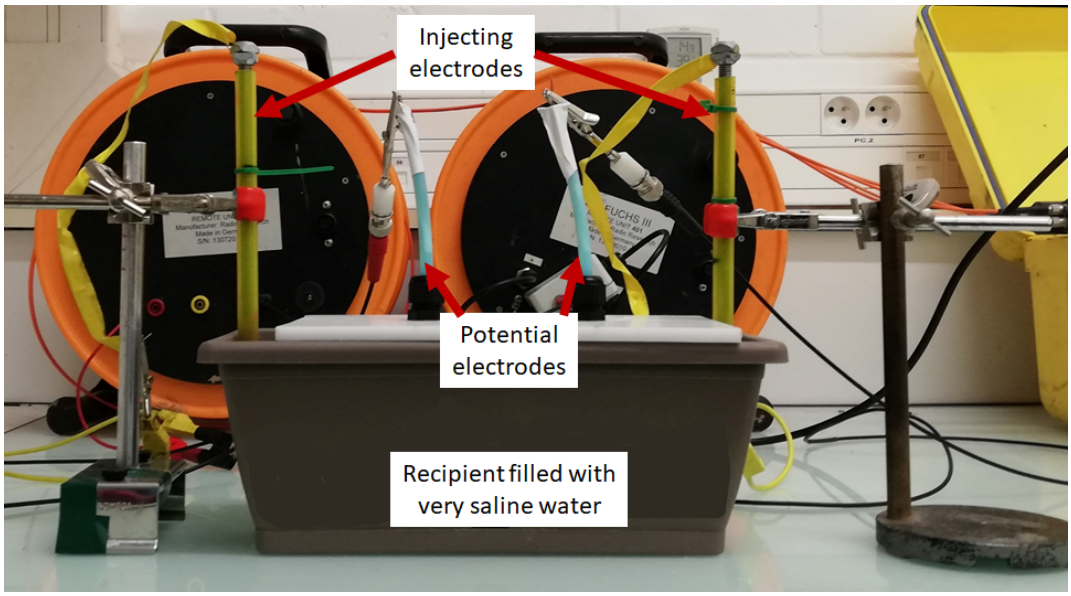

Figure 2.2: Set-up to test non-polarizable electrodes.

2.1.2 Path to finding a good electrode design

Type and amount of gelifying agent

A problem with electrodes of the first kind (including Cu-$CuSO_4$ electrodes) is that the chamber holding the aqueous solution ($CuSO_4$ in this case) may leak out of the chamber through the porous plug by diffusion. Kremer (2015) did an extensive study on the type of porous caps that can be used to plug the electrodes. Additionally, Kremer (2015) and Kremer et al. (2016) present a test using a gelifying agent to decrease the leakage of the solution (i.e. reduce the ionic mobility). I based the electrode construction off of their work. However, I decided to do further tests. I tested the concentration of $CuSO_4$, and type (and amount) of gelifying agent.

On table 2.1 I present a synthesis on the tests performed to obtain a suitable pair of non-polarizable Cu-$CuSO_4$ electrodes. Note, that all solutions were made from an amount of penta-dehydrated $CuSO_4$, 100 ml of de-ionized water, and an amount of a gelifying agent. For the first test, I was advised by Feras Abdulsamad to use 0.9 g of agar-agar. As to the amount of penta-dehydrated $CuSO_4$, I was advised to use an amount that would saturate the solution. The amount of $CuSO_4$ that saturates a solution varies with temperature, since these solutions are heated up to 100 °C, I decided to test the amount of $CuSO_4$ based of the temperature range I would heat the solution to. With the first test, I was able to narrow down the amount of penta-dehydrated $CuSO_4$, as most electrodes showed significant signs of precipitation (negative results, marked as "-" in table 2.1). I decided that visible signs of early precipitation in the electrodes meant the lack of chemical equilibrium in the solution. Constant chemical reactions within the solution itself could potentially affect the measured SIP signal.

For the second test, I decided to slightly increase the amount of agar-agar, as the first batch of electrodes did not all gelatinize. I decided also to narrow down the search on the proper amount of penta-dehydrated $CuSO_4$ needed for the electrode construction. The pair of 32 g of penta-dehydrated $CuSO_4$ still presented precipitation. To test these electrodes, I measured the SIP signal of the 23, 26 and 29 g of $CuSO_4$ electrodes in a recipient filled with saline water. For an improved readability of this text, I will not present the SIP measurements of all the electrode tests, just the final and most relevant tests. I singled out the pair of electrodes using 23 g of $CuSO_4$ because they had the best SIP signal. For the third test, I decided to vary the amount and type of gelifying agent. None of these electrodes precipitated.

To decide which pair of electrodes were optimal, I measured their SIP response (see figure 2.3), at different times after the making (the day after making the electrodes, a month later, and two months after construction). It is worth mentioning that in figure 2.3c and f, the SIP signal of the agar-agar electrodes is not presented, because the electrodes had visibly dete-

Table 2.1: Chronological tests to obtain a suitable pair of non-polarizable Cu-$CuSO_4$ electrodes. All these tests were done in 100 ml of de-ionized water. Note that by + and - in this table, I mean positive or negative results. By positive, I mean that the electrodes did not show any visible sign of precipitation, by negative I mean that they did show visible signs of precipitation.

Test	Amount of $CuSO_4$ [g]	Amount of gelifying agent [g]	Type of gelifying agent	Result of test	Tested with SIP
Range of	20	0.9	agar-agar	+	no
$CuSO_4$	40	0.9	agar-agar	-	no
with	60	0.9	agar-agar	-	no
agar-agar	80	0.9	agar-agar	-	no
Range of	20	1.2	agar-agar	+	no
$CuSO_4$	23	1.2	agar-agar	+	yes
with	26	1.2	agar-agar	+	yes
agar	29	1.2	agar-agar	+	yes
agar	32	1.2	agar-agar	-	no
Type and	23	1.2	agar-agar	+	yes
amount of	23	2.2	gelatine	+	yes
gelifying agent	23	4.4	gelatine	+	yes

riorated and I decided it was not worth measuring their SIP signal (at this time I was trying to find the best possible electrodes, and at that moment I had already discarded the agar-agar electrodes as candidates). From figure 2.3d and e, we can see that the pair of electrodes with the best phase spectra, at the medium and lowest frequencies (mHz to 100 Hz) are the electrodes with two gelatine leaves (red dots). In figure 2.3f, we can see that the best overall pair to describe the spectra was the pair with two gelatine leaves. I therefore chose to use electrodes using 23 g of $CuSO_4$ and two gelatin leaves.

Diffusion test

Jougnot and Linde (2013) describe a procedure to test the leakage of a pair of non-polarizable electrodes. Following their procedure, I did a diffusion test (see figure 2.4), that consisted in putting the pair of electrodes in a beaker with 100 ml of de-ionized water and measuring the conductivity of the solution with time (figure 2.4a), to test which pair of electrodes diffused the most. I also tried seeing how quickly the electrical conductivity was changing with respect to time (figure 2.4b). After all these tests, I chose the pair of electrodes with 23 g

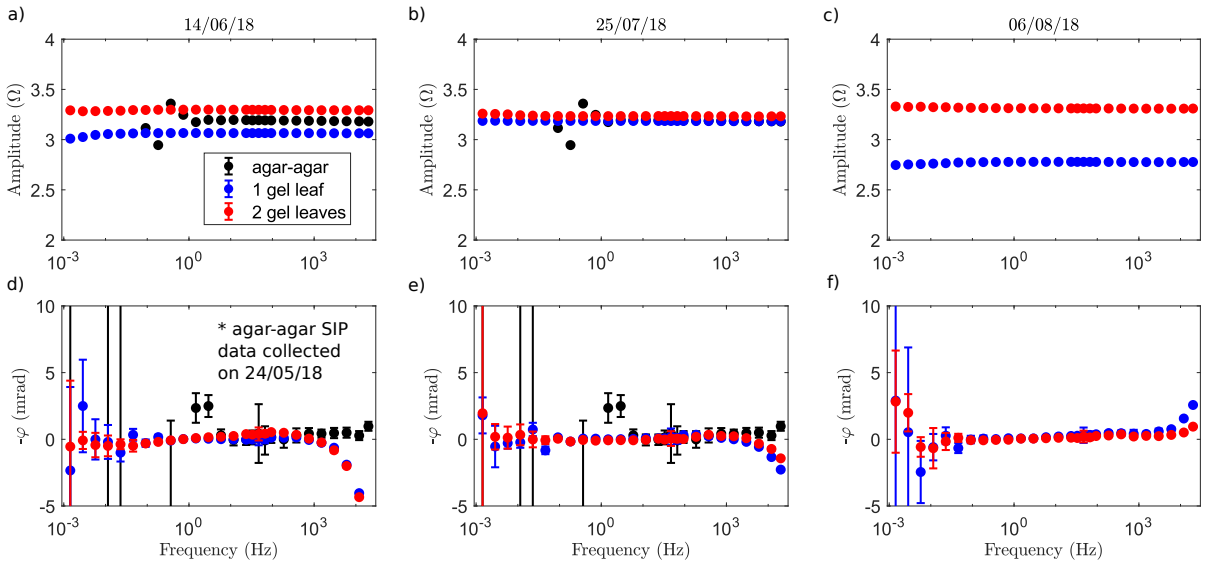

Figure 2.3: SIP test of electrodes: a) Amplitude of constructed electrodes 24h after construction, b) amplitude a month later, and c) amplitude roughly two months later. d) Measured phase of electrodes 24 h after construction, e) phase roughly one month after construction, and f) roughly after two months after construction. These tests were done in very saline water.

of $CuSO_4$ (in 100 ml of de-ionized water) and two gelatin leaves (4.4 g of gelatin) to be the optimal for my laboratory measurements. Both the time-lapse SIP measurements (figure 2.3) and the diffusion test (figure 2.4) show that the most enduring electrodes are the 23 g of $CuSO_4$ and two gelatin leaves.

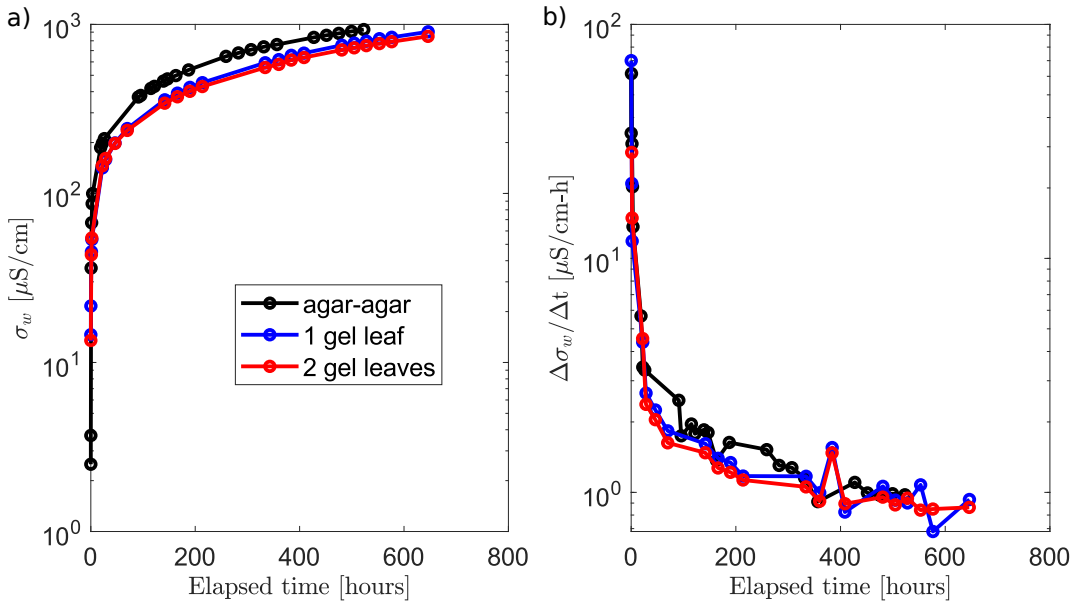

Figure 2.4: Diffusion test of electrodes: a) Increase of electric water conductivity and b) change of conductivity with respect to time. These tests were done in initially de-ionized water.

$CuSO_4$ saturation of porous caps

It is also worth mentioning that in the first batch of electrodes made in this manner (23 g

of $CuSO_4$ and two gelatin leaves), I had heated the water for the $CuSO_4$ solution at around 100 °C and some electrodes started diffusing the solution through the porous cap at the moment of their construction. These 23 g of $CuSO_4$ and two gelatin leaves are the ones tested previously in this chapter in figures 2.3 and 2.4. For the posterior electrode constructions, I decided to decrease the temperature of the mixture as to avoid this diffusion in the construction process. While I reduced the temperature in the mixing process to 40 °C, I was able to eliminate the leakage in the construction process. In figure 2.5 I compare the SIP signal of the original electrodes (made at 100 °C, red dots) versus the new ones (made at 40 °C, blue dots). We can see that the electrodes built at 40 °C had a relevant polarization signal (phase below -100 mrad). The porous caps in the electrodes built at 40 °C were not blue. I made the assumption that they were dry and that they were not saturated in a $CuSO_4$ solution. To fix this problem, I added a step in the protocol (see figure 2.6), a saturation of $CuSO_4$ solution (with the same $CuSO_4$ concentration as the solution inside the electrode) of the porous caps. In order to saturate the porous caps, I suctioned the $CuSO_4$ solution with a syringe. After adding this step, when the new electrodes were tested they had again a less polarized signal (smaller phase for the whole frequency range) as seen in figure 2.5 (black dots).

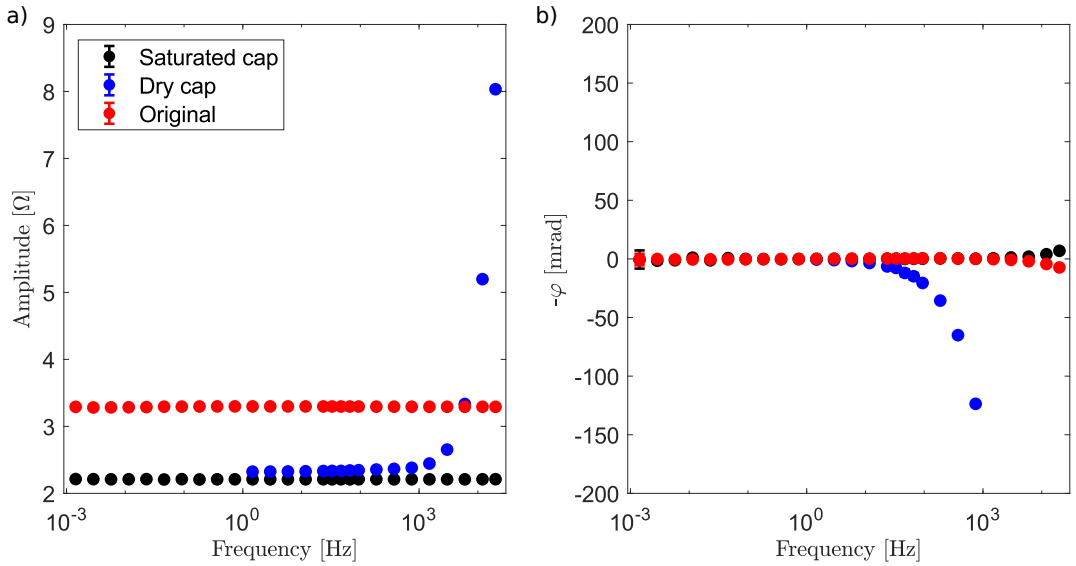

Figure 2.5: SIP measurement of original electrodes (first good batch), electrodes with a dry cap (second attempt at making electrodes), and electrodes with a Cu-$CuSO_4$ saturated cap (third batch of electrodes). a) Amplitude of SIP measurements and b) phase of SIP measurements. These electrode tests were done in very saline water.

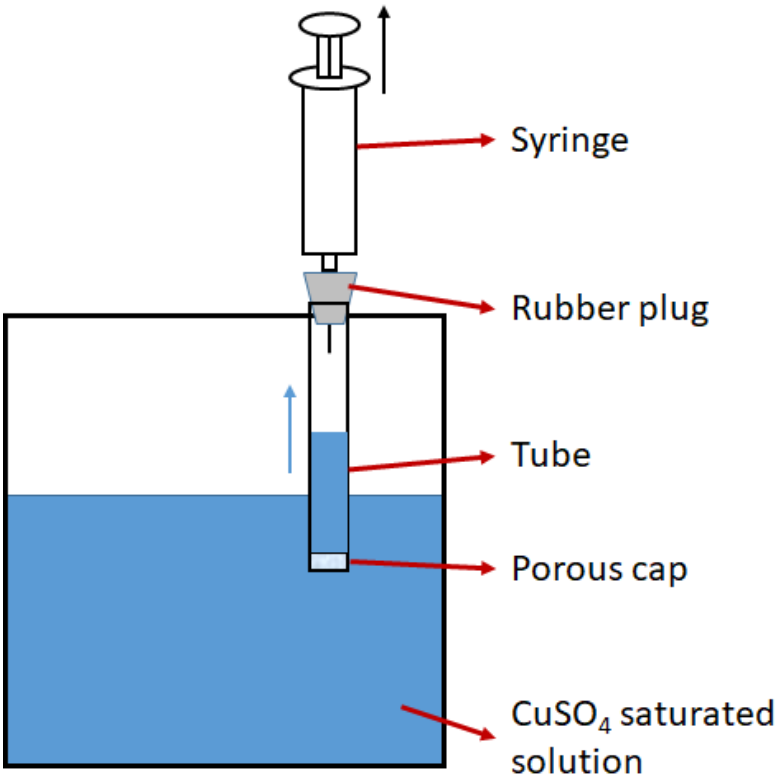

Figure 2.6: Technique used to saturate the porous caps, previous to building the electrode.

2.1.3 Brass electrodes testing

Building Cu-$CuSO_4$ electrodes is a tedious task that needs to be repeated every other month or so. This is why some researchers such as Huisman et al. (2016) have proposed to use brass electrodes (a brass rod) in contact with fluid from the same salinity as the one saturating the rock sample (see figure 2.7b and c).

The brass rod is retracted in a tube (figure 2.7b), so the streamlines of the SIP measurements will not pass through the metal, as the metal is connected to the sample through the liquid of the pore solution but is not inserted in the sample. This is ideally supposed to work, as what would create polarization is the contact between a metal and the rock sample. If the current lines are not in contact with the metal, no polarization should occur.

I purchased a few brass rods with a 5 mm diameter, with standards BS2874/CZ121M (1986)BS EN 12164/CW614N (from the specification sheet of the manufacturer). I retracted the electrodes by 1 cm from the end of the tube (see figure 2.7b) and filled this space with the same salted water as in the recipient (figure 2.7). I measured the SIP signal with these electrodes (see figure 2.8, this dataset corresponds to the date 25-06-19). I also attempted sanding the rods (in case the brass rods had some coating, see figure 2.7a), re-filled the recipient with new

very saline water and re-measured the SIP signal (see figure 2.8, this dataset corresponds to the date 26-06-19). The SIP signals I measured are presented in figure 2.8. The errorbars of these measurements reached 1500 mrad, and the lowest measured phases were around 400 mrad; significantly higher than the SIP signals I had measured in the clay samples. Something was obviously very wrong with my set-up. Many researchers (e.g., Huisman et al. 2016; Izumoto et al. 2020) have been able to use the brass electrodes without problems. I am not attempting to discourage the reader on the use of these electrodes, I am merely presenting a way that does not work so the reader does not follow this path. I am not sure why this attempt did not work. Although, brass is an alloy of metals, I wonder if a specific type of alloy is needed in order to get good measurements. I did not further investigate these types of electrodes for SIP, for time purposes. In the future, I would like to contact these researchers for more details on the use of their electrodes.

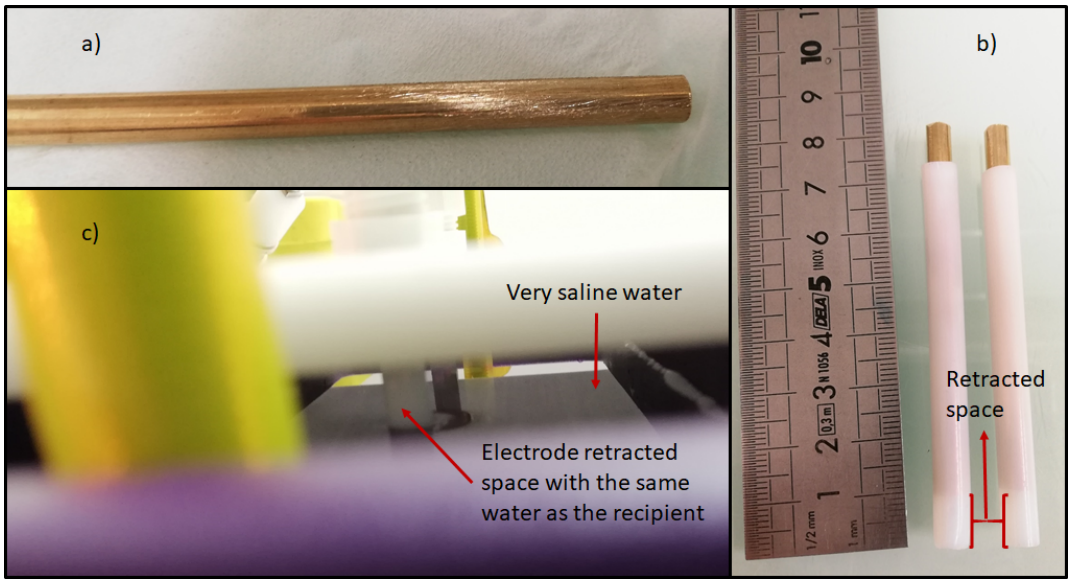

Figure 2.7: Elements of the brass electrode testing: a) sanded brass rod, b) brass rod inside tube retracted by 1 cm, and c) the SIP testing of the brass electrodes.

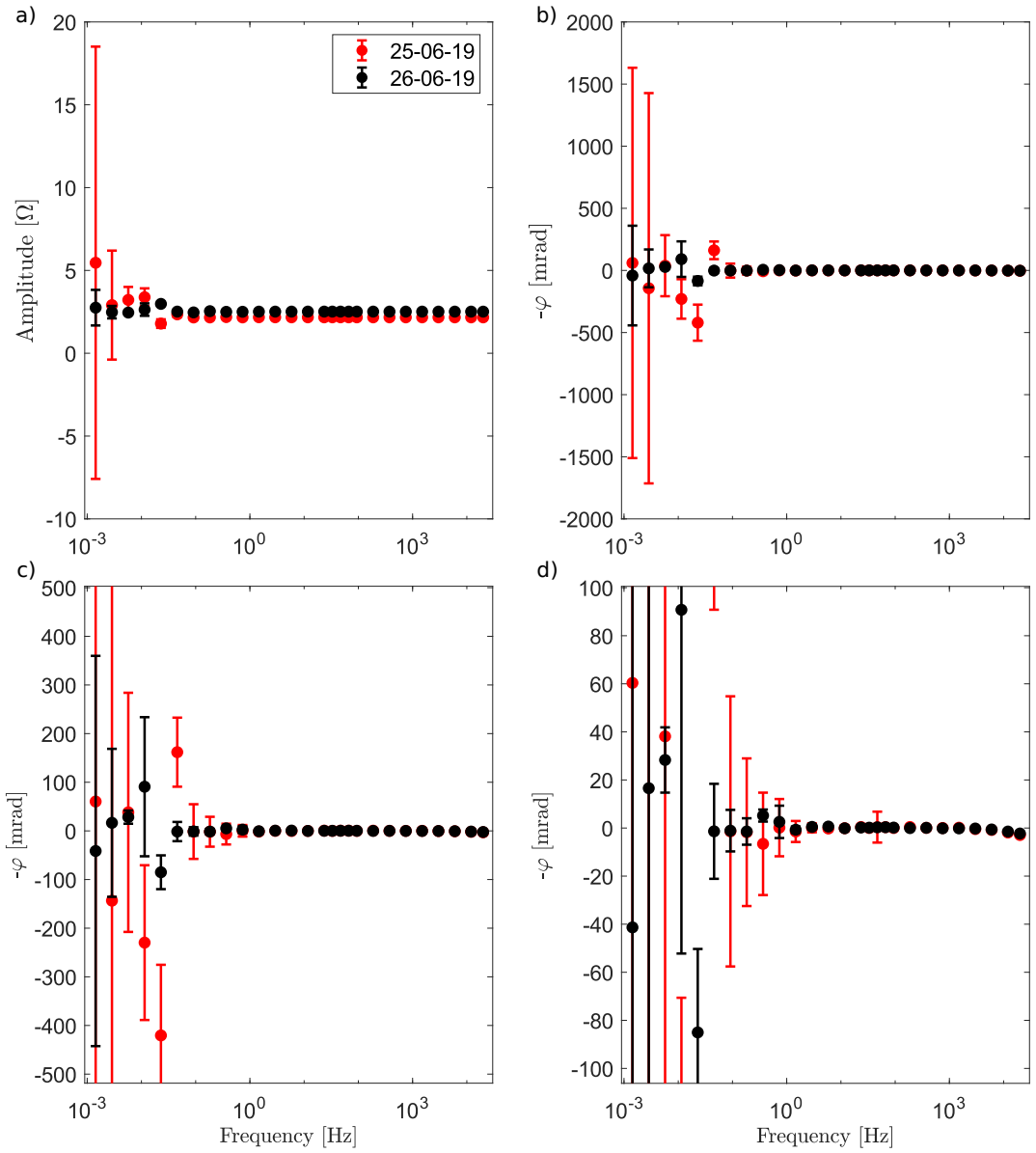

Figure 2.8: SIP measurements of brass electrodes: a) Measured amplitude, b) measured phase, c) measured phase zoomed-in between -500 and 500 mrad, and d) measured phase zoomed-in between -100 and 100 mrad.

2.1.4 Electrode correction

Another electrode-related improvement I attempted was the SIP signal electrode correction. Huisman et al. (2016) proposed a way to correct SIP measurements in a rock sample. They measure the SIP signal in the traditional configuration with 4 electrodes, then they measure the reciprocal. They use both measurements to determine the electrode impedance and substract it from the measured SIP signal. Later Wang and Slater (2019) proposed another correction in which the SIP signal is measured in 4 different configurations, then the metal of the electrode (copper wire for Cu-$CuSO_4$ electrodes) is inserted deeper gradually. At each metal insertion step, the 4 SIP configurations are measured. All of these measurements are

stored and then plotted all together in a phase vs electrode impedance plot for each frequency. Allowing to infer the phase for zero electrode impedance. In the results shown by Wang and Slater (2019) they were able to remove the high frequency noise of the measurements. I attempted to do this, however, after all the calculations I obtained a noisier signal than the original one I measured (see figure 2.9). I therefore did not remove the electrode error from the SIP measurements in this study. Again, this does not mean that the protocol proposed by Wang and Slater (2019) does not work. Here, I have some suggestions at elements that have to be taken into account for this test. Elements I had a hard time with in the measuring part of this test.

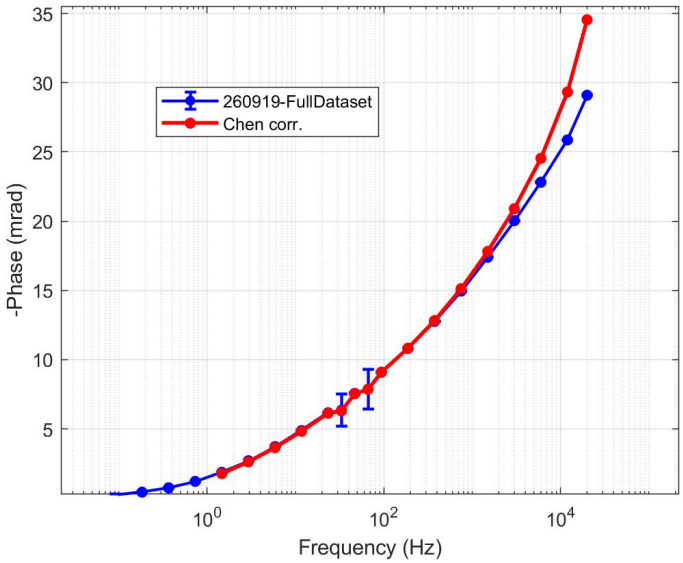

Figure 2.9: Electrode correction following the procedure proposed by Wang and Slater (2019).

First, electrodes with gelatin will be greatly altered when disturbing the created gelatin substance by inserting and moving the copper wire. Second, I had the rubber plugs cut in half to be able to move the copper wire easily. However, when I moved the wire (inserting or removing) the rubber plug would open right by the middle and I had to readjust it many times. I understand if all this manipulation had something to do with the lack of positive results. My suggestion then would be, thinking before doing this manipulation in a system were the copper wire can easily be moved but can be fixed for a period of time somehow to get the 4 SIP measurements with the same copper wire length.

2.2 Tests for water content

In this thesis, I used six types of clays: red, green, and beige montmorillonite, kaolinite, illite and a Boom clay. Boom clay is a clayrock used for nuclear waste storage in Belgium (Ortiz

et al. 2002). I measured the SIP signal of the six types of clay on de-ionized water, a 10^{-2}, and a 1 mol L^{-1} of NaCl solutions. For time constraining reasons, for salinities of 10^{-3} and 10^{-1} mol L^{-1} of NaCl, I only measured the SIP signal of: red and green montmorillonite, kaolinite, and illite. The SIP results and mineralogy and chemical analyses of the used clay materials will be presented in detail on chapter 3. In this section I present the procedure I followed to obtain the correct gravimetric water contents for the clay samples in which I measured the SIP signal.

A goal of the thesis was to create synthetic clay heterogeneities and locate them inside a sample holder to later measure their SIP signal. Indeed, when two heterogeneities are in physical contact both have to be of similar mechanical properties, so one clay does not "push" the other out of the sample holder easily. That is, both have to have similar plasticities. The goal was to have something like two different colors of "play-doh" together. I followed the Atterberg limits (liquid limit and plastic limit) presented in Wagner (2013) for different types of clays to create the clay samples. This is a rough guide, so I decided that before starting every SIP dataset (one salinity at a time), I would do a pre-test of gravimetric water content (m_{water}/m_{solid}) on each of the clay powders I had (see figure 2.10 for an example). I started with 100 g of each type of clay powder (figure 2.10a), and gradually added water (at the specific salinity, as seen in figure 2.10b) until I reached a water content that would allow me to mix properly with a spoon in the testing period (for the SIP measurements I used an electric drill to mix properly). When I obtained the correct plasticity that would allow me to easily mix, I would locate the clay samples on top of a small polyurethane foam to let the excess water evaporate (figure 2.10c). I regularly checked (twice a day) these clay samples until the right plasticity had been achieved (figure 2.10d). By checking, I mean I would physically touch the clay sample to see if it had the correct plasticity (if I was able to make a small clay ball, for example). In every step, I measured the mass of the system to keep a check on the gravimetric water content of the samples. Only until I had a measure of the correct water contents for a desired plasticity, I would start the protocols for the SIP measurements.

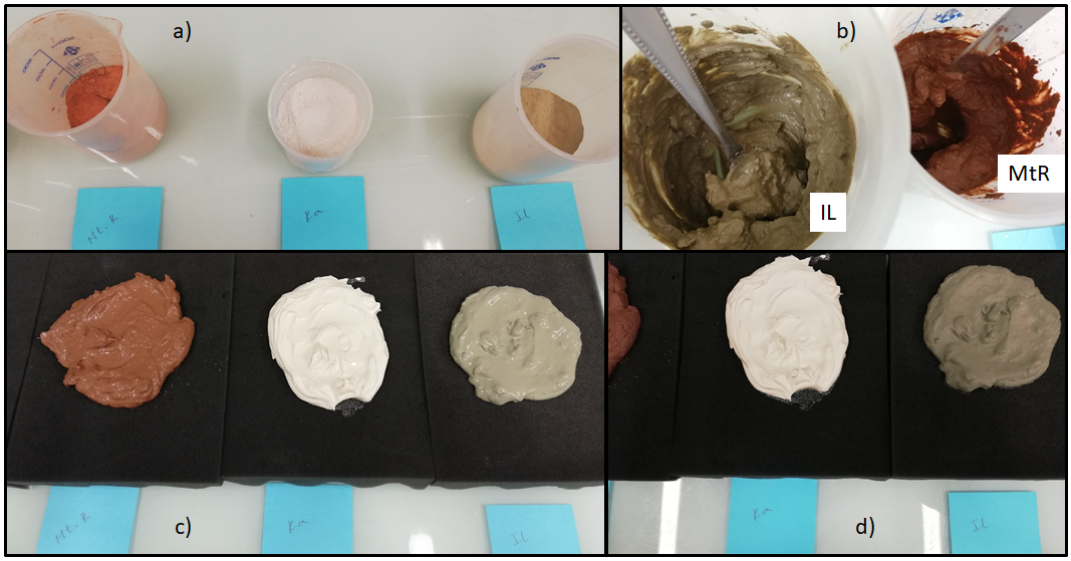

Figure 2.10: Demonstration of a test to determine the correct initial and final water contents: a) Clay powder, b) process of water addition to clay powder, c) optimal initial water content , and d) optimal final water content.

Furthermore, as a way of sharing this protocol I would like to present all the water contents (initial and final water content) I used for each type of clay and for each salinity. By initial water content, I mean the water content that allows for mechanical mixing of the sample. By final water content, I mean the water content the clay samples had in the SIP measurements (with the correct plasticity). The water contents per salinity are presented in tables 2.2, 2.3, 2.4, 2.5, and 2.6.

Table 2.2: Water contents used in the creation procedure of the clay samples used for the SIP measurements with initially de-ionized water.

Clay sample	**Initial water content**	**Final water content**	**Initial salinity**
Red mont.	1.21	0.71	D.W.
Green mont.	1.50	1.02	D.W.
Beige mont.	1.25	0.75	D.W.
Kaolinite	1.00	0.48	D.W.
Illite	0.81	0.49	D.W.
Boom	0.70	0.40	D.W.

D.W. means de-ionized water

Table 2.3: Water contents used in the creation procedure of the clay samples used for the SIP measurements with an initial salinity of 10^{-3} mol L^{-1} of NaCl.

Clay sample	**Initial water content**	**Final water content**	**Initial salinity [mol L^{-1}]**
Red mont.	1.01	0.63	1×10^{-3}
Green mont.	1.33	0.96	1×10^{-3}
Kaolinite	0.76	0.51	1×10^{-3}
Illite	0.77	0.41	1×10^{-3}

Table 2.4: Water contents used in the creation procedure of the clay samples used for the SIP measurements with an initial salinity of 10^{-2} mol L^{-1} of NaCl.

Clay sample	**Initial water content**	**Final water content**	**Initial salinity [mol L^{-1}]**
Red mont.	1.00	0.60	1×10^{-2}
Green mont.	1.36	0.91	1×10^{-2}
Beige mont.	1.33	0.75	1×10^{-2}
Kaolinite	0.81	0.55	1×10^{-2}
Illite	0.80	0.46	1×10^{-2}
Boom	0.77	0.39	1×10^{-2}

Table 2.5: Water contents used in the creation procedure of the clay samples used for the SIP measurements with an initial salinity of 10^{-1} mol L^{-1} of NaCl.

Clay sample	**Initial water content**	**Final water content**	**Initial salinity [mol L^{-1}]**
Red mont.	1.00	0.66	1×10^{-1}
Green mont.	1.33	0.93	1×10^{-1}
Kaolinite	1.00	0.54	1×10^{-1}
Illite	0.76	0.43	1×10^{-1}

Table 2.6: Water contents used in the creation procedure of the clay samples used for the SIP measurements with an initial salinity of 1 mol L^{-1} of NaCl.

Clay sample	**Initial water content**	**Final water content**	**Initial salinity [mol L^{-1}]**
Red mont.	1.00	0.67	1
Green mont.	1.27	0.85	1
Beige mont.	1.00	0.78	1
Kaolinite	0.76	0.44	1
Illite	0.75	0.40	1
Boom	0.76	0.47	1

According to Mitchell and Soga (2005), the concentration and valence of ions present in the pore water of clay samples affects the liquid and plastic limits. At the highest salinity, we can see a decrease of the final water content for almost all clay samples.

2.3 Sample holder

I would like to comment on the sample holder and the external sample holder structure I built. An important amount of work was put into the conception of the sample holder, thus I think some comments are needed.

2.3.1 Comments on sample holder construction

One of the goals for this thesis was to create clay heterogeneities. There was a need for a sample holder where clay heterogeneities could be located without major disruption to the sample (such as inserting air bubbles). That is, a sample holder that could be opened longitudinally. The best solution I found for this problem was a "sushi bazooka"; a plastic device created to locate sushi ingredients inside, close it giving the sushi ingredients the cylindrical shape, and then pushing it out. I transformed these devices into the sample holders by slightly modifying them. The dimensions of the sample holders are presented in table 2.7 and the complementary figure 2.11 showing the dimensions of the sushi bazooka.

Table 2.7: Dimensions of sample holder (or "sushi bazooka").

Symbol	Element	Size [mm]
L	Total length	229.32
ϕ_x	Horizontal diameter	41.20
ϕ_y	Vertical diameter	43.20
d_1	Distance to electrode 1	71.04
d_2	Distance to electrode 2	145.85

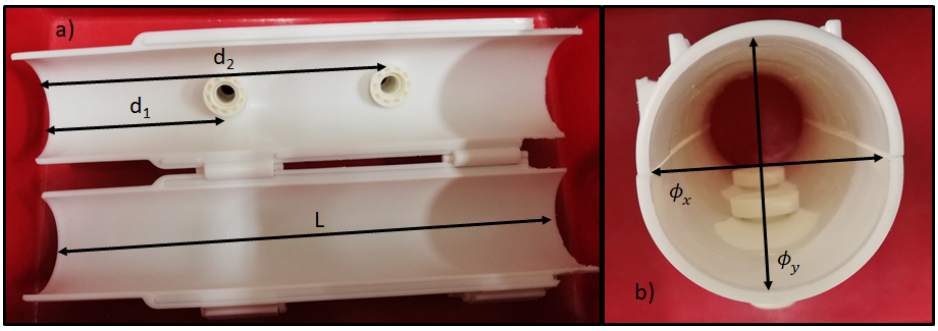

Figure 2.11: Diagram of sample holder: a) open longitudinally with the corresponding electrode separation and b) a side view demonstrating the vertical and horizontal diameter of the sushi bazooka.

I used a pair of stainless steel cylinders as injecting electrodes. There was a need to create a structure to hold the injecting electrodes in a consistent manner. The first attempt of external structure involved two parallel plastic rectangles, held together by four plastic threaded rods (one for each corner of the rectangle) and the sample holder (i.e. "sushi bazooka") located in the middle. A problem arose because it was not possible to locate the sample holder in the same exact location repeatedly. For this, I created an external structure with acrylic sheets cut by a laser cutter (see figure 2.12a). This allowed the creation of acrylic sheets of the same dimensions with more than millimeter precision. I also cut (with the laser cutter) four holes for the four threaded rods, and a smaller hole located exactly in the middle (to locate a small screw as a guide, see figure 2.12b). The screw guide allows for the sample holder to be located in the same exact position repeatedly.

I think that the use of new available technologies for the general public improved the creation of the sample holder (as the laser cutter). I think the SIP-laboratory community should further explore these new available technologies, such as laser cutters and 3D printers, and incorporate them to their laboratory equipment.

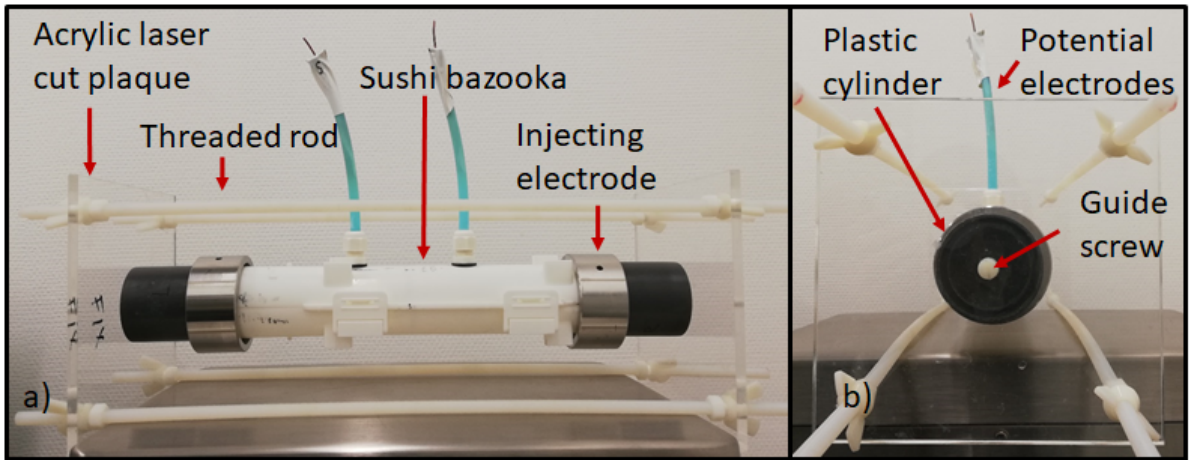

Figure 2.12: Sample holder and the external structure from a (a) frontal view, and (b) side view.

2.3.2 Geometrical factor of sample holder

As presented in equation 1.9, in order to calculate the complex electrical resistivity we need the geometrical factor. For this, often times in the laboratory the sample holder is filled with a solution with a known water conductivity and thus the geometrical factor is obtained through a SIP measurement. However, the sample holder I built is not completely water tight, therefore I could not obtain the geometrical factor from a direct measurement. I decided to obtain the geometrical factor of the sample holder using numerical methods (this had been previously done by Jougnot (2009) and Jougnot et al. (2010)).

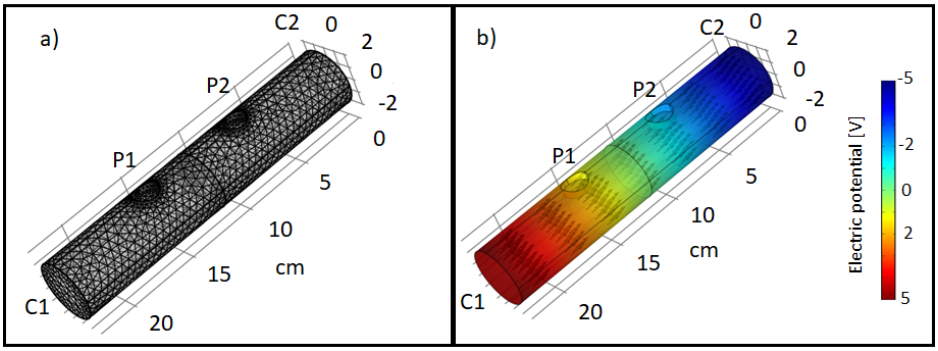

Figure 2.13: a) Mesh of the sample holder in COMSOL, and b) potential distribution within the numerical sample holder in COMSOL.

I created a numerical model of my sample holder in COMSOL (as presented in figure 2.13a), with the same exact dimensions. I input a potential difference on both sides of the sample holder (C1 and C2 as seen in figure 2.13). I located two measuring points and a surface in the exact middle of the sample holder to figure out the current density that passes through the sample holder. The idea is to solve Laplace equation (with appropriate boundary conditions):

$$-\sigma\nabla^2 V = 0. \tag{2.2}$$

For this system, I input a potential difference between C1 and C2 of -5 to 5 V, and I set the electrical conductivity of the medium to be 1 S m^{-1} (ρ = 1 Ω m). COMSOL solves equation 2.2 numerically (finite elements) and provides information about the distribution of the electric potential in the medium, as well as the current density passing through a given area. Knowing the current density, therefore the electrical current, the electric potential, and the electrical conductivity, I am able to obtain the geometrical factor of the sample holder (see subsection 1.2.2). The obtained geometrical factor is 0.018 m.

2.4 Compression and decompression tests

While trying to achieve repeatability of SIP measurements, I realized that I would only get similar electrical spectra when the sample was subjected to the same external pressure. Therefore I created an external structure to support the sample holder, where I could regulate the compression of the sample as presented in figure 2.14. I then decided to test how compression and later decompression would affect the SIP response in clays.

The compression and decompression tests were done as follows:

- Set a clay sample with minimum compression (enough for good electrical contact between the sample and the injecting electrodes), and measure the SIP signal from 91 mHz to 20 kHz. It is worth mentioning that upon setting the sample holder, I made sure both acrylic sheets were perfectly parallel by using a level on both sheets.
- Turn the four wing nuts (visible in figure 2.12) on the movable acrylic sheet by 360°, as to compress the sample. Repeat SIP measurement.
- Repeat previous step for a total of 8 times.
- Turn the four wing nuts (visible in figure 2.12) on the movable acrylic sheet by 360°, as to decompress the sample. Repeat SIP measurement.
- Repeat previous step for a total of 8 times.

In figures 2.15, 2.16, and 2.17, I present one example of the compression and decompression test, for the illite sample with initially de-ionized water. In figures 2.15a and 2.16a, we

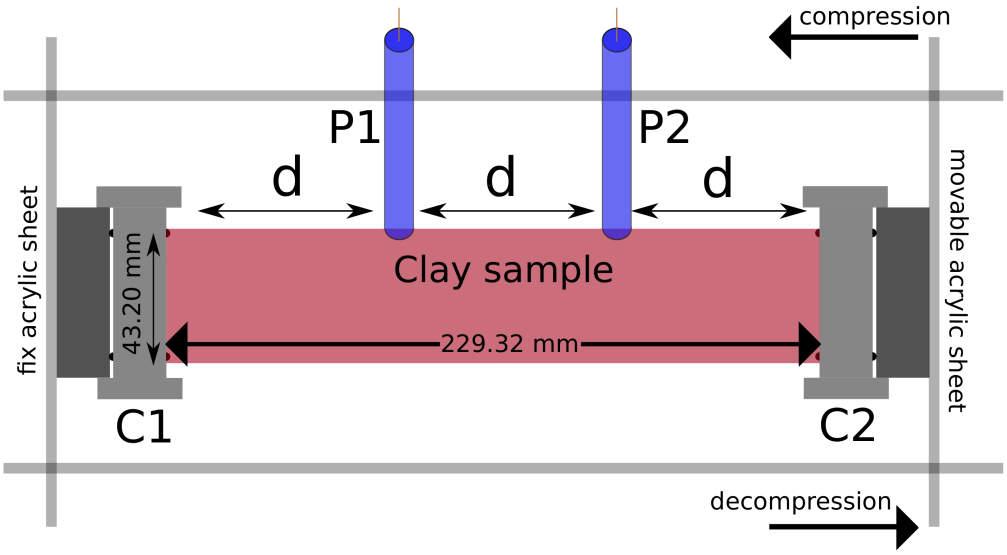

Figure 2.14: Diagram of the sample holder and its external structure, the compression and decompression capability of the system. Note: this figure is merely a sketch of the sample holder but the dimensions are not at a 1:1 scale.

can see that the measured electrical conductivity increases with compression. While, as presented in figures 2.15b and 2.16b, the measured phase remains unperturbed or has negligible changes. I present a hysteresis curve, to see how the conductivity and phase changed with compression (here presented by the number of turns of the wing nut) by plotting uniquely the conductivity at 1.46 Hz vs turns of the wing nut (see figure 2.17). It is evident that for this sample, the electrical conductivity does not go back to its original state. While the phase is minimally perturbed and within the error of the measurement. Further tests should be done at significantly higher external pressures to measure how pressure affects the SIP signal.

I repeated this test for 11 samples (initially de-ionized water and 1 M in NaCl concentration), in which I got a similar behavior. It is worth mentioning that each type of clay is described thoroughly in the article presented in chapter 3. In table 2.8, I present the maximum measured difference in the electrical conductivity at 1.46 Hz, for all the clay samples that this test was done for. From table 2.8, we can see that the compression effect is not the same for all types of clay and it varies with salinity.

I stopped doing this test for time constraining reasons (too time consuming). Also, the laboratory protocol I had devised was not ideal to relate pressure with electrical signal. The change in the electrical signal with change of compression is too small to be meaningful, and I also am not able to measure the applied pressure to the sample (there is no equivalence of turns of wing nut and applied pressure). A whole laboratory protocol needs to be

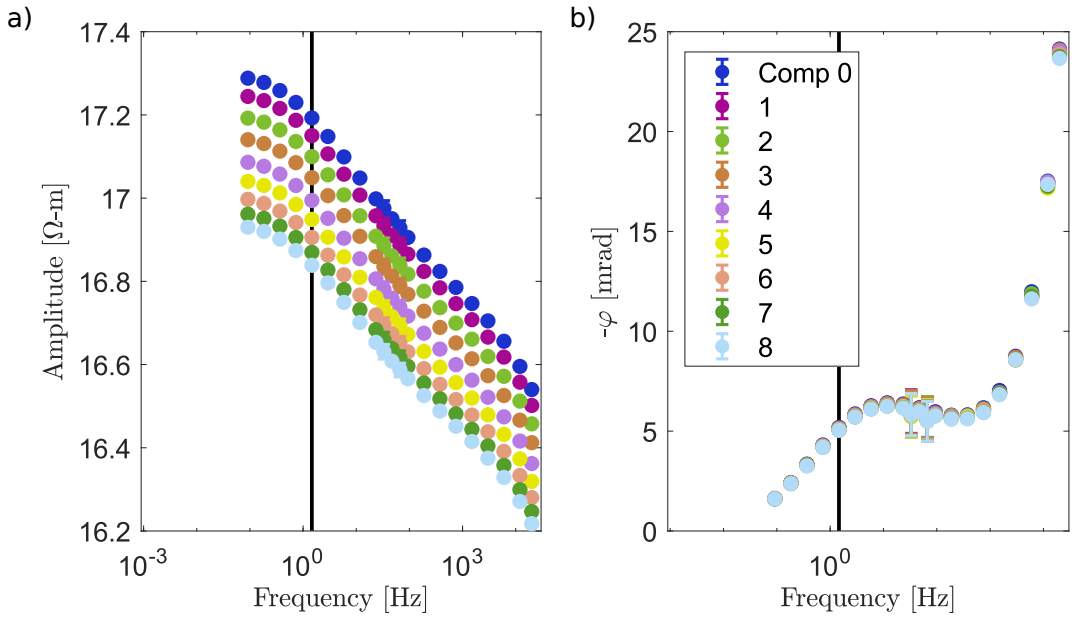

Figure 2.15: SIP measurement of the compression process: a) amplitude and b) phase of SIP for the illite sample at initially de-ionized water

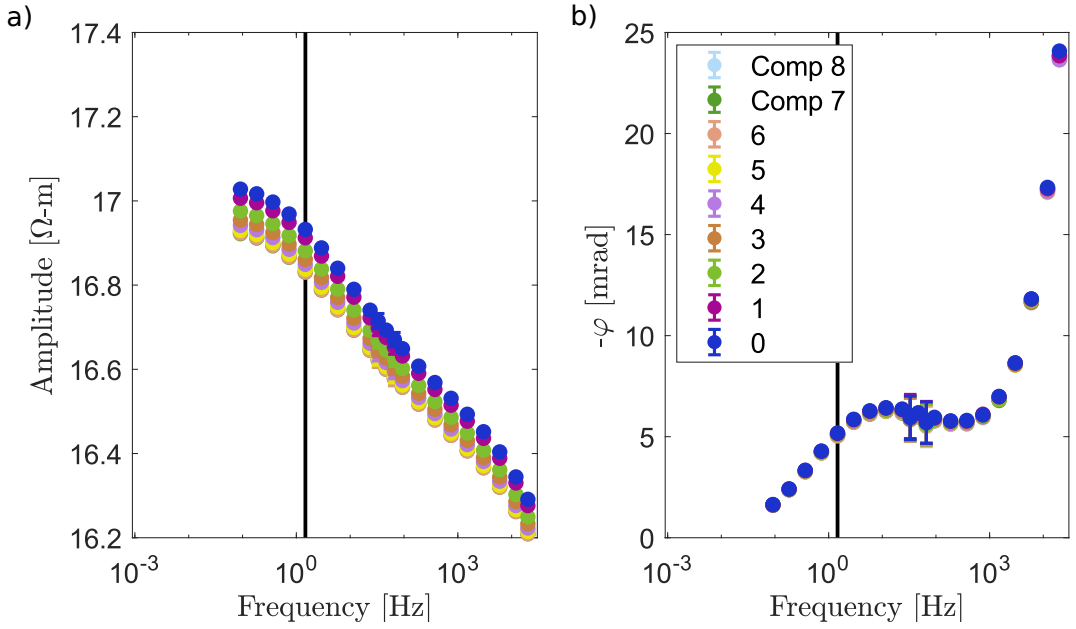

Figure 2.16: SIP measurement of the decompression process: a) amplitude and b) phase of SIP for the illite sample at initially de-ionized water

created in order to fully measure these changes. I think it can be done, but an important amount of logistics need to be dealt with (i.e. pressure sensor that will not interfere with the electrical measures, possible change of geometrical factor, among others). For the SIP measurements shown in chapters 3 and 4, I chose the zero compression level.

I actually wondered if the change in the SIP signal due to the compression could come from a change in the shape of the sample (i.e. change of the geometrical factor). Therefore, I de-

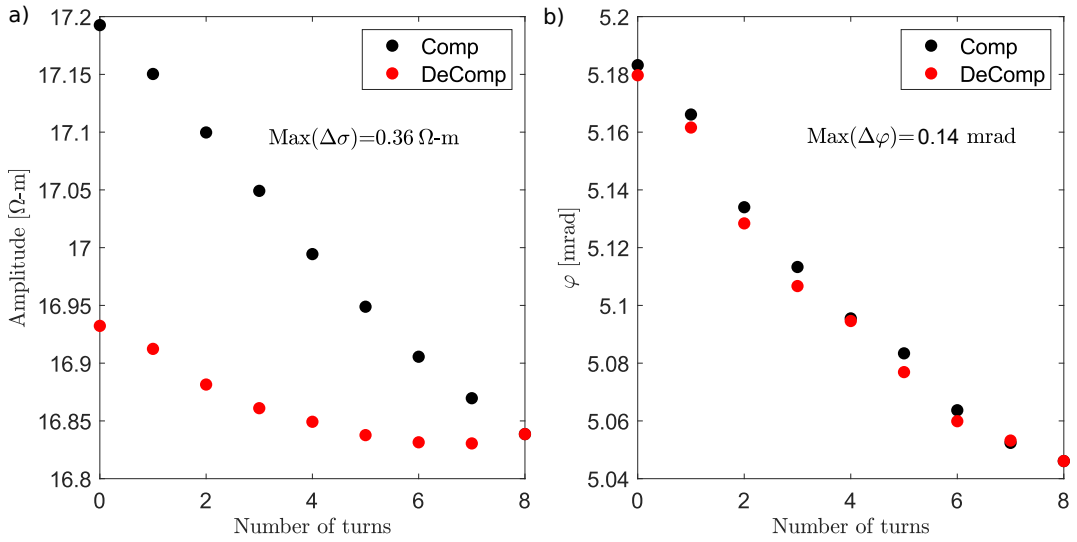

Figure 2.17: Hysteresis curve of the compression and decompression process for the illite sample at initially de-ionized water. a) Measured amplitude of the conductivity and b) phase at 1.46 Hz.

Table 2.8: Maximum measured difference in electrical conductivity at 1.46 Hz for all clay samples with initially de-ionized water and 1 M NaCl salinity.

Clay type	max($\Delta\sigma$) for D.W. [S]	max($\Delta\sigma$) for 1 M [S]
Red mont.	1.41×10^{0}	3.30×10^{-3}
Green mont.	4.45×10^{-2}	-
Beige mont.	8.13×10^{-2}	2.01×10^{-2}
Kaolinite	1.60×10^{-1}	1.97×10^{-3}
Illite	3.62×10^{-1}	5.04×10^{-3}
Boom	4.51×10^{-2}	2.14×10^{-2}

cided to measure the diameter at three different points of the sample holder (vertically and horizontally) for three consecutive pressure levels. I measured the diameters using a digital Vernier caliper with millimeter precision. The highest diameter change I measured was of 0.12 mm. This measure is within the measurement error of the measuring device, it is definitely not a change that would significantly affect the geometrical factor. It is possible that the sample holder was actually changing its shape, but we need a more precise measuring instrument (laser distance meter, for example) since the change is so small.

About the significance of these observations (change in electrical conductivity with pressure), it has been shown that clayrocks have different levels of porosity (Jougnot and Revil 2010; Kuila and Prasad 2013). I hypothesize that the compression I have exerted in the clay samples affects primarily one pore-size distribution and the change in porosity creates a change in electrical conductivity. It would be therefore interesting to test compression levels

with electrical conductivity and use a modified Archie's law to relate the porosity, cementation exponent, and electrical conductivity, through laboratory experiments. Furhtermore, some research has been done to test how pressure affects the electrical complex conductivity of a sample. Zisser and Nover (2009) measured the complex conductivity (from kHz to MHz) with increasing pressure (up to 100 MPa) in sandstones. They found that when increasing the pressure there is an increase in electrical resistivity, and they also see an increase in phase. Comparon (2005) in her doctoral dissertation studied (among other elements), the effect of compaction (6 bar to 560 bar) in clay samples with complex electrical conductivity (Hz - MHz), she also studied how this affected anisotropy. She compacted clay "tablets" at different pressures, and then she measured the complex conductivity. From her measurements it is hard to obtain a strict conclusion, it appears that the electrical conductivity has a non-linear behavior (increases and then decreases) with compaction. The peak of the phase, however, seems to only increase with increasing compaction. Anisotropy, though has a remarkable impact on the measured complex conductivity. Additionally, in recent years there has been in an increasing interest in how soil compaction can affect agriculture, and how we can measure this with geophysics. Romero-Ruiz (2021, doctoral defense at the University of Lausanne) presents a large dataset of time-lapse monitoring of electrical resistivity with compacted and non-compacted soils. For these type of studies, it would be interesting to have fundamental research that could explain the physical processes that affect the electrical signal of compacted geo-materials.

2.5 Water chemistry

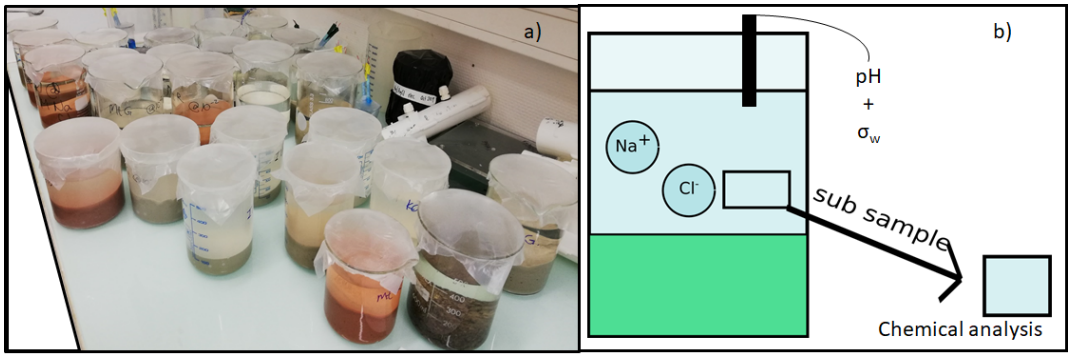

Figure 2.18: Monitoring of pH and water conductivity: a) Samples in which I monitored the pH and water conductivity, and b) diagram of the procedure.

I wanted to better understand the physical and chemical properties of the water in contact with the clay samples. For this purpose, I set-up an experiment for only the lowest water salinities used in this thesis: initially de-ionized water, 10^{-3}, and 10^{-2} mol L^{-1} of NaCl. I

placed a known amount of clay powder in a beaker and added a known amount of water (at one of the chosen salinities) and measured the pH and water conductivity of the aqueous solution for a period of time (figure 2.18b). In figure 2.18a, we can see an example of all the samples that were monitored in time. It is worth noting that I refer to these mixtures as water-clay samples, and not SIP clay samples. These water-clay samples are mixtures that would allow me to measure the pH and water conductivity (i.e. diluted clay samples). In figure 2.19 I present an example of pH and water conductivity monitoring for the red montmorillonite and initally de-ionized water. When the curve of pH and water conductivity versus time has flattened sufficiently (i.e. does not increase or decrease significantly with time), I consider a chemical equilibrium has been reached.

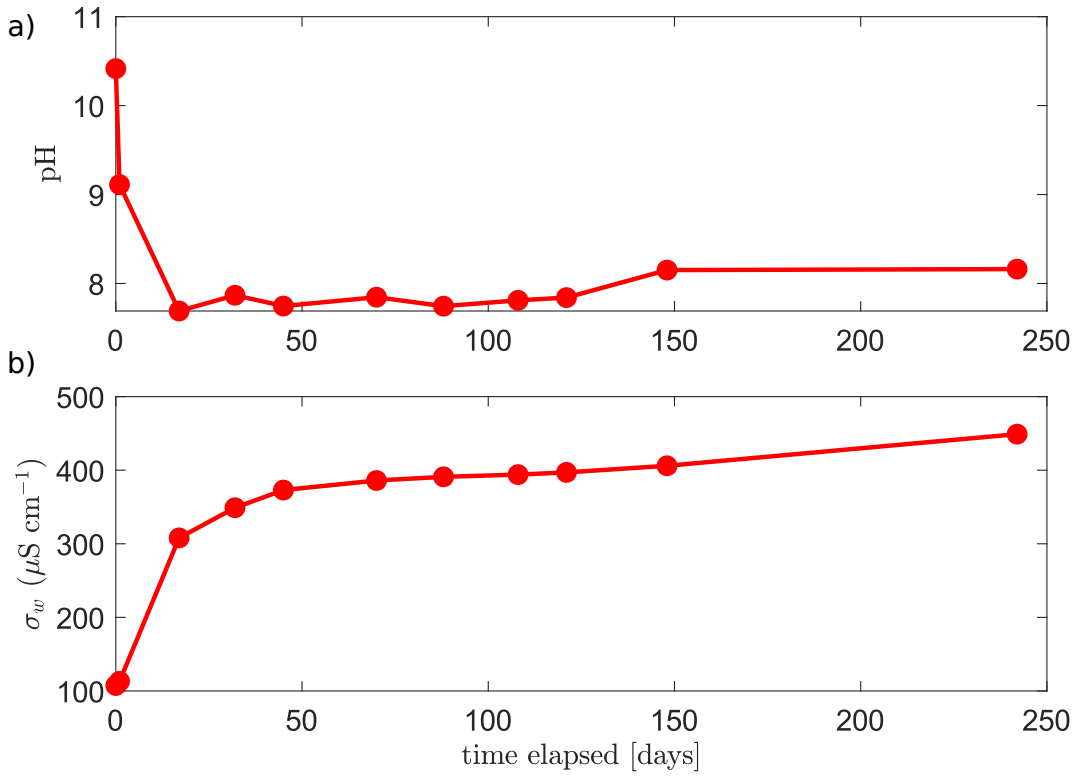

Figure 2.19: Example of the a) pH and b) water conductivity monitoring (after mixing) for the water-clay sample of red montmorillonite and initially de-ionized water.

For the initially de-ionized water, I measured the pH and water conductivity for a total of 242 days, and intermittently twice a month. In table 2.9, I present the values of the pH and water conductivity, when these achieved a chemical equilibrium. It is also worth mentioning, that the pH and water conductivity values kept on evolving with time, and that at the end of this experiment some of the samples had developped a biofilm (this is when I decided to interrupt this experiment). Therefore, I think the samples reached an equilibrium, but then other phenomena interfered and changed the signal. In table 2.9, I present the first achieved equilibrium for the clay samples of: red, green, and beige montmorillonite, illite, kaolinite,

and Boom clay.

Table 2.9: Water conductivity and pH monitoring for initially de-ionized water and clay samples. *The presented time in this table refers to the elapsed time until an equilibrium was observed in the particular parameter, pH or water conductivity.* The water conductivity and pH of the initial de-ionized water (before water and clay mixing) were 1.15 μS cm^{-1} and 6.2 respectively.

Clay type	Duration [days]	pH	Duration [days]	σ_w [μS cm^{-1}]	Initial salinity
Red mont.	17	7.7	32	349	D.W.
Green mont.	17	8.1	45	172.3	D.W.
Beige mont.	17	7.7	45	257	D.W.
Kaolinite	17	8.0	70	235	D.W.
Illite	17	7.6	70	137.9	D.W.
Boom	32	6.8	70	2870	D.W.

As seen in table 2.9, the conductivity of the water-Boom clay sample is one order of magnitude higher than the rest of the clays. We obtained cuttings of Boom clay, this is evidence that the samples that were provided already had salts in them, and when in contact with water, these increased the water conductivity immediately. For the initially de-ionized water SIP clay samples and these water-clay samples, most certainly some ions leached out of the interlayer spaces.

For the initial salinity of 10^{-3} mol L^{-1} of NaCl, I only monitored the water conductivity and pH of the types of clay: red and green montmorillonite, kaolinite, and illite. I measured the pH and water conductivity intermittently twice a month, for a total of 130 days. The values of pH and water conductivity are presented in table 2.10.

Table 2.10: Water conductivity and pH monitoring for water and clay samples, with an initial salinity of 10^{-3} mol L^{-1} of NaCl. *The presented time in this table refers to the elapsed time until an equilibrium was observed in the particular parameter, pH or water conductivity.* The water conductivity and pH of the initial 10^{-3} mol L^{-1} of NaCl solution were 97.7 μS cm^{-1} and 7.8 respectively.

Clay type	Duration [days]	pH	Duration [days]	σ_w [μS cm^{-1}]	Initial salinity [M]
Red mont.	9	8.1	23	340	10^{-3}
Green mont.	17	8.2	17	293	10^{-3}
Kaolinite	17	8.2	23	233	10^{-3}
Illite	17	8.2	17	200	10^{-3}

For the initial salinity of 10^{-2} mol L^{-1} of NaCl, I monitored the water conductivity and pH of the types of clay: red, green, and beige montmorillonite, kaolinite, illite, and Boom clay. I measured the pH and water conductivity every 7 days, for a total of 36 days. The values of

pH and water conductivity are presented in table 2.11.

Table 2.11: Water conductivity and pH monitoring for water and clay samples, with an initial salinity of 10^{-2} mol L^{-1} of NaCl. *The presented time in this table refers to the elapsed time until an equilibrium was observed in the particular parameter, pH or water conductivity.* The water conductivity and pH of the initial 10^{-2} mol L^{-1} of NaCl solution were 925 μS cm^{-1} and 7.7 respectively.

Clay type	Duration [days]	pH	Duration [days]	σ_w [μS cm^{-1}]	Initial salinity [M]
Red mont.	3	8.3	17	1141	10^{-2}
Green mont.	23	8.0	9	1066	10^{-2}
Beige mont.	23	8.1	17	1105	10^{-2}
Kaolinite	17	7.9	9	1025	10^{-2}
Illite	23	8.0	17	1024	10^{-2}
Boom	17	6.4	17	2520	10^{-2}

Again, from tables 2.9 and 2.11 we can see that the Boom clay-water mixture has not only higher water conductivity, but also a slightly more acid pH than the rest of the clays. It could be that the water dissolves this clay rock, or that some of the ions present in the interlayer space of the clay react with the water. Indeed, knowing which ions are present in the water is something to be understood. For this, as presented in figure 2.18b, I took a sub-sample of the aqueous solutions that had been in contact with the clay powders and did a chemical analysis to determine the major cations and anions present in the solution. In table 2.12 I present the major ions present in the aqueous solution with the initial de-ionized water, and 10^{-3} mol L^{-1} of NaCl, which were the prone ones to showing ions other than Na^+ and Cl^-.

Table 2.12: Major cations and anions present in the aqueous solution of the clay powders and water at initially de-ionized water and 10^{-3} mol L^{-1} of NaCl. *Cations* were measured using the inductively coupled plasma - optical emission spectrometry. Anions** were measured with chromatography.*

Clay type	Initial	Cations*				Anions**		
	salinity [M]	Ca^{2+} [ppm]	K^+ [ppm]	Mg^{2+} [ppm]	Na^+ [ppm]	Cl^- [ppm]	NO^{3-} [ppm]	SO_4^{2-} [ppm]
Red mont.	D.W.	46	8.8	15.3	33.2	4.3	<0.5	181.2
Green mont.	D.W.	35	7.9	22.9	16.9	1.3	0.9	112.3
Beige mont.	D.W.	16	3.6	4.6	43.2	1.2	0.8	7.6
Kaolinite	D.W.	15	1.4	16.3	16.5	5.7	8.7	9.8
Illite	D.W.	21	14.7	3.5	4.1	0.5	3.7	7.5
Boom	D.W.	355	50.9	92.0	245	1.1	<0.5	<0.1
Red mont.	10^{-3}	39	8.1	13.4	37.2	37.0	<0.5	120.2
Green mont.	10^{-3}	36	8.0	23.8	26.0	34.2	1.2	91.2
Kaolinite	10^{-3}	14	1.6	16.2	35.1	40.4	39.8	27.7
Illite	10^{-3}	25	16.4	4.0	18	33.0	1.4	7.2

From table 2.12, we can see that indeed the Boom clay has a higher concentration of cations

and anions that leached out to the aqueous solution.

2.6 Conclusion of this chapter

I did multiple tests of different types (compression, electrodes, clay water content, etc.) to converge to one precise laboratory protocol. This shows the need of an extensive and detail oriented work for SIP laboratory experiments and sets a basis for future clay laboratory SIP measurements. I propose the use of Cu-$CuSO_4$ electrodes for SIP measurements, as well as the concentration of $CuSO_4$ and amount and type of gelifying agent. I recognize there are improvements on the type of electrodes I used for the SIP measurements. I present a numerical way to calculate the geometrical factor of the sample holder. There is evidence that compression affects the measured electrical conductivity of the sample. Therefore, there is a need to establish a way to keep the compression level constant between measurements. Furthermore, I recommend previous tests on the water content needed for clay samples (issued from clay powder), as this is a varies from clay type in order to obtain a similar plasticity (if plasticity is the chosen parameter to keep constant between measurements). Even if plasticity were not an important parameter, I recommend doing previous water content tests as it allows to observe how the sample reacts with water. Finally, the chemical reaction between water with low salinity and clay powder is a complex one. Chemical analyses of water that has reacted with clay powder are a good addition to these type of problematic.

CHAPTER

3 SIP on individual types of clays

3.1 JGR article in the context of this thesis

The main goal of this thesis is to characterize clays using SIP. In this chapter, I present a scientific article published in JGR which deals with the SIP characterization of different types of clays at varying salinities. The SIP signal is frequency dependent and goes from the mHz to the kHz. We focused on the individual characterization of three clay families: illite, smectite, and montmorillonite. It is worth mentioning that none of the clay samples we used were 100% pure and the precise mineralogy is presented in the article. The factor to keep constant between measurements was the plasticity of the clay samples. The laboratory protocol to achieve this with good repeatability is presented in the article. The parameter to vary between measurements was salinity (from de-ionized water to 1 mol L^{-1} of NaCl). Most studies presented earlier dealing with individual types of clay samples, make use of a mix of quartz sand and clays, or they use a dilute clay sample. Otherwise, there are studies with clayrock samples, from a clayey geological formation. To the best of my knowledge, this is the first time such clay samples are studied. Here, I present the results of the SIP measurements at varying salinities and I interpret the results with the help of phenomenological models. I also compare my results to data presented in the literature.

3.2 JGR article

The article presented in this chapter is the submitted version to the *Journal of Geophysical Research - Solid Earth*. This is the accepted version, before edits of the publisher. The correct citation for this article is: Mendieta, A., Jougnot, D., Leroy, P., and A. Maineult (2021). Spectral induced polarization characterization of non-consolidated clays for varying salinities - an experimental study. *Journal of Geophysical Research: Solid Earth, 126*. doi:10.1029/

2020jb021125.

Spectral induced polarization characterization of non-consolidated clays for varying salinities - an experimental study

Aida Mendieta[1], Damien Jougnot[1], Philippe Leroy[2], and Alexis Maineult[1]

[1]Sorbonne Université, CNRS, EPHE, UMR 7619 METIS, 75005 Paris, France
[2]BRGM, French Geological Survey, 45060 Orléans, France

Key Points:

- The quadrature conductivity of clays behaves non-monotonously with increasing salinity
- Some polarization mechanisms may cease to act or decrease significantly at a specific salinity
- The quadrature to surface conductivity ratio is lower for clays than for other minerals

Corresponding author: Aida Mendieta, aida.mendieta_tenorio@upmc.fr

Abstract

Clay material characterization is of importance for many geo-engineering and environmental applications, and geo-electrical methods are often used to detect them in the subsurface. Spectral induced polarization (SIP) is a geo-electric method that non-intrusively measures the frequency-dependent complex electrical conductivity of a material, in the mHz to the kHz range. We present a new SIP dataset of four different types of clay (a red montmorillonite sample, a green montmorillonite sample, a kaolinite sample, and an illite sample) at five different salinities (initially de-ionized water, 10^{-3}, 10^{-2}, 10^{-1}, and 1 mol/L of NaCl). We propose a new laboratory protocol that allows the repeatable characterization of clay samples. The complex conductivity spectra are interpreted with the widely used phenomenological double-Pelton model. We observe an increase of the real part of the conductivity with salinity for all types of clay, while the imaginary part presents a non monotonous behavior. The decrease of polarization over conduction with salinity is interpreted as evidence that conduction increases with salinity faster than polarization. We test the empirical petrophysical relationship between σ''_{surf} and σ'_{surf} and validate this approach based on our experimental data and two other datasets from the literature. With this dataset we can better understand the frequency-dependent electrical response of different types of clay. This unique dataset of complex conductivity spectra for different types of clay samples is a step forward toward better characterization of clay formations in situ.

1 Introduction

Clay minerals are ubiquitous in the Earth's subsurface and can be found in many geological formations, from hard clay rocks to disseminated clay aggregates or lenses in other sedimentary rocks. These minerals are frequently the main components of extended sedimentary stratigraphic layers. Illite and smectite alone may constitute around 30% of all sedimentary rocks (Garrels & Mackenzie, 1971). Clay materials are fine-grained soil materials (particle size below 2 μm) characterized by a large fraction of nanopores, high specific surface area (between 10 and 1000 m^2/g), and a large negative surface charge (between -0.15 and -0.10 Cm^{-2}) (e.g., Michot & Villiéras, 2006), thus large cationic exchange capacity (CEC, between 0.03 and 1.5 meq g^{-1}) and low permeability (typically below 10^{-16} m^2)(Revil & Leroy, 2004). These properties make clay formations suitable to be, e.g.: cap rocks forming geo-reservoirs, aquitards defining the geometry of hydrosystems, or potential hosts for waste repositories. Studying the transport and mechanical properties of clay materials is crucial for many geoengineering and environmental applications, such as: oil and gas (e.g., Morsy & Sheng,

2014), geothermal energy exploration and production (e.g., Corrado et al., 2014), critical zone research (e.g., Chorover et al., 2007), nuclear waste storage (e.g., Ortiz et al., 2002; Gonçalvès et al., 2012), hydrogeology (e.g., Konikow et al., 2001; Parker et al., 2008), civil engineering (e.g., Islam et al., 2020), among others.

Clay formations are geological formations composed of a majority of clay minerals. Clay minerals are hydrous aluminium phyllosilicates, that is, silicates organized in stacks of tetrahedral (T) silica sheets and aluminium octahedral (O) sheets called platelets (Bergaya & Lagaly, 2006). The T and O sheets present an overall negative electrical charge at their surfaces because of deprotonated oxygen atoms and isomorphic substitutions in the crystal lattice (Leroy & Revil, 2004). Due to these charges on the clay surface, cations (e.g.: Ca^{2+}, Na^{+}, Mg^{2+}, K^{+}) can be adsorbed in the interlayer space of illite, smectite and chlorite minerals between platelets; and on the external surface in the electrical double layer (EDL) made of the Stern and diffuse layer (Leroy & Revil, 2009). The differences between clay minerals depend on the kind of tetrahedral and octahedral stacks (1:1 for TO or 2:1 for TOT) and adsorbed cations in the interlayer space (e.g., K^{+} for illite or Na^{+} and Ca^{2+} for montmorillonite) (Brigatti et al., 2006). The clay platelets are then organized in tactoids, that is, stacks of platelets having different geometries, which form aggregates (Bergaya & Lagaly, 2006). There are four main groups of clay minerals: kaolinite, illite, smectite, and chlorite.

The total specific surface area of a kaolinite tactoid, typically 10-20 m^2/g, is considerably lower than the total specific surface area of an illite and montmorillonite tactoid (typically 100-200 m^2/g for illite and 750-800 m^2/g for Na-montmorillonite)(Revil & Leroy, 2004; Hassan et al., 2006; Tournassat et al., 2011, 2015). Clay formations can be constituted of a mixture or stratifications of different clay minerals (e.g., interstratified illite-smectite). In the present work, we focus on the three more common groups: kaolinite (1:1), illite (2:1), and smectite (2:1, montmorillonites are part of the smectite family). As presented previously, kaolinite, illite and smectite groups present many different characteristics in terms of structure (e.g., number of stacked platelets, tactoid size and shape), physicochemical properties (e.g., surface charges, CEC), mechanical properties (e.g., plasticity, resistance to stress, swelling-shrinking), and also electrical properties. It is therefore crucial to electrically discriminate these minerals between each other in order to characterize the properties of the formation or predict its behavior if submitted to stress (e.g., hydraulic, mechanic, thermic).

In geophysics, the most common methods to identify the presence of clay minerals non-intrusively in the field are electrical and electromagnetic methods (e.g., Auken et al.,

2017): direct current electrical resistivity tomography (ERT) (e.g., Batayneh, 2006), induced polarization (IP) (e.g., Okay et al., 2013; Lévy et al., 2019a), time-domain electromagnetics (TDEM) (e.g., Finco et al., 2018), frequency-domain (FDEM) electromagnetics (e.g., Spichak & Manzella, 2009), and ground penetrating radar (GPR) (e.g., Looms et al., 2018). However, if clays are usually associated to high electrical conductivity zones, they can be mistaken with highly mineralized pore water when only the real electrical conductivity is considered. One way to avoid this misinterpretation is to use the complex conductivity (inferred from IP), that is the real and imaginary parts of the conductivity, or its spectral behavior, i.e. the dependence with frequency of the conductivity, to extract more information than from a single frequency measurement.

The spectral induced polarization (SIP) method can investigate the conduction and polarization of geological materials over a large range of frequencies: from the mHz to the kHz (e.g., Kemna et al., 2012; Revil et al., 2012). Indeed, in addition to the resistivity, the SIP method gives the chargeability of the investigated porous medium, which describes its capability to reversibly store electrical charges (e.g., Revil et al., 2012; Tabbagh et al., 2021). The chargeability is very sensitive to the pore structure and electrical surface properties (Leroy & Revil, 2009). When SIP measurements are coupled with a relevant petrophysical model, they can provide information on the nature and behavior of electrical phenomena (conduction and polarization) happening at the pore scale (Revil, 2012), helping to interpret field scale geophysical electrical measurements in terms of mineralogy, pore structure, water content, and permeability distribution (Ghorbani et al., 2009; Okay et al., 2013).

The frequency-dependent electrical response of clay minerals has been recently studied in well-controlled conditions in the laboratory. Many clayey materials have been studied, from mixtures containing quartz sand and clays (e.g., Breede et al., 2012; Okay et al., 2014; Wang & Slater, 2019), synthetic clay suspensions (e.g., Leroy et al., 2017a), to natural clays and clayrocks (e.g., Jougnot et al., 2010; Lévy et al., 2018). These measurements have been performed in saturated (e.g., Lévy et al., 2019b) or partially water-saturated (e.g., Cosenza et al., 2008; Ghorbani et al., 2009; Jougnot et al., 2010) conditions.

However, as pointed out by Leroy & Revil (2009) and Leroy et al. (2017a), there is a lack of SIP laboratory studies on individual clay minerals. Indeed, measuring the frequency-dependent electrical response of individual clay minerals is of great importance to better understand their specific conduction and polarization and to improve their geophysical imaging. This is needed in order to move towards a full discrimina-

tion of clay minerals when interpreting field electrical measurements. This can only be achieved by better understanding the electrical signal of each individual type of clay. In this paper, we intend to characterize the electrical signal of a variety of clay samples at multiple frequencies (from mHz to kHz) and at multiple salinities (from initially de-ionized water to 1 mol/L of NaCl) using laboratory SIP measurements on three groups of clay minerals: illite, smectite, and kaolinite.

In the present contribution, we first present the method and some theoretical background for the SIP of clay materials. Then, we detail the protocol we propose in order to obtain the clay samples, characterize them, perform the SIP measurements, and post-treat them. We present the results on four clay samples (two smectite samples, a kaolinite sample, and an illite sample) at five different salinities (initially de-ionized water, 10^{-3}, 10^{-2}, 10^{-1}, and 1 mol/L of NaCl) and analyze them using a phenomenological model. Finally, we discuss our results with respect to the existing literature.

2 Theory

2.1 Characteristics of kaolinite, illite, and montmorillonite

As mentioned earlier, clay minerals have a strong electrical conductivity response due to the high surface conductivity associated with the high electrical charge on their surface (Revil & Leroy, 2004; Revil, 2012). This particularity, in addition to the heterogeneities of the surface electrical properties of clay minerals (Leroy & Revil, 2004), makes clay systems quite complex but also, interesting to characterize electrically.

Kaolinite is a 1:1 clay, composed of a succession of silica tetrahedral (T) and aluminum octahedral (O) sheets (see Figure 1a) whereas illite and montmorillonite (member of the smectite group) are 2:1 clays made up of a succession of TOT sheets (see Figure 1b) (Leroy & Revil, 2009). The thickness of a TOT platelet is around 9.5 Å, its length is around 50-100 nm for illite and 50-1000 nm for montmorillonite (Tournassat et al., 2015). For kaolinite, the thickness of a TO platelet is around 7 Å and its length lies between around 200 nm to more than 1000 nm (Tournassat & Steefel, 2015). The number of stacked layers of a kaolinite tactoid ranges from 10 to more than 200 whereas this number ranges between 1 and 2, 6 and 10, and 5 and 20 for Na-montmorillonite, Ca-montmorillonite and illite, respectively (Tournassat et al., 2015; Tournassat & Steefel, 2015; Leroy et al., 2017a). The height of a kaolinite tactoid ranges between 7 and 150 nm and the height of an illite and montmorillonite tactoid lies between 5 and 20 nm, and, 1 and 10 nm, respectively (Hassan et al., 2006; Tournassat et al., 2011; Tournassat & Steefel, 2019). It results that the total specific surface

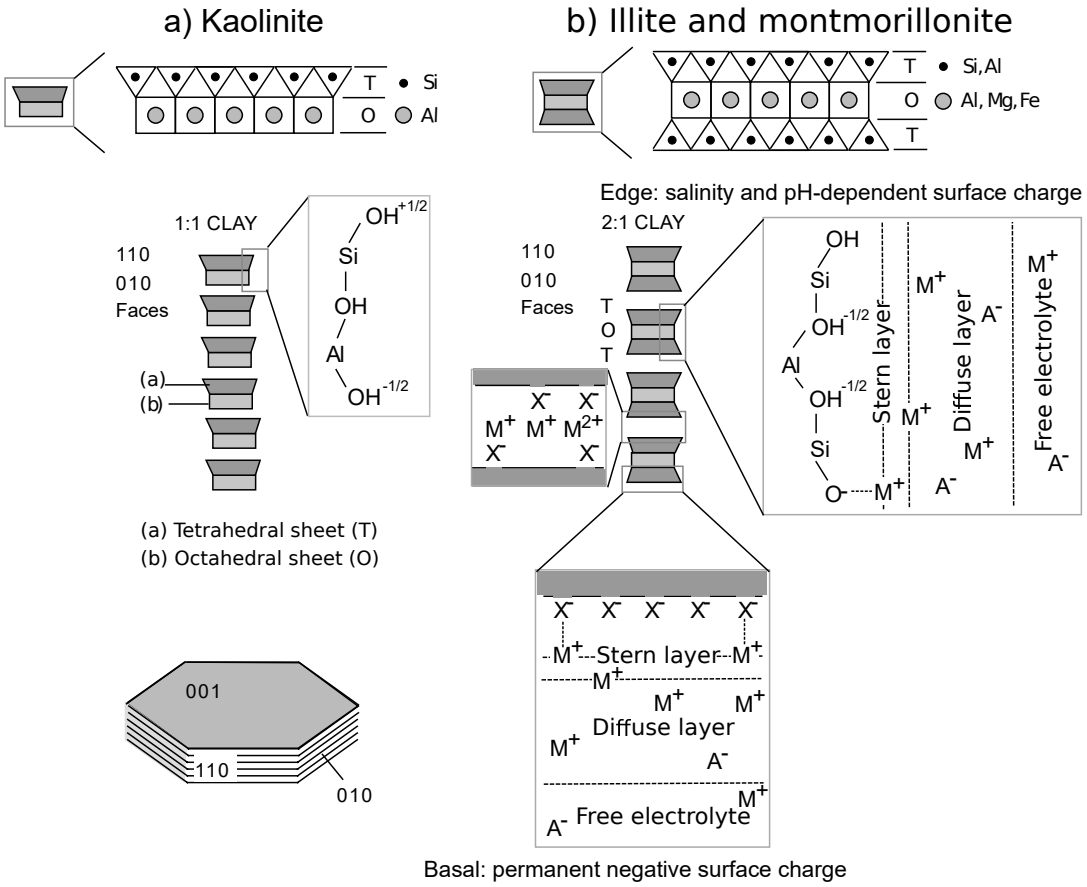

Figure 1. Sketch of a (a) kaolinite and an (b) illite or montmorillonite clay tactoid showing the different types of surface sites on the basal and edge surfaces as well as the electrical double layer around them (electrical double layer not shown for kaolinite) and the interlayer space between TOT sheets (modified from Leroy & Revil, 2009).

area of a kaolinite tactoid is considerably lower than the total specific surface area of an illite and montmorillonite tactoid (typically, 10-20 m^2/g versus 100-200 m^2/g and 750-800 m^2/g, respectively).

Consequently, clay minerals generally present a high aspect ratio with different morphologies: kaolinite and well-crystallized illite have a tendency toward hexagonal and elongated hexagonal morphologies respectively, whereas montmorillonite and less well-crystallized illite have mostly irregular platy or lath-shaped morphologies. The surface charge of the lateral (or edge) surface of kaolinite, illite and montmorillonite (to a lesser extent due to the influence of the basal surface) are controlled by the aluminol and silanol (>Al-OH and >Si-OH) surface sites and are thus sensitive to salinity and pH (Tombácz & Szekeres, 2006). When salinity and pH increase, the charge on these sur-

faces is generally more negative due to the >Si-O- surface sites. On the other hand, the basal surface of illite and montorillonite is permanently negative and less sensitive to salinity and pH because it mainly results from the isomorphic substitutions in the crystal lattice (e.g., Si^{4+} by Fe^{3+} or Al^{3+} ions in the T-sheet or Al^{3+} by Mg^{2+} or Fe^{2+} ions in the O-sheet). Most of the isomorphic substitutions in these minerals occur in the O-sheet. Because the specific surface area of the basal surface of these 2:1 clays is more than one order of magnitude higher than the specific surface area of the lateral surface (typically 760 m^2/g vs 20 m^2/g) (Tournassat et al., 2011), the basal surface may control the surface electrical properties of illite and montmorillonite. The CEC method can be used to measure the surface properties and then the surface charge of illite and montmorillonite, if the specific surface area is known (Okay et al., 2014). For kaolinite, the CEC is very sensitive to pH and salinity due to the pH and salinity dependent surface charge of the lateral surface. When a clay particle is put in water, an EDL mostly made of counterions builds up to compensate the external negative surface charge (Tsujimoto et al., 2013; Leroy et al., 2015). The internal negative surface charge of montmorillonite is compensated by cations in the interlayer space. The pore space is then made of the EDL and the free electrolyte. The EDL is thought to be composed of two portions, the Stern and the diffuse layer. The Stern layer is only made of counterions (cations for clays) and is thought to be fixed to the surface of the mineral (see Figure 1). The diffuse layer is made mostly of counterions that are more mobile than those of the Stern layer. When a clay particle and its surrounding electrolyte is submitted to a frequency dependent electrical field (for frequencies typically lower than 1 MHz), cations and anions around the clay particle separate, giving rise to different types of polarization mechanisms.

In the literature, three different polarization mechanisms have been proposed for clay samples in the mHz to the kHz frequency range: Maxwell-Wagner polarization, EDL polarization, and membrane polarization (e.g., Chen & Or, 2006; Leroy & Revil, 2009; Kemna et al., 2012; Bücker & Hördt, 2013; Bücker et al., 2019). The Maxwell-Wagner polarization mechanism is due to a charge build-up at boundaries between phases with different electrical properties (conductivity, permittivity) in geologic materials and happens at the highest frequencies (in the kHz range) for SIP. The EDL polarization happens when ions in the Stern and diffuse layers migrate around the surface of the mineral guided on the orientation of the time varying external electric field, leading to a charge separation in the EDL at the particle scale (Leroy et al., 2017a). This polarization mechanism typically occurs at the mid frequencies for SIP (below the kHz range). Finally, the membrane polarization mechanism happens when pore throats block electrical charges (anions for clays, due to their negative electrical charge)

mobilizing due to repulsive EDLs and a time varying external electric field, and thus charges separate in ion selective zones. This polarization mechanism happens in the lowest frequencies for SIP (typically in the mHz to the Hz range). With all these polarization mechanisms the question is open on what is the active polarization mechanism in clay samples at a given frequency of the injected sinusoidal electrical field.

2.2 Background on spectral induced polarization

The SIP geophysical method consists of a sinusoidal electric current injection in a rock sample and the measurement of a resulting electrical potential difference between two electrodes at multiple frequencies (from mHz to kHz). In addition to the electrical conductivity (or resistivity, $\rho^* = 1/\sigma^*$) of the sample, the phase-lag between injected and measured signal gives information about the petrophysical and surface electrical properties of clay samples at the pore scale (e.g., Kemna et al., 2012; Revil et al., 2012; Leroy et al., 2017a).

The frequency dependent complex conductivity $\sigma^*(\omega)$ is inferred from SIP. The angular frequency ω (rad/s) is related to the frequency f (Hz) by $\omega = 2\pi f$. There are two ways to express the complex conductivity, either by real σ' (S m^{-1}) and imaginary components σ'' (S m^{-1}), or amplitude $|\sigma|$ (S m^{-1}) and phase φ (rad):

$$\sigma^*(\omega) = |\sigma| e^{i\varphi} = \sigma' + i\sigma'', \tag{1}$$

where $i = \sqrt{-1}$ represents the imaginary unit. The resulting electric signal of a rock sample depends on the electrical properties of the pore water and the rock matrix itself. Following Waxman & Smits (1968), we assume then that the measured electrical conductivity (a complex quantity) is a result of the bulk pore water electrical conductivity (σ_w) in the rock acting in parallel to the surface conductivity (σ^*_{surf}) of the geologic material:

$$\sigma^* = \frac{\sigma_w}{F} + \sigma^*_{surf}, \tag{2}$$

where F is the electrical formation factor, sensitive to the electrically connected porosity and the shape of the grains. For clays, surface conduction is particularly strong due to their high specific surface area and surface charge, resulting in a strong EDL (Leroy & Revil, 2004). Weller et al. (2013) took equation 2 and proposed a linear relation between the real part of the measured conductivity, water conductivity, and surface conductivity:

$$\sigma'_{surf}(\sigma_w) = \sigma'(\sigma_w) - \frac{\sigma_w}{F}. \tag{3}$$

Following the notation of Weller et al. (2013), we have:

$$\sigma'' = \sigma''_{surf}. \tag{4}$$

Börner (1992) proposes to link the real and imaginary surface components as:

$$l = \frac{\sigma''_{surf}}{\sigma'_{surf}}. \tag{5}$$

2.3 Double-Pelton phenomenological model

In order to model SIP data there are several types of models available, some are physical models and some are phenomenological. Physical models are often complex and require a thorough knowledge of a plethora of physical and chemical properties of the rock sample in question. Phenomenological models are able to reproduce large datasets and do not require much knowledge on the physical and chemical properties of the rock sample that is being studied. We use a phenomenological double-Pelton model to fit our data. We use one Pelton model to describe the complex conductivity (the inverse of the complex resistivity) of the clay and the other Pelton model to explain the high frequency signal due to inductive and capacitive noise and also clay polarization. Our double-Pelton model consists of two individual Pelton (Pelton et al., 1978) electrical signals summed up together. The double-Pelton model originates from the Cole-Cole and Debye models (Cole & Cole, 1941). The double-Pelton model is defined by:

$$\rho^*(\omega) = \rho_0 \left[1 - m_1 \left(1 - \frac{1}{1 + (i\omega\tau_1)^{c_1}}\right) - m_2 \left(1 - \frac{1}{1 + (i\omega\tau_2)^{c_2}}\right)\right], \tag{6}$$

where ρ (Ω·m) is the electrical resistivity of the sample (inverse of the electrical conductivity σ), c (-) is the Cole-Cole exponent, τ (s) refers to the relaxation time, and m (mV/V) is the chargeability of the material. In general, ρ_0 is thought of as a direct current (DC) or low frequency term. In the case of c=0.5, the Pelton model becomes a Warburg model. Therefore, when in equation 6 we have $c_1 = 0.5$ and $c_2 = 0.5$, we obtain a double-Warburg model.

3 Materials and methods

3.1 CEC and XRD of clay samples

We performed the CEC measurements and the X-ray diffraction (XRD) characterization of all the clay types used in this work, to have the surface properties and the mineralogical composition of the samples. We present the results of the XRD analysis in Table 1. As for the CEC results, we obtained: 22 meq/100 g for the kaolinite sample, 47 meq/100 g for the illite sample, 132 meq/100 g for the green montmorillonite sample, and 135 meq/100 g for the red montmorillonite sample. From Table 1, we see that none of our clay samples are 100% pure. The XRD measurements were obtained using a Philips Xpert machine from clay powder and glycolated samples. The bulk clay powder samples were quantitatively analyzed with randomly oriented preparations following Brindley & Brown (1980) and Moore & Reynolds (1989). Furthermore, following the modified Chung method (Chung, 1974; Hillier, 1999) an analysis on glycolated oriented preparations was done in order to correct the measurements on the clay powder samples. The CEC measurement consists of replacing a cation present on the clay surface with another cation (Ma & Eggleton, 1999). Methods differ on the exchanged cation, the exchange solution (according to the AFNOR standard NF X31-108 and Khaled & Stucki, 1991), and if there are consecutive exchanges in the procedure (Ciesielski & Sterckeman, 1997; Meier & Kahr, 1999). For the CEC measurements presented in this paper, we determined the amount of recovered Mg^{2+} ions after a second exchange (Khaled & Stucki, 1991).

Table 1. Results of XRD analysis, showing the exact mineral content of each clay sample.

Clay sample	Smectite %	Illite %	Kaolinite %	Gypsum %	Quartz %	Microcline %	Albite %	Calcite %	Magnetite %
Kaolinite sample	4	3	84		10				
Illite sample		67	10			10		12	
Green mont. sample	90	1		*tr**	1	3	1	4	
Red mont. sample	66				11	18	3		1

*tr**: traces.

3.2 Preparation of clay samples

We developed a laboratory protocol that allowed us to have clay mixtures we could knead and place inside a sample holder, while ensuring a good reproducibility of the data. Plasticity is our criteria for a parameter to keep between all clay types, salinities and measurements. When we talk about plasticity, we need to take a look at the Atterberg limits in clays. The liquid and plastic limits are water contents that mark the limits of plastic behavior of clays (White, 1949). We chose a water content within those limits for each clay, to avoid a clay mixture too liquid (more water than the liquid limit), or a sample too dry that crumbles into pieces (smaller water content than the plastic limit). Wagner (2013) presents a table of liquid and plastic limits for illite, kaolinite, smectites, and others. Note that Mitchell & Soga (2005) explain that the availability of ions and the valence of the ions present in the pore water of the clay samples may affect these limits. As presented in Table 2, we see a decrease of porosity at the highest salinities in our clay samples, in accordance with Mitchell & Soga (2005).

Figure 2 describes the procedure used to prepare the clay samples. In order to obtain the adequate plasticity, we first combine water and clay powder at higher water contents than the objective (Figure 2a and b). We left the clay powder in contact with water for at least 24 hours to have a good imbibition process, and we then mix the whole mixture mechanically using a drill until we reach a homogeneous mixture (Figure 2c). In order to obtain the desired water content, we eliminate the water excess through evaporation by letting the clay mixture dehydrate on a polyurethane foam (Figure 2d). We use a polyurethane foam to have a homogeneous evaporation process, that is, to allow evaporation from the bottom, top and sides of the clay mixture. The mass of the mixture is monitored at every step to determine the evolution of water content at each step of the process. After obtaining the desired water content, we take the clay mixture out of the foam, knead it and locate it in our sample holder (Figure 2e). Once in place, we perform the SIP measurement of the clay sample twice, from 1 mHz to 20 kHz (see the following section and Figure 2f). We acknowledge that a total chemical equilibrium might not be achieved when measuring the SIP signal in the clay samples, but we assume that the difference between the SIP signal we measure and a true equilibrated sample is negligible. After the measurements are over, we take out the sample from the sample holder and dry it in an oven at 105° C during 25h (Figure 2g). By measuring the mass at every step of the process, we can calculate the water content (presented in Table 2) at each step and therefore determine the porosity of our clay sample during the SIP measurement. The calculated porosities

of the clay mixtures are presented in Table 2. These porosities help us keep a check on the water vs clay powder ratios of our samples. The porosity calculations present some experimental uncertainties, these porosity values are a good estimate but should not be over-interpreted.

Note that as the water content changed in the samples, so did the salinities. We originally started all samples with five different salinities: De-ionized water (D.W.), 1×10^{-3}, 1×10^{-2}, 1×10^{-1} , and 1 M (mol/L) of NaCl. To account for the water content decrease due to the evaporation procedure, we recalculated the salinities in our sample during the SIP measurements for all the salinities from 1×10^{-3} to 1 M of NaCl. Table 2 presents the corrected salinities using a simple proportion equivalence. From these post-dehydration salinity values we calculated the bulk water electrical conductivity, following the procedure proposed in Leroy et al. (2015), using:

$$\sigma_w = e10^3 N_A \sum_{i=1}^{N} z_i \beta_i^w C_i^w, \tag{7}$$

where β_i^w (in $\mathrm{m^2 s^{-1} V^{-1}}$) is the ionic mobility of an ion i in the bulk water, C_i^w (in mol $\mathrm{dm^{-3}}$) is its concentration, and z_i is its valence. Also, N_A is the Avogadro number ($6.022 \times 10^{23} \mathrm{mol^{-1}}$), and e is the elementary charge (1.602×10^{-19} C). It is worth noting that the ionic mobility values used in equation 7 have been corrected for the temperature and salinity, as presented in Leroy et al. (2015). It should be noted that the low-salinity water conductivity values may be underestimated because we do not consider clay dissolution as well as cation leaching from the interlayer space for the calculation of the ion concentrations.

3.3 SIP measurement setup

We conducted the SIP measurements on the clay samples using the SIP-FUCHS III equipment (Radic Research, www.radic-research.de). The setup for the measurements is presented in Figure 3a. The SIP-FUCHS III sends a sinusoidal current into the sample through the injection unit and then the so-called current electrodes (C1 and C2 in Figure 3b) by imposing a chosen potential difference. The second unit measures the resulting voltage through the so-called potential electrodes (P1 and P2 in Figure 3b). The communication between the units (injection and measurement) and the system is done through optic cables to reduce electromagnetic noise. The SIP-FUCHS III outputs the amplitude of the measured impedance (Ω), the phase shift between injected and measured signal (mrad), and their respective errors, for each measured frequency.

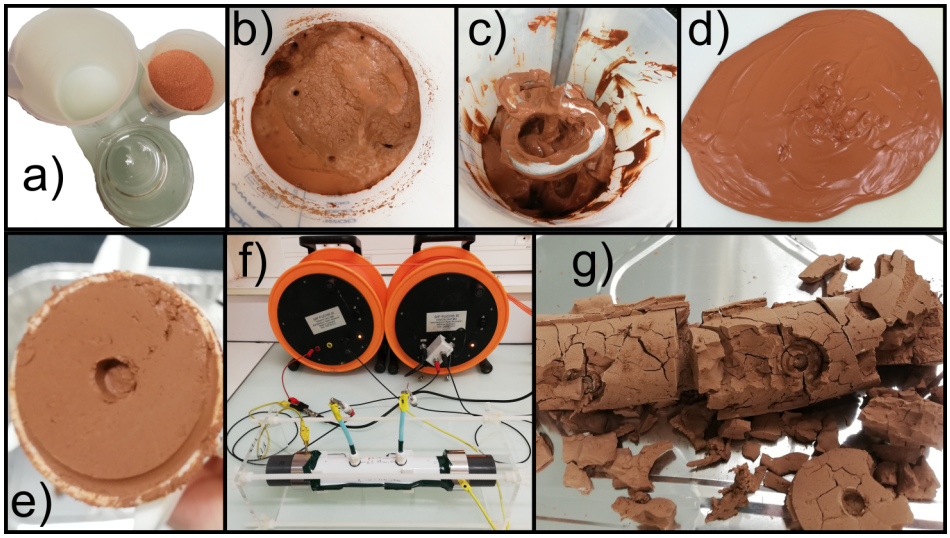

Figure 2. Laboratory protocol to create clay samples: a) Combination of clay powder and water. b) Saturation of clay powder for at least 24 h. c) Homogenization of mixture with drill. d) Excess water evaporation until correct plasticity is reached. e) Setting clay in sample holder. f) SIP measurements. g) Clay sample drying.

The current electrodes C1 and C2 are stainless steel cylinders that we use also as covers for the sample holder, while we use home-made non-polarizable electrodes for P1 and P2. We made our own Cu-$CuSO_4$ non-polarizable electrodes, following the procedure proposed by Kremer et al. (2016). They consist of a copper wire inserted in a plastic tube filled with a saturated solution of copper sulfate and gelatin, plugged by a porous filter at the bottom. We used a near cylindrical sample holder of length 22.9 cm and radius 2.1 cm, with electrode separation of 7.4 cm, that is separated roughly by a third of the sample holder's total length (Figure 3b); this pseudo-Wenner configuration has been used previously by Ghorbani et al. (2009), and Jougnot et al. (2010). The geometrical factor to convert measured impedances to conductivities has been determined using finite elements numerical methods, this approach has been used previously by Jougnot et al. (2010).

We created an external structure to hold the sample holder (Figure 3b) in order to achieve repeatability in our measurements. Indeed, we needed the ability to close the sample holder at the exact same position and with the same pressure between measurements. As repeatability test, we built two identical sample holders, made two individual green montmorillonite samples, and measured the SIP signal in both samples. The repeatability of the measurements shows a 4.7% difference on the real

Table 2. Post-dehydration calculated salinities, porosities, and gravimetric water contents (m_{fluid}/m_{solid}) for all the SIP-measured clay samples.

Initial Salinity	(D.water)	(10^{-3} M NaCl)	(10^{-2} M NaCl)	(10^{-1} M NaCl)	(1 M NaCl)
Clay type	Final salinity (M NaCl)	Final salinity (M NaCl)	Final salinity (M NaCl)	Final salinity (M NaCl)	Final salinity (M NaCl)
Kaolinite sample	D.W.	1.53×10^{-3}	1.54×10^{-2}	1.91×10^{-1}	1.76
Illite sample	D.W.	1.92×10^{-3}	1.80×10^{-2}	1.82×10^{-1}	1.91
Green montmorillonite sample	D.W.	1.39×10^{-3}	1.53×10^{-2}	1.46×10^{-1}	1.54
Red montmorillonite sample	D.W.	1.64×10^{-3}	1.71×10^{-2}	1.54×10^{-1}	1.51
Clay type	Porosity	Porosity	Porosity	Porosity	Porosity
Kaolinite sample	0.54	0.59	0.57	0.56	0.47
Illite sample	0.52	0.56	0.54	0.56	0.42
Green montmorillonite sample	0.65	0.68	0.68	0.71	0.57
Red montmorillonite sample	0.67	0.62	0.61	0.62	0.51
Clay type	Water content	Water content	Water content	Water content	Water content
Kaolinite sample	0.48	0.51	0.55	0.54	0.44
Illite sample	0.49	0.41	0.46	0.43	0.40
Green montmorillonite sample	1.02	0.96	0.91	0.93	0.85
Red montmorillonite sample	0.71	0.63	0.60	0.66	0.67

part of the electrical conductivity and a 0.47% difference on the imaginary part at 1.46 Hz. For the whole spectrum, we see a maximum percentage difference of 4.8% on the real part of the electrical conductivity (at 2.9 mHz) and 11.89% for the imaginary part (at 45.8 mHz). In average, for the whole spectrum, we see a difference of 4.6% for the real part of the spectrum, and 1.5% for the imaginary part. See the supplementary information file, to visualize the repeatability test. We acknowledge that the difference between the real part of the conductivity between both samples is surprising (although negligible). We think that such difference lies on the fact that we are dealing with two

different clay samples in two different sample holders. A minimal difference between these two will correspond to a minimal difference between their signals.

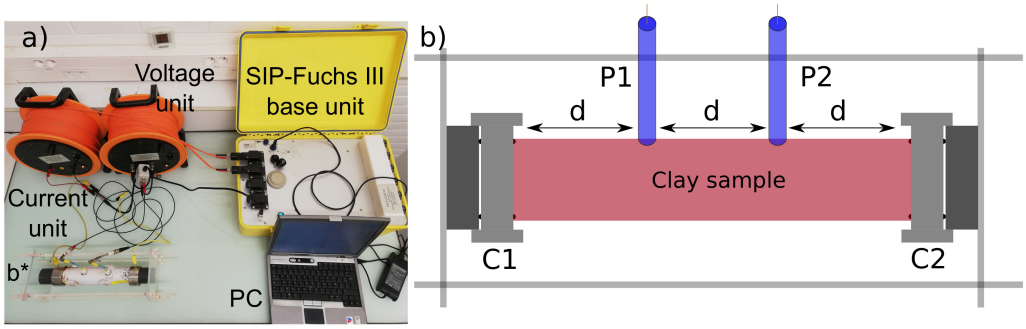

Figure 3. a) Laboratory set-up for SIP measurements on our clay samples with the sample holder, injecting and measuring units (orange), SIP-FUCHS III, and a computer to store the data. b) Sample holder sketch with the external structure. C1 and C2 are two cylindrical plates, our current electrodes that inject a sinusoidal electric current. P1 and P2 are a pair of non-polarizable electrodes that measure the resulting electrical potential difference, they are equally distanced from the current electrodes, making a pseudo-Wenner array.

3.4 Optimization of the double-Pelton model

For the optimization procedure, we use our SIP data as input, that is, conductivity amplitude (S m^{-1}) and phase (rad), and then fit a double-Pelton model (see equation 6). In this paper, we optimize for seven parameters: ρ_0, m_1, m_2, τ_1, τ_2, c_1, and c_2. The cost function is:

$$\Phi = \frac{\sum_{i=1}^{N_a}(A^i_{mes} - A^i_{mod})^2}{\sum_{i=1}^{N_a}(A^i_{mes} - \langle \mathbf{A}_{mes} \rangle)^2} + \frac{\sum_{i=1}^{N_p}(P^i_{mes} - P^i_{mod})^2}{\sum_{i=1}^{N_p}(P^i_{mes} - \langle \mathbf{P}_{mes} \rangle)^2}, \tag{8}$$

where, A_{mes} represents the measured amplitude vector, $\langle \mathbf{A_{mes}} \rangle$ represents the mean of the measured amplitude vector, A_{mod}, the modeled or calculated amplitude vector, via the double-Pelton model, N_a is the number of amplitude data points that have been preserved, P_{mes} is the measured phase vector, $\langle \mathbf{P_{mes}} \rangle$ is the mean of the measured phase vector, P_{mod} is the modeled or calculated phase vector, and N_p is the number of phase data points that have been kept. The strategy we used was to first optimize with a simulated annealing approach, that has been explained in detail in Maineult

(2016). For the parameters m_1, m_2, c_1, and c_2, we let them vary between [0 - 1], for ρ_0 we usually use $[\overline{\rho} \pm (0.2 \cdot \overline{\rho})\ \Omega \cdot m]$, for τ_1 we usually use $[10^{-3} - 10^{6}]$s, and finally for τ_2 we use $[10^{-10} - 10^{1}]$s. Here, $\overline{\rho}$ is the arithmetic mean electrical resistivity for all frequencies. We later optimize the double-Pelton parameters using a Simplex optimization procedure (Caceci & Cacheris, 1984). This same strategy has been used in Maineult et al. (2017). As input of the Simplex code we use our measured SIP data (amplitude and phase) and as initial model we use the result of the simulated annealing method. The simulated annealing step allows us to explore the parameter space preventing to get trapped in a local minimum, but this is done in a discrete manner. When we know the vicinity of the solution, we use the Simplex optimization procedure to refine the solution.

Moreover, we fixed a double-Warburg model for the red and green montmorillonite samples, as well as the kaolinite sample. A double-Warburg model is a double-Pelton model but with $c_1 = 0.5$ and $c_2 = 0.5$. In the case of these three types of clay samples, we turned the optimization code and obtained values of c_1 and c_2 near 0.5. Therefore, we opted that for these three types of clay samples, we would fix c_1 and c_2, and we would only optimize for the remaining five parameters, that is: ρ_0, m_1, m_2, τ_1, and τ_2. It is worth mentioning that we tried fixing c_1 and c_2 for the illite sample as we also obtained values near 0.5, but we obtained poor fits with $c_1 = 0.5$ and $c_2 = 0.5$. We assume then that the illite sample does not behave as a double-Warburg, but as a double-Pelton. The rest of the clay samples (kaolinite, red and green montmorillonite samples) do behave as double-Warburg models. The results of our fits are presented later on in this article, in Table 4.

3.5 Differentiation of clay minerals

In order to compare our SIP datasets, we calculated the normalized measured conductivity differences ($\Delta\sigma'_N$ or $\Delta\sigma''_N$) between each clay type for every salinity at 1.46 Hz, for both the real and imaginary parts of the complex conductivity. We chose 1.46 Hz because frequencies near 1 Hz represent a widely used choice in geophysics (Zanetti et al., 2011). Also, as it will be presented in the results and discussion sections, the local maximum polarization phenomena happens near 1 Hz. To choose this particular frequency, we also took into account that the highest measured errors in the data happened at the lowest frequencies (mHz range), because less stacking is possible, due to the long time periods for each measurement. The noisiest data happened at the highest frequencies (kHz range). Indeed, according to Huisman et al. (2016) the electromagnetic coupling effects happen at the highest frequency range of our SIP

measurements, in the kHz range. Therefore, when choosing near 1 Hz, we should get the most accurate data. We calculate Δx_N values between each clay type at 1.46 Hz, for the datasets shown in Figure 4. To calculate the Δx_N we use:

$$\Delta x_N(f = 1.46 \text{ Hz}) = 100 \times \frac{x_1 - x_2}{\frac{x_1 + x_2}{2}}, \tag{9}$$

where x_N, x_1 and x_2 can be substituted by the real and imaginary parts of the conductivity (so either $\Delta\sigma'_N$ or $\Delta\sigma''_N$), in such a way that the operation is done either for the real part or the imaginary part of the conductivity, separately. Additionally, x_1 and x_2 represent either the real or imaginary part of the conductivity at 1.46 Hz of an individual type of clay. The idea is to quantify if we are able to distinguish between two different clay minerals in a laboratory setting. That is, if the $\Delta\sigma'_N$ or $\Delta\sigma''_N$ value is low (e.g. below 10%) that means we are hardly able to differentiate two specific clay minerals at the laboratory scale, then at the field scale it would seem impossible to differentiate such clay minerals. Conversely, if we have a high $\Delta\sigma'_N$ or $\Delta\sigma''_N$ (e.g. above 100%) it would not mean that we could automatically differentiate two different clay minerals at the field scale.

4 Results

We obtained a large SIP dataset in the laboratory. To make our interpretation of this dataset more accessible, we decomposed their analysis into several subsections. First, we will present the complex conductivity values at 1.46 Hz vs. the calculated water conductivity, to get a quick view of the electric behavior of the clay samples at varying salinities. After that, we present the normalized spectrum of the real part of the complex conductivity per clay type; we show the evolution with salinity. We then present the full spectra of the complex conductivity for all clay samples and all salinities. Afterwards, we present the results of our double-Pelton fits, and the obtained parameters. We finally present a quantitative differentiation between clay samples at the same salinity. We filtered all of our datasets with a 5% percent filter. That is, if the error of the measured amplitude is larger than 5%, we remove the data point from our dataset. We performed our SIP measurements at five salinities on four types of clay: montmorillonite samples (red and green), a kaolinite sample and an illite sample (see Table 2). Additionally, we performed SIP measurements at three salinities (initially de-ionized water, 1×10^{-2}, and 1 M of NaCl) on two extra types of clay: beige montmorillonite sample and a Boom clay sample. Boom clay is a natural clayrock used for nuclear waste storage (Ortiz et al., 2002). The results of these additional types of clay are shown as supplementary information in this article.

4.1 Results at varying salinities at 1.46 Hz

We collected SIP measurements of four different types of clay (red and green montmorillonite samples, an illite sample, and a kaolinite sample) with the SIP-FUCHS III system. We used frequencies from 10^{-3} to 10^{4} Hz. The calculated water conductivity values (following equation 7) presented in Figure 4, correspond to those of the post-dehydration salinities (Figures 2d and e). We chose to present the data points at 1.46 Hz, because the highest measured errors and the noisiest data are present at the lowest and highest frequencies, respectively. It should be noted that the low salinity (initially 10^{-3} M NaCl) calculated water conductivity values may be underestimated because we did not consider clay dissolution as well as cation leaching from the interlayer space of montmorillonite.

In Figure 4a we observe that the real conductivity increases with an increase in the conductivity of the fluid saturating our clay mixtures for all salinities for all types of clay. In addition, Figure 4a shows that both montmorillonite samples exhibit higher surface conductivity than the illite and kaolinite samples. Due to their difference in surface electrical properties (see section 2.1), it is a bit surprising to see that the kaolinite and illite samples may have the same surface conductivity here. This may be due to the fact that the kaolinite sample is not pure and contains 4% in weight of more conducting smectite and 3% in weight of more conducting illite (see Table 1).

With the imaginary conductivity we see a different behavior. For the red and green montmorillonite samples, we see a peak of the imaginary conductivity at the second to highest salinity (corresponding to a water conductivity in the 10^{0} S m^{-1} range). For the kaolinite and illite samples, we see a similar behavior, however, we see the peak in the range of 10^{-1} S m^{-1} for the water conductivity. The imaginary conductivity amplitude is also roughly one order of magnitude higher for the montmorillonite samples than for other clay samples. Due to their higher CEC and stronger EDL, the montmorillonite samples polarize more than the illite and kaolinite samples. In addition, the zeta potential of Na-montmorillonite in a NaCl solution is higher in magnitude than the zeta potential of illite and kaolinite in a NaCl solution (Sondi et al., 1996; Leroy & Revil, 2004; Leroy et al., 2015). Consequently, membrane polarization effects may be higher for Na-montmorillonite than for illite and kaolinite. It results that more salt is necessary to decrease the imaginary conductivity of montmorillonite compared to illite and kaolinite at high salinity. Note that although we collected SIP data at five different salinities, the de-ionized water dataset are not presented in Figure 4. We chose not to present those data points because knowing or controlling the conductivity of the pore water at that salinity proved to be very complex, and out of the scope of

this paper. However, the datasets of de-ionized water are presented in the following parts of this paper.

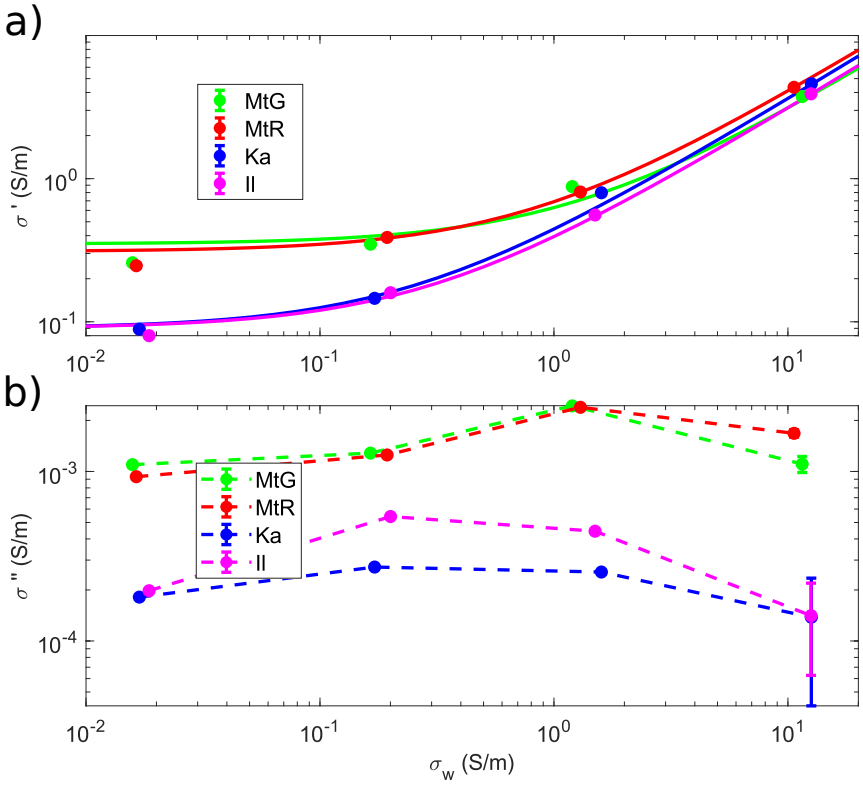

Figure 4. Measured (filled circles) real (a) and imaginary (b) conductivity of the four clay samples as a function of calculated water conductivity, at a frequency of 1.46 Hz. MtG represents the green montmorillonite sample, MtR the red montmorillonite sample, Ka the kaolinite sample, and Il the illite sample. The bold line on (a) is the calculated $\sigma'(\sigma_w)$ from equation 2, the parameters we fit are presented in Table 3.

Equation 2 was adjusted to the σ' values at 1.46 Hz (for 10^{-3}-1 M NaCl) by considering that the formation factor and the surface conductivity are independent from the pore water conductivity. For this adjustment, more weight was attributed to the values for the two highest pore water conductivities as they are expected to be less sensitive to the surface conductivity (see Weller et al., 2013). This procedure provides a single surface conductivity per sample presented in Table 3 and seems to overestimate its values for the lowest pore water conductivity. As expected, we see larger values of σ'_{surf} for both montmorillonite samples, because these clay samples have a more important surface electric charge and specific surface area than the illite or kaolinite samples. We recognise the formation factor values we obtained have some uncertainty and are only

meant as a mean of the electrical formation factor for each type of clay sample, as we are dealing with clay muds with varying porosities and not hard rocks with a specific formation factor. We present the σ' calculated values from the σ'_{surf} and F fitted values in Figure 4a. It is worth mentioning that the specific surface areas measured using the BET (Brunauer-Emmett-Teller) technique might not be representative of the true values for the montmorillonites mineral. Indeed, previous work from the literature indicate this technique is not able to properly probe interlayer space (e.g., Tournassat et al., 2003; Hassan et al., 2006). In order to do so, other methods such as wet-state methylene blue (MB) should be used (Weller et al., 2015a). Another possibility to better determine the real specific surface area could be through a calculation of the specific surface area based on the XRD characterisation of the samples. According to the literature the specific surface area of montmorillonites should be in the range of 390-780 m^2/g (see Tournassat et al., 2013).

Table 3. Formation factors (F) and σ'_{surf} fitted from equation 2 for the real conductivity values at 1.46 Hz, CEC and specific surface area (Ss) of the clay samples.

Clay type	F [-]	σ'_{surf} [Sm^{-1}]	CEC [meq/100 g]	Ss* [m^2/g, BET]
Kaolinite sample	2.82	0.09	22	16.94
Illite sample	3.29	0.09	47	101.60
Green mont. sample	3.60	0.35	132	77.71
Red mont. sample	2.63	0.31	135	71.09

*Specific surface area measured through the BET (Brunauer-Emmett-Teller) method for each sample. BET cannot probe the interlayer space of montmorillonites.

4.2 Normalized real conductivity

In Figure 5 we show the normalized real conductivity for all clay samples. For normalization value we used the amplitude of the conductivity at 1.46 Hz, per clay type, per salinity. We observe that overall the signal of the normalized real conductivity gets flattened as the salinity increases. In other words, we see less of a change in the normalized real conductivity within the measured frequency range as the salinity of the fluid increases. We interpret this as evidence that at the highest salinity, pore

conduction dominates over the surface conduction, and we are able to see this evolution with salinity. The normalized value presented in Figure 5 could be interpreted as a ratio of alternating current (AC) conduction vs. close to direct current (DC) conduction. Even though we see an overall decrease with salinity of $\sigma'/\sigma_{1.46}$. This decrease could be interpreted as evidence that the DC conduction increases faster with salinity than the AC conduction due to polarization. We used a frequency of 1.46 Hz as normalization value because, as mentioned previously in the paper, as it is the closest value to 1 Hz; a widely used choice in field geophysics. Also, in field geophysics, the measurements (i.e. electrical resistivity tomography) are thought of as DC measurements. A true DC value would make use of the lowest measured frequency.

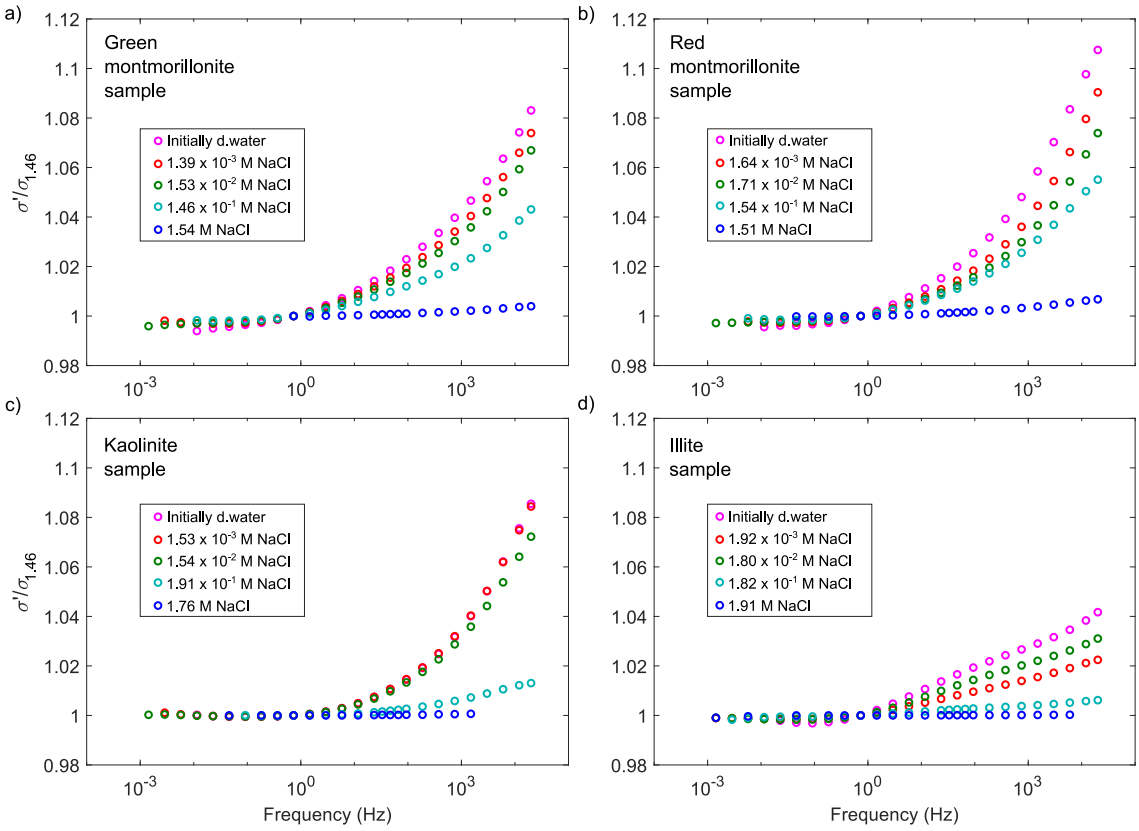

Figure 5. Normalized real conductivity for all salinities per clay type: a) green montmorillonite sample, b) red montmorillonite sample, c) kaolinite sample, and d) illite sample. All these spectra have been normalized by the conductivity amplitude at 1.46 Hz.

4.3 Effect of the salinity on the spectra

Figure 6 shows the real conductivity spectra of each clay per salinity, with the double-Pelton model superimposed onto the dataset. We see for all of the clay samples that as the salinity increases, the real conductivity also increases. We do however notice that the data seems more dispersed for the kaolinite and illite samples, meaning, the difference between maximum and minimum conductivities seems bigger for the kaolinite and illite samples, than for the montmorillonite samples.

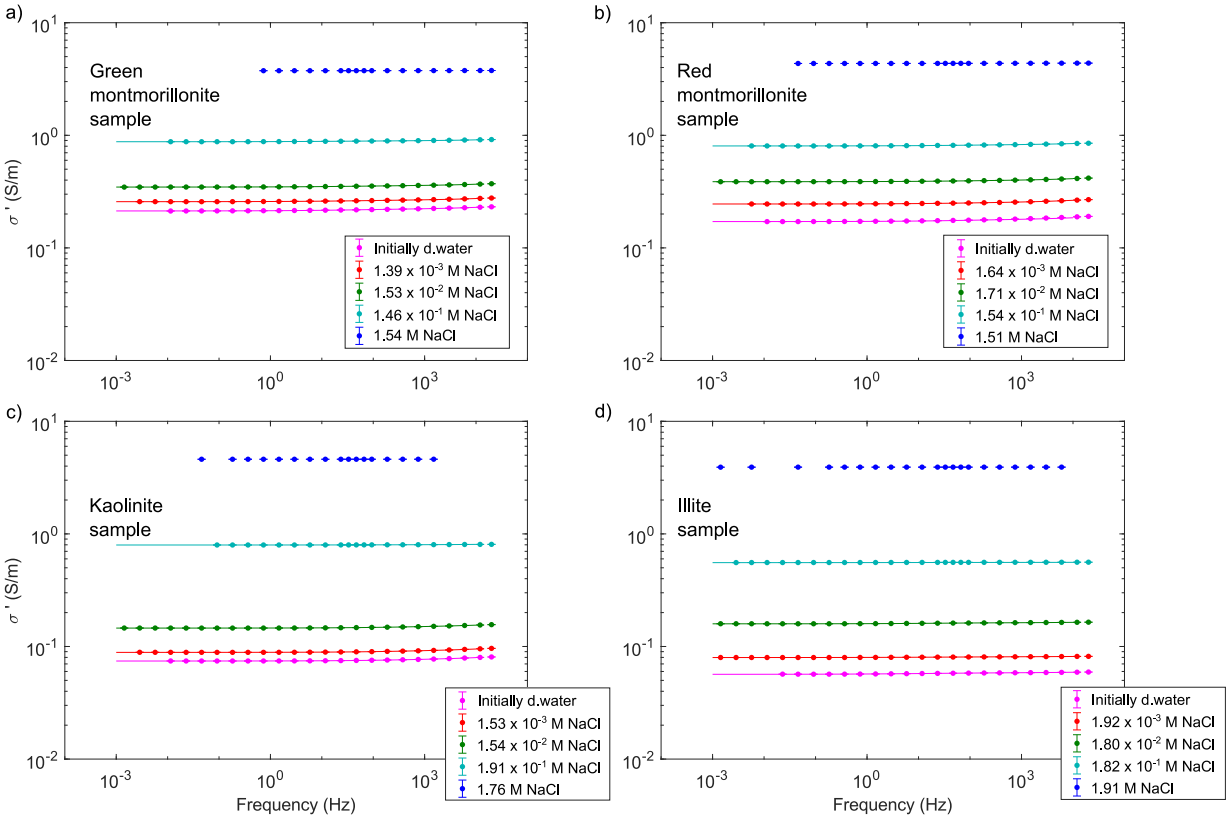

Figure 6. Real part of the complex conductivity per salinity of: a) green montmorillonite sample, b) red montmorillonite sample, c) kaolinite sample, and d) illite sample. The calculated salinity values at which the SIP measurements were collected are presented in the legends of each subplot. Dots with errorbars represent the measured SIP data, and the line represents the double-Pelton model predictions for each dataset.

Figure 7 shows the imaginary conductivity spectra of each clay per salinity, with the double-Pelton model predictions superimposed onto the dataset. For the montmorillonite samples we see the overall highest polarization at the second to highest salinity.

Finally, for the kaolinite and illite samples, we see the highest polarization at the middle salinity (10^{-2} M of NaCl salinity range), this is better seen for the illite sample.

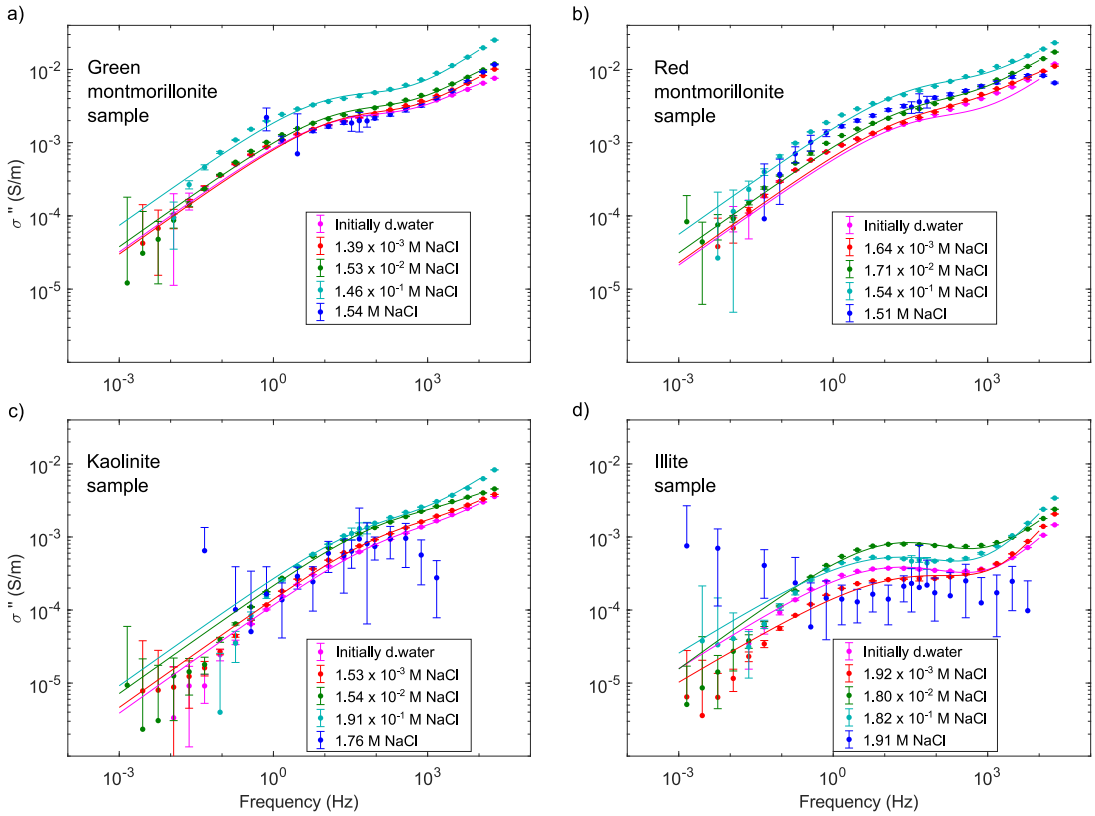

Figure 7. Imaginary part of the complex conductivity per salinity of: a) green montmorillonite sample, b) red montmorillonite sample, c) kaolinite sample, and d) illite sample. The calculated salinity values at which the SIP measurements were collected are presented in the legends of each subplot. Dots with errorbars represent the measured SIP data, and the line represents the double-Pelton model predictions for each dataset.

The errorbars become larger in the highest salinity measurements. This is expected from the measurement itself. Indeed, measuring low phases, that is, very small time differences between the injected current and the resulting measured voltage signal, is a real challenge for the electronics involved in SIP measurements (Zimmermann et al., 2008). Nevertheless, it is possible to distinguish a clear tendency with frequency, in most of the spectra, except for the illite and kaolinite samples at the highest salinity.

4.4 Double-Pelton model fits and variation of Pelton parameters with varying salinities

In Figure 8 we present the principle of the double-Pelton model decomposition. We sum two individual Pelton signals (see equation 6), the resulting signal is the one that we fit our data with. Note that we ran more than 3 simulated annealing optimizations to check for the repeatability of the solution and in all cases we found the same solution. It is also worth mentioning that we use filtered data for this process, for which the errorbars are negligible. We assume that the high frequency peak (in blue) happens due to partly an inductive and capacitive effect (Huisman et al., 2016) plus polarization of the clay (Leroy & Revil, 2009; Okay et al., 2014; Leroy et al., 2017a). We assume that the mid-frequency peak (in red) corresponds solely to the polarization of clay.

In Table 4 we have summarized the optimized Pelton parameters of both the red and blue peaks (Figure 8). Furthermore, as mentioned previously, we used a double-Warburg model (c_1=0.5 and c_2=0.5) for all clay samples except the illite sample, that was fitted with a double-Pelton (fitted c_1 and c_2). We present fully the double-Pelton parameters as we believe it will be of interest to the community to have access to Pelton parameters of individual types of clays at varying salinities, for possible forward-modeling opportunities.

For the four lowest salinity datasets, we observe how at the highest fitted salinity, there is a considerable decrease in the chargeability (m_1) parameter for the lower frequency local maxima. For all datasets we see chargeability values (in each individual local maxima) in the same magnitude order. We also see an increase on DC electrical conductivity with increasing salinity, as expected. Note that we present values of electrical conductivity, instead of resistivity (as shown in the double-Pelton model, equation 6), as the complex conductivity is only the inverse to the complex resistivity. As for the illite sample, we see that for c_1 all values linger near 0.5, but not quite 0.5. Finally, we see that the relaxation times for the second (high frequency) local maxima are mostly below the μs range, and that for the second local maxima, these are considerably above.

4.5 Differentiation of clay minerals

After calculating the $\Delta\sigma'_N$ and $\Delta\sigma''_N$ values (equation 9), we see that the values $\Delta\sigma'_N$ decrease with increasing salinities overall, agreeing with what we observe in Figure 5, for the normalized real conductivity. This behavior is not so clear or evident

Table 4. Double-Pelton parameters obtained from the optimization procedure of section 3.4 to reproduce SIP signal on the four studied clay types.

Clay type	Salinity [M NaCl]	σ_0 [S m^{-1}]	m_1 [mV/V]	τ_1 [μ s]	c_1	m_2 [mV/V]	τ_2 [μ s]	c_2	RMS [-]
Kaolinite	D.W.	0.074	40.14	333	0.5	345	0.327	0.5	1.78×10^{-3}
	1.53×10^{-3}	0.089	40.68	332	0.5	249	0.599	0.5	1.82×10^{-3}
sample	1.54×10^{-2}	0.146	34.86	413	0.5	142	1.483	0.5	1.52×10^{-3}
	1.91×10^{-1}	0.797	5.66	842	0.5	350	0.014	0.5	2.63×10^{-2}
Illite	D.W.	0.057	34.26	10110	0.45	682	0.063	0.66	4.82×10^{-3}
	1.92×10^{-3}	0.080	20.00	3261	0.42	740	0.143	0.84	5.26×10^{-3}
sample	1.80×10^{-2}	0.159	22.57	7662	0.51	515	0.021	0.56	6.18×10^{-3}
	1.82×10^{-1}	0.557	5.11	10369	0.44	342	0.043	0.76	7.21×10^{-3}
Green mont.	D.W.	0.213	37.40	4418	0.5	158	1.917	0.5	4.75×10^{-3}
	1.39×10^{-3}	0.257	32.55	3432	0.5	249	0.56	0.5	4.23×10^{-3}
sample	1.53×10^{-2}	0.347	28.27	3957	0.5	198	0.803	0.5	2.72×10^{-3}
	1.46×10^{-1}	0.877	18.48	5758	0.5	504	0.052	0.5	3.87×10^{-3}
Red mont.	D.W.	0.171	42.32	2266	0.5	958	0.048	0.5	9.61×10^{-2}
	1.64×10^{-3}	0.245	30.87	2046	0.5	200	1.88	0.5	3.78×10^{-3}
sample	1.71×10^{-2}	0.387	27.47	2033	0.5	306	0.452	0.5	3.85×10^{-3}
	1.54×10^{-1}	0.805	25.76	1846	0.5	188	0.528	0.5	7.41×10^{-3}

for the imaginary part. We also observe that the $\Delta\sigma'_N$ and $\Delta\sigma''_N$ values are smaller between the montmorillonite samples, as expected, that is the montmorillonite samples are electrically similar to each other. For the lowest salinity (initially de-ionized water) the biggest difference in real conductivity is between the illite and the green montmorillonite samples (-116%, the real conductivity of the illite sample is smaller than that of the montmorillonite sample), and for the imaginary part it is between the kaolinite and the green montmorillonite samples (-149%, the imaginary conductivity of the kaolinite sample is smaller than that of the montmorillonite sample). For the initial 10^{-3} M salinity (NaCl) the biggest difference in real conductivity is between the illite and the green montmorillonite samples (-105%), and for the imaginary part it is between the kaolinite and the green montmorillonite samples (-143%). For the initial 10^{-2} M salinity, the biggest difference in real conductivity is between the kaolinite and the red montmorillonite samples (-91%), and for the imaginary part it is between the kaolinite and the green montmorillonite samples (-130%). For the initial 10^{-1} M salinity, the biggest difference in real conductivity is between the illite and the green montmorillonite samples (-45%), and for the imaginary part it is between the kaolinite and the green montmorillonite samples (-162%). For the highest salinity, the biggest difference in real conductivity is between the kaolinite and the green montmorillonite samples (20%), and for the imaginary part it is between the kaolinite and the

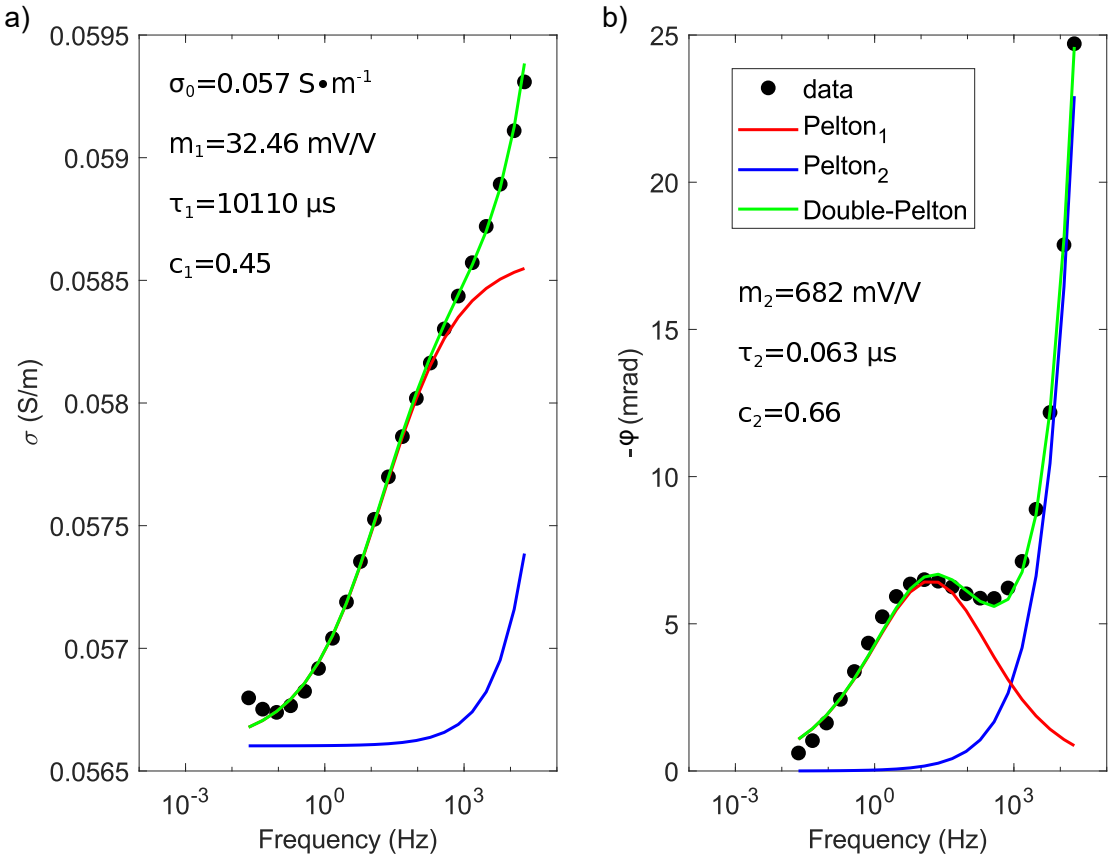

Figure 8. Fit of a double-Pelton model (equation 6) to our data, in both a) amplitude and b) phase. We present the illite sample dataset using initial de-ionized water (filled circles), and the corresponding double-Pelton model (green line), with two individual Pelton models (blue and red lines).

red montmorillonite samples (−169%). Table 5 presents the $\Delta\sigma'_N$ and $\Delta\sigma''_N$ values for the initial salinity of 10^{-2} M of NaCl. We use x_1 (see equation 9) as the value of the column, and x_2 of the row. For example, in Table 5, we obtained 10.85, using the σ' of the red montmorillonite sample as σ'_1, and of the green montmorillonite sample as σ'_2 (see equation 9). The lower left triangle corresponds to calculation for the real part ($\Delta\sigma'_N$) of the complex conductivity (in bold), and the upper right triangle corresponds to the imaginary part ($\Delta\sigma''_N$, in italics). The tables for the rest of the salinities are presented in the supplementary information part of this paper.

5 Discussion

In this study we propose a new experimental protocol with verified repeatability to characterize the complex electrical conductivity spectra of non-consolidated clay

Table 5. $\Delta\sigma'_N$ and $\Delta\sigma''_N$ values (in %) for the initially 10^{-2} M of NaCl clay mixtures. These calculations are made using the complex conductivity at 1.46 Hz, the real part ($\Delta\sigma'_N$) is on the lower left triangle (in bold), and the imaginary part ($\Delta\sigma''_N$) is on the upper right triangle (in italics). MtG represents the green montmorillonite sample, MtR the red montmorillonite sample, Ka the kaolinite sample, and IL the illite sample.

	MtG	MtR	Ka	IL
MtG	0	*2.56*	*129.84*	*81.20*
MtR	**10.85**	0	*128.34*	*79.06*
Ka	**-82.00**	**-90.83**	0	*-66.04*
IL	**-74.37**	**-85.53**	**9.01**	0

samples. We obtain a unique SIP dataset composed of four types of clay samples and saturated by a NaCl solution at five different salinities. We first interpreted the dataset at 1.46 Hz for the real and imaginary parts of the electrical conductivity before studying the entire spectra and fitting them with a double-Pelton phenomenological model, and presenting a schematic figure on how we interpret the polarization phenomena of our results.

Our measurements, at 1.46 Hz (Figure 4b), show that the quadrature conductivity (imaginary part of the complex conductivity) hits a maximum at a certain salinity and then decreases. The salinity at which this maximum exists depends on the type of clay. For the kaolinite and the illite samples, we have the maximum at the mid-salinity (around 10^{-2} M of NaCl salinity range), while it is a higher salinity for the montmorillonite samples (around 10^{-1} M of NaCl). It should be noted that we do not have the exact salinity at which the maximum quadrature conductivity happens because we investigated 5 finite salinities, that is, perhaps the maximum of the quadrature happens between two of our measured salinities. Among the published SIP datasets on clay samples, Vinegar & Waxman (1984) present an extensive dataset of the complex electrical conductivity from 21 shaly sands, measured at 4, 5 or 7 different salinities (0.01, 0.05, 0.1, 0.25, 0.5, 1.0, and 2.0 M NaCl); see Tables 1 and 2 of Vinegar & Waxman (1984). Some of their samples also exhibit the behavior with a maximum quadrature conductivity at a particular salinity, notably the samples with more shale content. They propose that the decrease of the quadrature conductivity happens due to a decrease of the membrane effect. Weller et al. (2010) proposed that the relationship between the imaginary conductivity and the water conductivity is guided by the

specific surface area per unit pore volume. For this, they analyzed IP or SIP data from 114 samples, including sandstones, and sand and clay mixtures. Revil & Skold (2011) also present a dataset composed of 7 samples of sandstones and unconsolidated sand from the literature where most of the datasets present the same trend where a maximum in quadrature conductivity appears at a particular salinity. The behavior shown in Figure 4b is also consistent with the one reported by Weller & Slater (2012), both share the same water conductivity range. They measured SIP on 67 samples of sandstones and unconsolidated sediments. Okay et al. (2014) measured SIP on bentonite and kaolinite quartz sand mixtures, at different clay contents 100%, 20%, 5%, and 1%. They present the behavior of the quadrature conductivity with respect to water conductivity at only three NaCl salinities. Their bentonite samples (95% smectite content) and kaolinite samples (15% smectite content) present an increase in the quadrature conductivity with salinity; the maximum water conductivity presented is around 1.5 S/m. Finally, Lévy et al. (2019b) measured the SIP response of a set of 88 volcanic altered rocks with varying amounts of smectite. They present the SIP spectra from four of their samples (Figure 1 in Lévy et al., 2019b), using four different fluid conductivities, 0.04, 0.1, 0.5, and 1.5 S m^{-1} (from four different NaCl concentrations). They show an overall increase in polarization (quadrature conductivity) with salinity for these four samples. If we only analyze the smectite samples of our dataset, we see a progressive increase in the quadrature conductivity with increase of fluid conductivity, until we reach the highest salinity, where we see a decrease (see Figure 4b). Only one of the samples presented with the full conductivity spectra (Figure 1 in Lévy et al., 2019b) has more than 20 % smectite. If we only take a look at this sample, it doesn't show a decrease in quadrature conductivity with the highest salinity, although, their highest presented pore water conductivity for this data subset is 1.5 S m^{-1}. For the smectite samples of our dataset, we see a decrease on the quadrature conductivity just at the highest pore water conductivity, around 10 S m^{-1}. According to these studies, it is interesting to notice that the increase of the quadrature conductivity with salinity is larger for sandstones and quartz sand than for smectite minerals. This observation confirms the assumption that the quadrature conductivity of these materials is directly sensitive to their surface charge controlling EDL polarization (Okay et al., 2014; Leroy et al., 2017a). Indeed, the surface charge of quartz strongly increases with pH and salinity due to the deprotonated silanol surface sites whereas the smectite minerals carry a permanent negative surface charge less sensitive to pH and salinity on their basal surface due to isomorphic substitutions in the crystal lattice. Weller & Slater (2012) suggest further investigation at even higher salinities, this could be important for high salinity environments, such as oceanic shale reservoirs (Morsy & Sheng, 2014).

Due to such a high electrical conductivity of such sample, the SIP measurement logistics could be complex, and better protocols and measuring equipment with low uncertainty at high conductivities are needed.

Furthermore, Weller et al. (2013), Woodruff et al. (2014), and Lévy et al. (2019b) observed a linear relation between σ''_{surf} and σ'_{surf}. Weller et al. (2013) used a database composed of 63 sandstones and unconsolidated sediment samples. They overall found the linear parameter (l) of equation 5 to be 0.042. Woodruff et al. (2014) worked on a variety of shales, and found $l = 0.022$ for their dataset, they call it parameter R in their work. In addition, Lévy et al. (2019b) studied a variety of volcanic rocks, with different smectite contents, and they found that the linear relation between σ''_{surf} and σ'_{surf} decreases in magnitude with smectite content. They calculate $l = 0.002$ for a data subset with more than 20% smectite content. According to Revil (2012), this very low l value of samples with high smectite content compared to the l value of sandstones and unconsolidated sediment samples may be due to the restricted cation mobility in the Stern layer of clays. Also, it is not sure that it is possible to correctly capture the surface conductivity of clays with such linear model (de Lima & Sharma, 1990).

We used σ' values at 1.46 Hz for the four highest salinities (10^{-3}-1 M of NaCl) to adjust one formation factor and one surface conductivity per clay type using equation 2. Then, we recalculated σ'_{surf} values for each salinity (using equation 3) and considered equation 4 to associate the measured values of σ'' to σ''_{surf}. Figure 9b shows the relation between σ'_{surf} and σ''. We obtained the best fit for equation 5 for $l = 0.0039$, that is, almost an order of magnitude smaller than the value of Weller et al. (2013)($l = 0.042$) from samples containing no clay. Our data agree more with the value of l proposed by Lévy et al. (2019b)($l = 0.002$, when samples had more than 20% smectite), than the one of Weller et al. (2013). As we only consider clay samples, this difference could be attributed to the difference in mineralogical composition. Perhaps sandstones and sediments behave more like what Weller et al. (2013) present, but as clay materials have a significant σ'_{surf}, they present a different, but also seemingly linear behavior.

In order to test the hypothesis that l decreases with clay content, in Figure 9a we evaluated the combined dataset of Woodruff et al. (2014), Lévy et al. (2019b), and ours. For Lévy et al. (2019b) we selected the data that contained more than 20% smectite, from their Table 1. As mentioned previously, using only our dataset we obtain $l = 0.0039$. From Figure 9a we can see that none of the proposed values for l fit perfectly this combined dataset. The results are in agreement with Lévy et al. (2019b) on the idea that l seems to decrease with increasing smectite content. Further than

that, these data would seem to suggest that the relation between σ'' and σ'_{surf} is a non-linear one over multiple types of minerals. A more thorough analysis over multiple types of minerals needs to be performed in order to determine if there is a larger obtainable linear or non-linear relation between σ'' and σ'_{surf}. Another interesting relationship that is studied between two SIP parameters is the relationship between σ'' and the surface area per unit volume (S_{por}), see Revil (2012) and Weller et al. (2015a). In the supplementary information, we present a comparison of our data and that presented in Börner (1992) and Weller et al. (2015a). It should be noted that we use clay samples and not a mix of sand and clay, and thus the results between the data presented in Börner (1992), Weller et al. (2015a), and our data do not align perfectly. As a whole, we observe that the imaginary conductivity increases with the surface area per unit volume, as previously observed by Börner (1992), Revil (2012), and Weller et al. (2015a).

Among the various existing phenomenological models, we used a double-Pelton model to fit our data. We noticed that a double-Warburg model (c=0.5) was suitable for three of our datasets (kaolinite, red, and green montmorillonite samples). Revil et al. (2014) have proposed rather the use of a Warburg model over a Debye or Pelton model, after analyzing SIP datasets of metal-free and clayey materials. This holds true for three of the measured types of clay, that is the kaolinite, red and green montmorillonite samples. Only the illite sample cannot be fitted by a double-Warburg and presents the most noticeable mid-frequency (around 10 Hz) peak of all the measured types of clay. We present in Figure 10, trends we found among all double-Pelton parameters. To further interpret the results of the double-Pelton model, one can consider the classic formula of chargeability (m):

$$m = \frac{\sigma_\infty - \sigma_0}{\sigma_\infty}, \tag{10}$$

where σ_∞ can be thought of as the conductivity at high frequency or the AC conductivity due to polarization plus the DC conductivity, and σ_0 can be thought of as the conductivity at low frequency or only the DC conductivity. In this way, if we notice an increase of m_1 or m_2, we could interpret this as that possibly AC conductivity increases faster with respect to DC conductivity. Similarly, if we notice a decrease of m_1 or m_2, we could interpret this as DC conductivity increasing faster than the AC conductivity. We see an overall decrease of m_1 with an increase of σ_0, and we observe a decrease of τ_2 with an increase of m_2. We could interpret the first as a direct result of our data processing protocol. By optimizing the Pelton parameters from the curves of amplitude and phase, we see an overall decrease of the mid-frequency peak

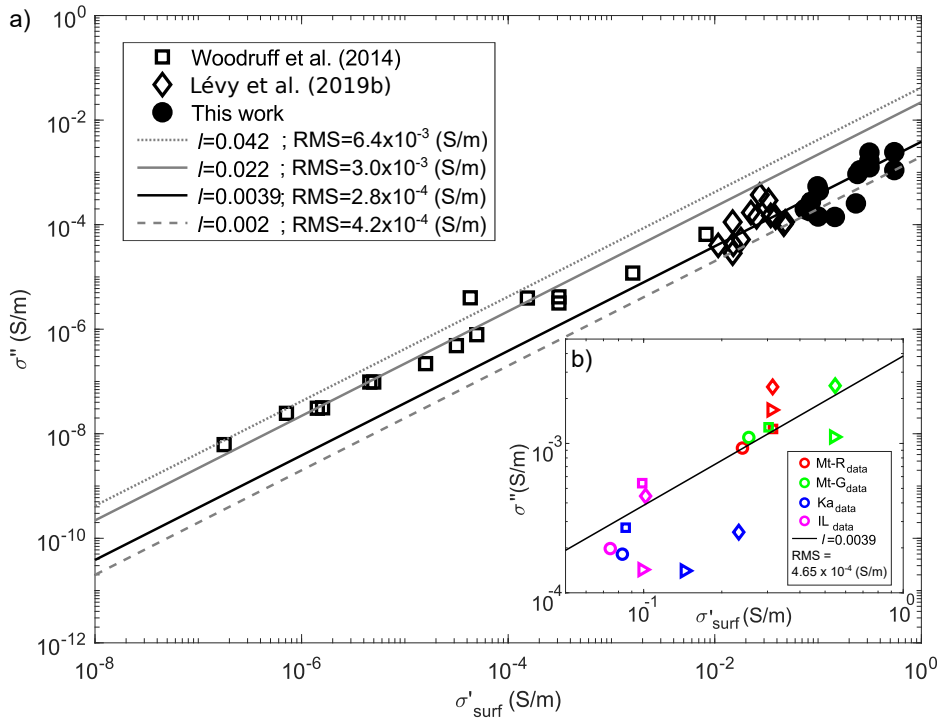

Figure 9. Relationship between σ'' and σ'_{surf}. a) Comparison of different linear parameters presented in the literature and the datasets from Woodruff et al. (2014) and Lévy et al. (2019b). b) Linear fit ($l = 0.0039$) between σ'' and σ'_{surf}, with our data at 1.46 Hz and with the four highest salinities. The red symbols represent the red montmorillonite sample, the green represent the green montmorillonite sample, the blue symbols the kaolinite sample, and the magenta represent the illite sample. The symbols (in b) representing data from the lower to higher salinity are: circle, square, diamond, and triangle.

(red peak in Figure 8b) with an increase in salinity of the clay sample. We attribute the decrease of m_1 with salinity to maybe the cease of a polarization mechanism at a particular salinity. The fact that we don't necessarily see a decrease of m_2 with salinity means that perhaps, at a certain salinity some other polarization mechanisms are still active. Which polarization mechanism acts at which salinity is still an open question. Further investigation needs to be done, specifically on the modeling side, to better understand the SIP response of clay samples for varying salinities, with individual polarization mechanisms in mind. The correlation of τ_2 and m_2 could be an artifact present in our optimization process. However, we do not see such a behavior between τ_1 and m_1. Schwartz & Furman (2015) adjust a single Pelton on their SIP data on soil organic matter, and they also see a decrease of τ with an increase of m.

They attribute this phenomenon to the fact that an ion mobility reduction causes an increase in the relaxation time and a decrease in polarization. Indeed, as presented in Table 4 and Figure 10b, we see that for m_2 and τ_2 of our dataset this holds truth as well. An explanation of the observed inverse correlation between m_2 and τ_2 could be also due to the EDL polarization of the smallest clay particles at high frequency. Large clay particles tend to polarize less than smaller clay particles due to their lower total specific surface area, and thus lower surface conductivity. However, the relaxation time of the EDL polarization increases when the size of the particle increases. Therefore, the chargeability due to these small clay particles may decrease when the relaxation time increases. More modeling work is necessary on the polarization of the EDL of clay particles to better interpret our results with respect to individual polarization mechanisms, in particular the EDL polarization.

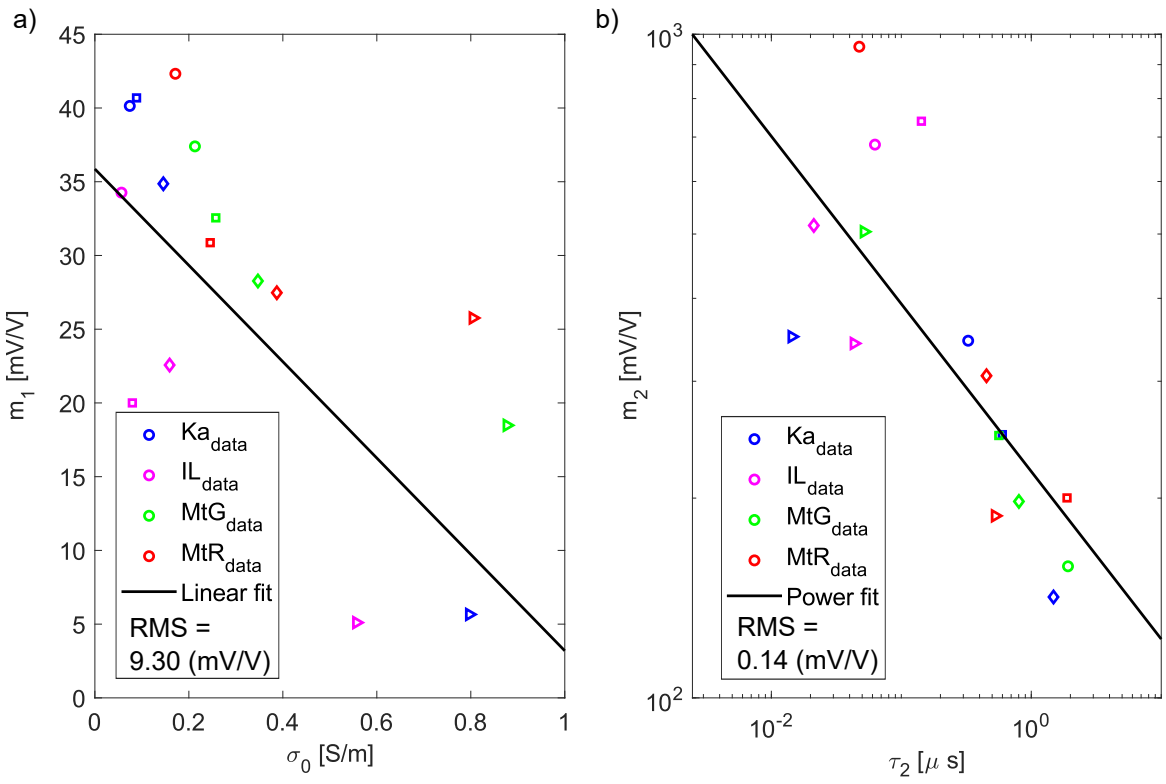

Figure 10. From the double-Pelton optimization parameters: a) dependence of m_1 and σ_0, and b) dependence of τ_2 and m_2. The red symbols represent the red montmorillonite sample, the green represent green montmorillonite sample, the blue the kaolinite sample, and the magenta represent the illite sample. The symbols representing data from lower to higher salinity are: circle, square, diamond, and triangle.

Our $\Delta\sigma'_N$ and $\Delta\sigma''_N$ calculations agree with the fact that the highest conduction and polarization values come from the smectite samples. We could interpret this as a result of the fact that the smectite samples have a higher specific surface area than illite sample, which has a higher specific surface area than the kaolinite sample. The surface charge of montmorillonite and illite may also be higher in magnitude than the surface charge of kaolinite. The imaginary conductivity amplitude is roughly one order of magnitude higher for the montmorillonite samples than for other clay samples. Due to their higher specific surface area and stronger EDL (reflected in the CEC measurements, see Table 3), the montmorillonite samples may polarize more than the kaolinite and illite samples, and this may also explain why more salt is necessary to "saturate" the EDL polarization controlling imaginary conductivity. For the red and green montmorillonite samples, we interpret the fact that the peak of polarization (see Figure 4) happens around a 10^{-1} M NaCl salinity due to the high electrical charge (see the CEC values in Table 3) on the basal surfaces of all smectites. Diffuse layers around montmorillonite particles are strongly repulsive, meaning that a high ion concentration in the pore water is necessary to compress the diffuse layers which decreases membrane polarization effects and favour coagulation of the particles (Tombácz & Szekeres, 2006). Coagulated particles exhibit a smaller external surface area available for polarization. Illite and kaolinite have a smaller specific surface area, therefore, the peak in their imaginary conductivity may happen at a smaller ion concentration in the pore water.

If we take a look at Figures 6 and 7, we see that for both conductivities (real and imaginary), the montmorillonite samples are less dispersed than the kaolinite and illite samples. Meaning, the maximum and minimum values are closer together for the montmorillonite samples than for the illite and kaolinite samples. This could be due to the fact that montmorillonites have a far more important specific surface area than illite and kaolinite, therefore a change in salinity effects more the conductivities (real and imaginary) of kaolinite and illite. Furthermore, we can observe in Figure 6 that the surface conductivity of the montmorillonite samples is higher than the surface conductivity of the kaolinite and illite samples. We can see this as in the lowest salinity, we have higher values for the real conductivity of the montmorillonite samples in comparison to the kaolinite and illite samples. At the lowest salinity, we can assume that the surface conductivity is the most important between pore water conductivity and surface conductivity (see equation 2). The high surface conductivity of the montmorillonite samples could also explain the fact that the difference between maximum and minimum conductivities is bigger for the kaolinite and illite samples, than for the montmorillonite samples (see Figure 6). Again, as the salinity increases (more available ions), it can significantly effect the pore water conductivity and thus the total

measured conductivity of the kaolinite and illite samples. As for the montmorillonite samples, this is less clear because of the high surface conductivity. For the montmorillonite and kaolinite samples, the imaginary conductivity spectra are less sensitive to salinity than for the illite sample. This may be due to the permanent negative surface charge of the basal surface of montmorillonite (see Figure 1) which may control polarization of montmorillonites and kaolinite (to a lesser extent due to a significant content of smectite). In addition, the illite sample exhibits a polarization peak at a frequency of around 10 Hz, which is not seen for the other clay types (flatter signals). Following Schwarz (1962), we could attribute this 10 Hz peak of polarization in the illite sample to a possible presence of bigger clay aggregates compared to the rest of the clay samples. The illite sample used for our measurements (see Table 1) has 12% calcite that could perhaps correspond to polarization around large calcite grains, or a smaller polarization of grains themselves, as shown by Leroy et al. (2017b).

In Figure 11 we present a conceptual sketch of what we interpret occurs to clay particles with increasing salinity. As the salinity increases, it seems plausible that clay particles coagulate; and thus the distance between clay particles decreases with increasing salinity, up until a point of coagulation where two clay particles can be thought of as a thicker clay particle. As a result, initially at the lowest salinity (Figure 11a), we have two clay particles with a negative surface charge, and an overlapping diffuse layer, with a membrane effect polarization. At the mid-salinity (Figure 11b), we have a larger ionic concentration (NaCl), thus more available ions to polarize, and so we see an increase in polarization from Figure 11a to Figure 11b. However, we see an overlap in the diffuse layer, with a possible reduced membrane effect polarization. Therefore the overall total polarization increases from Figure 11a to Figure 11b (even if individual polarization mechanisms such as the membrane polarization decreases from Figure 11a to Figure 11b). On the contrary, at the highest salinity (Figure 11c), where clay particles have coagulated and thus we have a smaller external specific surface charge; a smaller area for ions to polarize. In addition, we have a null membrane polarization effect at the highest salinity. To make the link with Figure 4b, for the montmorillonite samples, the two lowest salinities (10^{-2}-10^{-1} S/m range) would correspond to the state presented in Figure 11a, the 10^{0} S/m salinity would correspond to in Figure 11b, and the 10^{1} S/m would correspond to Figure 11c. For the kaolinite and illite samples, we would rather couple the 10^{-2} S/m (presented in Figure 4b) to Figure 11a, the 10^{-1} S/m to Figure 11b, and finally the two highest salinities (10^{0}-10^{1} S/m range) to 11c. This is consistent with, Vinegar & Waxman (1984), who proposed that the decrease of the quadrature conductivity with salinity in shaly sands happens due to a decrease of the membrane effect. Revil (2012) mentions that there is a relative

change on the effect of polarization mechanisms with salinity. Furthermore, Hördt et al. (2016) made a numerical membrane polarization study of wide and narrow pores of different sizes and varying salinity and pH. They find that specially for narrow pores, the imaginary conductivity increases with salinity until a maximum value, and then decreases. Additionally, Weller et al. (2015b) and Lesmes & Frye (2001) have interpreted the decrease of the polarization of sandstones at high salinities by a decrease of the ionic mobility at high salinities in the EDL. Although according to molecular dynamics (MD) predictions (Bourg & Sposito, 2011), the mobility of counter-ions (Na^+) in the Stern layer does not decrease when salinity increases. More physical or numerical modeling of clays needs to be done to better understand exactly how each phenomenon (clay coagulation and decrease of ionic mobility) effects the polarization of clay samples at varying salinities.

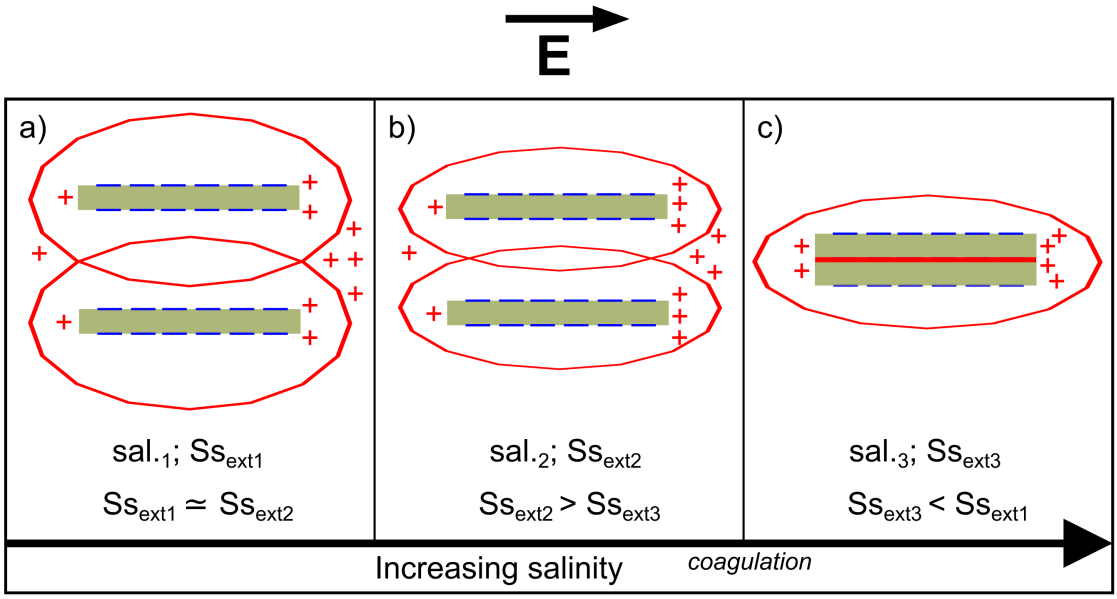

Figure 11. An interpreted process of how clay particles behave with increasing salinity. The state of two clay particles at a) the lowest salinity, b) mid-salinity and c) highest salinity. In green we present individual clay particles. In blue the negative surface charge of the clay particle, and in red the EDL (Stern and diffuse layer). In this figure, we refer as sal. to salinity, and Ss_{ext} to the specific surface area of the clay particle. Numbers 1, 2, and 3 represent different stages of increasing salinity and therefore coagulation.

On the differentiation of clay types by using SIP, we can think of two things. If we take a look at the parameters of Table 4, we could say these parameters are very close

to each other, and on a field scale experiment, realistically differentiating two types of clay seems very ambitious. The success of such a task would depend on the fieldwork planning, so a correct resolution is used, but with single parameters such as σ_0, the task would seem complicated. However, if we take a look at figures 6 and 7, differentiating types of clay using multiple frequencies seems easier of a task. Therefore, if a fieldwork campaign is carried out with the objective of differentiating two or more types of clay in a formation, we recommend using multi-frequency electrical methods. Moreover, differentiating two types of montmorillonites in the field and laboratory scale seems impossible if only using geo-electrical methods. However, differentiating between a montmorillonite and illite or kaolinite seems more achievable of a task in both the field and laboratory scales. If in the laboratory we run experiments in a controlled environment using relatively pure clays, the application of our findings in the field will be more challenging due to a combination of subsurface heterogeneity and greater measurement noise due to larger coupling effects.

Zonge et al. (2005) mention that the differentiation of clay types in IP is possible at frequencies above 1000 Hz. Our dataset could help establishing a basis to differentiate types of clay at lower frequencies (<1000 Hz) using the widely used low frequency geo-electrical methods. We understand that, just because we can see a clear difference in the resistivity values of our clay samples (see Table 5), this does not necessarily mean that, this differentiation could be done for all field conditions. Differentiating types of clay would depend on the clay samples themselves and the resolution of method used for the data collection in the field. As future work, we could use our dataset as a basis for forward-modeling to better understand if the differentiation of types of clay would be possible at the field scale. Also more experiments at a larger laboratory scale (pluri-decimetric) to test if we are able to differentiate types of clay using geo-electrical methods in a controlled environment.

6 Conclusions

We present a new laboratory protocol to characterize clay samples with good repeatability, and a new SIP dataset consisting of four different types of clay (red and green montmorillonite samples, an illite sample, and a kaolinite sample) at five different NaCl salinities (from initially de-ionized water to 1 M NaCl). Our data shows an increase of the real part of the conductivity with salinity, while there is a non-monotonous behavior with the imaginary conductivity. A possible interpretation of this behavior could be that as salinity increases, coagulation happens. At a particular salinity threshold some polarization mechanisms cease to act, possibly membrane po-

larization effects, thus decreasing at a particular salinity the imaginary conductivity of the clay sample. There is a difference in the peak of polarization between clay types, varying both with salinity and in amplitude. Montmorillonite samples may present this polarizability peak at a higher salinity than the kaolinite and illite samples. This agrees with the fact that smectites need a higher ion concentration in the pore water to diminish membrane polarization effects and favour particle coagulation. We calculate the surface conductivities of the clay samples for the four highest salinities and we confirm that both montmorillonite samples have higher surface conductivities with respect to the kaolinite and illite samples and correlate well with the measured CEC. We found the linear parameter (l) between both surface conductivities to be 0.0039 for our dataset. A wider dataset of clayey materials would seem to suggest that l decreases with clay content.

More work on the side of the physical modeling needs to be done in order to be able to interpret our dataset by polarization mechanisms. Additionally more laboratory work, at a slightly bigger scale (pluri-decimetric) or directly field scale using multi-frequency geo-electrical methods could be used to validate the differentiation of clay types at bigger scales.

Acknowledgments

The authors strongly thank the financial support of ANR EXCITING (grant ANR-17-CE06-0012) for this work and for the PhD thesis funding of A. Mendieta. We would also like to thank: Claude Fontaine, Philippe Cosenza, Céline Boissard, and Patricia Patrier. Members of the HydrASA team of the University of Poitiers for performing the XRD and CEC measurements on the different types of clay samples. We thank the associate editor, Niklas Linde, Lee Slater and two anonymous reviewers for their insightful comments that allowed us to improve our manuscript immensely. The data used in this study will be available on a zenodo repository (doi:10.5281/zenodo.4050345) after acceptance of the paper.

References

Auken, E., Boesen, T., & Christiansen, A. V. (2017). A review of airborne electromagnetic methods with focus on geotechnical and hydrological applications from 2007 to 2017. In *Advances in geophysics* (Vol. 58, pp. 47–93). Elsevier Inc. doi: 10.1016/bs.agph.2017.10.002

Batayneh, A. T. (2006). Resistivity tomography as an aid to planning gas-pipeline construction, Risha area, north-east Jordan. *Near Surface Geophysics*, *4*(5), 313–

319. doi: 10.3997/1873-0604.2005053

Bergaya, F., & Lagaly, G. (2006). General introduction: clays, clay minerals, and clay science. In B. F., T. B.K.G., & L. G. (Eds.), *Handbook of clay science* (1st ed., Vol. 1, pp. 1–18). Elsevier Ltd. doi: 10.1016/S1572-4352(05)01001-9

Börner, F. (1992). Complex conductivity measurements of reservoir properties. In P. Worthington & C. Chardaire-Rivière (Eds.), *Advances in core evaluation: Reservoir management: Reviewed proceedings of the society for core analysis third european core analysis symposium* (pp. 359–386). Hardwood Academic.

Bourg, I. C., & Sposito, G. (2011). Molecular dynamics simulations of the electrical double layer on smectite surfaces contacting concentrated mixed electrolyte (NaCl-CaCl2) solutions. *Journal of Colloid and Interface Science*, *360*(2), 701–715. doi: 10.1016/j.jcis.2011.04.063

Breede, K., Kemna, A., Esser, O., Zimmermann, E., Vereecken, H., & Huisman, J. A. (2012). Spectral induced polarization measurements on variably saturated sand-clay mixtures. *Near Surface Geophysics*, *10*(6), 479–489. doi: 10.3997/1873-0604.2012048

Brigatti, M. F., Galan, E., & Theng, B. K. (2006). Structures and mineralogy of clay minerals. In B. F., T. B.K.G., & L. G. (Eds.), *Handbook of clay science* (Vol. 1, pp. 19–86). Elsevier Ltd. doi: 10.1016/S1572-4352(05)01002-0

Brindley, G., & Brown, G. (1980). *Crystal structures of clay minerals and their X-ray identification. Mineralogical Society Monograph No. 5.* London: The Mineralogical Society of Great Britain and Ireland.

Bücker, M., Flores Orozco, A., Undorf, S., & Kemna, A. (2019). On the role of Stern- and diffuse-layer polarization mechanisms in porous media. *Journal of Geophysical Research: Solid Earth*, *124*(6), 5656–5677. doi: 10.1029/2019JB017679

Bücker, M., & Hördt, A. (2013). Analytical modelling of membrane polarization with explicit parametrization of pore radii and the electrical double layer. *Geophysical Journal International*, *194*(2), 804–813. doi: 10.1093/gji/ggt136

Caceci, M., & Cacheris, W. (1984). Fitting curves to data. The Simplex algorithm is the answer. *Byte*, *9*, 340–348.

Chen, Y., & Or, D. (2006). Effects of Maxwell-Wagner polarization on soil complex dielectric permittivity under variable temperature and electrical conductivity. *Water Resources Research*, *42*(6), 1–14. doi: 10.1029/2005WR004590

Chorover, J., Kretzschmar, R., Garica-Pichel, F., & Sparks, D. L. (2007). Soil biogeochemicial processes within the critical zone. *Elements*, *3*(5), 321–326. doi: 10 .2113/gselements.3.5.321

Chung, F. H. (1974). Quantitative interpretation of X-ray diffraction patterns of mixtures. I. Matrix-flushing method for quantitative multicomponent analysis. *Journal of Applied Crystallography*, *7*, 519–525. doi: 10.1107/s0021889874010375

Ciesielski, H., & Sterckeman, T. (1997). Determination of cation exchange capacity and exchangeable cations in soils by means of cobalt hexamine trichloride. Effects of experimental conditions. *Agronomie*, *17*(1), 1–7. doi: 10.1051/agro:19970101

Cole, K. S., & Cole, R. H. (1941). Dispersion and absorption in dielectrics. *Journal of Chemical Physics*, *9*(4), 341–351. doi: https://doi.org/10.1063/1.1750906

Corrado, S., Aldega, L., Celano, A. S., De Benedetti, A. A., & Giordano, G. (2014). Cap rock efficiency and fluid circulation of natural hydrothermal systems by means of XRD on clay minerals (Sutri, Northern Latium, Italy). *Geothermics*, *50*(4), 180–188. doi: 10.1016/j.geothermics.2013.09.011

Cosenza, P., Ghorbani, A., Revil, A., Zamora, M., Schmutz, M., Jougnot, D., & Florsch, N. (2008). A physical model of the low-frequency electrical polarization of clay rocks. *Journal of Geophysical Research: Solid Earth*, *113*(B8), 1–9. doi: 10.1029/2007JB005539

de Lima, O. A., & Sharma, M. M. (1990). A grain conductivity approach to shaly sandstones. *Geophysics*, *55*(10), 1347–1356. doi: 10.1190/1.1442782

Finco, C., Pontoreau, C., Schamper, C., Massuel, S., Hovhannissian, G., & Rejiba, F. (2018). Time-domain electromagnetic imaging of a clayey confining bed in a brackish environment: A case study in the Kairouan Plain Aquifer (Kelbia salt lake, Tunisia). *Hydrological Processes*, *32*, 3954–3965. doi: 10.1002/hyp.13303

Garrels, R. M., & Mackenzie, F. (1971). *Evolution of sedimentary rocks.* New York.

Ghorbani, A., Cosenza, P., Revil, A., Zamora, M., Schmutz, M., Florsch, N., & Jougnot, D. (2009). Non-invasive monitoring of water content and textural changes in clay-rocks using spectral induced polarization: A laboratory investigation. *Applied Clay Science*, *43*(3), 493–502. doi: 10.1016/j.clay.2008.12.007

Gonçalvès, J., de Marsily, G., & Tremosa, J. (2012). Importance of thermo-osmosis for fluid flow and transport in clay formations hosting a nuclear waste repository. *Earth and Planetary Science Letters*, *339-340*, 1–10. doi: 10.1016/j.epsl.2012.03.032

Hassan, M. S., Villieras, F., Gaboriaud, F., & Razafitianamaharavo, A. (2006). AFM and low-pressure argon adsorption analysis of geometrical properties of phyllosilicates. *Journal of Colloid and Interface Science*, *296*(2), 614–623. doi: 10.1016/j.jcis.2005.09.028

Hillier, S. (1999). Quantitative analysis of clay and other minerals in sandstones by

X-ray powder diffraction (XRPD). In R. H. Worden & S. Morad (Eds.), *Clay mineral cements in sandstones* (Vol. 34, pp. 213–251). John Wiley & Sons, Ltd. doi: 10.1002/9781444304336.ch11

Hördt, A., Bairlein, K., Bielefeld, A., Bücker, M., Kuhn, E., Nordsiek, S., & Stebner, H. (2016). The dependence of induced polarization on fluid salinity and pH, studied with an extended model of membrane polarization. *Journal of Applied Geophysics*, *135*, 408–417. doi: 10.1016/j.jappgeo.2016.02.007

Huisman, J. A., Zimmermann, E., Esser, O., Haegel, F. H., Treichel, A., & Vereecken, H. (2016). Evaluation of a novel correction procedure to remove electrode impedance effects from broadband SIP measurements. *Journal of Applied Geophysics*, *135*, 466–473. doi: 10.1016/j.jappgeo.2015.11.008

Islam, M., Chittoori, B., & Burbank, M. (2020). Evaluating the applicability of biostimulated calcium carbonate precipitation to stabilize clayey soils. *Journal of Materials in Civil Engineering*, *32*(3), 1–11. doi: 10.1061/(ASCE)MT.1943-5533.0003036

Jougnot, D., Ghorbani, A., Revil, A., Leroy, P., & Cosenza, P. (2010). Spectral induced polarization of partially saturated clay-rocks: a mechanistic approach. *Geophysical Journal International*, *180*(1), 210–224. doi: 10.1111/j.1365-246X.2009.04426.x

Kemna, A., Binley, A., Cassiani, G., Niederleithinger, E., Revil, A., Slater, L., ... Zimmermann, E. (2012). An overview of the spectral induced polarization method for near-surface applications. *Near Surface Geophysics*, *10*(6), 453–468. doi: 10.3997/1873-0604.2012027

Khaled, E. M., & Stucki, J. W. (1991). Iron oxidation state effects on cation fixation in smectites. *Soil Science Society of America Journal*, *55*(2), 550–554. doi: 10.2136/sssaj1991.03615995005500020045x

Konikow, L., August, L., & Voss, C. (2001). Effects of clay dispersion on aquifer storage and recovery in coastal aquifers. *Transport in Porous Media*, *43*, 45–64. doi: 10.1023/A:1010613525547

Kremer, T., Schmutz, M., Maineult, A., & Agrinier, P. (2016). Laboratory monitoring of CO2 injection in saturated silica and carbonate sands using spectral induced polarization. *Geophysical Journal International*, *207*(2), 1258–1272. doi: 10.1093/gji/ggw333

Leroy, P., Li, S., Jougnot, D., Revil, A., & Wu, Y. (2017b). Modelling the evolution of complex conductivity during calcite precipitation on glass beads. *Geophysical Journal International*, *209*(1), 123–140. doi: 10.1093/gji/ggx001

Leroy, P., & Revil, A. (2004). A triple-layer model of the surface electrochemical

properties of clay minerals. *Journal of Colloid and Interface Science*, *270*(2), 371–380. doi: 10.1016/j.jcis.2003.08.007

Leroy, P., & Revil, A. (2009). A mechanistic model for the spectral induced polarization of clay materials. *Journal of Geophysical Research*, *114*(B10202), 1–21. doi: 10.1029/2008JB006114

Leroy, P., Tournassat, C., Bernard, O., Devau, N., & Azaroual, M. (2015). The electrophoretic mobility of montmorillonite. Zeta potential and surface conductivity effects. *Journal of Colloid And Interface Science*, *451*, 21–39. doi: 10.1016/j.jcis.2015.03.047

Leroy, P., Weigand, M., Mériguet, G., Zimmermann, E., Tournassat, C., Fagerlund, F., ... Huisman, J. A. (2017a). Spectral induced polarization of Na-montmorillonite dispersions. *Journal of Colloid And Interface Science*, *505*, 1093–1110. doi: 10.1016/j.jcis.2017.06.071

Lesmes, D. P., & Frye, K. M. (2001). Influence of pore fluid chemistry on the complex conductivity and induced polarization responses of Berea sandstone. *Journal of Geophysical Research: Solid Earth*, *106*(B3), 4079–4090. doi: 10.1029/2000jb900392

Lévy, L., Gibert, B., Sigmundsson, F., Flóvenz, O. G., Hersir, G. P., Briole, P., & Pezard, P. A. (2018). The role of smectites in the electrical conductivity of active hydrothermal systems: Electrical properties of core samples from Krafla volcano, Iceland. *Geophysical Journal International*, *215*(3), 1558–1582. doi: 10.1093/gji/ggy342

Lévy, L., Maurya, P. K., Byrdina, S., Vandemeulebrouck, J., Sigmundsson, F., Árnason, K., ... Labazuy, P. (2019a). Electrical resistivity tomography and time-domain induced polarization field investigations of geothermal areas at Krafla, Iceland: Comparison to borehole and laboratory frequency-domain electrical observations. *Geophysical Journal International*, *218*(3), 1469–1489. doi: 10.1093/gji/ggz240

Lévy, L., Weller, A., & Gibert, B. (2019b). Influence of smectite and salinity on the imaginary and surface conductivity of volcanic rocks. *Near Surface Geophysics*, *17*(6), 653–673. doi: 10.1002/nsg.12069

Looms, M. C., Klotzsche, A., van der Kruk, J., Larsen, T. H., Edsen, A., Tuxen, N., ... Nielsen, L. (2018). Mapping sand layers in clayey till using crosshole ground-penetrating radar. *Geophysics*, *83*(1), A21–A26. doi: 10.1190/geo2017-0297.1

Ma, C., & Eggleton, R. (1999). Cation exchange capacity of kaolinite. *Clays and Clay Minerals*, *47*, 174–180. doi: 10.1346/CCMN.1999.0470207

Maineult, A. (2016). Estimation of the electrical potential distribution along metal-

lic casing from surface self-potential profile. *Journal of Applied Geophysics*, *129*, 66–78. doi: 10.1016/j.jappgeo.2016.03.038

Maineult, A., Revil, A., Camerlynck, C., Florsch, N., & Titov, K. (2017). Upscaling of spectral induced polarization response using random tube networks. *Geophysical Journal International*, *209*(2), 948–960. doi: 10.1093/gji/ggx066

Meier, L. P., & Kahr, G. (1999). Determination of the cation exchange capacity (CEC) of clay minerals using the complexes of copper(II) ion with triethylenetetramine and tetraethylenepentamine. *Clays and Clay Minerals*, *47*(3), 386–388. doi: 10.1346/ccmn.1999.0470315

Michot, L. J., & Villiéras, F. (2006). Surface area and porosity. In F. Bergaya, B. K. Theng, & G. Lagaly (Eds.), *Handbook of clay science* (Vol. 1, pp. 965–978). Elsevier Ltd. doi: 10.1016/S1572-4352(05)01035-4

Mitchell, J. K., & Soga, K. (2005). *Fundamentals of soil behavior* (3rd ed.). John Wiley & Sons. doi: 10.1097/00010694-199407000-00009

Moore, D., & Reynolds, R. (1989). *X-ray diffraction and the identification and analysis of clay minerals*. Oxford University Press.

Morsy, S., & Sheng, J. (2014). Effect of water salinity on shale reservoir productivity. *Advances in Petroleum Exploration and Development*, *8*(1), 9–14. doi: 10.3968/5604

Okay, G., Cosenza, P., Ghorbani, A., Camerlynck, C., Cabrera, J., Florsch, N., & Revil, A. (2013). Localization and characterization of cracks in clay-rocks using frequency and time-domain induced polarization. *Geophysical Prospecting*, *61*(1), 134–152. doi: 10.1111/j.1365-2478.2012.01054.x

Okay, G., Leroy, P., Ghorbani, A., Cosenza, P., Camerlynck, C., Cabrera, J., ... Revil, A. (2014). Spectral induced polarization of clay-sand mixtures : Experiments and modeling. *Geophysics*, *79*(6), 353–375. doi: 10.1190/geo2013-0347.1

Ortiz, L., Volckaert, G., & Mallants, D. (2002). Gas generation and migration in Boom Clay, a potential host rock formation for nuclear waste storage. *Engineering Geology*, *64*(2), 287–296. doi: 10.1016/S0013-7952(01)00107-7

Parker, B. L., Chapman, S. W., & Guilbeault, M. A. (2008). Plume persistence caused by back diffusion from thin clay layers in a sand aquifer following TCE source-zone hydraulic isolation. *Journal of Contaminant Hydrology*, *102*(1), 86–104. doi: 10.1016/j.jconhyd.2008.07.003

Pelton, W., Ward, S. H., Hallof, P. G., Sill, W. R., & Nelson, P. H. (1978). Mineral discrimination and removal of inductive coupling with multifrequency IP. *Geophysics*, *43*(3), 588–609. doi: 10.1190/1.1440839

Revil, A. (2012). Spectral induced polarization of shaly sands: Influence of the electrical double layer. *Water Resources Research*, *48*(2), 1–23. doi: 10.1029/2011WR011260

Revil, A., Florsch, N., & Camerlynck, C. (2014). Spectral induced polarization porosimetry. *Geophysical Journal International*, *198*(2), 1016–1033. doi: 10.1093/gji/ggu180

Revil, A., Karaoulis, M., Johnson, T., & Kemna, A. (2012). Review : Some low-frequency electrical methods for subsurface characterization and monitoring in hydrogeology. *Hydrogeology Journal*, *20*, 617–658. doi: 10.1007/s10040-011-0819-x

Revil, A., & Leroy, P. (2004). Constitutive equations for ionic transport in porous shales. *Journal of Geophysical Research: Solid Earth*, *109*(B3), 1–19. doi: 10.1029/2003jb002755

Revil, A., & Skold, M. (2011). Salinity dependence of spectral induced polarization in sands and sandstones. *Geophysical Journal International*, *187*(2), 813–824. doi: 10.1111/j.1365-246X.2011.05181.x

Schwartz, N., & Furman, A. (2015). On the spectral induced polarization signature of soil organic matter. *Geophysical Journal International*, *200*(1), 589–595. doi: 10.1093/gji/ggu410

Schwarz, G. (1962). A theory of the low-frequency dielectric dispersion of colloidal particles in electrolyte solution. *Journal of Physical Chemistry*, *66*, 2636–2642. doi: 10.1021/j100818a067

Sondi, I., Biscan, J., & Pravdic, V. (1996). Electrokinetics of pure clay minerals revisited. *Journal of Colloid And Interface Science*, *178*(2), 514–522. doi: 10.1006/jcis.1996.0403

Spichak, V., & Manzella, A. (2009). Electromagnetic sounding of geothermal zones. *Journal of Applied Geophysics*, *68*(4), 459–478. doi: 10.1016/j.jappgeo.2008.05.007

Tabbagh, A., Rejiba, F., Finco, C., Schamper, C., Souffaché, B., Camerlynck, C., ... Maineult, A. (2021). The case for considering polarization in the interpretation of electrical and electromagnetic measurements in the 3 kHz to 3 MHz frequency range. *Surveys in Geophysics*, *42*, 377–397. doi: 10.1007/s10712-020-09625-1

Tombácz, E., & Szekeres, M. (2006). Surface charge heterogeneity of kaolinite in aqueous suspension in comparison with montmorillonite. *Applied Clay Science*, *34*(1), 105–124. doi: 10.1016/j.clay.2006.05.009

Tournassat, C., Bizi, M., Braibant, G., & Crouzet, C. (2011). Influence of montmorillonite tactoid size on Na-Ca cation exchange reactions. *Journal of Colloid and*

Interface Science, *364*(2), 443–454. doi: 10.1016/j.jcis.2011.07.039

Tournassat, C., Bourg, I. C., Steefel, C. I., & Bergaya, F. (2015). Surface Properties of Clay Minerals. In C. Tournassat, C. I. Steefel, I. C. Bourg, & F. Bergaya (Eds.), *Developments in clay science* (Vol. 6, pp. 5–31). Elsevier. doi: 10.1016/B978-0-08-100027-4.00001-2

Tournassat, C., Grangeon, S., Leroy, P., & Giffaut, E. (2013). Modeling specific pH dependent sorption of divalent metals on montmorillonite surfaces. A review of pitfalls, recent achievements and current challenges. *American Journal of Science*, *313*(5), 395–451.

Tournassat, C., Neaman, A., Villéras, F., Bosbach, D., & Charlet, L. (2003). Nanomorphology of montmorillonite particles: Estimation of the clay edge sorption site density by low-pressure gas adsorption and AFM observations. *American Mineralogist*, *88*, 1989–1995. doi: 10.2138/am-2003-11-1243

Tournassat, C., & Steefel, C. I. (2015). Ionic transport in nano-porous clays with consideration of electrostatic effects. *Reviews in Mineralogy and Geochemistry*, *80*(1), 287–329. doi: 10.2138/rmg.2015.80.09

Tournassat, C., & Steefel, C. I. (2019). Reactive transport modeling of coupled processes in nanoporous media. *Reviews in Mineralogy and Geochemistry*, *85*(1), 75–109. doi: 10.2138/rmg.2019.85.4

Tsujimoto, Y., Chassagne, C., & Adachi, Y. (2013). Dielectric and electrophoretic response of montmorillonite particles as function of ionic strength. *Journal of Colloid and Interface Science*, *404*, 72–79. doi: 10.1016/j.jcis.2013.03.033

Vinegar, H. J., & Waxman, M. H. (1984). Induced polarization of shaly sands - the effect of clay counterion type. *Log Analyst*, *25*, 11–21.

Wagner, J. F. (2013). Mechanical properties of clays and clay minerals. In F. Bergaya & G. Lagaly (Eds.), *Handbook of clay science* (2nd ed., Vol. 5A, pp. 347–381). Elsevier Inc. doi: 10.1016/B978-0-08-098258-8.00011-0

Wang, C., & Slater, L. D. (2019). Extending accurate spectral induced polarization measurements into the kHz range: Modelling and removal of errors from interactions between the parasitic capacitive coupling and the sample holder. *Geophysical Journal International*, *218*(2), 895–912. doi: 10.1093/gji/ggz199

Waxman, M. H., & Smits, L. J. (1968). Electrical conductivities in oil-bearing shaly sands. *Society of Petroleum Engineers Journal*, *243*(2), 107–122. doi: 10.2118/1863-A

Weller, A., & Slater, L. (2012). Salinity dependence of complex conductivity of unconsolidated and consolidated materials: Comparisons with electrical double layer

models. *Geophysics*, *77*(5), D185–D198. doi: 10.1190/geo2012-0030.1

Weller, A., Slater, L., Huisman, J. A., Esser, O., & Haegel, F. H. (2015a). On the specific polarizability of sands and sand-clay mixtures. *Geophysics*, *80*(3), A57–A61. doi: 10.1190/GEO2014-0509.1

Weller, A., Slater, L., & Nordsiek, S. (2013). On the relationship between induced polarization and surface conductivity: Implications for petrophysical interpretation of electrical measurements. *Geophysics*, *78*(5), D315–D325. doi: 10.1190/geo2013-0076.1

Weller, A., Slater, L., Nordsiek, S., & Ntarlagiannis, D. (2010). On the estimation of specific surface per unit pore volume from induced polarization: A robust empirical relation fits multiple data sets. *Geophysics*, *75*(4), WA105–WA112. doi: 10.1190/1.3471577

Weller, A., Zhang, Z., & Slater, L. (2015b). High-salinity polarization of sandstones. *Geophysics*(3), D309–D318. doi: 10.1190/GEO2014-0483.1

White, W. A. (1949). Atterberg plastic limits of clay minerals. *American Mineralogist*, *34*, 508–512. doi: https://doi.org/

Woodruff, W. F., Revil, A., & Torres-Verdín, C. (2014). Laboratory determination of the complex conductivity tensor of unconventional anisotropic shales. *Geophysics*, *79*(5), E183–E200. doi: 10.1190/geo2013-0367.1

Zanetti, C., Weller, A., Vennetier, M., & Mériaux, P. (2011). Detection of buried tree root samples by using geoelectrical measurements: A laboratory experiment. *Plant Soil*, *339*(1), 273–283. doi: 10.1007/s11104-010-0574-0

Zimmermann, E., Kemna, A., Berwix, J., Glaas, W., Münch, H. M., & Huisman, J. A. (2008). A high-accuracy impedance spectrometer for measuring sediments with low polarizability. *Measurement Science and Technology*, *19*(10), 1–9. doi: 10.1088/0957-0233/19/10/105603

Zonge, K., Wynn, J., & Urquhart, S. (2005). Resistivity, induced polarization, and complex resistivity. In D. K. Butler (Ed.), *Near surface geophysics* (pp. 265–300). Society of Exploration Geophysicists. doi: 10.1190/1.9781560801719.ch9

3.3 Main results of JGR article

- We see an increase of the real part of the electrical conductivity with salinity, as expected. The imaginary part presents a non-monotonous behavior; the signal increases in amplitude with salinity until a maximum and then it decreases.
- The position of the maximum with respect to salinity depends on the type of clay. We interpret this decrease is due to a decrease in polarization processes, in specific, the membrane polarization.
- We calculate the real surface conductivity and compare it to values of the literature. The relation between the imaginary and real surface conductivity does not appear to be linear, but to decrease with clay content. Thus this relation appears to vary with mineralogy.

3.4 Supplementary information of JGR article

Here, I present the supplementary information corresponding to the JGR article. In this supplementary information section I present the SIP data of two types of clay (Boom clay and beige montmorillonite), only at three salinities (initially de-ionised water, 10^{-2}, and 1 M NaCl). Furthermore, I present the repeatability test for the laboratory protocol and sample holder chosen, and the real and imaginary percentage difference calculated by salinity (referred to as $\Delta\sigma'$ and $\Delta\sigma''$ in the article). Additionally, I compare the SIP data I collected with data from Börner (1992) and Weller et al. (2015a) in the light of the relation between the imaginary conductivity and the surface area per unit pore volume (S_{por}, in $1/\mu$m).

3.4.1 SIP measurements on additional samples

Spectral induced polarization (SIP) measurements on the beige montmorillonite sample, and the Boom clay sample, at three different salinities (de-ionised water, $\sim 10^{-2}$, and 1 mol/L NaCl).

The data presented in figures 3.1 and 3.2 have been filtered with a 5% filter. That is, if the error in the measured amplitude exceeds 5%, we remove the data point.

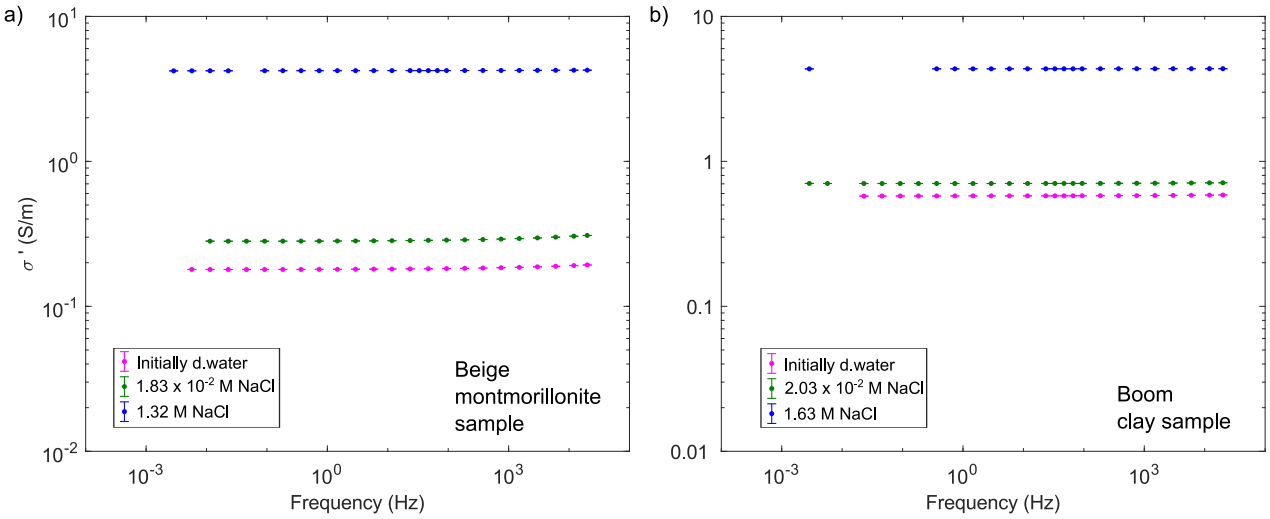

Figure 3.1: Real part of the complex conductivity per salinity of: a) beige montmorillonite sample, and b) Boom clay sample. The calculated salinity values at which the SIP measurements were collected are presented in the legends of each subplot. Dots with errorbars represent the SIP measured data.

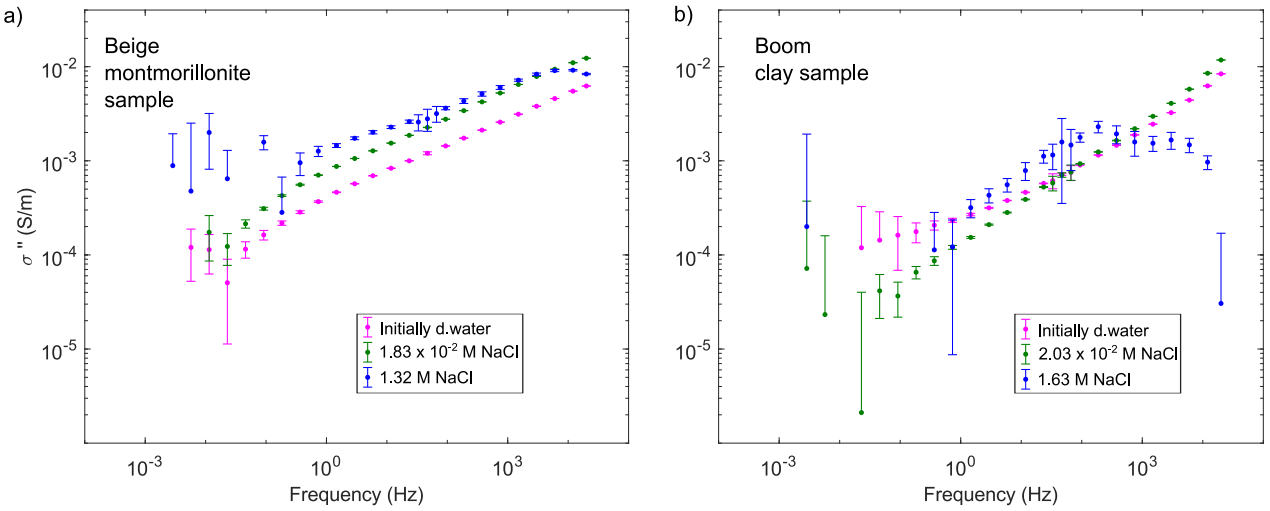

Figure 3.2: Imaginary part of the complex conductivity per salinity of: a) beige montmorillonite sample, and b) Boom clay sample. The calculated salinity values at which the SIP measurements were collected are presented in the legends of each subplot. Dots with errorbars represent the SIP measured data.

3.4.2 Differentiation of clay minerals

To compare datasets (red and green montmorillonite samples, kaolinite sample, and illite sample) we calculated a normalized measured conductivity difference ($\Delta\sigma'_N$ and $\Delta\sigma''_N$) between each clay type at 1.46 Hz, for the real and imaginary conductivities. We calculated Δx_N as:

$$\Delta x_N(f = 1.46Hz) = 100 \times \frac{x_1 - x_2}{\frac{x_1+x_2}{2}}, \tag{3.1}$$

where x_N, x_1, and x_2 represent either the real or the imaginary part of the conductivity at 1.46 Hz. Equation 3.1 is performed for either the real or the imaginary conductivities at 1.46 Hz. Moreover, x_1, and x_2 represent the measurement of an individual clay type at 1.46 Hz.

In the paper we presented the table of the salinity $\sim 10^{-2}$ mol/L (M) NaCl salinity. Here, in the tables 3.1, 3.2, 3.3, and 3.4, we present the $\Delta\sigma^*_N$ values for the salinities: de-ionised water, $\sim 10^{-3}$, $\sim 10^{-1}$, and ~1 M NaCl.

Table 3.1: $\Delta\sigma'_N$ and $\Delta\sigma''_N$ (in %) for the initially de-ionised water clay mixtures. The calculations are made using the complex conductivity at 1.46 Hz, the real part ($\Delta\sigma'_N$) is on the lower left triangle (in bold), and the imaginary part ($\Delta\sigma''_N$) is on the upper right triangle (in italics). MtG represents the green montmorillonite sample, MtR the red montmorillonite sample, Ka the kaolinite sample, and IL the illite sample.

	MtG	MtR	Ka	IL
MtG	0	*14.00*	*149.08*	*112.30*
MtR	**-21.73**	0	*142.51*	*102.32*
Ka	**-96.92**	**-79.37**	0	*-63.25*
IL	**-115.92**	**-100.52**	**-26.42**	0

Table 3.2: $\Delta\sigma'_N$ and $\Delta\sigma''_N$ (in %) for the initially 10^{-3} M NaCl water clay mixtures. The calculations are made using the complex conductivity at 1.46 Hz, the real part ($\Delta\sigma'_N$) is on the lower left triangle (in bold), and the imaginary part ($\Delta\sigma''_N$) is on the upper right triangle (in italics). MtG represents the green montmorillonite sample, MtR the red montmorillonite sample, Ka the kaolinite sample, and IL the illite sample.

	MtG	MtR	Ka	IL
MtG	0	*16.31*	*142.23*	*138.88*
MtR	**-4.80**	0	*134.79*	*129.93*
Ka	**-97.78**	**-94.09**	0	*-8.65*
IL	**-105.49**	**-101.98**	**-10.39**	0

Table 3.3: $\Delta\sigma'_N$ and $\Delta\sigma''_N$ (in %) for the initially 10^{-1} M NaCl water clay mixtures. The calculations are made using the complex conductivity at 1.46 Hz, the real part ($\Delta\sigma'_N$) is on the lower left triangle (in bold), and the imaginary part ($\Delta\sigma''_N$) is on the upper right triangle (in italics). MtG represents the green montmorillonite sample, MtR the red montmorillonite sample, Ka the kaolinite sample, and IL the illite sample.

	MtG	MtR	Ka	IL
MtG	0	*1.85*	*162.12*	*138.28*
MtR	**-8.66**	0	*161.48*	*137.31*
Ka	**-9.87**	**-1.21**	0	*-54.24*
IL	**-44.89**	**-36.59**	**-35.41**	0

Table 3.4: $\Delta\sigma'_N$ and $\Delta\sigma''_N$ (in %) for the initially 1 M NaCl water clay mixtures. The calculations are made using the complex conductivity at 1.46 Hz, the real part ($\Delta\sigma'_N$) is on the lower left triangle (in bold), and the imaginary part ($\Delta\sigma''_N$) is on the upper right triangle (in italics). MtG represents the green montmorillonite sample, MtR the red montmorillonite sample, Ka the kaolinite sample, and IL the illite sample.

	MtG	MtR	Ka	IL
MtG	0	*-41.04*	*154.93*	*154.20*
MtR	**14.82**	0	*169.10*	*168.57*
Ka	**20.47**	**5.69**	0	*-1.82*
IL	**4.40**	**-10.44**	**-16.11**	0

3.4.3 Repeatability test

In figure 3.3 we present an example of repeatability test. We made two identical sample holder structures, made a green montmorillonite batch with de-ionised water. From the batch, we obtained two samples to be tested independently. We present the SIP signature of the test, and also the percentage difference (as in equation 3.1) of the real and imaginary parts of the electrical conductivity.

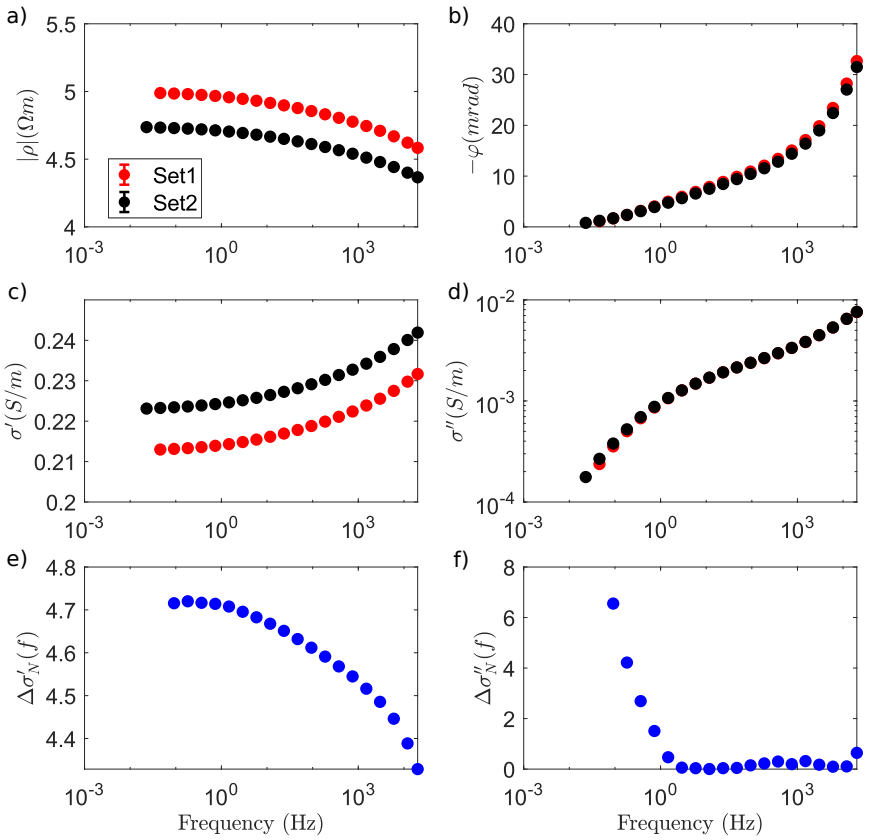

Figure 3.3: SIP repeatability test for a green montmorillonite using de-ionised water, with two datasets and their a) amplitude, b) phase, c) real conductivity, d) imaginary conductivity, e) percentage difference for the real part of the conductivity, and f) percentage difference for the imaginary part of the conductivity.

3.4.4 Relationship between the imaginary conductivity at a frequency of 1.46 Hz and surface area per unit pore volume

In figure 3.4 we compare our dataset with that of Weller et al. (2015a) and Börner (1992). We present only data points where the surface area per unit pore volume (S_{por}) was measured using BET method. Weller et al. (2015a) propose the relation $\sigma'' = C_p S_{por}$, they find the value of Cp_1 for their dataset. We found a value of Cp_2 for our dataset only, and a value of Cp_3 for all the datasets together (see figure 3.4, for the values of Cp). The data extracted from Weller et al. (2015a) corresponds to the data presented on their figure 1, consisting only of sand-clay mixtures. The sand-clay mixtures of Weller et al. (2015a) vary in clay content from 0.023% and 1.85%. The difference between clay content between the data presented in Weller et al. (2015a) and this study could explain the slight difference between the fitted values of Cp.

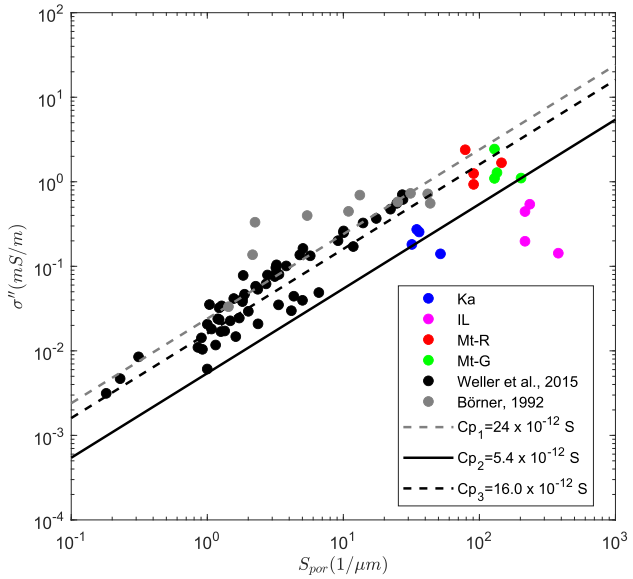

Figure 3.4: Relationship between σ'' and surface area per unit pore volume (S_{por}), obtained by BET measurements. We compare our data (in color), to that presented in Weller et al. (2015a) and Börner (1992).

3.5 Comment on pore water equilibrium

As mentioned in Mendieta et al. (2021), in our SIP measurements we assume a near chemical equilibrium of the pore water of the studied samples. We make the SIP measurement on each clay sample twice (see figure 3.5) with 24h in between measurements. The goal of the sample holder was one that could be open and locate individual types of clay or different types of clay in the same sample holder. In order to create such a sample holder, we had to sacrifice the water tightness of the sample holder. When we let time pass from the moment we locate the clay sample inside, we need to achieve some equilibrium and yet not let enough pass that the sample will desiccate significantly to change the SIP signal. From figure 3.5, we can see that the first collected dataset (date:09-09-2019, as in dd-mm-yyyy) shows a decrease in the amplitude at the lowest frequencies, approaching the values measured in the second dataset (date:10-09-2019). When we see the lack of decrease, which is always the case for the second measurement, collected after around 24h of the placement of the clay sample in the sample holder, we assume we have reached some equilibrium. We believe that with the fact that we mix and homogenize the sample, we are accelerating the mixing process, thus reaching an equilibrium faster than if we would not have the mixing portion in our laboratory protocol. We want to point out that, for this example (illite at initially 10^{-2} M NaCl), the difference in phase of the two signals appears negligible, and the difference between the amplitude is around 0.2 Ω m, which is quite small. When comparing this signal to the other signals at different salinities for the illite sample, a difference of 0.2 Ω m is negligible. However, we

acknowledge that in fact the signal could still evolve in time in order to reach a different signal in due time, but for our laboratory protocol it is impossible to reach.

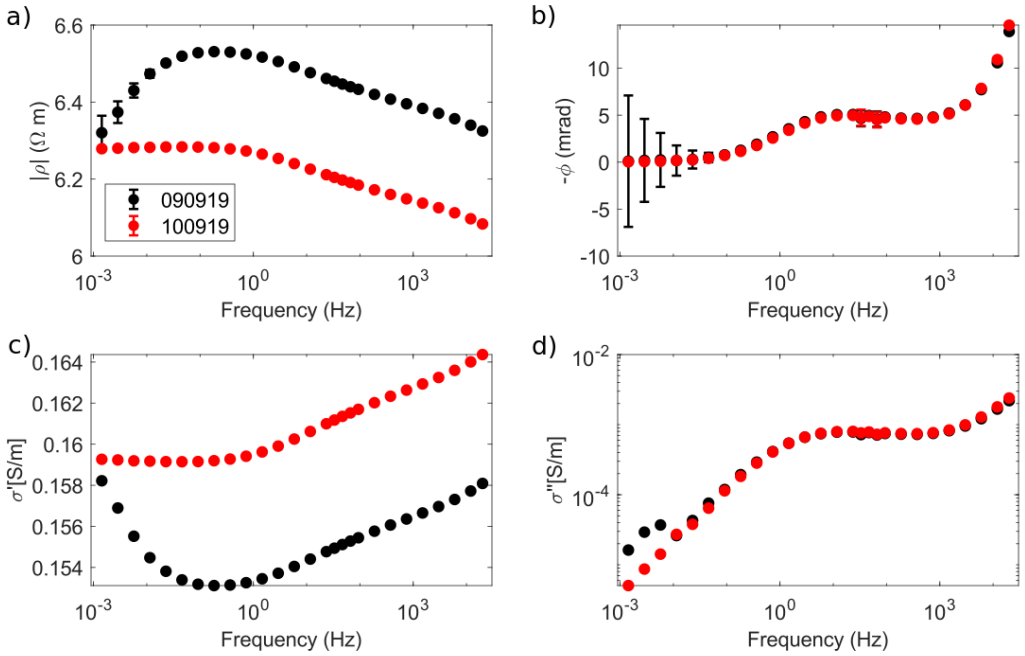

Figure 3.5: SIP measurement of the illite sample (initially at 10^{-2} M NaCl), for the dates of 09/09/19 and 10/09/19, that is an equilibration time of 24h. a) Electrical resistivity, b) phase, c) real electrical conductivity, and d) imaginary conductivity for frequencies between 1 mHz-20 kHz.

CHAPTER

4 SIP on heterogeneous clays

4.1 Introduction to manuscript

As mentioned before (see chapter 2), one of the goals of this thesis was to work with artificial (self-made) clay heterogeneities. This chapter deals with these experiments. Below, I present an early draft for a manuscript we intend to submit to *Geophysical Journal International*. As this is an early draft, complements to the manuscript are added later in this chapter.

The manuscript deals with the electrical characterization of mixtures of non-consolidated clays in different arrangements, a transversal, a longitudinal, and a homogeneous mix. Based off of the knowledge gathered in Mendieta et al. (2021) (see chapter 3), we decided to use illite and red montmorillonite, only at initially 10^{-2} mol L^{-1} of NaCl. We modeled such mixtures with complex conductance networks, using the data obtained in chapter 3 as a basis. Additionally, we modeled the data with traditional mixing laws (Voigt, Reuss, and self-consistent scheme). We compare both approaches.

4.2 Manuscript

This article is intended for publication in *Geophysical Journal International*. This is an early draft and modifications could still be done to this article.

Spectral induced polarization of heterogeneous non-consolidated clays

A. Mendieta[1], A. Maineult[1], P. Leroy[2], and D. Jougnot[1]

[1]Sorbonne Université, CNRS, EPHE, UMR 7619 METIS, 75005 Paris, France
[2]BRGM, Department of Water, Environment, Processes and Analysis, Orléans, France

Corresponding author: Aida Mendieta, aida.mendieta_tenorio@upmc.fr

Abstract

Clays are ubiquitously located in the Earth's near surface and have a high impact on the subsurface permeability. Characterizing clay systems is therefore of importance for a variety of geo-applications. Most geo-electrical characterizations of clays, do not take into account the heterogeneous nature of these systems. We present a dataset of spectral induced polarization (SIP) of artificial heterogeneous non-consolidated clay samples. The artificial heterogeneous samples are made of illite and red montmorillonite in a parallel, and perpendicular disposition (with respect to the applied electric field). Another sample is a homogeneous mixture composed of the same volumetric fraction of illite and red montmorillonite. For all the samples, the polarization is dominated by the red montmorillonite. We compared the experimental data with traditional mixing laws and complex conductance network models to test our ability to predict the SIP signal of such mixtures based on the known nature of the two components. The real conductivity is better predicted by the mixing laws, but the shape of the spectra is best predicted by the conductance network models. These data and models are a step forward towards a better characterization of complex clay systems using SIP.

1 Introduction

Clay systems exist in a variety of geologic formations and at various scales, from cap rocks to clay lenses or clay fractions in soils. Most laboratory geo-electrical characterizations of clays are done for a homogeneous mixture of clays, a mixture of sand and clays, or a clayrock sample from a particular geological formation (e.g., Cosenza et al., 2008; Ghorbani et al., 2009; Jougnot et al., 2010; Breede et al., 2012; Okay et al., 2014). However, most clay systems are heterogeneous and/or anisotropic (e.g., Wenk et al., 2008; Revil et al., 2013; Woodruff et al., 2014), thus these laboratory characterizations can fall short to predict the electrical signal of a heterogeneous and/or anisotropic clay system. There is a lack of geo-electrical laboratory experiments that better represent the complexity of clay systems. Additionally, there is a need to bridge the knowledge gaps between scales (clay sample to clay system), moreover, there is a need to better understand the electrical conduction and polarization phenomena at the mesoscopic scale (that is between the pore and the measurement scale, see Jougnot, 2020).

An approach to predict the physical properties of mixtures (hydraulic, electrical, elastic, among others) is the use of mixing laws, such as Voigt (1910), Reuss (1929), and the self-consistent approach (Hashin, 1968). This is a traditional, yet still effective ap-

proach used in geophysics (e.g., Renard & de Marsily, 1997; Berryman, 1995; Jougnot et al., 2018).

Another approach to bridge the scales in the geosciences is through pore network modeling (e.g., Bernabe, 1995; Day-Lewis et al., 2017). This approach when adapted to the electrical properties of media, becomes impedance or conductance networks (e.g., Madden, 1976). Other authors, such as Maineult et al. (2018), have related the pore properties (like pore radius) to electrical properties through phenomenological models, like a Pelton model (Pelton et al., 1978).

Here, we studied the complex conductivity signal of a heterogeneous and homogeneous mixture of two types of clay, illite and red montmorillonite that were extensively studied in the previous work of Mendieta et al. (2021). The samples are disposed in a parallel, a perpendicular manner, and a homogeneous mixture of both types of clays. We applied a complex conductance network model and widely used mixing laws to check their ability to predict the complex electrical conductivity response of the red montmorillonite and illite (initially at 0.01 M of NaCl) spectral induced polarization (SIP) data (presented in Mendieta et al., 2021). In this case, we consider extreme cases of mixtures and heterogeneities taking a step forward towards a better characterization of complex clay systems.

2 Theory

2.1 SIP

SIP is a geophysical method that consists in injecting a sinusoidal-shaped electrical current into a rock sample and measuring the resulting electric potential difference and the phase-lag between the injected and measured electrical signals, at different finite frequencies (mHz-kHz). The amplitude of the measured signal yields information about the electrical impedance of the rock sample, while the phase-lag (φ, in rad) informs about the capacity of the rock sample to reversibly store electrical charges (Revil, 2012). With the proper geometrical factor of the rock sample, we can obtain the electrical resistivity (ρ, in Ω m) or conductivity (σ, in S m^{-1}) of the sample. The complex electrical conductivity ($\sigma^*(\omega)$, or the complex resistivity, its inverse $\rho^*(\omega)$) is frequency dependent and can be presented as:

$$\frac{1}{\rho^*(\omega)} = \sigma^*(\omega) = |\sigma|e^{i\varphi} = \sigma' + i\sigma'', \tag{1}$$

where ω is the angular frequency (rad s^{-1}), $i = \sqrt{-1}$ represents the imaginary unit, $|\sigma|$ is the amplitude of the measured signal (S m^{-1}), σ' (S m^{-1}) is the real component of the electrical conductivity, and σ'' (S m^{-1}) is the imaginary component. The relation between ω and the frequency (f, Hz) is $\omega = 2\pi f$.

2.2 Mixing laws

When confronted to a mixture of two different materials, there are a plethora of ways to calculate the resulting electrical signal of either a heterogeneous or homogeneous mixture. Commonly used mixing laws in geophysics (electric, elastic, magnetic, among many other physical properties) are the Voigt (1910), Reuss (1929), and self-consistent approach (Hashin, 1968) to mixtures (see Renard & de Marsily, 1997, for a review), the volume averaging approach (Pride, 1994; Revil et al., 2007), and the differential effective medium theory (e.g., de Lima & Sharma, 1992; Cosenza et al., 2008).

Here, we focus on the Voigt, Reuss, and self-consistent theory. For a mixture made of two materials, the resulting electrical signal will be bound (minimum and maximum) by the electrical signal of the individual materials. When the mixture is disposed in parallel, we can use the Voigt (1910) approach to calculate the resulting electrical signal, that is:

$$\sigma_V^* = (1-c)\sigma_1^* + c\sigma_2^*, \tag{2}$$

where, σ_V^* represents the complex electrical conductivity of the mixture disposed parallel to the applied electrical field, σ_1^* represents the complex electrical conductivity of the first material, and σ_2^* of the second material, c is the volumetric proportion of material 1 with respect of the whole volume of the mixture. For a series disposition (perpendicular to the applied electrical field), we use the Reuss (1929) approach, that is:

$$\sigma_R^* = \left(\frac{1-c}{\sigma_1^*} + \frac{c}{\sigma_1^*}\right)^{-1}, \tag{3}$$

where σ_R^* is the complex electrical conductivity of the mixture disposed in a series manner. Finally, when there is a homogeneous mixture of two materials, we can use the self-consistent (Hashin, 1968) approach, that is:

$$\sigma^*_{SC} = \sigma^*_1 + \frac{3c\sigma^*_1}{3\sigma^*_1 + (1-c)(\sigma^*_2 - \sigma^*_1)}(\sigma^*_2 - \sigma^*_1) \quad (4)$$

where σ^*_{SC} is the complex electrical conductivity of the homogeneous mixture of two materials, note that this is valid for $\sigma_1 < \sigma_2$. When $\sigma_1 > \sigma_2$, equation 4 needs to be slightly modified and the terms σ_1 and σ_2 need to be switched, as well as the term c needs to be replaced by $(1 - c)$ and viceversa. In our case $c = 0.5$ for all mixtures, that is for equations 2, 3, and 4. Note that when $c = 0.5$, equation 2 becomes a simple arithmetic mean, and equation 3 becomes a harmonic mean. Furthermore, these expressions have previously been used for the amplitude of the electrical conductivity, not for the complex conductivity (e.g., Berryman, 1995), we wanted to test if these mixing laws were valid for the complex conductivity.

2.3 Complex conductance network modeling

To simulate the SIP signal of the clay mixtures, we used complex conductance networks (see for instance Maineult et al., 2017; Maineult, 2018; Maineult et al., 2018). Briefly, we designed a network on a regular 2D mesh (see the example given in Figure 1). Each link of the network consists of a given complex conductance. By applying Kirchhoff's law (1845), we obtain a linear equation expressing the current continuity at each node of the network. Replacing the current in a given link by the product of the complex conductance of this link and the electrical potential difference between the two nodes delimiting this link, and applying the boundary conditions (i.e., the potential is equal to $e^{i\omega t}$ at the bottom and 0 at top, with no flux on the lateral faces, see Figure 1), we can obtain a linear system that is solved for each angular frequency ω in order to get the potentials at the nodes. Afterwards, the total current flowing inward or outward the top or bottom faces can be computed. It is then straightforward to deduce the ratio of the potential difference applied between the two end faces to the computed total inflowing/outflowing current, as well as the phase-shift between these two quantities (please note that the full derivation for a square mesh can be found in Maineult et al., 2017, corrected by Maineult, 2018). In the case of an illite and red montmorillonite mixture, we use the impedance spectra reported in Mendieta et al. (2021) for illite and red montmorillonite at 0.01 M. Please note that this type of modeling can be done for different types of connectivity (i.e. triangular, rectangular, or hexagonal mesh).

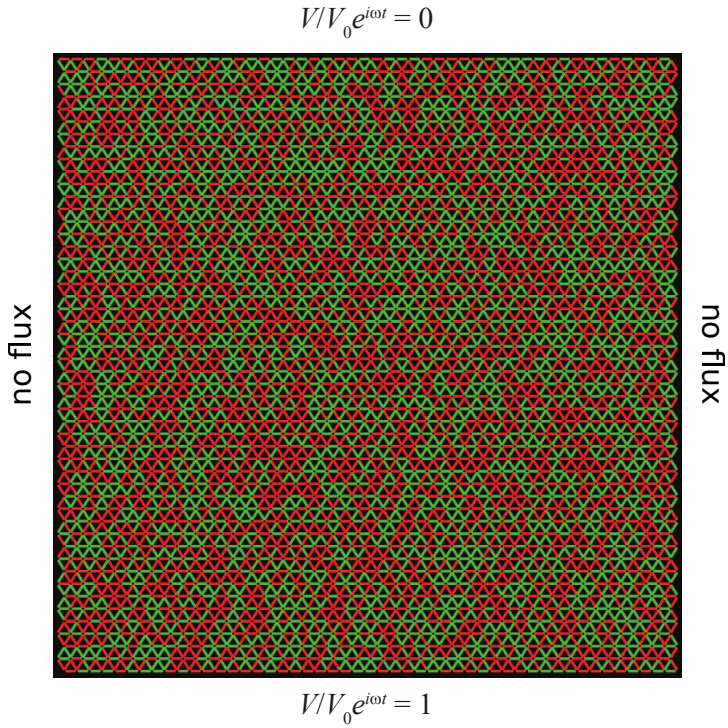

Figure 1. 50x50 triangular complex conductance network simulating a random homogeneous mixture of illite and red montmorillonite. The green links correspond to illite, the red ones to red montmorillonite.

3 Materials and Methods

3.1 Materials

We had already characterized individually the SIP response of four different types of clays at different salinities (see Mendieta et al., 2021), and from that we decided to use two completely different clays (with respect to their electrical signature): illite and red montmorillonite. We also decided to use an initial salinity that would show a difference between both clay types. A too important salinity would have created extremely conductive clay samples, yielding SIP data with high noise, and a too low salinity sample would have created important non-equilibrium in the pore-water chemistry (possible ion release from the interlayer space of clay tactoids). Thus we decided to use an initial salinity of 10^{-2} M of NaCl. As described in Mendieta et al. (2021), the clay samples follow an evaporation period, thus the salinity of the SIP measured clay sample is in the same order of magnitude as the initial salinity but not the same.

A detailed description and analysis of the clays used in this study, with a detailed explanation of the laboratory protocol is presented in Mendieta et al. (2021). We will however, briefly describe the used materials and laboratory protocol.

In the present study we used two types of non-pure clays, a red montmorillonite and an illite. A chemical analysis of the clay samples shows that the red montmorillonite sample is made of: 66% smectite, 11% quartz, 18% microcline, 3% albite, and 1% magnetite. The illite sample is made of: 67% illite, 10% kaolinite, 10% microcline, and 12% calcite. The measured cationic exchange capacity (CEC) values are 135 meq/100 g for the red montmorillonite sample, and 47 meq/100 g for the illite sample. Finally, the measured specific surface area through the Brunauer-Emmett-Teller (BET) method is 71.09 m^2/g for the red montmorillonite sample, and 101.60 m^2/g for the illite sample. It is worth noting that the use of the BET method has proven to not be optimal for smectites, as the BET method is unable to probe the interlayer space. Proposed surface area values in the literature for smectites are in the range of 390-780 m^2/g (see Tournassat et al., 2013).

3.2 Laboratory protocol

In this study we prepared two types of clay samples, three heterogeneous mixtures, and one homogeneous mixture of red montmorillonite and illite. For the heterogeneous mixtures, we decided to locate the individual clay types in two different arrangements: a transversal (Figure 2b) and longitudinal arrangements (Figures 2c and d). We aimed at creating a 50-50% volume ratio, for each type of clay. For the creation of the heterogeneous mixtures, we created individual clay samples of illite and red montmorillonite, following the protocol proposed by Mendieta et al. (2021) (see their subsection 3.2). For the homogeneous mixture, there are extra steps in the laboratory protocol. For the homogeneous mixture (Figure 2a), we first mixed the dry clay powders of illite and montmorillonite using an electrical drill. Here, we used the same mass proportions as in the 50-50% volumetric heterogeneous mixtures. We then followed the protocol proposed by Mendieta et al. (2021) (see their subsection 3.2). This laboratory protocol consists in: a combination of clay powder and the aqueous solution, a period of at least 24 h for saturation and equilibrium of the mixture, mixing of the sample with an electric drill, disposition of the clay sample on top of a polyurethane foam until the correct water content is achieved through evaporation, the placement of the clay sample inside the sample holder for the SIP measurements, and finally the drying of the clay sample.

For the SIP measurements, all clay samples are placed in a cylindrical-shaped sample holder, the injecting electrodes are located on the sides of the cylinder, and the measuring electrodes are located on top of the cylinder casing (Figure 2e). This is why we measured the SIP signal of two longitudinal heterogeneous mixtures, once the upper half (in contact with the measuring electrodes) was filled with illite (Figure 2c), and once with red montmorillonite (Figure 2d).

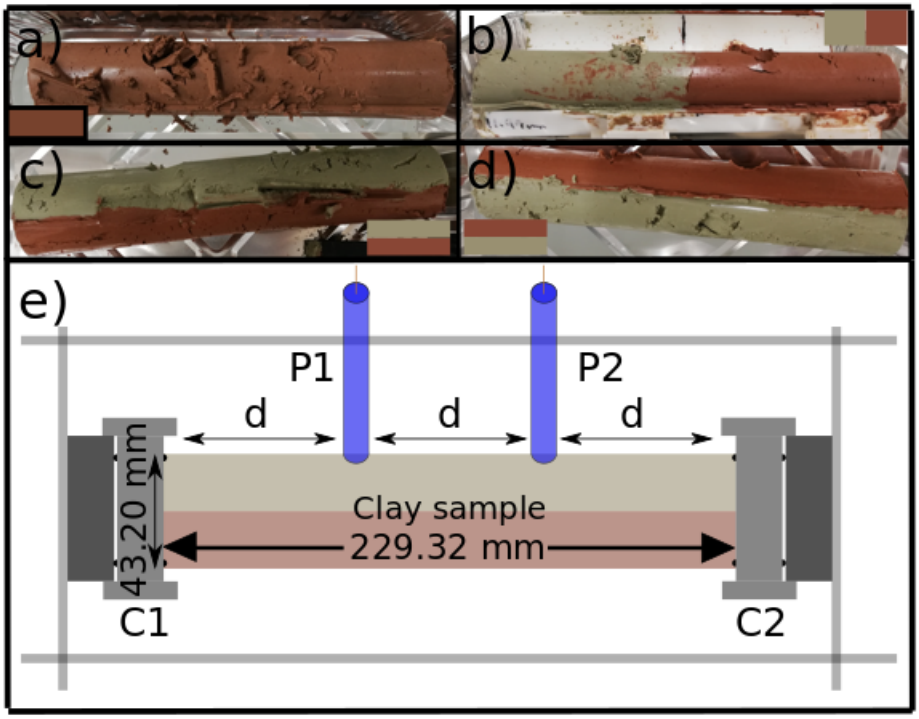

Figure 2. Different clay samples prepared in the laboratory. a) A homogeneous mixture of illite and red montmorillonite, b) heterogenous-transversal mixture of illite and red montmorillonite, c) longitudinal mixture with illite on the side of the measuring electrodes and d) longitudinal mixture with red montmorillonite on the side of the measuring electrodes. Note that these pictures correspond to the clay samples after taking them out of the sample holder. e) Sketch of the clay sample holder and holder structure, where C1 and C2 are the injecting electrodes, P1 and P2 are the potential electrodes. Note that this is merely a sketch of the SIP measurement setup and is not at a 1:1 scale.

3.3 SIP measurement

For the SIP measurements we used the SIP-FUCHS III equipment (Radic Research, www.radic-research.de). See figure 2e for a sketch of the SIP measuring setup. For the SIP measurements we used Cu-$CuSO_4$ non-polarizable electrodes, as electric potential measuring electrodes. For the injecting electrodes we used two stainless steel cylinders that also served as covers of the sample holder. We used a four-electrode system for the SIP measurements, as according to Kemna et al. (2012) using a two-electrode system introduces unacceptably large errors in the measurement. We measured the SIP signal from 1 mHz to 20 kHz twice, separated by around 24h. The SIP data we present in this work, corresponds to the second measurement, as the signal is more stable for the second measurement.

3.4 Complex conductance network models

The principles of the complex conductance network models we used are explained in section 2.3. Figure 1 represents a homogeneous mix of illite and red montmorillonite with a triangular mesh. Additionally, we modeled a complex conductance network where the top half was solely illite and the bottom solely red montmorillonite. We also modeled a complex conductance network with the right half corresponding to illite, and the left half corresponding to red montmorillonite. It is worth mentioning that the order of the location (which clay is located on which half) is irrelevant, as in this model there is not a point measurement for the electric potential (opposite to laboratory measurements). Locating the illite on the top or bottom will not alter the results, as the impedance network will yield the resulting electric potential difference of the system as a whole. Note that we performed the calculations for a triangular mesh (as shown in Figure 1), but also for a rectangular and hexagonal mesh. The results of the rectangular and hexagonal meshes are presented in the supplementary information. We chose the triangular mesh, as it fits the data better. Overall, the triangular mesh proves to be the best option because it has the highest connectivity among the rectangular, hexagonal, and triangular meshes.

4 Results

4.1 Complex conductivity measurements

The results of the SIP measurements of the heterogeneous mixtures are presented in figure 3. Note that the dataset of the individual clay types, illite and red montmorillonite has been added for reference, this data was taken from Mendieta et al. (2021).

From the results we can see that all mixtures of illite and red montmorillonite fall in between the data points of illite and red montmorillonite, which is expected. Here, we measured the SIP signal of a homogeneous mixture of illite and red montmorillonite, and three heterogeneous mixtures placed in a longitudinal and transversal manner. For the longitudinal set-ups, we conducted two measurements, one locating the illite on the top portion of the sample holder (near the measuring electrodes, see figure 2c) and the second with the red montmorillonite on the top (see figure 2d). We can see that these longitudinal measurements do not match perfectly, and that makes sense, we do not have the same sensitivity immediately at 1 or 2 cm below the measuring electrodes. However, we see that the longitudinal mixture with the illite on the top portion of the sample holder, is not identical to the measurement of solely illite, that means that the longitudinal mixture with the illite on top, is still affected by the red montmorillonite below. If we take a look at figure 3, we verify that the transversal mixture is in fact closer in both value and shape to the individual illite than the longitudinal mixture with illite on the top. This also proves that the red montmorillonite in the longitudinal mixture with illite on the top affects the SIP signal (the SIP measurement is sensitive to the red montmorillonite on the bottom of the sample holder), which proves that the chosen dimensions of the sample holder are in fact good. We follow the advice by Zimmermann et al. (2008), thus we separated the potential electrodes by the same distance between potential and current electrodes.

Note that the mixtures and the individual SIP data of illite and red montmorillonite, were collected at different temperatures. The illite SIP data was collected at 21.9 °C, and the montmorillonite data was collected at 23.1 °C. The heterogeneity dataset was collected at around 18.9 °C. We corrected the heterogeneity dataset to a 22.5 °C temperature. We used the temperature correction proposed by Hayley et al. (2007). It is worth mentioning that we only corrected the conductivity, because to the best of our knowledge there is not a temperature correcting procedure for the phase. Although it has been pointed out that temperature influences the complex conductivity of a geo-material (e.g., Binley et al., 2007; Bairlein et al., 2016; Iravani et al., 2020), there is still a need to find a petro-physical law or relation to correct for it (see Kemna et al., 2012).

4.2 Complex conductance network modeling results

As mentioned in section 3.4, we modeled the complex conductivity of three different mixtures: a homogeneous mixture, a transversal-heterogeneous mixture, and a longitudinal-heterogeneous mixture. For each type of mixture we did three types of

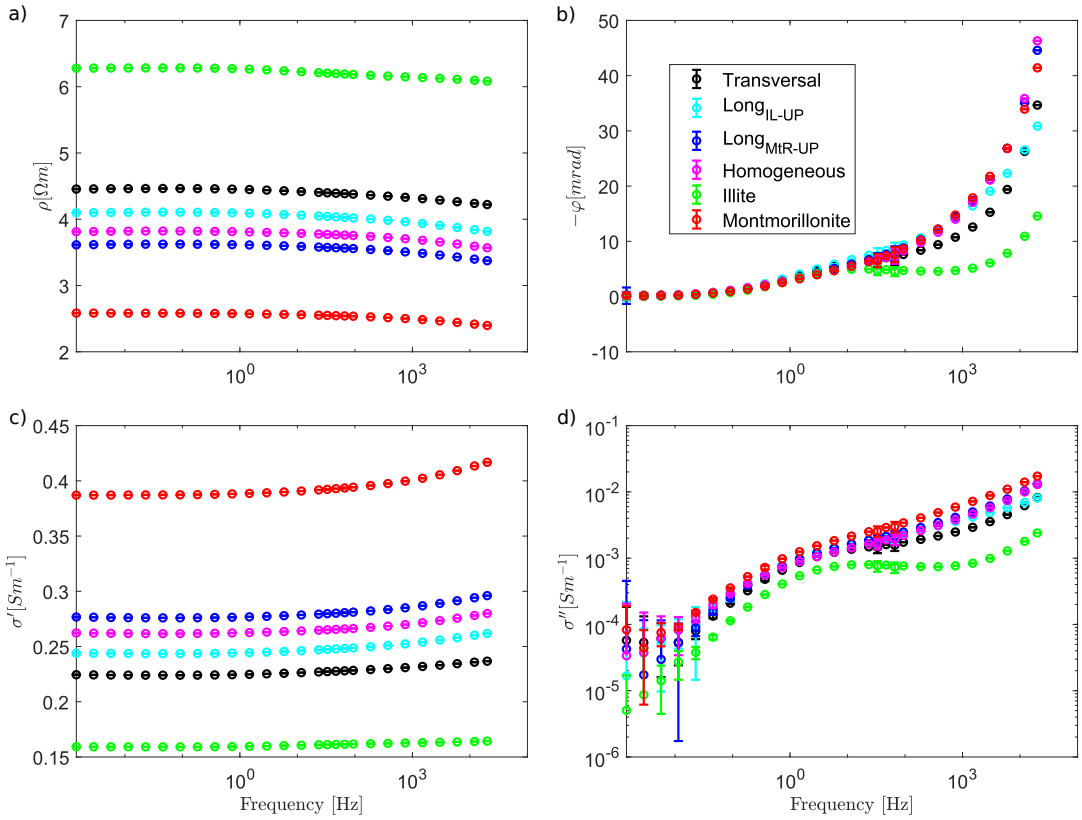

Figure 3. SIP data, as a) amplitude, b) phase, c) real component and d) imaginary components of the complex conductivity. The illite and red montmorillonite clay samples have been taken from Mendieta et al. (2021). The rest of the datasets here presented are a homogeneous mixture of illite and red montmorillonite, as well as three heterogeneous mixtures: a transversal mixture, and two longitudinal mixtures, one with illite in contact with the measuring electrodes (Long$_{\text{IL-UP}}$), and one with red montmorillonite (Long$_{\text{MtR-UP}}$).

connectivity: a rectangular, a hexagonal, and a triangular mesh. In this contribution we will only present the simulations results using the triangular mesh, the simulations using other meshes are presented in the supplementary material. In figure 4 we present the SIP data overlaid by the results of the complex conductance network models with a triangular mesh; that is the real and imaginary part of the conductivity (figures 4a and b, respectively), and the normalized real and imaginary conductivities (figures 4c and d, respectively). We have normalized the spectra by the conductivity value at 1.46 Hz. We chose the closest value to 1 Hz, as this is a widely used value in geophysics (e.g., Zanetti et al., 2011).

Both models and data (figure 4) resemble more the red montmorillonite than the illite complex conductivity spectra, in shape. It appears that the red montmorillonite effects more the resulting polarization than the illite in a mixture, whether it is a homogeneous mixture or a heterogeneous one. We also notice that the fit between the triangular conductance model is not a perfect fit of the data. It is possible that the difference is due to 3D effects while the conductance network is in 2D.

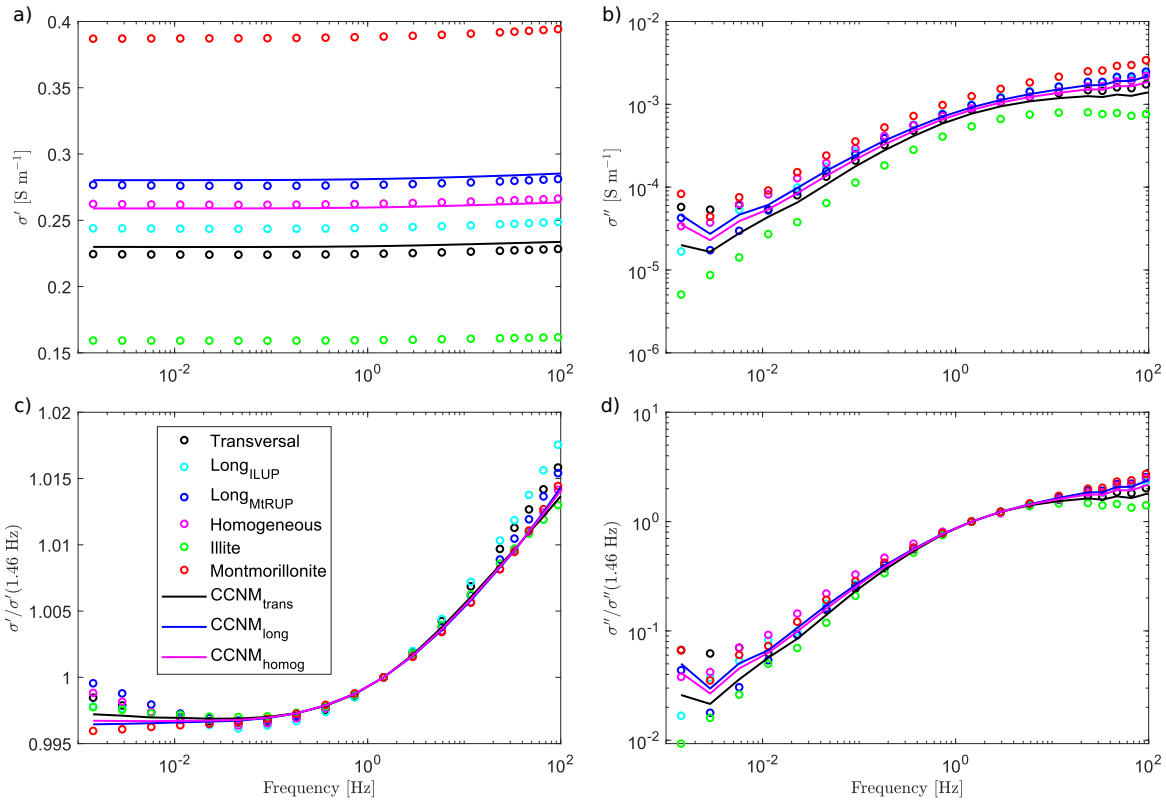

Figure 4. a) Real conductivity measurements and conductance network models, b) imaginary conductivity measurements overlain by the conductance network models, c) normalized real conductivity of the measurements and conductance network models, and d) normalized imaginary conductivity of the measurements and conductance network models of the illite and red montmorillonite mixtures. Long$_{\text{IL-UP}}$ and Long$_{\text{MtR-UP}}$ refer to the longitudinal mixtures, with illite and red montmorillonite near the potential electrodes, respectively. CCNM-trans, long, and homog refer to the complex conductance network models using the transversal, longitudinal and homogeneous arrangements, respectively.

4.3 Comparison with mixing laws

We additionally modeled the SIP signal of the different mixtures using the mixing laws proposed by Voigt (1910), Reuss (1929) and Hashin (1968). In figure 5, we confront the SIP data versus these models. Note that we present a Voigt$_{IL-UP}$ and a Voigt$_{MtR-UP}$ model. As it can be seen in figures 2, each potential electrodes uses a small volume (0.184 cm^3), so the volume fraction between the clay positioned on the half of the potential electrode is not exactly equal to the other half. For the case of both volume fractions being equal $c = 0.5$, but when the electrode volume has been removed, we obtain $c = 0.5005$ (see equation 2). Therefore, we used Voigt's model for an illite in the top half (IL-UP, in contact with the potential electrodes), and a model with the red montmorillonite on the top half (MtR-UP). We see that overall the modeled values are effected by both members of the mixtures, the red montmorillonite and illite (see Figures 5a and b). As to the shape of the spectra, if we take a look at Figures 5 c and d, we could interpret that the shape of the curve of both Voigt's models are more effected by the red montmorillonite content, and so are the data. However, Reuss and self-consistent models seem to be affected by both the illite and red montmorillonite content, the data does not follow this trend, as for the shape of the curve.

5 Discussion

We created a numerical model (with finite elements) of the electric potential and the current density of the samples (heterogeneous longitudinal mixture with montmorillonite on top, then illite on top, and finally the transversal mixture, see Figure 6). We can see that there is a higher current density on the montmorillonite half, for the longitudinal samples (Figure 6a and b). This makes sense, as montmorillonite is more conductive (0.16 S m^{-1} at 1.46 Hz) than illite (0.39 S m^{-1} at 1.46 Hz). For the transversal sample (Figure 6c), the current density seems unchanged from one half to the other. This also makes sense, as all the current lines that pass through the montmorillonite half have to pass through the illite half. This phenomenon could explain why, in the longitudinal measurements (Figure 3) we see a small mismatch, in amplitude and phase.

An interesting result of both SIP measurements (see figure 3), is that the real conductivity of the mixtures approaches more the signal of the illite than the montmorillonite (in amplitude). The amplitude of the imaginary conductivity of the mixtures appears to be closer to the red montmorillonite than to the illite. On the other hand, the shape of the spectra of the mixtures resembles more for both conductivities (real and

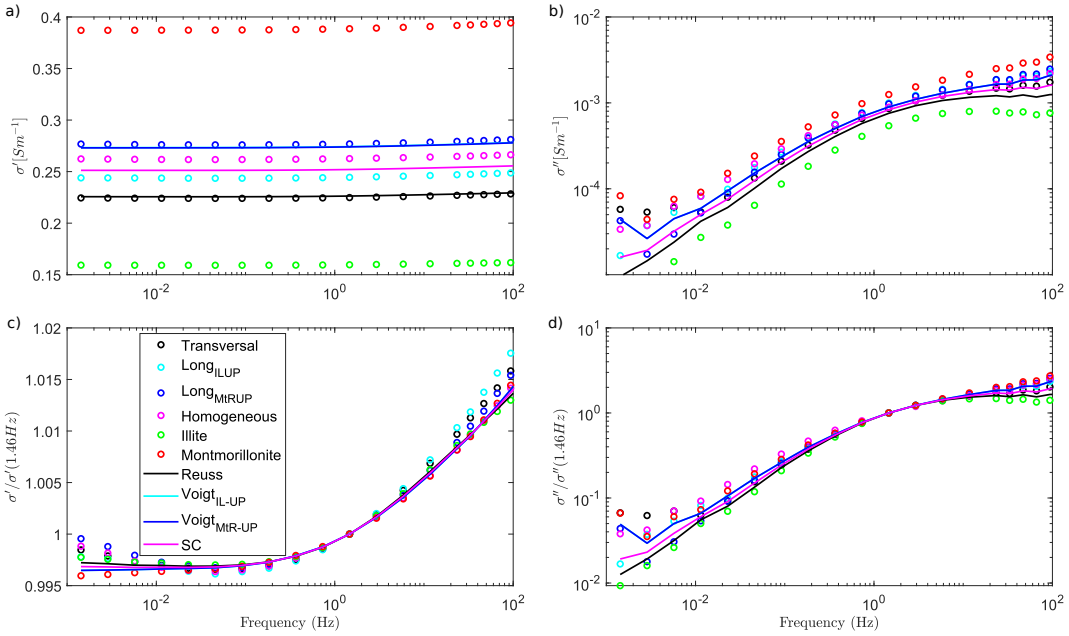

Figure 5. a) Real conductivity measurements, b) imaginary conductivity measurements overlain by the Reuss, Voigt (IL-UP and MtR-UP), and self-consistent models, c) normalized real conductivity of the measurements, and d) normalized imaginary conductivity of the measurements overlain by the normalized Reuss, Voigt (IL-UP and MtR-UP), and self-consistent models. $\text{Long}_{\text{IL-UP}}$ and$\text{Long}_{\text{MtR-UP}}$ refer to the longitudinal mixtures, with illite and red montmorillonite near the potential electrodes, respectively. Reuss and Voigt refer to their corresponding models, and SC corresponds to the self-consistent model. $\text{Voigt}_{\text{IL-UP}}$ refers to a model with illite filling the half with the potential electrodes, and $\text{Voigt}_{\text{MtR-UP}}$ to the red montmorillinite filling the half with the potential electrodes; these models are superposed.

imaginary) the shape of the montmorillonite. As to physical explanations of this phenomenon, we could say that perhaps the specific area of the montmorillonite is more important for montmorillonite than for illite (Tournassat et al., 2013). Thus, we can think that simply the component that polarizes the most (red montmorillonite in this case) dominates the polarization of the mixtures (shape of the spectra and amplitude of imaginary conductivity). However, the amplitude of the conductivity will be affected by both components of the mixture. We would have liked to compare these results to others presented in the literature, however, to the best of our knowledge, measurements as the ones presented in this study have not been done previously.

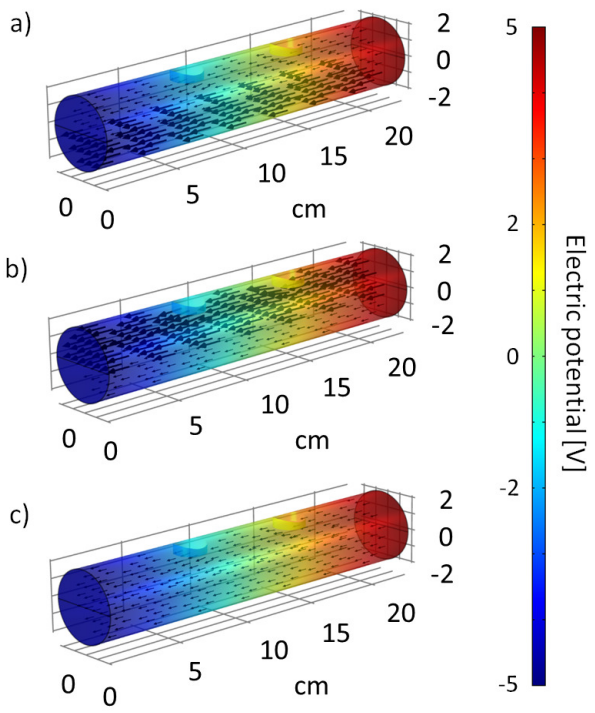

Figure 6. Numerical modeling of the electric potential distribution of heterogeneous clay samples for: a) longitudinal sample with illite on the top portion, b) red montmorillonite on the top portion and c) a transversal sample with equal volumetric amounts of illite and red montmorillonite. All of the models were subjected to an electric potential difference of -5 to 5 V. The arrows are a graphic representation of the current density.

We propose that for these illite and red montmorillonite mixtures, the red montmorillonite dominates the polarization. However, there is probably a percolation threshold, meaning that the red montmorillonite dominates the polarization as long as a certain amount is present in the mixture. To test for this hypothesis, we did a homogeneous complex conductance network model varying the amount of illite; from 100 % red montmorillonite, to 10 % illite, then 20 % illite, all the way to 100 % illite. The results of this test are presented in figure 7. It is hard to see where the inflexion point is in the illite content. That is, at which illite content the SIP signal starts appearing to be more like a red montmorillonite than an illite. Further tests should be done on the percolation thresholds of illite content to determine a specific value.

We calculated the difference ($\Delta\sigma = \sqrt{(\sigma_{model} - \sigma_{data})^2}$) between the models (both conductance networks, and Voigt, Reuss, and self consistent) and the data (see figure 8). We were unable to calculate a difference for the longitudinal datasets and the con-

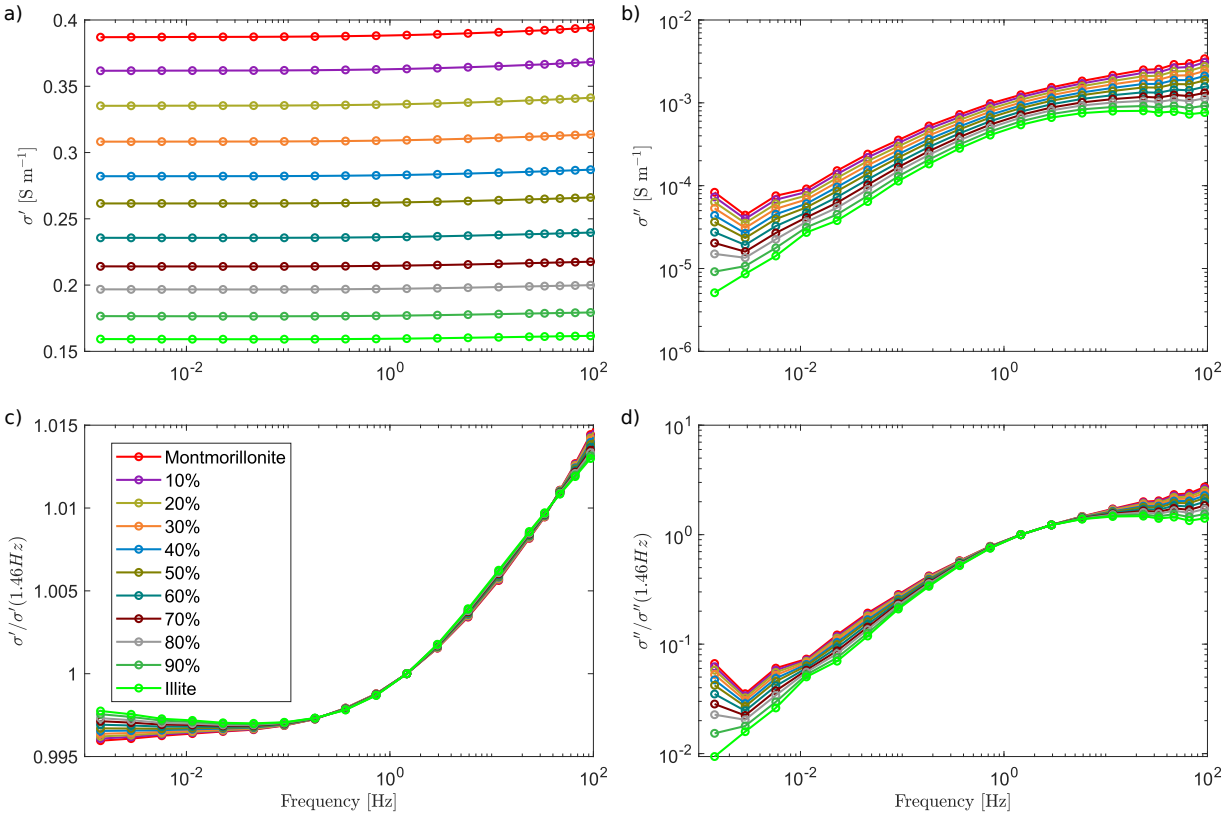

Figure 7. SIP modeling with complex conductance networks of a mixture of illite and red montmorillonite, varying in illite content (from 0 %, to 10 %, all the way to 100 %): a) real and b) imaginary part of the conductivity, c) real and d) imaginary normalized by their respective conductivities at 1.46 Hz.

ductance network models, as there is no measuring point in the complex conductance network models. However, for the Voigt models, we calculated this difference between the dataset with the illite next to the potential electrodes, and the model with the volume fraction corresponding to that of having the space for the electrodes on its half. We did this calculation in the same manner for the red montmorillonite, next to the potential electrodes. This calculation determines how good the fit is, so how the values of the models approached the measured data, it is not a good comparison for a goodness of shape of the curve. For the real part of the conductivity (Figure 8a), definitely the Reuss, the Voigt with the red montmorillonite next to the potential electrodes and the complex conductance network of the homogeneous mix fit the data the best. For the imaginary part of the data (Figure 8b), at frequencies above 10^1 Hz, the best fit is overall from the impedance network approach and the Voigt model with illite next to the potential electrodes. For lower frequencies, it is hard to say, for the

imaginary conductivity. As for the shape of the curves, comparing Figures 4c and d, and 5c and d, it seems that the conductance network models follow better the trend of the data, that is the shape of the curve.

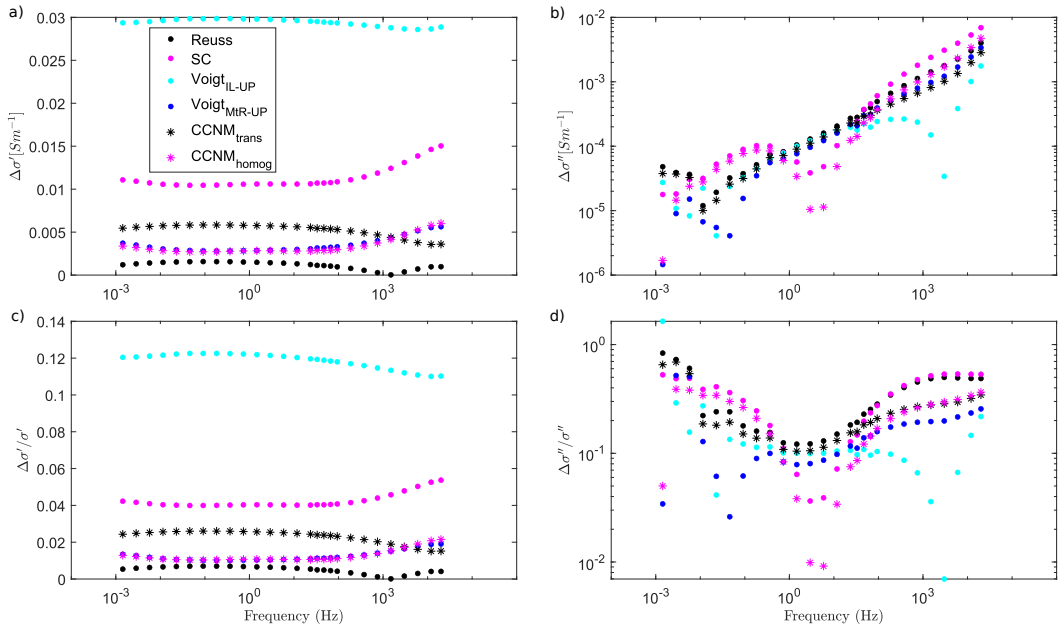

Figure 8. Comparison between the Reuss and self-consistent (SC) approach to the impedance network models, with the a) real and b) imaginary part of the electrical conductivity, c) normalized real and d) imaginary electrical conductivity.

One of the few studies that deals with modeling the electrical signature of anisotropic samples using impedance networks was done by Madden (1976). He created different conductance networks, trying to represent different anisotropic media through pore networks, he took a pore size distribution into account and obtained a conductivity distribution for different scales of anisotropy in a simulated rock sample. He concludes that a geometric mean of the components of the mixture is a good predictor of the physical parameters of a rock (electrical parameters for the purposes of this study), but such approach does not take into account the possible complexity of the inner-connectivity of the pores or cracks of the rock sample. This could greatly alter the resulting electrical conductivity of a rock sample. This is clearly in agreement with our results, as the Reuss and self-consistent are a better fit to the real conductivity, than the impedance network models (Figure 8a). We also agree, that this approach fails to fully take into account the complexity of the polarization of the clay samples, that could come from a complex connectivity as well.

In this contribution we have presented a way to model the resulting electrical conductivity of a mixture of two clays, red montmorillonite and illite, and compare it to SIP measurements of heterogeneous mixtures of clays. However, an interesting next step would be the inverse problem. Determining from a given SIP spectra the types of clays that conform the sample, knowing what the individual SIP spectra of the components look like.

6 Conclusions

We present a dataset of illite and red montmorillonite mixtures, in a parallel, perpendicular, and homogeneous manner. Our data shows that the polarization of all mixtures follows rather the shape of red montmorillonite. We interpret this as montmorillonite dominating polarization over illite. We model these mixtures through traditional mixing laws and complex conductance networks. The mixing laws are better at predicting the amplitude of the response of the mixtures, but the complex conductance models allow to better predict the shape of the curves.

More work needs to be done in order to determine the percolation threshold, that is the amount of montmorillonite needed in a mixture for it to dominate the polarization of the mixture.

Acknowledgments

The authors strongly thank the financial support of ANR EXCITING (grant ANR-17-CE06-0012) for this work and for the PhD thesis funding of A. Mendieta. The data used in this study will be available on a zenodo repository after acceptance of the paper.

References

Bairlein, K., Bücker, M., Hördt, A., & Hinze, B. (2016). Temperature dependence of spectral induced polarization data: experimental results and membrane polarization theory. *Geophysical Journal International*, *205*(1), 440–453. doi: 10.1093/gji/ggw027

Bernabe, Y. (1995). The transport properties of networks of cracks and pores. *Journal of Geophysical Research*, *100*(B3), 4231–4241. doi: 10.1029/94JB02986

Berryman, J. G. (1995). Mixture theories for rock properties. In T. J. Ahrens (Ed.), *Rock physics & phase relations: a handbook of physical constants* (pp. 205–228). American geophysical union.

Binley, A., Kruschwitz, S., & Lesmes, D. (2007). Spectral induced polarization of sandstones: Temperature effects. In *Agu fall meeting abstracts* (pp. NS13A–02).

Breede, K., Kemna, A., Esser, O., Zimmermann, E., Vereecken, H., & Huisman, J. A. (2012). Spectral induced polarization measurements on variably saturated sand-clay mixtures. *Near Surface Geophysics*, *10*(6), 479–489. doi: 10.3997/1873-0604.2012048

Cosenza, P., Ghorbani, A., Revil, A., Zamora, M., Schmutz, M., Jougnot, D., & Florsch, N. (2008). A physical model of the low-frequency electrical polarization of clay rocks. *Journal of Geophysical Research*, *113*(B8), 1–9. doi: 10.1029/2007JB005539

Day-Lewis, F. D., Linde, N., Haggerty, R., Singha, K., & Briggs, M. A. (2017). Pore network modeling of the electrical signature of solute transport in dual-domain media. *Geophysical Research Letters*, *44*(10), 4908–4916. doi: 10.1002/2017GL073326

de Lima, O. A., & Sharma, M. M. (1992). A generalized Maxwell-Wagner theory for membrane polarization in shaly sands. *Geophysics*, *57*(3), 431–440. doi: https://doi.org/10.1190/1.1443257

Ghorbani, A., Cosenza, P., Revil, A., Zamora, M., Schmutz, M., Florsch, N., & Jougnot, D. (2009). Non-invasive monitoring of water content and textural changes in clay-rocks using spectral induced polarization: A laboratory investigation. *Applied Clay Science*, *43*(3-4), 493–502. doi: 10.1016/j.clay.2008.12.007

Hashin, Z. (1968). Assessment of the self consistent scheme approximation: conductivity of particulate composites. *Journal of Composite Materials*, *2*(3), 284–300. doi: 10.1177/002199836800200302

Hayley, K., Bentley, L. R., Gharibi, M., & Nightingale, M. (2007). Low temperature dependence of electrical resistivity: Implications for near surface geophysical monitoring. *Geophysical Research Letters*, *34*(18), 1–5. doi: 10.1029/2007GL031124

Iravani, M. A., Deparis, J., Davarzani, H., Colombano, S., Guérin, R., & Maineult, A. (2020). The influence of temperature on the dielectric permittivity and complex electrical resistivity of porous media saturated with DNAPLs: A laboratory study. *Journal of Applied Geophysics*, *172*, 1–11. doi: 10.1016/j.jappgeo.2019.103921

Jougnot, D. (2020). *Developing hydrogeophysics for critical zone studies, importance of heterogeneities and processes at the mesoscopic scale* (Habilitation dissertation). Sorbonne Université.

Jougnot, D., Ghorbani, A., Revil, A., Leroy, P., & Cosenza, P. (2010). Spectral induced polarization of partially saturated clay-rocks: a mechanistic approach. *Geo-*

physical Journal International, *180*(1), 210–224. doi: 10.1111/j.1365-246X.2009.04426.x

Jougnot, D., Jiménez-Martínez, J., Legendre, R., Le Borgne, T., Méheust, Y., & Linde, N. (2018). Impact of small-scale saline tracer heterogeneity on electrical resistivity monitoring in fully and partially saturated porous media: Insights from geoelectrical milli-fluidic experiments. *Advances in Water Resources*, *113*, 295–309. doi: 10.1016/j.advwatres.2018.01.014

Kemna, A., Binley, A., Cassiani, G., Niederleithinger, E., Revil, A., Slater, L., ... Zimmermann, E. (2012). An overview of the spectral induced polarization method for near-surface applications. *Near Surface Geophysics*, *10*(6), 453–468. doi: 10.3997/1873-0604.2012027

Kirchhoff, G. (1845). Ueber den Durchgang eines elektrischen Stromes durch eine Ebene, insbesondere durch eine kreisförmige. *Annalen der physik und chemie*, *140*, 497–514. doi: 10.1002/andp.18451400402

Madden, T. R. (1976). Random networks and mixing laws. *Geophysics*, *41*(6 A), 1104–1125. doi: 10.1190/1.2035907

Maineult, A. (2018). Corrigendum to "Upscaling of spectral induced polarization response using random tube networks", by Maineult et al. (2017, Geophysical Journal International, 209, pp. 948–960). *Geophysical Journal International*, *213*, 1296–1296. doi: 10.1093/gji/ggy052

Maineult, A., Jougnot, D., & Revil, A. (2018). Variations of petrophysical properties and spectral induced polarization in response to drainage and imbibition: A study on a correlated random tube network. *Geophysical Journal International*, *212*(2), 1398–1411. doi: 10.1093/gji/ggx474

Maineult, A., Revil, A., Camerlynck, C., Florsch, N., & Titov, K. (2017). Upscaling of spectral induced polarization response using random tube networks. *Geophysical Journal International*, *209*(2), 948–960. doi: 10.1093/gji/ggx066

Mendieta, A., Jougnot, D., Leroy, P., & Maineult, A. (2021). Spectral induced polarization characterization of non-consolidated clays for varying salinities - an experimental study. *Journal of Geophysical Research: Solid Earth*, *126*(4). doi: 10.1029/2020jb021125

Okay, G., Leroy, P., Ghorbani, A., Cosenza, P., Camerlynck, C., Cabrera, J., ... Revil, A. (2014). Spectral induced polarization of clay-sand mixtures : Experiments and modeling. *Geophysics*, *79*(6), 353–375. doi: 10.1190/GEO2013-0347.1

Pelton, W., Ward, S. H., Hallof, P. G., Sill, W. R., & Nelson, P. H. (1978). Mineral discrimination and removal of inductive coupling with multifrequency IP. *Geophysics*, *43*(3), 588–609. doi: https://doi.org/10.1190/1.1440839

Pride, S. (1994). Governing equations for the coupled electromagnetics and acoustics of porous media. *Physical Review B*, *50*(21), 15678–15696.

Renard, P., & de Marsily, G. (1997). Calculating equivalent permeability: a review. *Advances in Water Resources*, *20*(5-6), 253–278. doi: https://doi.org/10.1016/S0309-1708(96)00050-4.

Reuss, A. (1929). Berechnung der Fließgrenze von Mischkristallen auf Grund der Plastizitätsbedingung für Einkristalle. *Zeitschrift für Angewandte Mathematik und Mechanik*, *9*(1), 49–58. doi: https://doi.org/10.1002/zamm.19290090104

Revil, A. (2012). Spectral induced polarization of shaly sands: Influence of the electrical double layer. *Water Resources Research*, *48*(2), 1–23. doi: 10.1029/2011WR011260

Revil, A., Linde, N., Cerepi, A., Jougnot, D., Matthäi, S., & Finsterle, S. (2007). Electrokinetic coupling in unsaturated porous media. *Journal of Colloid and Interface Science*, *313*(1), 315–327. doi: 10.1016/j.jcis.2007.03.037

Revil, A., Woodruf, W. F., Torres-Verdín, C., & Prasad, M. (2013). Complex conductivity tensor of anisotropic hydrocarbon-bearing shales and mudrocks. *Geophysics*, *78*(6), E299–E314. doi: 10.1190/GEO2012-0548.1

Tournassat, C., Grangeon, S., Leroy, P., & Giffaut, E. (2013). Modeling specific pH dependent sorption of divalent metals on montmorillonite surfaces. A review of pitfalls, recent achievements and current challenges. *American Journal of Science*, *313*(5), 395–451.

Voigt, W. (1910). *Lehrbuch der Kristallphysik*. Leipzig, Germany: Teubner-Verlag.

Wenk, H. R., Voltolini, M., Mazurek, M., Van Loon, L. R., & Vinsot, A. (2008). Preferred orientations and anisotropy in shales: Callovo-oxfordian shale (France) and opalinus clay (Switzerland). *Clays and Clay Minerals*, *56*(3), 285–306. doi: 10.1346/CCMN.2008.0560301

Woodruff, W. F., Revil, A., & Torres-Verdín, C. (2014). Laboratory determination of the complex conductivity tensor of unconventional anisotropic shales. *Geophysics*, *79*(5), E183–E200. doi: 10.1190/GEO2013-0367.1

Zanetti, C., Weller, A., Vennetier, M., & Mériaux, P. (2011). Detection of buried tree root samples by using geoelectrical measurements: A laboratory experiment. *Plant Soil*, *339*(1), 273–283. doi: 10.1007/s11104-010-0574-0

Zimmermann, E., Kemna, A., Berwix, J., Glaas, W., Münch, H. M., & Huisman, J. A. (2008). A high-accuracy impedance spectrometer for measuring sediments with low polarizability. *Measurement Science and Technology*, *19*(10), 1–9. doi: 10.1088/0957-0233/19/10/105603

4.3 Main results of manuscript

- The best approach to model the amplitude of the real part of the electrical conductivity of clay mixtures are the traditional Voigt, Reuss, and self-consistent approaches. There is not a clear best approach to model the amplitude of the imaginary part of the electrical conductivity of clay mixtures.

- Between the illite and red montmorillonite, the shape of the polarization (imaginary conductivity) curve is rather dominated by the montmorillonite.

- The complex conductance network modeling approach is able to better predict the resulting shape of the polarization curve of the clay mixes, in comparison to traditional mixing laws.

4.4 Complements to manuscript

Further explanations are needed on some aspects dealt in the manuscript. Such complements would normally be added to the supplementary information part of the manuscript. The complementary information is described in this subsection.

4.4.1 Mesh types on complex conductance networks

As mentioned on the manuscript, we modeled SIP signals (from the SIP data of red montmorillonite and illite, at initially 10^{-2} M of NaCl) using complex conductance networks. We computed these simulations with a triangular, a rectangular, and a hexagonal mesh (see figure 4.1). All meshes were made of 50 × 50 nodes. From figure 4.1, we see that the type of mesh with the highest connectivity between nodes is the triangular mesh, thus, we expect a better SIP model from the triangular mesh.

Below, I present the results of the complex conductance network models from the triangular (figure 4.2, also presented on the manuscript), rectangular (figure 4.3), and hexagonal mesh (figure 4.4).

We see slight differences between the three meshes, for example, the signal of the homogeneous mixture seems to be completely off, in comparison to the results of the models from the rectangular and triangular meshes. In order to test the goodness of the model, I calculated the difference ($\Delta\sigma = \sqrt{(\sigma_{model} - \sigma_{data})^2}$) between the models and the data (see figure 4.5). We can see that overall, the best fit comes from the triangular mesh, and the worst from

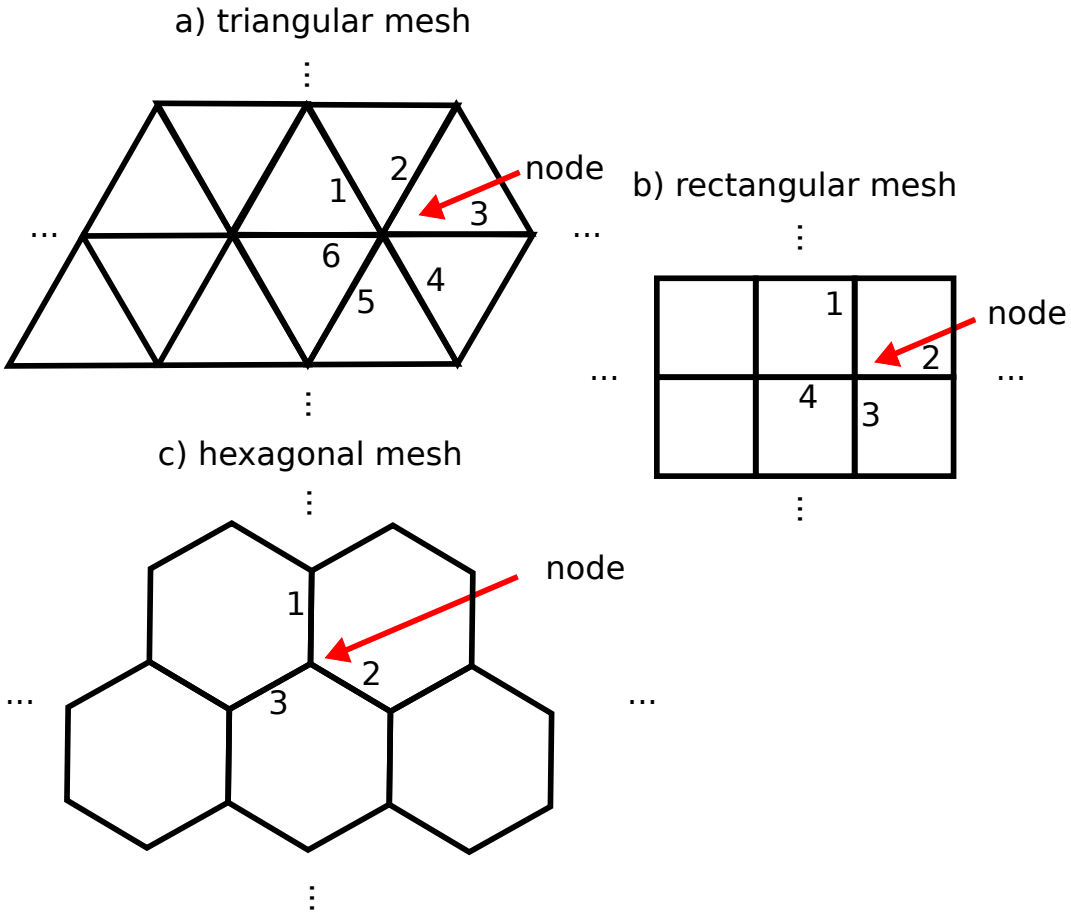

Figure 4.1: Diagrams of different types of meshes used in the complex conductance network models: a) triangluar, b) rectangular, and c) hexagonal mesh. I also present the amount of connections per node for each type of mesh.

the hexagonal mesh. This makes sense, because, as presented in figure 4.1, the triangular mesh, has the highest connectivity, and the hexagonal mesh, the lowest.

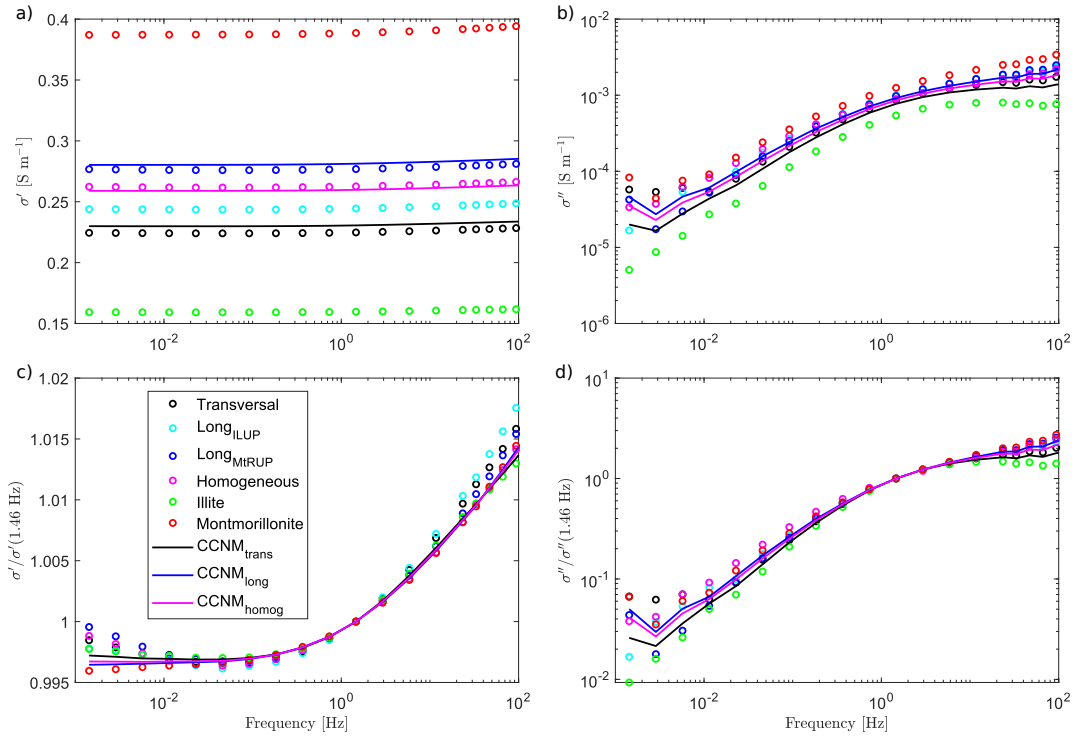

Figure 4.2: a) Real conductivity measurements and triangular conductance network models, b) imaginary conductivity measurements overlain by the triangular conductance network models, c) normalized real conductivity of the measurements and triangular conductance network models, and d) normalized imaginary conductivity of the measurements and triangular conductance network models of the illite and red montmorillonite mixtures. Long-IL-UP and Long-MtR-UP refer to the longitudinal mixtures, with illite and red montmorillonite near the potential electrodes, respectively. CCNM-trans, long, and homog refer to the triangular complex conductance network models using the corresponding arrangements.

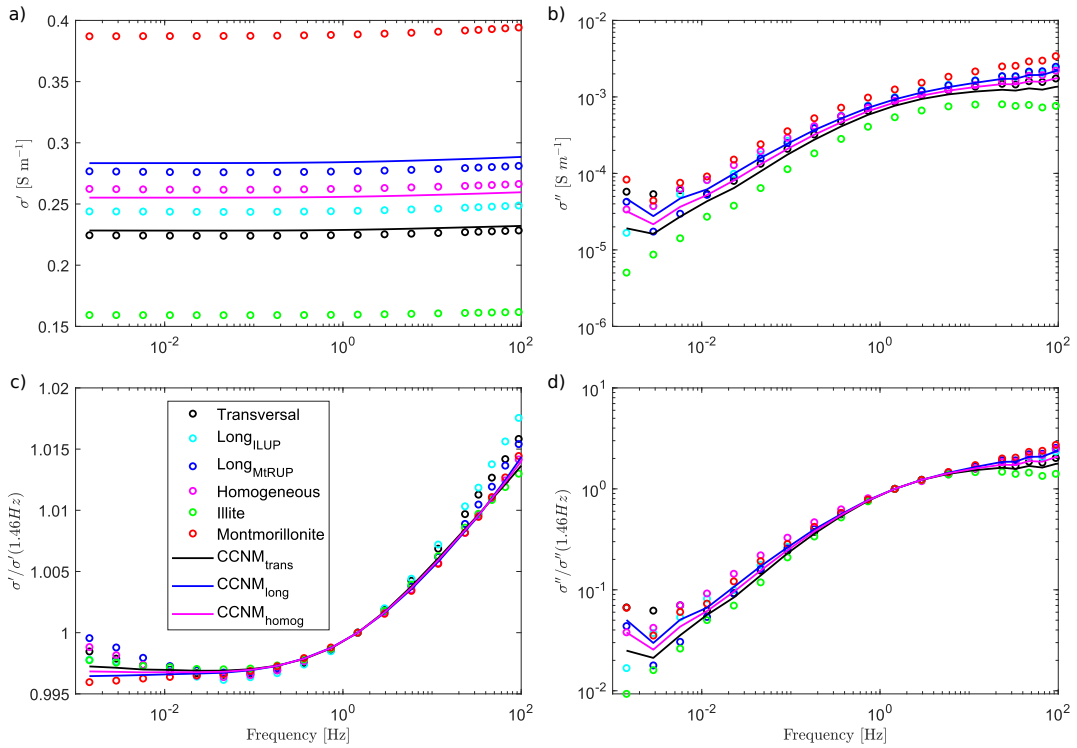

Figure 4.3: a) Real conductivity measurements and rectangular conductance network models, b) imaginary conductivity measurements overlain by the rectangular conductance network models, c) normalized real conductivity of the measurements and rectangular conductance network models, and d) normalized imaginary conductivity of the measurements and rectangular conductance network models of the illite and red montmorillonite mixtures. Long-IL-UP and Long-MtR-UP refer to the longitudinal mixtures, with illite and red montmorillonite near the potential electrodes, respectively. CCNM-trans, long, and homog refer to the complex triangular conductance network models using the corresponding arrangements.

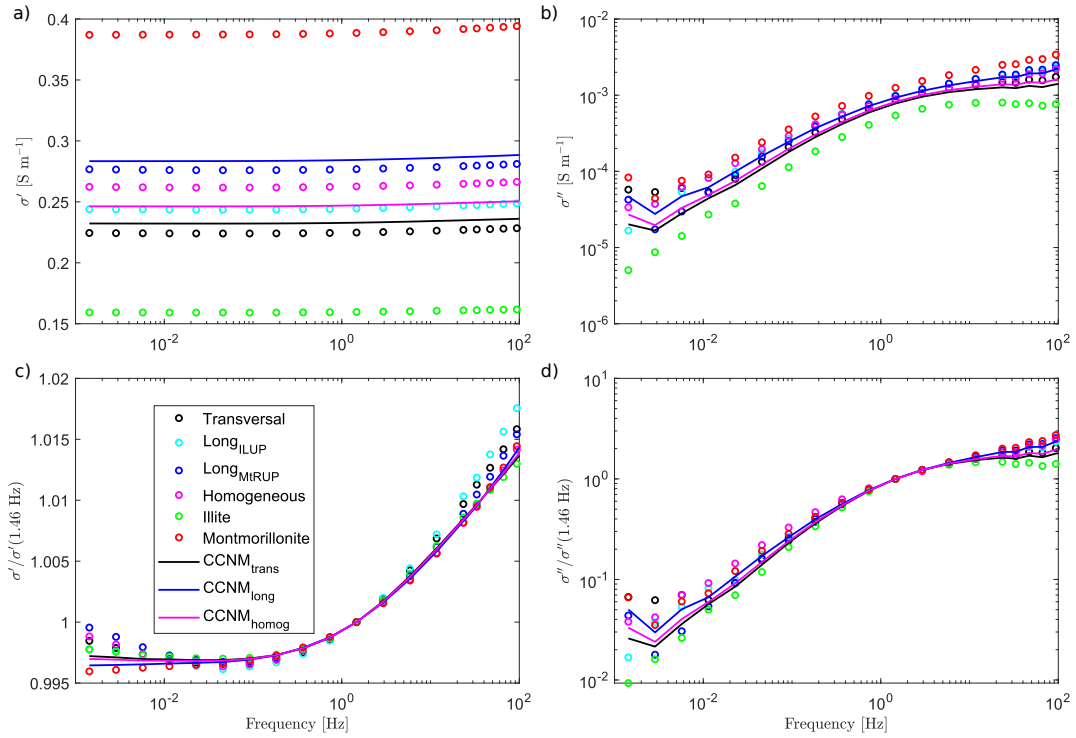

Figure 4.4: a) Real conductivity measurements and hexagonal conductance network models, b) imaginary conductivity measurements overlain by the hexagonal conductance network models, c) normalized real conductivity of the measurements and hexagonal conductance network models, and d) normalized imaginary conductivity of the measurements and hexagonal conductance network models of the illite and red montmorillonite mixtures. Long-IL-UP and Long-MtR-UP refer to the longitudinal mixtures, with illite and red montmorillonite near the potential electrodes, respectively. CCNM-trans, long, and homog refer to the hexagonal complex conductance network models using the corresponding arrangements.

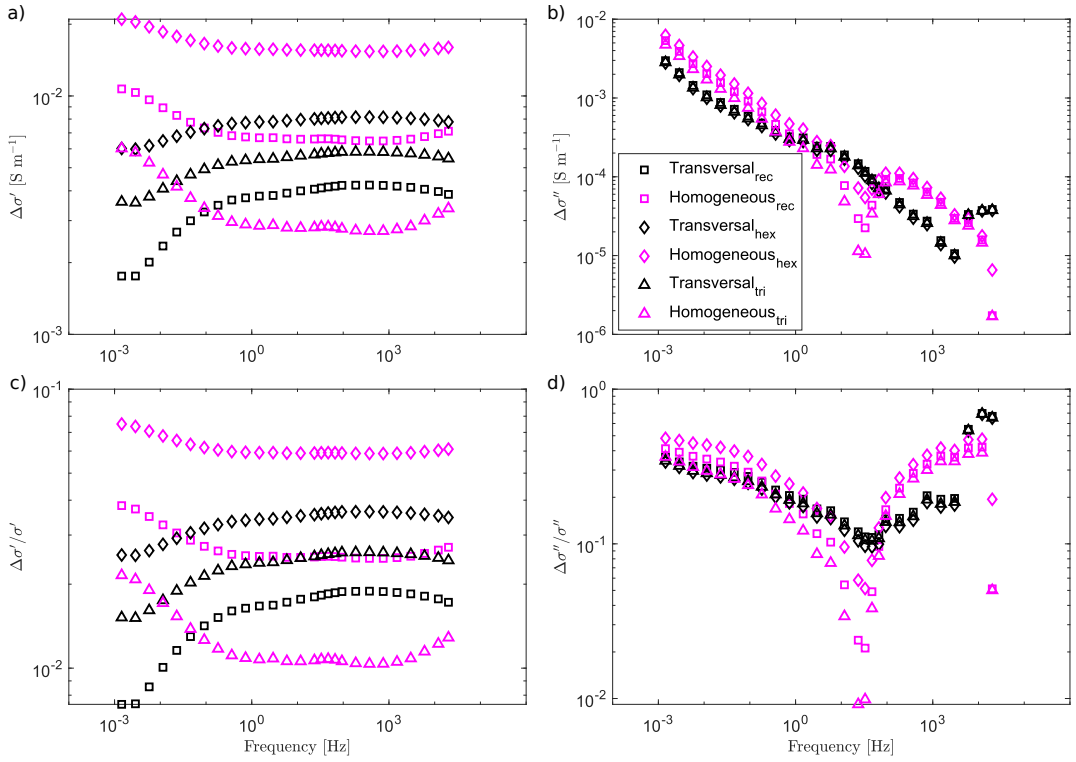

Figure 4.5: Difference between the complex network models (triangular, rectangular, and hexagonal) and the SIP measured data. a) Difference in the real conductivity, b) difference in the imaginary conductivity, c) normalized difference of the real conductivity, and d) normalized difference of the imaginary conductivity.

CHAPTER

5 Perspectives

In this chapter I propose future work to be done with SIP and clays, to further advance the knowledge on polarization phenomena in clays. I think that these research perspectives would be beneficial to the geophysics community so that we continue to obtain a better understanding of the complex electrical conductivity response of clay systems. I initiated some works in these directions but the preliminary results are not mature enough to be added to the main body of this thesis.

Overall, I think there are advances to be done at the laboratory scale, such as: improvement of protocols, variation of other chemical and/or physical properties. I also propose further modeling, so that we can better understand the fundamental physical processes that govern the pore scale electrical phenomena of clays.

5.1 Varying pH on individual clay samples

From this work, we know that there is a variation of SIP with salinity, and that this variation is mineralogy dependent. Bergaya et al. (2013) mentions that clays are greatly affected by the pH of its saturating solution, especially kaolinite, as it has a far more important edge surface than basal surface. Leroy et al. (2017) measured the SIP of a Na-montmorillonite varying the pH and salinity. They found no major control on the imaginary conductivity from variation of the pH. The authors mention that this might be due to the fact that montmorillonites have an important charge of the basal surface. Hördt et al. (2016) performed a numerical analysis of a sequence of 2D pores (a sequence of wide and narrow pores) by varying fluid salinity and pH. They predict that when pH decreases so does the polarization (phase and imaginary conductivity). From these studies we could expect that a pH variation will have an effect on the polarization of clays. Therefore, I think a next step forward would be to do a

SIP study of different types of clays (different mineralogies) with varying pH of the saturating solution in the laboratory.

5.2 Clay heterogeneity mixtures

As presented in chapter 4, I mention that montmorillonite dominates the polarization over illite in the clay mixtures. I say this because the shape of the SIP curves of the mixtures resemble more to the red montmorillonite SIP curve. This statement comes from a qualitative observation. It would be ideal to quantify how the shapes of the curves actually resemble. For this purpose, if we analyze the Pelton model (equation 1.17), with the explicit chargeability term:

$$\rho^*(\omega) = \rho_0 \left[1 - m_k \left[1 - \frac{1}{1 + (i\omega\tau)^c} \right] \right], \tag{5.1}$$

we can see that ρ_0 determines the location on the Y-axis of the curves $|\rho|$, and $|\sigma|$ vs frequency. The relaxation time (τ) rather determines how the spectral curves shift with frequency. The chargeability (m_k) is just a relation between the high and low frequency resistivity (or conductivity), but can thus describe how "flat" or how steep the increase or decrease of the resistivity (or conductivity) with frequency is. Finally, the Cole-Cole parameter (c) describes how wide the polarization peak is (see Tarasov and Titov 2013, for a careful explanation of the Pelton model for SIP).

A Pelton or double-Pelton model (as the one used in the JGR article), could help us to better quantify how the shape of the curve changes with illite content. Thus, I propose that for future work, the modeled spectra with varying illite content can be fitted with a double-Pelton model. The variation of c and m_k with illite content, can give us a better clue to where the illite content threshold is. With varying m_k and c we can see the evolution of the "flatness" of the curve and the width of the local maxima in the curve, this is with varying illite content. Thus the Pelton (or double-Pelton model) can help us determine the illite content threshold where red montmorillonite dominates the polarization.

5.3 Clay compaction

As presented in section 2.4 of this thesis, the SIP data shows that the amplitude of the electrical conductivity varies with compression, while the measured phase changes are minimal. I present the compaction dataset with the electrical conductivity at 1.46 Hz in a compression

and decompression state. Although this suggests that there is a dependence of electrical conductivity to pressure, the used protocol is insufficient to formally prove this. A new protocol needs to be created, in order to formally prove this dependence. We need a protocol, where we can measure the external pressure applied to the clay sample. It would also be interesting to expand such a protocol to other materials other than clays, to see how pressure affects the electrical conductivity depending on material. In particular, the influence of forming interlayer space for montmorillonite during compaction on the SIP electrical signature should be investigated. For this purpose, I believe a collaboration between geophysicists and rock mechanics would be most fruitful.

As the logistics for such an experiment fathom to be complex, I believe the use of newly available technologies (such as laser cutters, and 3D printers) would be helpful to achieve such a goal.

The comprehension of how electrical resistivity varies with compaction would be useful for many applications such as:

- Agriculture: Recently, geophysics has been used to characterize the near surface in agricultural land (e.g.: plant root characterization). Soil compaction affects agriculture and thus having a geophysical method that could allow us to link a geophysical signal to compaction (after a proper calibration of the method) would be of great use for agriculture. Romero-Ruiz (2021, doctoral defense at the University of Lausanne) compared the time-lapse electrical resistivity at the field scale of a compacted versus a non compacted soil. I believe fundamental geo-electrical studies (first at the laboratory scale) can help the geo-electrical field investigations to better understand their measurements and their physical causes.

- Nuclear waste storage: In some countries, such as France, Belgium and Switzerland, there are plans to use clayrock formations to bury nuclear waste (Boom clay for Belgium, Callovo-Oxfordian formation for France, and Opalinus clay for Switzerland) (see for instance Ortiz et al. 2002; Jougnot et al. 2010; Kruschwitz and Yaramanci 2004). These clay systems are deeply buried in the ground (> 200 m depth), and thus support great confining pressures. In order to better understand the geo-electrical signals of a possible in-situ monitoring, we need to take into account that the laboratory experiments are not under the same confining pressures anymore. If we have a better understanding of how the electrical conductivity is affected with pressure in clay sys-

tems, we can better calibrate the laboratory measurements to be more representative of possible in-situ measurements.

- Geothermal: Geothermal systems have clay cap-rocks in their reservoirs (Corrado et al. 2014). Geo-electrical or electromagnetic methods are used to characterize geothermal systems, where clayrocks play an important role. As these clayrocks are buried deep in the subsurface, better understanding how pressure affects the electrical signal of clays would be of great importance for geothermal applications.

As clays are ubiquitously present in the Earth's near surface, there are a myriad of other possible applications. I think better understanding the relation between compaction and electrical signature is a nice step forward towards a better understanding of clay systems and the near surface, in general. More work should be done to better understand this phenomenon.

5.4 Numerical modeling

Finite element analysis is used to model physical laws through established partial differential equations. They are used for a plethora of applications in physics, including geophysics, and also SIP.

One of the drawbacks of this method is that the calculations are computationally expensive. The discretization of the system needs to be done carefully, as it affects the results. Also, for practical reasons, only few parameters can be exploited using this method.

5.4.1 Numerical models in SIP

Most of the numerical models used in SIP thus far deal with the physical phenomena happening at the small scale (pore or particle scale), to try to better understand the fundamentals of physics at these scales.

Blaschek and Hördt (2009) propose a numerical model of IP at the pore scale. They try to understand the physical processes that drive the low frequency polarization at the pore scale, using a 1D pore model. Volkmann and Klitzsch (2010) created a 3D pore system model, with two different pore sizes and included the EDL. They solve the Poisson-Nernst-Planck equation for this system, assuming a decreased cationic mobility within the EDL. Bücker and Hördt (2013a) propose a 1D cylindrical pore system with continuous wide and narrow pores. They explore polarization properties in the light of a membrane polarization model.

They assume that the ionic concentration parallel and perpendicular to the pore are independent of each other. Additionally, Bücker and Hördt (2013b) present a model of long and short narrow pore models for membrane polarization. They analyze the dependence on the characteristic time of the system to pore length. Hördt et al. (2016) create a 1D model of continuous wide and narrow pores and they analyze the influence of pH and salinity of the fluid on the SIP response. This model predicts a decrease of polarization at the highest salinities. Bairlein et al. (2016) perform a numerical analysis on how temperature affects the SIP signal of a 1D series of continuous wide and narrow pores. They predict that the characteristic time of the system decreases with increasing temperatures. Finally, Bücker et al. (2019) compare the numerical SIP model of a grain versus the 1D wide and narrow pores submerged in an electrolyte.

5.4.2 Numerical models of clays

Since numerical models have proved successful to determine the SIP response of particles (e.g., Bücker et al. 2019); I would like to build a numerical model of a clay particle. As exposed in section 1.1, different types of clays have different structures (length, width, etc). I would therefore have to pick one particular type of clay, montmorillonite for example, as it dominates polarization when in mixtures with other types of clays.

Specifically, I would like to do the following numerical experiment:

- Create a numerical model of a montmorillonite particle. Since montmorillonites are rather small and elongated, I would have to choose a particular orientation with respect to the external electrical field. See figure 5.1a for a model of a montmorillonite clay particle with realistic size characteristics. Note that the meshing of the clay particle must be very fine, as there are many physical processes that happen right at the surface of the clay particle. In figure 5.1b, we see the electric potential of a clay particle submerged in an electrolyte. It would be ideal to repeat this numerical experiment at different orientations with respect to the external electrical field. I am not presenting the results of this experiment, as there are still technical difficulties that must be resolved, but it is an experiment I would like to see through to the end.

- Later, I would like to fix two clay particles near each other and vary the ionic concentration in the bulk water (and thus the ionic mobility). I would like to study how the SIP signal varies with varying salinity, coming only from varying ionic mobility. In short, I would like to test the hypothesis proposed by Weller et al. (2015b) where he explains

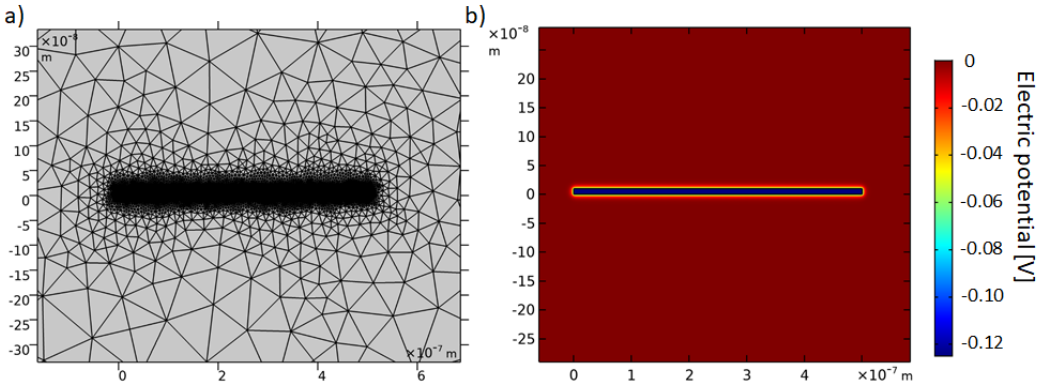

Figure 5.1: Numerical model of a montmorillonite particle. a) Meshing of a montmorillonite particle. b) Frequency-dependent electric potential of a montmorillonite particle subjected to an external frequency varying electric field.

the decrease of the imaginary conductivity at the highest salinities with a decrease of ionic mobilities, from a SIP dataset on sandstones.

- Next, I would like to fix the ionic mobility, but at increasing salinity decrease the space between the two montmorillonite particles. In this way, I would like to numerically test the hypothesis we propose on Mendieta et al. (2021). That is, that with increasing salinity clays coagulate and membrane polarization effects decrease and thus the imaginary conductivity also decreases at the highest salinities.

- Finally, I would like to combine both phenomena in one numerical experiment, to weigh the individual contribution to polarization of each phenomenon.

These numerical experiments would shed light onto the fundamental physical processes that govern the pore scale polarization of clays. I understand that there are limitations to these models, like they are not representative of a clay sample (pluri-centimetric sample), I would not be taking into account the interlayer space in the model. However, I believe it is a good step forward towards better understanding pore scale electrical phenomena in clays. One interesting idea would be to use complex conductance network modeling to try to upscale the signal of single modeled clay pore spaces.

5.5 Various recommendations

Indeed, there is still a lot to understand about clays, particularly through the lens of geoelectrical methods and SIP in specific.

The experiments I have carried out throughout this thesis are at the cm scale. It would be interesting to scale up this experiments to the decimetric level (one level between the cm scale of my experiments and the field-meter scale). One way to do this, would be to create laboratory experiments in tanks of tens of cm in size. It would be interesting to see if at a bigger scale the relationships we observed for the heterogeneous mixtures still stand, for example. It would also be interesting to create a small experiment (in the tanks) mimicking a field arrangement, but in a controlled laboratory environment. The protocol I created to make the clay samples could be used to fill the tanks with clays. It is worth mentioning that some experiments of this type have been done already at the BRGM (French geological survey), but more experiments are needed.

Furthermore, as explained in Mendieta et al. (2021), more physico-chemical models are needed to predict the SIP response of clays at varying salinities, with individual polarization mechanisms in mind. There are models that are valid for clay dilutions (Leroy et al. 2017), but not for non-consolidated clays like the ones used in this study. There are also valid models mixtures of clays and sand (Okay et al. 2014), but not purely for clays. A dedicated physico-chemical model taking the strong EDL contribution into account for the type of clays we have studied in this contribution would be ideal.

Another interesting idea would be to do a quantitative comparison between the two types of physics based models for SIP in clays. I think doing a comparison between a numerical (finite elements) and a physico-chemical SIP model of clay particles, could be interesting. This would help the community better understand the strengths of each model, with respects to clays and SIP.

Conclusions

The goal of the ANR-EXCITING project was to characterize electrically clays at different scales and at multiple frequencies (from the mHz to the kHz). I believe this thesis positively contributes to better understand the electrical signature of different types of clays at the laboratory scale, from the mHz to the kHz. Both from samples of individual types of clays (at varying salinities) and from heterogeneous non-consolidated clay mixtures (of illite and red montmorillonite). An important amount of work was dedicated to the laboratory setup to carry out the SIP experiments. We used phenomenological models to fit the SIP measurements of individual types of clay at different salinities. For the mixtures of illite and red montmorillonite, we were able to model their SIP signals with mixing laws (Voigt, Reuss, and self-consistent) as well as complex conductance networks.

From the SIP measurements at increasing salinities of red and green montmorillonite, kaolinite and illite, we observe an increase of the real electrical conductivity. However, for the imaginary conductivity we see an increase with salinity until a maximum is reached and then we see a decrease of the imaginary conductivity. The maximum of the imaginary conductivity depends on the type of mineralogy. Montmorillonites need a higher salinity to attain this maximum, with respect to illite and kaolinite. Montmorillonites have a higher surface charge (also higher specific surface area) with respect to illite and kaolinite, this indicates why more salinity is needed to achieve this maximum. The decrease of the imaginary conductivity with increasing salinity could be explained with the coagulation of clays. Clays coagulate with increasing salinity, and can thus significantly reduce the possibility for membrane polarization, therefore reducing the imaginary conductivity. Furthermore, we calculated the relationship between the imaginary and real surface conductivities for this SIP dataset and compared it with other datasets in the literature. We observe that this relationship decreases with clay content.

From the SIP measurements of a mixture of red montmorillonite and illite, we observe that for the amplitude of the real and imaginary conductivity both clays contribute similarly. However, for the shape of the complex conductivity spectra, thus polarization, the mixtures rather follow the shape of the red montmorillonite. This is evidence that red montmorillonite dominates polarization over illite. Mixing laws provide a good approach to model the amplitude of the complex electrical conductivity of the mixtures of illite and red montmorillonite. However, this approach is not as good to predict the shape of the curve. On the other hand, complex conductance networks provide a better way to predict the shape of the curve of the mixtures with respect to mixing laws.

Preparing laboratory experiments with non-consolidated clays is a complicate task that requires attention to detail. The construction of electrodes is of utmost importance and although new types of electrodes and/or electrode correction show promise, Cu-$CuSO_4$ are a good alternative for SIP laboratory measurements. The amount of external pressure that clay samples are subjected to needs to be regulated. Even though the sample holder I used for the SIP measurements is not water tight, I was able to calculate the geometrical factor using a numerical model for the sample holder. Indeed, a numerical model of the sample holder is a good alternative when directly measuring the conductivity of a water filled sample holder is not possible. Furthermore, several mechanical tests need to be performed onto the clay samples to find the best water contents for the SIP measurements. The experiments monitoring the pH and water conductivity of mixtures of water and clay powder show that the chemistry of the pore water is a complicated and evolving one, thus more research needs to be done on this particular aspect.

Clay materials are complex and present various structures; they polarize differently depending on their mineralogy, pore water, the external applied pressure onto non-consolidated samples. Basic properties of clays seem to drive their polarization, such as their specific surface area and surface charge. More research is needed to better understand these complex structures and their geo-electrical signal in a natural environment at larger scales.

Appendix 1

Electrode construction

In order to have good SIP measurements, having good non-polarizable electrodes is paramount. In the literature, two types of electrodes have been presented (see Jougnot and Linde 2013): electrodes of first and second kind, notably Cu-$CuSO_4$ electrodes and Ag-AgCl electrodes. These are differentiated by the type of chemical reaction that happens between a metal and a surrounding electrolyte. More recently, some authors have suggested that as long as the electrical current lines do not touch the metal part of the measuring electrode, these should not polarize (Huisman et al. 2016). It should be noted that the chemistry of the solution in contact with the rock sample and the metal part of the electrode should be in equilibrium with the sample. Many authors just use a tube with a small brass rod inside, and a solution between the rock sample and the brass (see Huisman et al. 2016; Izumoto et al. 2020). I started using non-polarizable Cu-$CuSO_4$ electrodes, from the beginning of my laboratory data collection, thus the entirety of my data was collected with Cu-$CuSO_4$ electrodes. I will describe as best as I can the laboratory protocol I followed to build them.

Items:

- Plastic tube: diameter 5mm, length ~8-9 cm.
- Rubber plugs (one per electrode) smaller diameter <5 mm (correct diameter to plug the plastic tube).
- Copper wire (inserted in a rubber plug, length of wire must be smaller than the plastic tube).
- Syringe, with the needle inserted in a rubber plug.

- New syringe (no needle needed).
- Penta-hydrated copper sulfate.
- De-ionized water
- Ceramic porous caps
- 2 Gelatin leaves (~4.5 g, I used the brand "Vahiné")

Preceding procedure to making the gelatin Cu-$CuSO_4$ electrodes:

1. Creation of saturated solution of $CuSO_4$, that is 23 g of $CuSO_4$ in 100 ml of de-ionized water.
2. Location of porous cap on one end of plastic tube.
3. On the other side of the tube locate a rubber plug with the needle of a syringe already inserted in it.
4. While the side of the porous cap is submerged in the $CuSO_4$ solution, create a vacuum in the plastic tube. The idea is to force the porous cap to imbibe in the $CuSO_4$ solution.

Procedure:

1. Gelatin leaves soak in de-ionized water, for 10 min approximately.
2. Mixing of 100 ml de-ionized water and 23 g of $CuSO_4$ with magnetic mixer on stove. Addition of $CuSO_4$ incrementally. Temperature of stove (on screen): 45 °C. Revolutions of stove (on screen): 850 rpm.
3. Incorporation of gelatin leaves (after hydration), make sure there is no excess water on gelatin leaves. Make sure that the measured temperature of the mix is 40 °C, and lower the revolutions to 500 rpm. Add one gelatin leaf at a time.
4. Five minutes after the addition of the first leaf and after everything is well mixed, lower the revolutions to 120 rpm. A small white foam should form.
5. Get rid of the $CuSO_4$ solution previously filling the plastic tubes. Fill new syringe with the $CuSO_4$ and gelatin mix, and then fill the tubes.

6. Plug the tube with a rubber plug, twist if necessary. To avoid the rubber plug to come out easily from the tube, put electric tape, from the tube passing over the rubber plug and finally taping back to the tube.

7. The new electrodes should be stored with the porous cap end submerged in a $CuSO_4$ solution. Before using, or testing, they should be left in this position for at least 24h.

As reference, I used these plastic tubes: https://fr.vwr.com/store/catalog/product.jsp?catalog_number=228-0748.

The porous caps I acquired are:http://www.envexp.com/products/12-Chromatography/IC-Ion_Chromatography/ICD-Dionex/K4270-0_5mL_Vial_and_Filter_Cap_for_Dionex%C2%AE_AS40%2C_250pk.

The gelatin leaves were of this sort: https://www.vahine.fr/produits/gelifiants-et-aides-patissgelatine-alimentaire-en-feuilles.

Calculation of errorbars for the complex conductivity

I carried out the SIP measurements with the SIP-FUCHS III. This equipment measures an electric impedance [Ω], and the phase-lag [mrad] between the signal of the electrical current and the measured electric potential, with errorbars for each. The most common ways to present SIP results is through the conductivity amplitude ($|\sigma|$, in S m^{-1}) and phase (φ, in mrad) or real (σ', in S m^{-1}) and imaginary conductivity (σ', in S m^{-1}), as:

$$\sigma^* = |\sigma| e^{i\varphi} = \sigma' + i\sigma'' \tag{A1-2}$$

As all physical measurements, these quantities should be presented with its corresponding errorbar. The challenge is to convert errorbars as complex quantities. I calculated the complex errorbars in the following way:

$$\begin{aligned} |\sigma_{max}| &= \sigma_{measured} + \Delta\sigma; \\ |\sigma_{min}| &= \sigma_{measured} - \Delta\sigma; \\ |\varphi_{max}| &= \varphi_{measured} + \Delta\varphi; \\ |\varphi_{min}| &= \varphi_{measured} - \Delta\varphi; \end{aligned} \tag{A1-3}$$

where $\sigma_{min,max}$ represents a maximum and minimum electrical conductivity, $\Delta\sigma$ represents the error of the amplitude of the electrical conductivity, $\varphi_{min,max}$ are the maximum and minimum phases, and $\Delta\varphi$ is the measured error of the phase. From here, I calculated the maximum and minimum complex electrical conductivities as:

$$\begin{aligned} \sigma^*_{max} &= |\sigma_{max}|e^{i\varphi_{max}} \\ \sigma^*_{max} &= \sigma'_{max} + i\sigma''_{max}, \end{aligned} \tag{A1-4}$$

in the same way, we have:

$$\begin{aligned} \sigma^*_{min} &= |\sigma_{min}|e^{i\varphi_{min}} \\ \sigma^*_{min} &= \sigma'_{min} + i\sigma''_{min}. \end{aligned} \tag{A1-5}$$

This procedure allows us to carry the errorbars from the amplitude and the phase to the real and imaginary measured conductivities. For further development Hall (2015) proposes a more thorough process to expand the uncertainty analysis to complex quantities.

Appendix 2

This appendix will deal solely with the articles I am not the primary author in but worked in during the duration of this thesis. I only present those articles that have a relation to this thesis. This is to avoid making the body of the thesis too heavy to read.

Article Jougnot et al. (2019)

In this section I present the article Jougnot et al. (2019), that deals with the effect of pore size distribution on streaming potential generation using pore network modeling in a saturated case. Particularly for this thesis, working in this article allowed me to better understand the electric potential distribution in a single pore. The models that are used to describe such electric potential and the strengths and weaknesses of each model.

The citation for this article is: Jougnot, D., Mendieta, A., Leroy, P., and A. Maineult (2019). Exploring the effect of the pore size distribution on the streaming potential generation in saturated porous media, insight from pore network simulations. *Journal of Geophysical Research: Solid Earth, 124*. 10.1029/2018JB017240.

Exploring the effect of the pore size distribution on the streaming potential generation in saturated porous media, insight from pore network simulations

Damien Jougnot[1,*], Aida Mendieta[1], Philippe Leroy[2], and Alexis Maineult[1]

[1]Sorbonne Université, CNRS, EPHE, UMR 7619 METIS, Paris, France.
[2]BRGM, Water, Environment, and Ecotechnologies Department, Orléans, France.

Corresponding author: Damien Jougnot, damien.jougnot@upmc.fr

Keypoints:

- We simulate streaming potentials for 2D networks with different pore size distributions
- The pore size distribution has a very restricted influence on electrokinetic coupling coefficients
- A recent effective excess charge density model accounts for all the pore size distributions

This paper is published in Journal of Geophysical Research - Solid Earth, please cite as:
D. Jougnot, A. Mendieta, P. Leroy, A. Maineult (2019) Exploring the effect of the pore size distribution on the streaming potential generation in saturated porous media, insight from pore network simulations, *Journal of Geophysical Research - Solid Earth*, 124(6), 5315-5335, doi10.1029/2018JB017240.

Abstract

Understanding streaming potential generation in porous media is of high interest for hydrological and reservoir studies as it allows to relate water fluxes to measurable electrical potential distributions. This streaming potential generation results from an electrokinetic coupling due to the presence of an electrical double layer developing at the interface between minerals and pore water. Therefore, the pore sizes of the porous medium are expected to play an important role in the streaming potential generation. In this work we use 2D pore network simulations to study the effect of the pore size distribution upon this electrokinetic mechanism. Our simulations allow a detailed study of the influence of a large range of permeabilities (from 10^{-16} to 10^{-10} m^2) for different ionic concentrations (from 10^{-4} to 1 mol L^{-1}). We then use and compare two different approaches that have been used over the last decades to model and interpret the streaming potential generation: the classical coupling coefficient or the effective excess charge density, which has been defined recently. Our results show that the four pore size distributions tested in the present work have a restricted influence on the coupling coefficient for ionic concentration smaller than 10^{-3} mol L^{-1} while it completely drives the behaviour of the effective excess charge density over orders of magnitude. Then, we use these simulation results to test an analytical model based on a fractal pore size distributions. This model predicts well the effective excess charge density for all pore size distributions under the thin double layer assumption.

1 Introduction

Self-Potential (SP) is one of the oldest geophysical methods (*Fox*, 1830) and consists in measuring the naturally occurring electrical field at the surface of or within geological media. The SP signal results from the superposition of multiple sources coming from contributions of two main processes: the electrokinetic (EK) contribution (i.e., related to water flux) and the electrochemical contributions (i.e., related to ionic concentration, thermal gradient, or redox gradient). In this work we focus on SP signals generated by electrokinetic phenomena: the so-called streaming potential. Details on the possible contributions to the SP signal can be found in *Revil and Jardani* (2013) or *Jouniaux et al.* (2009), among other references.

The streaming potential has been the subject of numerous scientific studies over the last two centuries (since *Quincke*, 1859) and involved in many applications: from oil and gas reservoir exploration to more recent critical zone studies (e.g., *Revil et al.*, 1999a; *Jougnot et al.*, 2015). In geological media, minerals and organic matter exhibit a charged surface (usually negative) that is compensated by an excess of charges in the pore water distributed in the so-called electrical double layer (EDL) surrounding these grains (e.g. *Hunter*, 1981). These charges can be dragged by a water flow, generating a charge separation that in turn generates an electrical current and a resulting electrical potential distribution. Given the difficulty of directly measuring the water flow in geological media, relating this measurable electrical potential distribution to the water flux is therefore of interest for many reservoir or environmental applications (e.g., *Jouniaux et al.*, 2009; *Revil and Jardani*, 2013).

For more than a century, the classical approach to quantitatively relate the electrical potential field to the water flux (or to a hydraulic pressure field) has been achieved by the use of the EK coupling coefficient, C_{EK} (V Pa^{-1}),

$$C_{EK} = \frac{\partial V}{\partial P}\Big|_{\mathbf{J}=\overrightarrow{0}}, \tag{1}$$

where V is the electrical potential (V) and is P the water pressure (Pa), in the assumptions that the system is under a quasi-static equilibrium and that no external current $\mathbf{J}$ is injected into the medium. *Helmholtz* (1879) and *von Smoluchowski* (1903) proposed the so-called Helmholtz-Smoluchowski (HS) equation to determine C_{EK} from a limited amount of parameters:

$$C_{EK}^{HS} = \frac{\varepsilon_w \zeta}{\eta_w \sigma_w}, \tag{2}$$

where ε_w, σ_w, and η_w are the dielectric permittivity (F m^{-1}), the electrical conductivity (S m^{-1}), and the dynamic viscosity (Pa s) of the pore water, respectively. The ζ-potential, ζ (V), corresponds to the electrical potential at the shear plane in the EDL, which is the plane separating mobile and immobile water molecules (e.g. *Hunter*, 1981; *Leroy et al.*, 2012; *Li et al.*, 2016, Fig. 1). The HS equation has been successfully used to predict streaming potential measurements in geological media (e.g., *Jouniaux and Pozzi*, 1995a; *Pengra et al.*, 1999). It is interesting to note that the HS equation seems completely independent from the pore space geometry of the medium. However, there is a strong assumption in this model: the surface conductivity of the grains, σ_s (S m^{-1}), must be negligible compared to the pore water conductivity, that is $\sigma_s \ll \sigma_w$. When this is not the case, alternative formulas have been proposed by several researchers (e.g., *Morgan et al.*, 1989; *Revil et al.*, 1999b; *Glover and Déry*, 2010), taking into account surface conductivity and making some assumptions on the pore space geometry.

More recently, an alternative approach to quantify the streaming potential generation has been proposed, focusing on the excess charge effectively dragged by the water flow. To the best of the authors knowledge, the first occurrence of this approach in the literature in english is in *Kormiltsev et al.* (1998) and was later independently found by *Revil and Leroy* (2004). This parameter is an alternative to the coupling coefficient and can easily be related to it by re-writing the water flow and electrical current equations (see *Kormiltsev et al.*, 1998, for the first derivation)

$$C_{EK} = -\frac{\hat{Q}_v k}{\sigma \eta_w}, \tag{3}$$

where σ and k are the electrical conductivity (S m^{-1}) and permeability (m^2) of the medium, respectively. Following the formalism of Revil and co-authors, we call $\hat{Q}_v$ the effective excess charge density (C m^{-3}). Note that it is called α in *Kormiltsev et al.* (1998).

Several studies have shown empirical evidence to prove that the effective excess charge density depends on the permeability of the porous media (*Titov et al.*, 2002; *Jardani et al.*, 2007; *Bolève et al.*, 2012), indicating that this parameter is strongly influenced by the petrophysical properties of the considered geological medium. It has been shown that the pore water chemistry, both the composition and the ionic concentration, also have a significant effect on $\hat{Q}_v$ (e.g., *Jougnot et al.*, 2012, 2015; *Cherubini et al.*, 2018).

Recently, *Guarracino and Jougnot* (2018) proposed an analytical model directly relating $\hat{Q}_v$ to the permeability, porosity, pore water chemistry (through the ionic concentration), and the ζ-potential. This closed-form equation was derived with the assumptions of a simple binary symmetric pore water electrolyte and pore radii much larger than the diffuse layer thickness. In order to achieve the derivation of this analytical solution, the authors based their approach on the use of tortuous capillaries and a fractal pore size distribution. Interestingly, the pore size distribution does not directly appear in the closed-form equation. *Guarracino and Jougnot* (2018)'s model performs very well with different SP datasets from laboratory measurements (*Pengra et al.*, 1999; *Glover and Déry*, 2010). Note that *Soldi et al.* (2019) propose an extension of this model to partially saturated conditions.

Pore network simulations can be used as a numerical tool to predict the electrokinetic coupling coefficient, and consequently the effective excess charge density, for different pore size distributions. *Bernabé* (1998) proposed a pioneer work to model streaming potential in heterogeneous media. Based on this work, further investigations on coupling effects in charged media in 2 or 3D have been performed (e.g., *Brovelli and Cassiani*, 2010; *Obliger et al.*, 2014; *Zhang et al.*, 2015), mainly to evaluate the impact of the electrokinetic coupling on the permeability in microporous media.

In this work, we use a pore network numerical code based on the works of *Bernabé* (1998) and *Maineult et al.* (2018). It allows for the prediction of the coupling coefficient, permeability, and formation factor of a 2D pore network with well-controlled pore size distributions, and therefore the effective excess charge density from Eq. 3. After presenting the theoretical framework for the electrokinetic phenomena and the numerical method that we implemented, we will (1) study the effect

of the pore size distribution on the streaming potential generation and (2) check for the applicability of the *Guarracino and Jougnot* (2018) analytical model for the prediction of the effective excess charge density obtained for different pore size distributions.

2 Theory of streaming current generation

2.1 Governing equations

Streaming current generation in geological media can be described by the following macroscopic governing equations (e.g., *Sill*, 1983):

$$\mathbf{J} = \sigma \mathbf{E} + \mathbf{J}_s, \tag{4}$$

$$\nabla \cdot \mathbf{J} = 0, \tag{5}$$

where $\mathbf{J}$ is the total current density (A m^{-2}), $\mathbf{E} = -\nabla V$ is the electrical field (V m^{-1}), and $\mathbf{J}_s$ is the source current density (A m^{-2}). In the absence of external current, that is when no current is injected into the medium, combining Eqs. (4) and (5) yields,

$$\nabla \cdot (\sigma \nabla V) = \nabla \cdot \mathbf{J}_s. \tag{6}$$

When considering only EK processes in the SP signals, the source current density (i.e., streaming current density) can then be expressed as,

$$\mathbf{J}_s = \sigma C_{EK} \nabla \left(P - \rho_w g z \right), \tag{7}$$

where ρ_w is the water density (kg m^{-3}), g is the gravitational acceleration (m s^{-2}), and z is the elevation (m). We call Eq. (7) the coupling coefficient approach.

As described in *Kormiltsev et al.* (1998), combining Eq. 3 and Darcy's equation (*Darcy*, 1856), we obtain the Darcy velocity:

$$\mathbf{u} = -\frac{k}{\eta_w} \nabla \left(P - \rho_w g z \right). \tag{8}$$

Including Eq. 8 in Eq. 7, one can obtain the streaming current density from the effective excess charge approach,

$$\mathbf{J}_s = \hat{Q}_v \mathbf{u}. \tag{9}$$

Combining Eqs. 6 and 9 allows relating the streaming potential distribution to the Darcy velocity, a variable of uttermost interest in hydrology or reservoir studies, through the medium conductivity and effective excess charge density:

$$\nabla \cdot (\sigma \nabla V) = \nabla \cdot \left(\hat{Q}_v \mathbf{u} \right). \tag{10}$$

2.2 Electrochemical properties

Most geological materials have a solid matrix made of components with charged surfaces (mostly minerals but also organic matter) in contact with water due to the hydroxilation of the surface sites and ion substitutions in the crystal (*Hiemstra and Van Riemsdijk*, 2006; *Leroy et al.*, 2013, 2015; *Li et al.*, 2016). An EDL is formed at the pore surface to compensate the surface charge as the system "solid matrix plus pore water" must satisfy the electroneutrality principle (e.g., *Hunter*, 1981; *Leroy and Revil*, 2004). As shown in Fig. 1, the surface charge Q_0 (C m^{-2}) is counterbalanced by charges in the EDL of the pore water: (1) by charges adsorbed in the compact Stern layer Q_β (often considered

to have a negligible thickness, therefore expressed in C m^{-2}) and (2) by a distribution of charges in the diffuse layer $\bar{Q}_v$ (C m^{-3}). This yields

$$\frac{S_{sw}}{V_w}\left(Q_0 + Q_\beta\right) + \bar{Q}_v = 0, \tag{11}$$

where S_{sw} is the surface of the solid in contact with water (m^2) and V_w is the pore water volume (m^3). The term $\bar{Q}_v$ is called the excess charge density in the diffuse layer. We call co-ions and counter-ions the ions with the same and the opposite sign of the surface charge density, respectively. In typical silica rocks, under typical environmental conditions, surfaces are usually negatively charged; the co-ions and counter-ions are therefore anions and cations, respectively (e.g., *Sverjensky*, 2006).

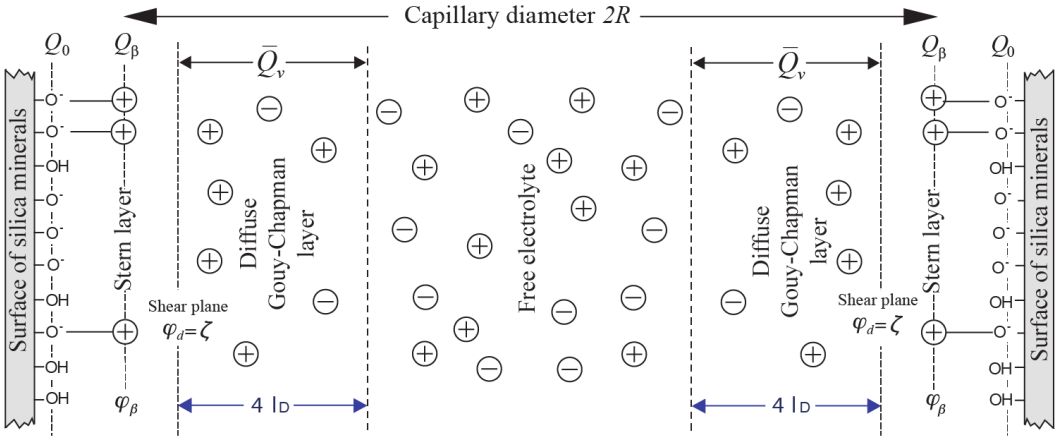

Figure 1: Scheme of the electrical double layer at the surface of silica minerals in contact with water for a given capillary radius R. l_D correspond to the Debye length (Eq. 18).

The distribution of ions in the diffuse layer depends on the distribution of the microscopic (or local) electrical potential in the pores, ψ (V), which follows the Poisson equation:

$$\nabla^2\psi = -\frac{\bar{Q}_v}{\varepsilon_w} \tag{12}$$

where ε_w is the dielectric permittivity of the pore water (F m^{-1}). We consider that the bulk pore water (i.e., the part of the electrolyte free from the effects of the charged surfaces) is an electrolyte composed of M ionic species i with a bulk concentration C_i^w (mol m^{-3}). The excess charge density in the diffuse layer is supposed to follow a Boltzmann distribution yielding:

$$\bar{Q}_v(r) = N_A \sum_{i=1}^{M} q_i C_i^w \exp\left(-\frac{q_i\psi(r)}{k_B T}\right) \tag{13}$$

where r is the distance from the shear plane (m) (that is the pore wall as we neglect the Stern layer thickness), $N_A = 6.022 \times 10^{23}$ mol^{-1} is the Avogadro's number, $k_B = 1.381 \times 10^{-23}$ J K^{-1} is the Boltzmann constant, T is the absolute temperature (K), and $q_i = \pm z_i e_0$ is the ion charge (C) which depends on its valency, z_i, and the elementary charge, $e_0 = 1.602 \times 10^{-19}$ C. Note that the extension of the diffuse layer corresponding to the fraction of the pore space in which the excess charge density is not negligible, can be approximated by a thickness equal to $4l_D$ (Fig. 1).

The excess charge density which is effectively displaced by the water flow is called effective or dynamic excess charge, depending on the authors, and symbolized as $\hat{Q}_v$ or $\bar{Q}_v^{eff}$ (C m^{-3}). It has to be distinguished from the other excess charge densities contained in the pore space (see the discussion in

Revil, 2017). The total excess charge density Q_v (C m^{-3}), which includes all the charges of the EDL, is given by:

$$Q_v = \frac{S_{sw}}{V_w}\left(Q_\beta\right) + \bar{Q}_v = \rho_s \left(\frac{1-\phi}{\phi}\right) e_0 N_A CEC, \tag{14}$$

where CEC is the cationic exchange capacity (meq kg^{-1}), ϕ is the porosity, and ρ_s is the solid grain density (kg m^{-3}). Note that the CEC of hydroxide minerals such as quartz strongly depends on the pH and salinity (*Leroy et al.*, 2013). As discussed in *Jougnot et al.* (2012), the excess charge density of the diffuse layer $\bar{Q}_v$ (Fig. 1) is usually considerably smaller than the total excess charge density Q_v and larger than the effective excess charge density $\hat{Q}_v$:

$$\hat{Q}_v \ll \bar{Q}_v \ll Q_v. \tag{15}$$

This is due to the fact that the effective excess charge density is weighted by the pore water velocity distribution through the pore (Fig. 10a). This concept is described in detail in *Jougnot et al.* (2012) and called "flux-averaging" in opposition to the "volume-averaging" up-scaling technique described in *Revil et al.* (2007).

2.3 Electrokinetic coupling at the pore scale

Following the capillary-based approaches proposed by *Jackson* (2008, 2010) and *Linde* (2009), *Jougnot et al.* (2012) consider the porous medium as a bundle of capillaries to develop the flux-averaging up-scaling procedure. The effective excess charge density $\hat{Q}_v^R$ dragged by the water flow in a single tube of radius R (m) is defined by:

$$\hat{Q}_v^R = \frac{\int_{r=0}^{R} \bar{Q}_v(r) v(r) dr}{\int_{r=0}^{R} v(r) dr}, \tag{16}$$

where $v(r)$ is the pore water velocity across the capillary (m s^{-1}).

In order to propose an analytical solution for Eq. (16), *Guarracino and Jougnot* (2018) consider the Debye-Hückel approximation, an usual way to derive analytically the distribution of the local electrical potential (e.g., *Jougnot et al.*, 2012, 2015; *Guarracino and Jougnot*, 2018; *Soldi et al.*, 2019). This approximation is an accurate solution of the Poisson-Boltzmann equation (Eq. 12) for low local electrical potentials, i.e., $|\zeta| << (k_B T)/|q_i| \simeq 25$ mV (for T= 298 K) and monovalent ions. The microscopic electrical potential distribution in the diffuse layer of a NaCl pore water solution can then be expressed as,

$$\psi(r) = \zeta \exp\left(-\frac{r}{l_D}\right), \tag{17}$$

where l_D is the Debye length (m) defined as,

$$l_D = \sqrt{\frac{\varepsilon_w k_B T}{2 e_0^2 C^w N_A}}. \tag{18}$$

Note that this is a solution obtained for a flat surface (e.g., *Hunter*, 1981). Nevertheless, it can be used for large pores, that is for a small curvature compared to the diffuse layer thickness (see discussion in *Jougnot et al.*, 2012; *Thanh*, 2018). For a NaCl solution, Eq. (13) becomes,

$$\bar{Q}_v(r) = N_A e_0 C^w_{NaCl}\left[e^{-\frac{e_0\psi(r)}{k_B T}} - e^{\frac{e_0\psi(r)}{k_B T}}\right]. \tag{19}$$

Then the exponential terms of Eq. (19) are approximated by a four-term Taylor series:

$$e^{\pm\frac{e_0\psi(r)}{k_B T}} = 1 \pm \frac{e_0\psi(r)}{k_B T} + \frac{1}{2}\left(\frac{e_0\psi(r)}{k_B T}\right)^2 \pm \frac{1}{6}\left(\frac{e_0\psi(r)}{k_B T}\right)^3. \tag{20}$$

Substituting Eq. (20) in Eq. (19) and solving (16) considering a Poiseuille flow, it yields:

$$\begin{aligned}\hat{Q}_v^R = \; & -\frac{8N_A e_0^2 C_{NaCl}^w \zeta}{k_B T (R/l_D)^4}\left\{6 - e^{-\frac{R}{l_D}}\left[\left(\frac{R}{l_D}\right)^3 + 3\left(\frac{R}{l_D}\right)^2 + 6\left(\frac{R}{l_D}\right) + 6\right]\right\} \\ & + \frac{24N_A e_0^2 C_{NaCl}^w \zeta}{k_B T (R/l_D)^3}\left\{2 - e^{-\frac{R}{l_D}}\left[\left(\frac{R}{l_D}\right)^2 + 2\left(\frac{R}{l_D}\right) + 2\right]\right\} \\ & - \frac{16N_A e_0^2 C_{NaCl}^w \zeta}{k_B T (R/l_D)^2}\left\{1 - e^{-\frac{R}{l_D}}\left[\left(\frac{R}{l_D}\right) + 1\right]\right\} \\ & - \frac{4N_A e_0^4 C_{NaCl}^w \zeta^3}{3(k_B T)^3 (3R/l_D)^4}\left\{6 - e^{-\frac{3R}{l_D}}\left[\left(\frac{3R}{l_D}\right)^3 + 3\left(\frac{3R}{l_D}\right)^2 + 6\left(\frac{3R}{l_D}\right) + 6\right]\right\} \\ & + \frac{4N_A e_0^4 C_{NaCl}^w \zeta^3}{(k_B T)^3 (3R/l_D)^3}\left\{2 - e^{-\frac{3R}{l_D}}\left[\left(\frac{3R}{l_D}\right)^2 + 2\left(\frac{3R}{l_D}\right) + 2\right]\right\} \\ & - \frac{8N_A e_0^4 C_{NaCl}^w \zeta^3}{3(k_B T)^3 (3R/l_D)^2}\left\{1 - e^{-\frac{3R}{l_D}}\left[\left(\frac{3R}{l_D}\right) + 1\right]\right\}.\end{aligned} \tag{21}$$

Considering the thin double layer assumption $l_D \ll R$, *Guarracino and Jougnot* (2018) simplify Eq. 21 to obtain the following analytical solution to predict the effective excess charge in a single capillary with a radius R,

$$\hat{Q}_v^R = \frac{8N_A e_0 C_{NaCl}^w}{(R/l_D)^2}\left[-2\frac{e_0\zeta}{k_B T} - \left(\frac{e_0\zeta}{3k_B T}\right)^3\right]. \tag{22}$$

This solution is considered valid for $R > 5l_D$, see discussion in *Guarracino and Jougnot* (2018) (their Fig. 2) and in *Thanh* (2018). Note that the rather simple Eq. (22) is influenced both by geometry (R), interface (ζ, l_D), and chemical properties (C_{NaCl}^w).

2.4 Electrokinetic coupling at the REV scale

In order to study the streaming potential generation in natural geological media, a second upscaling procedure has to be performed to go from $\hat{Q}_v^R$ to the effective excess charge density at the Representative Elementary Volume (REV) scale, $\hat{Q}_v^{REV}$. The flux-averaging approach proposed by *Jougnot et al.* (2012) yields,

$$\hat{Q}_v^{REV} = \frac{\int_{R_{min}}^{R_{max}} \hat{Q}_v^R v^R f_D dR}{\int_{R_{min}}^{R_{max}} v^R f_D dR}, \tag{23}$$

where v^R is the average pore water velocity (m s^{-1}) in capillaries having a radius R, and f_D is the capillary size distribution. Eq. 23 holds for any capillary size distribution. *Jougnot et al.* (2012) propose to determine f_D from the hydrodynamic curves of the considered porous medium. This can be accomplished by two approaches: one based on the water retention curve f_D^{WR}, the other based on the relative permeability curve f_D^{RP}. Both approaches require numerical simulation.

Guarracino and Jougnot (2018) recently proposed an analytical approach to determine $\hat{Q}_v^{REV}$ at the REV scale considering a fractal pore size distribution under water saturated conditions. They solve Eq. 23 with $\hat{Q}_v^R$ from Eq. 22. Their analytical developments, based on the Debye-Hückel approximation, yield the following rather simple formula,

$$\hat{Q}_v^{REV} = N_A e_0 C^w l_D^2 \left[-2\frac{e_0\zeta}{k_B T} - \left(\frac{e_0\zeta}{3k_B T}\right)^3\right]\frac{1}{\tau^2}\frac{\phi}{k}. \tag{24}$$

where τ is the dimensionless hydraulic tortuosity of the medium. The above equation predicts the effective excess charge density in terms of both macroscopic hydraulic parameters (porosity, permeability, and tortuosity) and parameters of chemical or interfacial nature (ionic concentration, ζ-potential and Debye length). One can see that the fractal pore size distribution does not explicitely appear in

Eq. 24, as it is included in the porosity and permeability terms. Indeed, when developping the analytical solution presented above (Eq. 24), all the information related to the pore space geometry (e.g., the fractal pore size distribution) was included in the definition of porosity and permeability (see *Guarracino and Jougnot*, 2018, for more details on the model development). This model has been recently extended to partially saturated conditions by *Soldi et al.* (2019). Note that *Thanh* (2018) proposed an expression similar to Eq. 24 but only valid for a single capillary radius instead of a distribution of radii.

While the *Guarracino and Jougnot* (2018) analytical solution proposes an explicit link between $\hat{Q}_v$ and the medium's permeability, numerous previous studies have shown an empirical relationship between these two parameters before (e.g., *Titov et al.*, 2002; *Jardani et al.*, 2007; *Bolève et al.*, 2012; *Cherubini et al.*, 2018). Among these works, *Jardani et al.* (2007) propose the following empirical relationship

$$\log_{10}(\hat{Q}_v^{REV}) = A_1 + A_2 \log_{10}(k), \tag{25}$$

where $A_1 = -9.2349$ and $A_2 = -0.8219$ are constant values obtained by fitting Eq. 25 to a large set of experimental data that includes various lithologies and ionic concentrations. It has been widely used for SP (e.g. *Jardani and Revil*, 2009; *Linde et al.*, 2011; *Soueid Ahmed et al.*, 2014; *Roubinet et al.*, 2016) and seismoelectrics (e.g. *Jougnot et al.*, 2013; *Revil et al.*, 2015; *Monachesi et al.*, 2015) applications.

3 Streaming potential modeling in a 2D pore network

The present section describes the pore network model that we developed and used to simulate the streaming potential generation in synthetic porous media. We first describe the electrokinetic coupling at the capillary scale and then how the up-scaling is performed in 2D pore networks with different pore size distributions. Note that the simulations are based on the classical coupling coefficient approach (Eq. 7) and that the effective excess charge density is obtained from the numerical simulation results and Eq. 3.

3.1 Coupled transport equations in a single capillary

The pore network simulations consider the electrokinetic coupling occuring in capillaries (i.e., pores). Our numerical simulations are based on the numerical framework of *Bernabé* (1998), where the magnitudes of the hydraulic, Q ($m^3\ s^{-1}$), and electrical, J ($A\ s^{-1}$), fluxes in a single capillary of radius R (m) and length l (m) are given by the following equations:

$$\begin{cases} Q = -\dfrac{\pi R^4}{8\eta_w}\dfrac{(P_u - P_d)}{l} + \dfrac{\pi \epsilon_w R^2 \zeta}{\eta_w}\left(1 - \dfrac{2}{R^2\zeta}\int_0^R r\psi(r)dr\right)\dfrac{(V_u - V_d)}{l} \\ J = \dfrac{\pi \epsilon_w R^2 \zeta}{\eta_w}\left(1 - \dfrac{2}{R^2\zeta}\int_0^R r\psi(r)dr\right)\dfrac{(P_u - P_d)}{l} \\ \quad - \left[\dfrac{2\pi\epsilon_w^2}{\eta_w}\int_0^R r\left(\frac{d\psi(r)}{dr}\right)^2 dr + 2\pi\sigma_w\int_0^R r\cosh\left(\frac{ze\psi(r)}{k_B T}\right)dr\right]\dfrac{(V_u - V_d)}{l} \end{cases}, \tag{26}$$

where P is the hydraulic pressure, V is the electrical potential and where the subscripts u and d are for the up and down water pressure and electrical potential values, respectively. This set of equations is a fully coupled system taking into account the classical Poiseuille flow, Ohm's law, and both the electrofiltration (i.e., a water displacement generating an electrical field) and the electroosmotic (i.e., an electrical field generating a water displacement) couplings (e.g., *Nourbehecht*, 1963). Eq. 26 can be condensed into,

$$\begin{cases} Ql = -\gamma^h(P_u - P_d) + \gamma^c(V_u - V_d) \\ Jl = \gamma^c(P_u - P_d) + \gamma^e(V_u - V_d) \end{cases}, \tag{27}$$

where γ^h is the modified hydraulic conductance (in $m^4\ Pa^{-1}\ s^{-1}$), γ^e is the modified electrical conductance (in S m), and γ^c is the modified coupling conductance (in $m^4\ V^{-1}\ s^{-1}$). Note that the capillaries are submitted to a gradient of water pressure in steady-state conditions and that generates, in turn, an electrical potential gradient.

Given the importance of the local electrical potential, ψ, in the above equations, we use the code proposed by *Leroy and Maineult* (2018) to solve the general Poisson-Boltzmann equation in each cylindrical pore at a given ionic concentration.

In the simulations, the ζ-potential depends on the ionic concentration in the bulk pore water and is determined by the following relationship (*Pride and Morgan*, 1991):

$$\zeta(C^w) = a + b\log_{10}(C^w), \tag{28}$$

where a and b are fitting parameters. For this study we use the parameter values obtained by *Jaafar et al.* (2009) for NaCl brine: a=-6.43 mV and b=20.85 mV for silicate materials. Note that *Cherubini et al.* (2018) propose different values of a and b for carbonates based on experimental streaming potential measurements.

The electrical conductivity of the water also depends on the ionic concentration. In our simulation, we consider the *Sen and Goode* (1992) empirical model:

$$\sigma_w(C^w, T) = \left(a_1 + a_2 T + a_3 T^2\right) C^w - \left(\frac{a_4 + a_5 T}{1 - a_6\sqrt{C^w}}\right), \tag{29}$$

with $a_1 = 5.6$ S L m^{-1} mol^{-1}, $a_2 = 0.27$ S L m^{-1} mol^{-1} $°C^{-1}$, $a_3 = -1.51 \times 10^{-4}$ S L m^{-1} mol^{-1} $°C^{-2}$, $a_4 = 2.36$ (S L m^{-1} mol^{-1})$^{3/2}$, $a_5 = 0.099$ (S L m^{-1} mol^{-1} $°C^{-1}$)$^{3/2}$, $a_6 = 0.214$ $(mol^{-1})^{-1/2}$, and in which the ionic concentration and the temperature are expressed in mol L^{-1} and °C, respectively.

3.2 2D pore network and related equation system

We consider a 2D pore network as shown in Fig. 2. At each node (i, j) of the grid, we applied *Kirchhoff* (1845)'s law for the conservation of the mass and of the electrical charge, which yields:

$$\begin{cases} -\gamma^h_{i-1,j\to i,j}(P_{i,j} - P_{i-1,j}) + \gamma^c_{i-1,j\to i,j}(V_{i,j} - V_{i-1,j}) \\ \quad -\gamma^h_{i+1,j\to i,j}(P_{i,j} - P_{i+1,j}) + \gamma^c_{i+1,j\to i,j}(V_{i,j} - V_{i+1,j}) \\ \quad -\gamma^h_{i,j-1\to i,j}(P_{i,j} - P_{i,j-1}) + \gamma^c_{i,j-1\to i,j}(V_{i,j} - V_{i,j-1}) \\ \quad -\gamma^h_{i,j+1\to i,j}(P_{i,j} - P_{i,j+1}) + \gamma^c_{i,j+1\to i,j}(V_{i,j} - V_{i,j+1}) = 0 \\ \gamma^c_{i-1,j\to i,j}(P_{i,j} - P_{i-1,j}) - \gamma^e_{i-1,j\to i,j}(V_{i,j} - V_{i-1,j}) \\ \quad \gamma^h_{i+1,j\to i,j}(P_{i,j} - P_{i+1,j}) - \gamma^e_{i+1,j\to i,j}(V_{i,j} - V_{i+1,j}) \\ \quad \gamma^h_{i,j-1\to i,j}(P_{i,j} - P_{i,j-1}) - \gamma^e_{i,j-1\to i,j}(V_{i,j} - V_{i,j-1}) \\ \quad \gamma^h_{i,j+1\to i,j}(P_{i,j} - P_{i,j+1}) - \gamma^e_{i,j+1\to i,j}(V_{i,j} - V_{i,j+1}) = 0 \end{cases} \tag{30}$$

where $\gamma_{x\to y}$ is the modified conductance of the tube linking node x to node y. With the appropriate boundary conditions (i.e., no fluxes over the lateral boundaries, no inflowing electrical flux at the upstream boundary and no outflowing electrical flux at the downstream boundary), we obtain a linear system whose unknowns are the $N_i \times N_j$ hydraulic pressure values at the nodes, the $N_i \times N_j$ electrical potential values at the nodes, the value of the electrical potential V_u in the upstream reservoir, and the value of the electrical potential V_d in the downstream reservoir. Note that all the tubes connecting two nodes have the same length l. See Appendix A for the full derivation of the system.

3.3 Pore size distribution

In this work, we investigate the effect of four different pore size distributions on streaming current generation: fractal, exponential symmetric, lognormal and double lognormal (i.e., bimodal). Note that

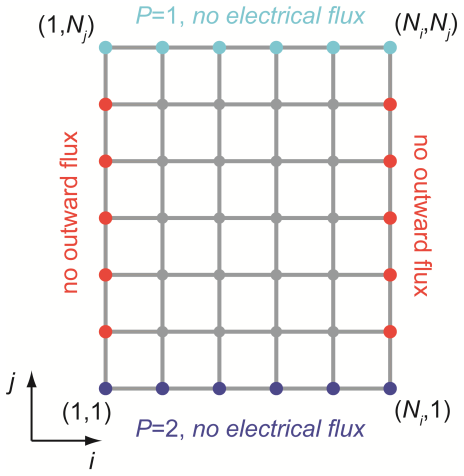

Figure 2: Scheme of the pore network organization and the boundary conditions used in our simulations. Note that all tubes have the same length l.

we first built the networks for a pore size range between 1 and 100 μm (Fig. 3), then we shifted this range towards smaller pores in order to obtain smaller permeabilities while keeping constant the ratio $\alpha = R_{max}/R_{min}$. Hence, we obtained five different permeabilities for each pore size distribution.

3.3.1 Fractal distribution

We start with a fractal pore size distribution (Fig. 3a) as many geological porous media exhibit frequency distribution skewed towards smaller pore radii (*Dullien*, 2012). It is also the pore size distribution used by *Guarracino and Jougnot* (2018) to develop their analytical model (i.e., Eq. 24).

The cumulative size distribution of pores whose radii are greater than or equal to R (m) is assumed to obey the following fractal law (*Tyler and Wheatcraft*, 1990; *Yu et al.*, 2003; *Guarracino et al.*, 2014):

$$N(R) = \left(\frac{R_{REV}}{R}\right)^D, \tag{31}$$

where D is the fractal dimension of pore size with $1 < D < 2$ and $0 < R_{min} \leq R \leq R_{max} < R_{REV}$. Differentiating (31) with respect to R we obtain the number of pores whose radii are in the infinitesimal range R to $R + dR$:

$$dN = -DR_{REV}^D R^{-D-1} dR, \tag{32}$$

where the negative sign implies that the number of pores decreases with the increase of pore radius R. In fact, the resulting distribution is a decreasing exponential in a semilogarithmic space.

3.3.2 Exponential symmetric distribution

To generate the exponential symmetric distribution (Fig. 3b), we contracted the fractal distribution over one decade, we shifted it to the range 10-100 μm, then we added the symmetric part over the range 1-10 μm to obtain the exponentially increasing part, and finally we normalized the distribution to get a cumulative distribution comprised between 0 and 1.

3.3.3 Lognormal distribution

The lognormal distribution (Fig. 3c) is so that the decimal logarithm of the radius is normally distributed, as done in *Maineult et al.* (2017). The probability P that $\log_{10}(R)$ is less than X is given

by:

$$P(\log_{10}(R) \leq X) = \frac{1}{2} + \frac{1}{2} erf\left(\frac{X - \log_{10}(R_{peak})}{s\sqrt{2}}\right), \tag{33}$$

where R_{peak} is the value of the radius associated to the peak of the distribution, and s is the standard deviation.

3.3.4 Double lognormal distribution

The double lognormal distribution (Fig. 3d) is the sum of two lognormal distributions with the same standard deviation s, and writes :

$$P(\log_{10}(R) \leq X) = \frac{1}{2} + \frac{1}{4} erf\left(\frac{X - \log_{10}(R_{peak,1})}{s_1\sqrt{2}}\right) + \frac{1}{4} erf\left(\frac{X - \log_{10}(R_{peak,2})}{s_2\sqrt{2}}\right), \tag{34}$$

where the bimodal distribution is obtained through the choice of the two peaks for the distribution $R_{peak,1}$ and $R_{peak,2}$.

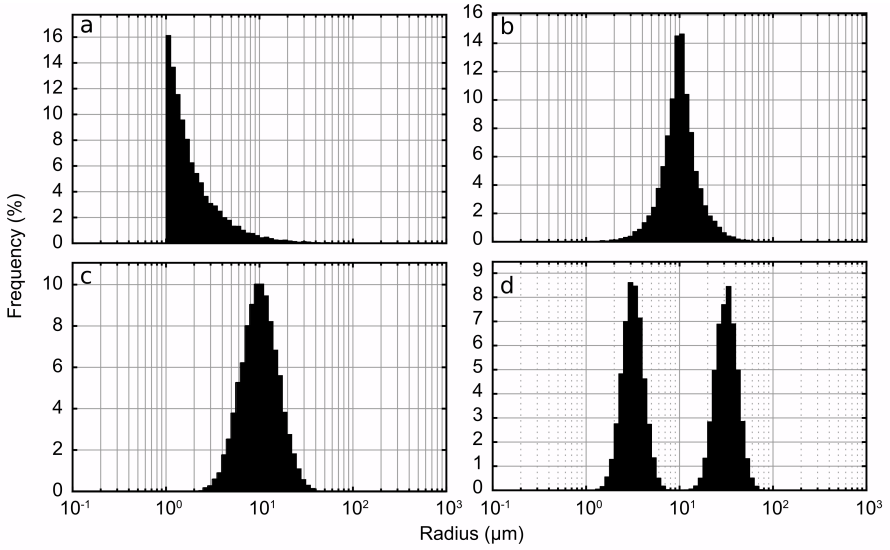

Figure 3: Pore size distributions used in this work: (a) fractal ($D = 1.5$), (b) exponential symmetric, (c) lognormal ($R_{peak} = 10\mu$m and $s = 0.45973$), and (d) double lognormal ($R_{peak,1} = 3.166\mu$m, $R_{peak,2} = 31.66\mu$m, and $s_1 = s_2 = s/2$). Note that the different permeabilities are obtained by shifting the distribution towards smaller pores but keeping constant the ratio $\alpha = R_{max}/R_{min}$.

3.4 Petrophysical parameters computation

In our numerical simulations, we impose a hydraulic pressure gradient and obtain the resulting voltage values V_u and V_d. It is then trivial to compute the corresponding electrokinetic coupling coefficient using,

$$C_{EK} = \frac{\Delta V}{\Delta P} = \frac{V_d - V_u}{P_{i,N_j} - P_{i,1}} = \frac{V_d - V_u}{2 - 1} = V_d - V_u. \tag{35}$$

Then, the effective excess charge density is obtained by modifying Eq. 3:

$$\hat{Q}_v = -\frac{\eta_w \sigma C_{EK}}{k}. \tag{36}$$

where the permeability is deduced from the pore network simulation. As we neglect the surface electrical conductivity, Eq. 36 can then be expressed by,

$$\hat{Q}_v = -\frac{\eta_w \sigma_w C_{EK}}{kF}. \tag{37}$$

where F is the formation factor, also deduced from the pore network simulation. Note that, as we neglect the surface conductivity of the medium, the formation factor is the ratio between the pore network and the pore water electrical conductivities: $F = \sigma_w/\sigma$. The computation of k/ϕ and $F\phi$ are described in Appendix B.

4 Numerical results

The simulations were run once for each given distribution (5 pore size distributions for each of the 4 types) and concentration (9 different concentrations) by solving the linear system described in the previous section; that is results for 180 pore networks with a size of 100×100. The results obtained from these simulations can be found in Appendix C. In our simulations, the temperature is fixed to 20°C. This section presents the simulation results on the effect of the pore size distributions on the two electrokinetic coupling parameters, C_{EK} and $\hat{Q}_v$, for a large range of permeabilities (from 10^{-16} to 10^{-10} m^2) and ionic concentrations (from 10^{-4} to 1 mol L^{-1}).

4.1 Influence of the pore size distribution on the permeability

The pore size distribution has a major impact on the pore network effective permeability. As one can see on Figs. 3 and 4, for a given range of capillary radius (i.e., from 1 to 100 μm), the fractal distribution contains a much higher number of thin capillaries than the exponential symmetric and the lognormal distributions. This yields a smaller effective permeability of the 2D pore network with fractal pore size distribution. By its bimodal nature, double lognormal networks (Figs. 3d) contain both larger and smaller pores than the exponential symmetric and lognormal networks (Figs. 3b and c). However, Fig. 4d shows that their random distribution yields that larger pores are isolated from each other by smaller pores, hence yielding a smaller effective permeability of the double lognormal networks.

Given the important similarity between the exponential symmetric and lognormal pore size distribution (Figs. 3b and c), it is not surprising that both networks have similar permeabilities.

The Johnson's length (*Schwartz et al.*, 1989), Λ (m), is a petrophysical parameter that has been shown to be representative of a medium permeability. *Revil and Cathles* (1999) proposes a simple model to predict the medium permeability:

$$k = \frac{\Lambda^2}{8F}. \tag{38}$$

Figures 5a and b compare the permeability resulting from the pore network simulations and the ones predicted by the model of *Revil and Cathles* (1999) (Eq. 38) using the hydraulic (Λ_h) and electrical (Λ_e) Johnson's lengths deduced from the pore network simulations (see *Bernabé and Revil*, 1995, and Appendix B), respectively. One can see that the model from *Revil and Cathles* (1999) tends to overpredict the effective permeabilities of the networks, except for the double lognormal network permeabilities predicted by Λ_h. Nevertheless, both predictions are rather good (within half an order of magnitude), showing the interest of Eq. (38) to characterize a porous medium (see also the discussions in *Maineult et al.*, 2018).

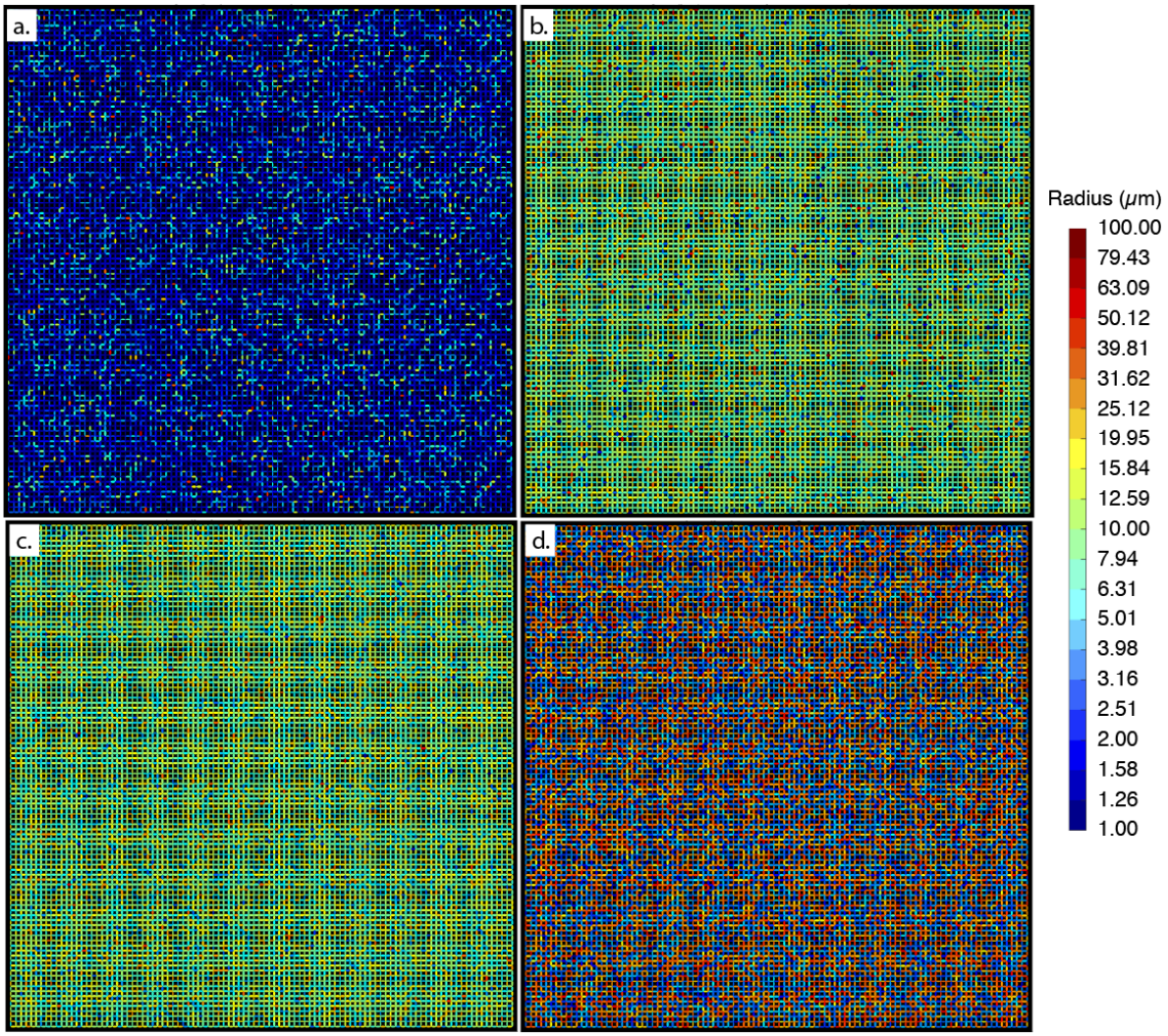

Figure 4: Examples of the pore networks used in this work: (a) fractal, (b) exponential symmetric, (c) lognormal, and (d) double lognormal (in these examples, the capillary sizes range from 1 to 100 μm). Note that the size of the networks was 100×100 nodes. See the corresponding frequency pore size distributions in Fig. 3.

4.2 Evolution of the coupling parameters with the ionic concentration and permeability

Figure 6a presents the evolution of the coupling coefficient as a function of the pore water ionic concentration. The simulation results clearly indicate that the NaCl ionic concentration drives the amplitude of the coupling coefficient, while the influence of pore size distribution is rather small (from less than 1% for 1 mol L^{-1} up to 66% for 10^{-4} mol L^{-1}). This is consistent with the Helmholtz-Smoluchowski equation (Eq. 2) that contains two parameters which are concentration dependent, the ζ-potential (Eq. 28) and the pore water electrical conductivity (Eq. 29), but none related to the medium geometrical properties.

Linde et al. (2007) proposed an empirical model depending only on the pore water ionic concentation (through its electrical conductivity) based on a large data set of coupling coefficients:

$$\log |C_{EK}| = b_1 + b_2 \log(\sigma_w) + b_3 \log(\sigma_w)^2, \tag{39}$$

where b_1 = -0.895, b_2 = -1.319, and b_3 = -0.1227. Fig. 6a shows that this empirical model matches rather well for ionic concentrations between 10^{-4} to 10^{-2} mol L^{-1}, clearly confirming that ionic concentration is the main driver.

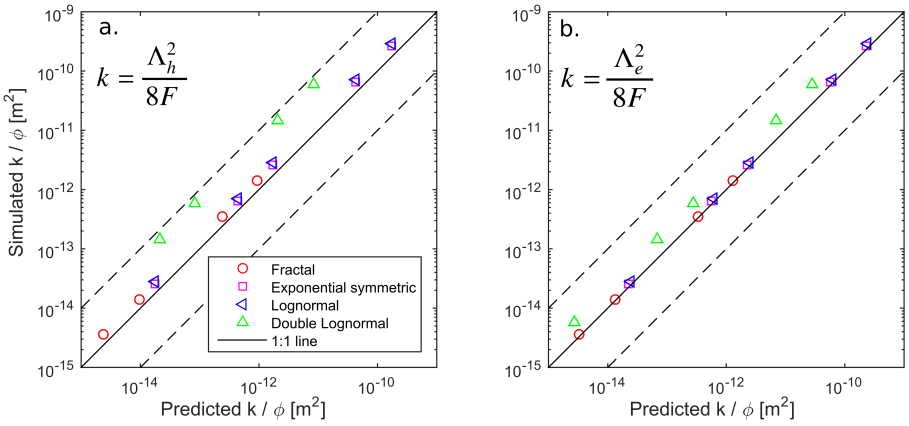

Figure 5: Comparison between the simulated permeabilities (normalized by the porosities) with the pore network model and the ones predicted by the model of *Revil and Cathles* (1999) based on the (a) hydraulic, Λ_h, and (b) electrical, Λ_e, Johnson's lengths, respectively (see definitions in Appendix B). The solid black line corresponds to the 1:1 line, while the dashed lines correspond to the one order of magnitude range.

Figures 7a and b show that the variation of C_{EK} as a function of the network permeability (hence of the network pore size distribution, see previous subsection) strongly depends on the ionic concentration. Indeed, C_{EK} diminishes importantly when permeability increases at low salinity ($C^w_{NaCl} = 10^{-4}$ mol L^{-1} in Fig. 7a), but it barely varies for higher salinity ($C^w_{NaCl} = 1$ mol L^{-1} in Fig. 7b). As for the permeabilities, C_{EK} for the exponential symmetric and lognormal networks are very similar, while the fractal distribution has a very different behaviour, probably related to the larger number of smaller pores.

Contrarily to the electrokinetic coupling coefficient, the effective excess charge density computed from Eq. (37) strongly depends both on ionic concentration and network permeability. Figures 6b and 7c show that the permeability is the most important parameter controlling the magnitude of $\hat{Q}_v$: a decrease of 4 orders of magnitude in permeability yields an increase of 4 orders of magnitude for $\hat{Q}_v$. This behaviour is consistent with experimental data and models from the literature (e.g., *Titov et al.*, 2002; *Jardani et al.*, 2007; *Jougnot et al.*, 2012). The influence of the ionic concentration on the effective excess charge density is also consistent with experimental data from the litterature: an increase of 4 orders of magnitude in the ionic concentration yields a decrease of around 1 order of magnitude for $\hat{Q}_v$ (e.g., *Pengra et al.*, 1999; *Jougnot et al.*, 2015; *Cherubini et al.*, 2018).

4.3 Testing the model of *Guarracino and Jougnot* (2018)

The dependence of the effective excess charge on both the permeability and the pore water ionic concentration is discussed in details in *Guarracino and Jougnot* (2018) and taken into account in their model (Eq. 24). Figures 6b and 7c show the very good agreement between the $\hat{Q}_v$ obtained from the network simulations and the one predicted by the *Guarracino and Jougnot* (2018)'s model as a function of the ionic concentration and permeability, respectively. All the parameters needed for the model (Eq. 24) are either input parameters (C^w, thus ζ and l_D, from Eqs. 28 and 18, respectively) or calculated outputs from the simulations (k/ϕ, from Eq. 63). Following the proposition of *Guarracino*

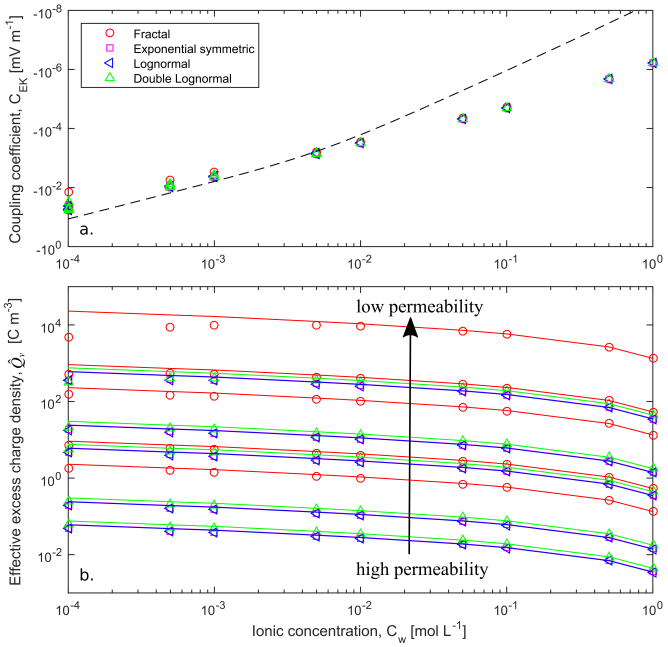

Figure 6: Simulation results presented as (a) electrokinetic coupling coefficient and (b) effective excess charge density as a function of the ionic concentrations for the different pore size distributions. In the (a) subplot, the dashed black line corresponds to the empirical relationship proposed by *Linde et al.* (2007) (Eq. 39). In the (b) subplot, the solid lines in colors correspond to the model predictions of *Guarracino and Jougnot* (2018) (Eq. 24).

and Jougnot (2018), we use the *Winsauer et al.* (1952) model to determine the hydraulic tortuosity from:

$$\tau = \sqrt{F\phi}. \tag{40}$$

Therefore, none of the parameters were fitted in order to obtain these predictions in very good agreement with the computations from our numerical simulations. Note that the *Jardani et al.* (2007)'s model corresponds fairly well to an average trend, regardless the network and the ionic concentration.

Figure 8 represents the same data (i.e., for all networks and ionic concentrations) along a 1:1 line. One can notice that the model slightly overpredicts the numerical effective excess charge for very high $\hat{Q}_v$, that is for low permeability and low ionic concentration. This can be explained by the model limitation: the capillary radius has to be significantly larger than the Debye length $R \gg 5l_D$.

4.4 Limitation of the model *Guarracino and Jougnot* (2018) in small pores at low ionic concentration

In this subsection, we investigate why the largest misfits are obtained for the highest values of effective excess charge, that is, for the lowest ionic concentrations (i.e., thickest diffuse layers) and for the lowest permeabilities (i.e., smallest pore sizes). In Fig. 8, one can see that it is especially the case for the fractal distribution, where the amount of small pores is larger than in the other distributions (see Fig. 3).

Therefore, we consider the smallest investigated capillaries ($R = 0.1\mu$m) filled by a pore water containing the lowest ionic concentration of NaCl, $C^w_{NaCl} = 10^{-4}$ mol L^{-1} (i.e., $l_D = 3.04 \times 10^{-8}$ m, hence $R = 3.29l_D < 4l_D$), i.e., the most extreme case for the present study. Then, we use the numerical code of *Leroy and Maineult* (2018) to solve for the Poisson-Boltzmann equation in an infinite charged cylinder and the ζ-potential is $\zeta = -89.8$ mV following *Jaafar et al.* (2009) (Eq. 28).

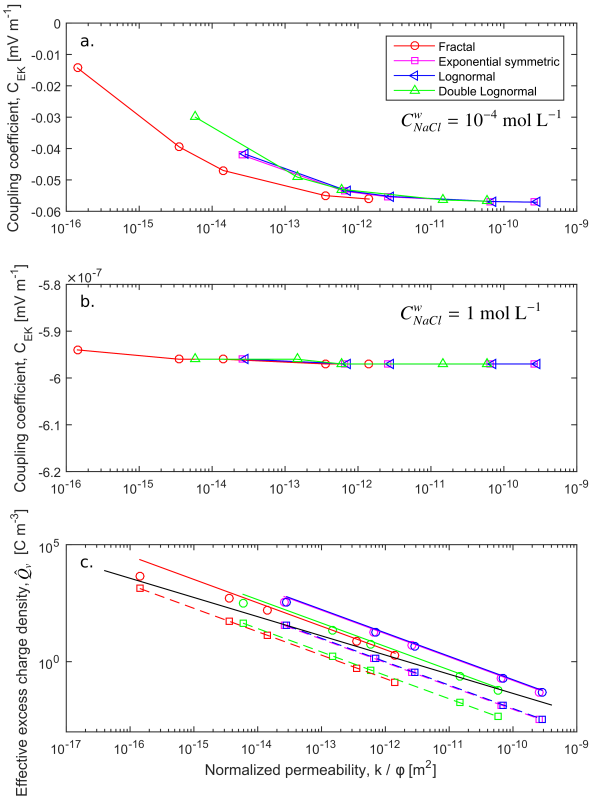

Figure 7: Electrokinetic coupling coefficient as a function of the permeability normalized by the porosity for (a) $C_w = 10^{-4}$ mol L^{-1} and (b) $C_w = 1$ mol L^{-1} from our numerical simulation. (c) Effective excess charge density as a function of the permeability normalized by the porosity for the different pore size distributions for $C_w = 10^{-4}$ and 1 mol L^{-1}. Note that each point corresponds to the simulation result for a given network. On the (c) subplot, the solid and dashed colored lines correspond to the model predictions of *Guarracino and Jougnot* (2018) (Eq. 24) for $C_w = 10^{-4}$ mol L^{-1} and $C_w = 1$ mol L^{-1}, respectively; while the single black solid line is the prediction from *Jardani et al.* (2007) with a fixed porosity $\phi = 0.4$.

Figures 9 and 10 illustrate the limitation of the Debye-Hückel approximation used by *Guarracino and Jougnot* (2018) by comparing its results to the Poisson-Boltzmann numerical resolution using *Leroy and Maineult* (2018).

Figure 9a compares the local electrical potential calculated with the Debye-Hückel approximation (Eq. 17) and the general Poisson-Boltzmann (Eq. 12), while Figure 9b displays the corresponding residual potential. Given that $R < 4l_D$, one can see that $\psi \neq 0$ mV in the middle of the pore, this implies that the EDL overlap (e.g., *Gonçalvès et al.*, 2007). The effect on the local electrical potential is substantial: the residual is close to 50% at the center of the pore. This has a significant effect on the distribution of the ions as shown in Figs. 9c and d. For $R = 0.1\mu$m and $C^w_{NaCl} = 10^{-4}$ mol L^{-1}, one can see that there is no free electrolyte, therefore the local ionic concentrations are different from the bulk water concentrations $C_{Na} \gg C^w_{Na}$ and $C_{Cl} \ll C^w_{Cl}$ in the entire capillary. Consequently, the distribution of the excess charge density $\bar{Q}_v$ calculated from Eq. 19 in a small capillary for low concentrations is strongly affected by the Debye-Hückel approximation (Fig. 10b and c). This example on the most extreme case used in the previous simulation clearly demonstrates why the model of *Guarracino and Jougnot* (2018) cannot correctly predict the effective excess charge density in pores such as $R < 5l_D$, that is when the thin double layer assumption is not respected.

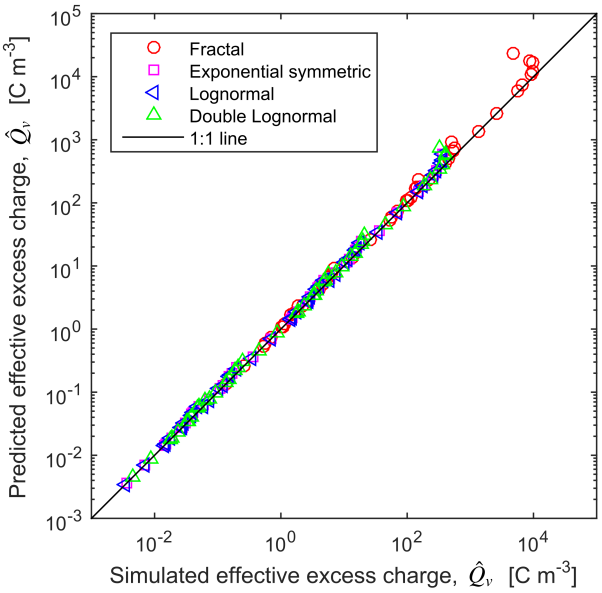

Figure 8: Comparison between the simulated effective excess charge density with the pore network model and the one predicted by the analytical model of *Guarracino and Jougnot* (2018). The solid black line corresponds to the 1:1 line.

5 Discussion and conclusion

In the present paper, we present numerical simulations of streaming current generation in water saturated 2D pore networks with different pore size distributions, hence different permeabilities (from 10^{-16} to 10^{-10} m^2). We performed the simulations to obtain the electrokinetic coupling coefficients for pore water having a NaCl concentrations ranging from 10^{-4} to 1 mol L^{-1}. From these simulations we deduced the effective excess charge density from the corresponding coupling coefficient and performed a detailed analysis of the behaviour of these two electrokinetic coupling parameters.

Our first finding is that the pore size distribution has a primary influence on the medium's permeability (Fig. 5) as expected from the literature, but almost no influence on the electrokinetic coupling coefficient (Figs. 6a and 7b). This is consistent with the widely used model of Helmholtz-Smoluchowski (Eq. 2) which does not include any information nor parameters about the medium's texture and has been proven to be useful in a large range of natural geological media (as long as the surface conductivity can be neglected). It is therefore clear that the pore water chemistry is the main driver for the C_{EK} as proposed by the empirical model of *Linde et al.* (2007).

On the contrary, the pore size distribution has a strong influence on the effective excess charge density through the permeability, as it was expected from both empirical (e.g., *Titov et al.*, 2002; *Jardani et al.*, 2007; *Cherubini et al.*, 2018) and theoretical evidence (e.g., *Jougnot et al.*, 2012; *Guarracino and Jougnot*, 2018). When considering Eq. 3 and Eq. 24 (*Guarracino and Jougnot*, 2018), it is clear that the permeability simplifies out in the electrokinetic coupling coefficient C_{EK}. One can also note that the analytical model of *Guarracino and Jougnot* (2018), originally defined for fractal media, performs well for any kind of pore size distribution (even double porosity ones) given that this information is included in the model through the medium's permeability and porosity that appear explicitely.

Nevertheless, the observations from the previous paragraphs are not valid for very small pores filled by pore water with a low ionic concentration, that is $C^w < 10^{-3}$ mol L^{-1} (Figs. 6a and 7a). Indeed, when the salinity decreases and if the medium has small pores (Fig. 7a), C_{EK} becomes highly dependent on the permeability. This behaviour is consistent with the previous work of *Bernabé* (1998) on pore networks, but also with the experimental results of *Jouniaux and Pozzi* (1995b) (using

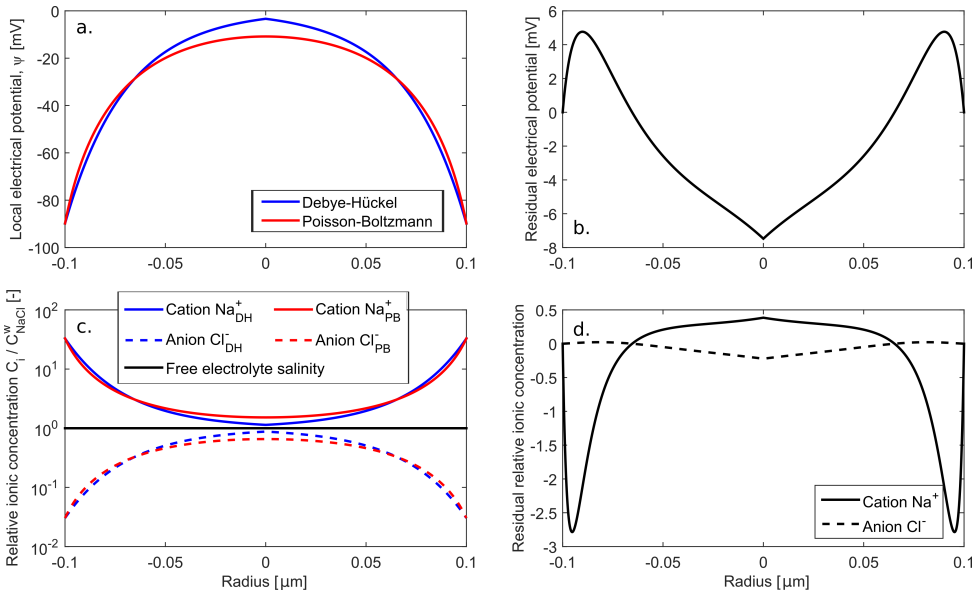

Figure 9: Comparison between the Debye-Hückel approximation and the Poisson-Boltzmann equation to compute (a) the electrical potential distribution and (c) the ionic species relative concentration distribution in a small capillary ($R = 10^{-7}$ m) containing a NaCl electrolyte with $C^w_{NaCl} = 10^{-4}$ mol L^{-1} (i.e., $l_D = 3.04 \times 10^{-8}$ m). (b) and (d) show the corresponding residual electrical potential and relative ionic concentration, respectively. Note that the x-axis is a modified coordinate $r' = R - r$ such as $r' = 0$ m in the middle of the capillary.

a very resistive water). This effect is directly related to the EDL in the pore space: when l_D becomes important in comparison to the pore radius ($R < 4l_D$), the diffuse layers from both sides of the capillary start to overlap, yielding a strong effect on the amount of excess charge that can be dragged by the water flow (e.g. Figs. 9 and 10). Such effect also impacts the performance of the model of *Guarracino and Jougnot* (2018) to reproduce the simulated effective excess charge densities (Fig. 8).

In geological media and under most environmental conditions (i.e. groundwater for human consumption or subsurface reservoirs), 10^{-4} mol L^{-1} represents an extreme case scenario (e.g., *McCleskey*, 2011). Indeed, ionic strengths (i.e., a proxy for ionic concentration) in potable water typically vary between 10^{-3} and 10^{-2} mol L^{-1}, while reservoirs can be saturated with brines having much higher ionic concentrations depending on the formation. Therefore, the assumption of $R \gg 4l_D$ can be considered valid in most natural systems, which allows the use of the model recently proposed by *Guarracino and Jougnot* (2018) (valid for $R > 5l_D$).

In addition to the intrinsic limitation of the model proposed by *Guarracino and Jougnot* (2018), the fact that we neglect the surface conductivity in Eq. 37 even for the lowest ionic concentration and smaller pores can also contribute to the misfit. Further developments of the present 2D pore network code should also include an explicit calculation of the surface conductivity for the determination of the effective excess charge density. This would open the possibility of studying the behaviour of micro-porous media such as clay rocks. Additional improvements on our pore network modeling approach could also allow further studies, among which: relating pore lengths to pore sizes to mimic more natural observations (e.g., small pore sizes are usually related to small pore length), considering connectivities higher than 4 for each nodes. Nevertheless, despite all these limitations, the two approaches that we consider here converge towards similar predictions, and this is remarkable, since they are totally independent. Further works will require the overcoming of these limitations, and also to implement 3D network, in order to produce synthetic media closer to real ones. A more advance approach would be extracting pore networks that replicates the pore space obtain from rock sample imagery (e.g., *Bryant and Blunt*, 1992) to solve for the electrokinetic coupling.

We believe that the present study will help to better understand the theoretical links between the

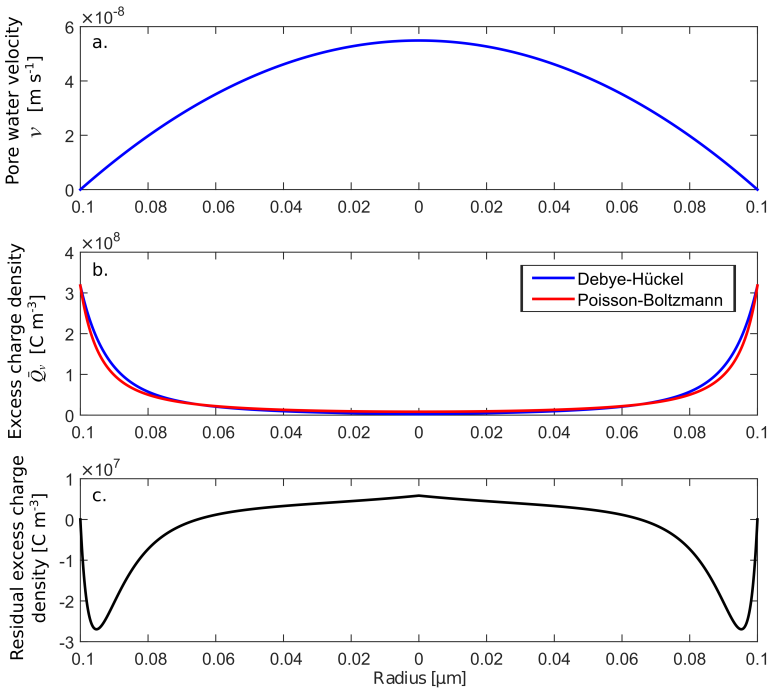

Figure 10: (a) Distribution of the pore water velocity in a small capillary ($R = 10^{-7}$ m) following Poiseuille's law. (b) Comparison of the excess charge density distribution obtained from the Debye-Hückel approximation and the numerical Poisson-Boltzmann resolution in the same capillary ($R = 10^{-7}$ m) containing a NaCl electrolyte with $C^w_{NaCl} = 10^{-4}$ mol L^{-1} (i.e., $l_D = 3.04 \times 10^{-8}$m), and (c) the corresponding residual. Note that the x-axis is a modified coordinate $r' = R - r$ such as $r' = 0$ m in the middle of the capillary.

electrokinetic coupling coefficient and the effective excess charge approaches, providing a mechanistic study of the streaming potential generation under water saturated conditions. In the future, we will try to extend this approach and the corresponding study for partially saturated conditions (see *Jougnot et al.*, 2012; *Soldi et al.*, 2019).

Appendix A: Pressure and electrical potential equations in the pore network

Inside the network, that is for the indexes $(i,j) \in [2, N_i - 1] \times [2, N_j - 1]$, Eq. 30 is rewritten as,

$$\left\{ \begin{array}{l} \gamma^h_{i-1,j\to i,j} P_{i-1,j} + \gamma^h_{i+1,j\to i,j} P_{i+1,j} - \kappa^h_{i,j} P_{i,j} + \gamma^h_{i,j-1\to i,j} P_{i,j-1} + \gamma^h_{i,j+1\to i,j} P_{i,j+1} \\ \quad -\gamma^c_{i-1,j\to i,j} V_{i-1,j} - \gamma^c_{i+1,j\to i,j} V_{i+1,j} + \kappa^c_{i,j} V_{i,j} - \gamma^c_{i,j-1\to i,j} V_{i,j-1} - \gamma^c_{i,j+1\to i,j} V_{i,j+1} = 0 \\ -\gamma^c_{i-1,j\to i,j} P_{i-1,j} - \gamma^c_{i+1,j\to i,j} P_{i+1,j} + \kappa^c_{i,j} P_{i,j} - \gamma^c_{i,j-1\to i,j} P_{i,j-1} - \gamma^c_{i,j+1\to i,j} P_{i,j+1} \\ \quad +\gamma^e_{i-1,j\to i,j} V_{i-1,j} + \gamma^e_{i+1,j\to i,j} V_{i+1,j} - \kappa^e_{i,j} V_{i,j} + \gamma^e_{i,j-1\to i,j} V_{i,j-1} + \gamma^e_{i,j+1\to i,j} V_{i,j+1} = 0 \end{array} \right. \tag{41}$$

with,

$$\left\{ \begin{array}{l} \kappa^h_{i,j} = \left(\gamma^h_{i-1,j\to i,j} + \gamma^h_{i+1,j\to i,j} + \gamma^h_{i,j-1\to i,j} + \gamma^h_{i,j+1\to i,j}\right) \\ \kappa^c_{i,j} = \left(\gamma^c_{i-1,j\to i,j} + \gamma^c_{i+1,j\to i,j} + \gamma^c_{i,j-1\to i,j} + \gamma^c_{i,j+1\to i,j}\right) \\ \kappa^e_{i,j} = \left(\gamma^e_{i-1,j\to i,j} + \gamma^e_{i+1,j\to i,j} + \gamma^e_{i,j-1\to i,j} + \gamma^e_{i,j+1\to i,j}\right) \end{array} \right. \tag{42}$$

in $i = 1$ (no outward current) and $j \in [2, N_j - 1]$, we have

$$\left\{ \begin{array}{l} \gamma^h_{2,j\to 1,j} P_{2,j} - \kappa^h_{1,j} P_{1,j} + \gamma^h_{1,j-1\to 1,j} P_{1,j-1} + \gamma^h_{1,j+1\to 1,j} P_{1,j+1} \\ \quad -\gamma^c_{2,j\to 1,j} V_{2,j} + \kappa^c_{1,j} V_{1,j} - \gamma^c_{1,j-1\to 1,j} V_{1,j-1} + \gamma^c_{1,j+1\to 1,j} V_{1,j+1} = 0 \\ -\gamma^c_{2,j\to 1,j} P_{2,j} + \kappa^c_{1,j} P_{1,j} - \gamma^c_{1,j-1\to 1,j} P_{1,j-1} - \gamma^c_{1,j+1\to 1,j} P_{1,j+1} \\ \quad +\gamma^e_{2,j\to 1,j} V_{2,j} - \kappa^e_{1,j} V_{1,j} - \gamma^e_{1,j-1\to 1,j} V_{1,j-1} + \gamma^e_{1,j+1\to 1,j} V_{1,j+1} = 0 \end{array} \right. \tag{43}$$

with

$$\left\{ \begin{array}{l} \kappa^h_{1,j} = \left(\gamma^h_{2,j\to 1,j} + \gamma^h_{1,j-1\to 1,j} + \gamma^h_{1,j+1\to 1,j}\right) \\ \kappa^c_{1,j} = \left(\gamma^c_{2,j\to 1,j} + \gamma^c_{1,j-1\to 1,j} + \gamma^c_{1,j+1\to 1,j}\right) \\ \kappa^e_{1,j} = \left(\gamma^e_{2,j\to 1,j} + \gamma^e_{1,j-1\to 1,j} + \gamma^e_{1,j+1\to 1,j}\right) \end{array} \right. \tag{44}$$

in $i = N_i$ (no outward current) and $j \in [2, N_j - 1]$, we have

$$\left\{ \begin{array}{l} \gamma^h_{N_i-1,j\to N_i,j} P_{N_i-1,j} - \kappa^h_{N_i,j} P_{N_i,j} + \gamma^h_{N_i,j-1\to N_i,j} P_{N_i,j-1} + \gamma^h_{N_i,j+1\to N_i,j} P_{N_i,j+1} \\ \quad -\gamma^c_{N_i-1,j\to N_i,j} V_{N_i-1,j} + \kappa^c_{N_i,j} V_{N_i,j} - \gamma^c_{N_i,j-1\to N_i,j} V_{N_i,j-1} + \gamma^c_{N_i,j+1\to N_i,j} V_{N_i,j+1} = 0 \\ -\gamma^c_{N_i-1,j\to N_i,j} P_{N_i-1,j} + \kappa^c_{N_i,j} P_{N_i,j} - \gamma^c_{N_i,j-1\to N_i,j} P_{N_i,j-1} - \gamma^c_{N_i,j+1\to N_i,j} P_{N_i,j+1} \\ \quad +\gamma^e_{N_i-1,j\to N_i,j} V_{N_i-1,j} - \kappa^e_{N_i,j} V_{N_i,j} - \gamma^e_{N_i,j-1\to N_i,j} V_{N_i,j-1} + \gamma^e_{N_i,j+1\to N_i,j} V_{N_i,j+1} = 0 \end{array} \right. \tag{45}$$

with

$$\left\{ \begin{array}{l} \kappa^h_{N_i,j} = \left(\gamma^h_{N_i-1,j\to N_i,j} + \gamma^h_{N_i,j-1\to N_i,j} + \gamma^h_{N_i,j+1\to N_i,j}\right) \\ \kappa^c_{N_i,j} = \left(\gamma^c_{N_i-1,j\to N_i,j} + \gamma^c_{N_i,j-1\to N_i,j} + \gamma^c_{N_i,j+1\to N_i,j}\right) \\ \kappa^e_{N_i,j} = \left(\gamma^e_{N_i-1,j\to N_i,j} + \gamma^e_{N_i-1,j-1\to N_i-1,j} + \gamma^e_{N_i-1,j+1\to N_i-1,j}\right) \end{array} \right. . \tag{46}$$

In $j = 1$, the following conditions are imposed for the hydraulic pressure and electrical potential:

$$\left\{ \begin{array}{l} P_{i,1} = 2 \\ V_{i,1} = V_u \end{array} \right. , \tag{47}$$

There is no inflowing electrical current, that is:

$$\sum_{i=1}^{N_i} J_{i,1\to i,2} l = \sum_{i=1}^{N_i} \left(\gamma^c_{i,1\to i,2} \left(P_{i,2} - P_{i,1}\right) - \gamma^e_{i,1\to i,2} \left(V_{i,2} - V_{i,1}\right)\right) = 0, \tag{48}$$

which yields:

$$-\sum_{i=1}^{N_i}\gamma^c_{i,1\to i,2}P_{i,1}+\left(\sum_{i=1}^{N_i}\gamma^e_{i,1\to i,2}\right)V_u+\sum_{i=1}^{N_i}\gamma^c_{i,1\to i,2}P_{i,2}-\sum_{i=1}^{N_i}\gamma^e_{i,1\to i,2}V_{i,2}=0. \tag{49}$$

Finally, in $j=N_j$, the conditions are:

$$\begin{cases} P_{i,N_j}=1 \\ V_{i,N_j}=V_d \end{cases}, \tag{50}$$

There is no outflowing electrical current, that is:

$$\sum_{i=1}^{N_i}J_{i,N_j-1\to i,N_j}l=\sum_{i=1}^{N_i}\left(\gamma^c_{i,N_j-1\to i,N_j}\left(P_{i,N_j}-P_{i,N_j-1}\right)-\gamma^e_{i,N_j-1\to i,N_j}\left(V_{i,N_j}-V_{i,N_j-1}\right)\right)=0, \tag{51}$$

which yields:

$$-\sum_{i=1}^{N_i}\gamma^c_{i,N_j-1\to i,N_j}P_{i,N_j-1}+\left(\sum_{i=1}^{N_i}\gamma^e_{i,N_j-1\to i,N_j}\right)V_{i,N_j-1}+\sum_{i=1}^{N_i}\gamma^c_{i,N_j-1\to i,N_j}P_{i,N_j}-\sum_{i=1}^{N_i}\gamma^e_{i,N_j-1\to i,N_j}V_d=0. \tag{52}$$

The set of equations described above (Eqs. 41-47, 49-50, 52) forms a linear system. The unknowns are the hydraulic pressure, $P_{i,j}$, and the electrical potential, $V_{i,j}$, at all nodes and the two boundary electrical potentials V_u and V_d.

Appendix B: Numerical determination of the pore network permeability, formation factor, and Johnson's lengths

For a laminar flow, i.e. following Poiseuille's law, the hydraulic flux $F_{x\to y}$ through a capillary linking two nodes x and y writes:

$$F_{x\to y} = \frac{\pi R_{x\to y}^4}{8\eta_w}\frac{P_x - P_y}{l} = g_{x\to y}^h \left(P_x - P_y\right). \tag{53}$$

The length of the capillary, l, is eliminated by introducing a modified hydraulic flux defined as:

$$\Phi_{x\to y}^h = F_{x\to y} l = \frac{\pi R_{x\to y}^4}{8\eta_w}\left(P_x - P_y\right) = \gamma_{x\to y}^h \left(P_x - P_y\right). \tag{54}$$

Neglecting the surface electrical conductivity, the electrical flux $J_{x\to y}$ corresponds to:

$$J_{x\to y} = \sigma_w \pi R_{x\to y}^2 \frac{V_x - V_y}{l} = g_{x\to y}^e \left(V_x - V_y\right). \tag{55}$$

The length of the capillary, l, is eliminated by introducing a modified electrical flux defined as:

$$\Phi_{x\to y}^e = \frac{J_{x\to y} l}{\sigma_w} = \pi R_{x\to y}^2 \left(V_x - V_y\right) = \gamma_{x\to y}^e \left(V_x - V_y\right). \tag{56}$$

At any node in the square network, *Kirchhoff* (1845)'s law yields

$$Z_{i,j-1\to i,j} + Z_{i-1,j\to i,j} + Z_{i+1,j\to i,j} + Z_{i,j+1\to i,j} = 0. \tag{57}$$

with Z standing for F or J, respectively. Eq. 53 or 55, leads to

$$\begin{array}{c} a_{i,j-1\to i,j} X_{i,j-1} + a_{i-1,j\to i,j} X_{i-1,j} - \left(a_{i,j-1\to i,j} + a_{i-1,j\to i,j} + a_{i+1,i\to i,j} + a_{i,j+1\to i,j}\right) \\ + a_{i+1,j\to i,j} X_{i+1,j} + a_{i,j+1\to i,j} X_{i,j+1} = 0. \end{array} \tag{58}$$

with $a = R^4$ and $X = P$ or $a = R^2$ and $X = V$ for the hydraulic or the electrical case, respectively.

For the nodes at the border of the network, Eq. 58 is easily modified to take into account the boundary conditions (i.e., no outward flow for $i = 1$ and $i = N_i$, $P = 1$ or $V = 1$ for $j = 1$, and $P = 0$ or $V = 0$ for $j = N_j$).

A linear system is obtained; the $N_i N_j$ unknowns are the hydraulic pressure or electrical potential at the nodes of the network. Once the system is solved, the modified fluxes can be computed using Eqs. 54 or 56.

The effective permeability of the pore network k (m^2) is then computed using Darcy's law:

$$k = \frac{\eta_w Q L}{S \mid \Delta P \mid} = \frac{\eta_w}{l^2}\frac{N_j - 1}{N_i - 1}\frac{\Phi_{\sum out/in}^h}{\mid \Delta P \mid}, \tag{59}$$

where Q is the hydraulic flux, L the length of the network along the flux direction (i.e., the j-direction), S the transversal section, and the total out-flowing and in-flowing fluxes are given by:

$$\left\{ \begin{array}{l} \Phi_{\sum out}^h = \sum_{i=1}^{N_i - 1} \Phi_{i,N_j-1\to i,N_j}^h \\ \Phi_{\sum in}^h = \sum_{i=1}^{N_i - 1} \Phi_{i,1\to i,2}^h \end{array} \right. \tag{60}$$

In order to estimate the section and porosity of the network, we extend the 2D network into a virtual 3D one by adding two vertical capillaries of length $l/2$ at each node, but not contributing to the transport. This yields:

$$S = \left(N_i - 1\right) l^2 \tag{61}$$

$$\phi = \frac{\left(\left(N_i - 1\right) N_j + \left(N_j - 1\right) N_i + N_i N_j\right) \pi \langle R^2 \rangle l}{\left(N_i - 1\right) \left(N_j - 1\right) l^3} \tag{62}$$

Extracting l^2 from Eq. 62 and given that $\mid \Delta P \mid = 1$, the effective permeability can be determined by:

$$\frac{k}{\phi} = \frac{\eta_w}{\pi \langle R^2 \rangle} \frac{\left(N_j - 1\right)^2}{\left(N_i - 1\right) N_j + \left(N_j - 1\right) N_i + N_i N_j} \Phi^h_{\sum out/in}. \tag{63}$$

Given that the surface conductivity can be neglected, the formation factor F of the network can be computed by:

$$\frac{1}{F} = \frac{\sigma}{\sigma_w} = \frac{1}{\sigma_w} \frac{JL}{S \mid \Delta V \mid} = \frac{1}{l^2} \frac{N_j - 1}{N_i - 1} \frac{\Phi^e_{\sum out/in}}{\mid \Delta V \mid}. \tag{64}$$

Then, considering that $\mid \Delta V \mid = 1$, the formation factor is then defined by:

$$\frac{1}{F\phi} = \frac{1}{\pi \langle R^2 \rangle} \frac{\left(N_j - 1\right)^2}{\left(N_i - 1\right) N_j + \left(N_j - 1\right) N_i + N_i N_j} \Phi^e_{\sum out/in}. \tag{65}$$

The Johnson's length, Λ (m), is a petrophysical parameter proposed by *Schwartz et al.* (1989) that quantifies a representative length of a porous medium. Following *Bernabé and Revil* (1995), we computed two Johnson's lengths for each of our networks:

$$\Lambda_h = \frac{\sum_{i=1}^{N_t} R_i^2 |\Delta P_i|^2}{\sum_{i=1}^{N_t} R_i |\Delta P_i|}. \tag{66}$$

and

$$\Lambda_e = \frac{\sum_{i=1}^{N_t} R_i^2 |\Delta V_i|^2}{\sum_{i=1}^{N_t} R_i |\Delta V_i|}. \tag{67}$$

where N_t is the total number of nodes and ΔP_i (resp. ΔV_i) is the gradient of hydraulic pressure (resp. electrical potential) between the two ends of capillary I (of radius R_i). By definition, the hydraulic and electrical Johnson's lengths are based on the hydraulic (Eq. 66) and the electrical potentials (Eq. 67), respectively. These two lengths are expected to have close values.

Appendix C: Simulation results

This table regroups all the numerical results from the simulation of the present study for the different types of pore size distributions: fractal (Fract.), exponential symmetric (Exp. Sym.), lognormal (Log.), and double lognormal (Dbl. Log.).

Type	R range (μm)	C^w_{NaCl} (mol/L)	C_{EK} (mV/m)	k/phi (mD)	$F \times phi$ (-)	σ_w (S/m)	$\hat{Q}_v$ (C/m^3)	Λ_h (μm)	Λ_e (μm)
Fract.	0.1-10	0.0001	-140.6379	1.44E-01	23.51	1.09E-03	4.674E+03	0.1337	0.1567
Fract.	0.1-10	0.0005	-52.6636	1.44E-01	23.51	5.42E-03	8.708E+03	0.1337	0.1567
Fract.	0.1-10	0.001	-29.6833	1.44E-01	23.51	1.08E-02	9.781E+03	0.1337	0.1567
Fract.	0.1-10	0.005	-6.1136	1.44E-01	23.51	5.32E-02	9.914E+03	0.1337	0.1567
Fract.	0.1-10	0.01	-2.8766	1.44E-01	23.51	1.05E-01	9.219E+03	0.1337	0.1567
Fract.	0.1-10	0.05	-0.4461	1.44E-01	23.51	4.99E-01	6.789E+03	0.1337	0.1567
Fract.	0.1-10	0.1	-0.1902	1.44E-01	23.51	9.61E-01	5.575E+03	0.1337	0.1567
Fract.	0.1-10	0.5	-0.0209	1.44E-01	23.51	4.12E+00	2.626E+03	0.1337	0.1567
Fract.	0.1-10	1	-0.0058	1.44E-01	23.51	7.49E+00	1.331E+03	0.1337	0.1567
Fract.	0.5-50	0.0001	-387.0505	3.60E+00	23.51	1.09E-03	5.146E+02	0.6687	0.7836
Fract.	0.5-50	0.0005	-82.9874	3.60E+00	23.51	5.42E-03	5.489E+02	0.6687	0.7836
Fract.	0.5-50	0.001	-40.1124	3.60E+00	23.51	1.08E-02	5.287E+02	0.6687	0.7836
Fract.	0.5-50	0.005	-6.7928	3.60E+00	23.51	5.32E-02	4.406E+02	0.6687	0.7836
Fract.	0.5-50	0.01	-3.0721	3.60E+00	23.51	1.05E-01	3.938E+02	0.6687	0.7836
Fract.	0.5-50	0.05	-0.4560	3.60E+00	23.51	4.99E-01	2.776E+02	0.6687	0.7836
Fract.	0.5-50	0.1	-0.1929	3.60E+00	23.51	9.61E-01	2.261E+02	0.6687	0.7836
Fract.	0.5-50	0.5	-0.0210	3.60E+00	23.51	4.12E+00	1.056E+02	0.6687	0.7836
Fract.	0.5-50	1	-0.0058	3.60E+00	23.51	7.49E+00	5.344E+01	0.6687	0.7836
Fract.	1-100	0.0001	-461.1766	1.44E+01	23.51	1.09E-03	1.532E+02	1.3374	1.5672
Fract.	1-100	0.0005	-88.5209	1.44E+01	23.51	5.42E-03	1.463E+02	1.3374	1.5672
Fract.	1-100	0.001	-41.7734	1.44E+01	23.51	1.08E-02	1.376E+02	1.3374	1.5672
Fract.	1-100	0.005	-6.8843	1.44E+01	23.51	5.32E-02	1.116E+02	1.3374	1.5672
Fract.	1-100	0.01	-3.0976	1.44E+01	23.51	1.05E-01	9.925E+01	1.3374	1.5672
Fract.	1-100	0.05	-0.4573	1.44E+01	23.51	4.99E-01	6.958E+01	1.3374	1.5672
Fract.	1-100	0.1	-0.1932	1.44E+01	23.51	9.61E-01	5.662E+01	1.3374	1.5672
Fract.	1-100	0.5	-0.0210	1.44E+01	23.51	4.12E+00	2.640E+01	1.3374	1.5672
Fract.	1-100	1	-0.0059	1.44E+01	23.51	7.49E+00	1.336E+01	1.3374	1.5672
Fract.	5-500	0.0001	-539.0909	3.60E+02	23.51	1.09E-03	7.167E+00	6.6872	7.8362
Fract.	5-500	0.0005	-93.3707	3.60E+02	23.51	5.42E-03	6.176E+00	6.6872	7.8362
Fract.	5-500	0.001	-43.1767	3.60E+02	23.51	1.08E-02	5.691E+00	6.6872	7.8362
Fract.	5-500	0.005	-6.9587	3.60E+02	23.51	5.32E-02	4.514E+00	6.6872	7.8362
Fract.	5-500	0.01	-3.1182	3.60E+02	23.51	1.05E-01	3.997E+00	6.6872	7.8362
Fract.	5-500	0.05	-0.4583	3.60E+02	23.51	4.99E-01	2.790E+00	6.6872	7.8362
Fract.	5-500	0.1	-0.1935	3.60E+02	23.51	9.61E-01	2.269E+00	6.6872	7.8362
Fract.	5-500	0.5	-0.0210	3.60E+02	23.51	4.12E+00	1.057E+00	6.6872	7.8362
Fract.	5-500	1	-0.0059	3.60E+02	23.51	7.49E+00	5.348E-01	6.6872	7.8362
Fract.	10-1000	0.0001	-550.3921	1.44E+03	23.51	1.09E-03	1.829E+00	13.3744	15.6723
Fract.	10-1000	0.0005	-94.0061	1.44E+03	23.51	5.42E-03	1.554E+00	13.3744	15.6723
Fract.	10-1000	0.001	-43.3571	1.44E+03	23.51	1.08E-02	1.429E+00	13.3744	15.6723
Fract.	10-1000	0.005	-6.9680	1.44E+03	23.51	5.32E-02	1.130E+00	13.3744	15.6723
Fract.	10-1000	0.01	-3.1208	1.44E+03	23.51	1.05E-01	1.000E+00	13.3744	15.6723
Fract.	10-1000	0.05	-0.4584	1.44E+03	23.51	4.99E-01	6.977E-01	13.3744	15.6723
Fract.	10-1000	0.1	-0.1935	1.44E+03	23.51	9.61E-01	5.672E-01	13.3744	15.6723
Fract.	10-1000	0.5	-0.0210	1.44E+03	23.51	4.12E+00	2.642E-01	13.3744	15.6723
Fract.	10-1000	1	-0.0059	1.44E+03	23.51	7.49E+00	1.337E-01	13.3744	15.6723
Exp. Sym.	0.1-10	0.0001	-413.1205	2.62E+01	4.88	1.09E-03	3.636E+02	0.8264	0.9395

Exp. Sym.	0.1-10	0.0005	-85.0421	2.62E+01	4.88	5.42E-03	3.724E+02	0.8264	0.9395
Exp. Sym.	0.1-10	0.001	-40.7362	2.62E+01	4.88	1.08E-02	3.555E+02	0.8264	0.9395
Exp. Sym.	0.1-10	0.005	-6.8276	2.62E+01	4.88	5.32E-02	2.932E+02	0.8264	0.9395
Exp. Sym.	0.1-10	0.01	-3.0818	2.62E+01	4.88	1.05E-01	2.615E+02	0.8264	0.9395
Exp. Sym.	0.1-10	0.05	-0.4565	2.62E+01	4.88	4.99E-01	1.840E+02	0.8264	0.9395
Exp. Sym.	0.1-10	0.1	-0.1930	2.62E+01	4.88	9.61E-01	1.498E+02	0.8264	0.9395
Exp. Sym.	0.1-10	0.5	-0.0210	2.62E+01	4.88	4.12E+00	6.991E+01	0.8264	0.9395
Exp. Sym.	0.1-10	1	-0.0058	2.62E+01	4.88	7.49E+00	3.539E+01	0.8264	0.9395
Exp. Sym.	0.5-50	0.0001	-525.6708	6.55E+02	4.88	1.09E-03	1.851E+01	4.1317	4.6975
Exp. Sym.	0.5-50	0.0005	-92.5948	6.55E+02	4.88	5.42E-03	1.622E+01	4.1317	4.6975
Exp. Sym.	0.5-50	0.001	-42.9554	6.55E+02	4.88	1.08E-02	1.499E+01	4.1317	4.6975
Exp. Sym.	0.5-50	0.005	-6.9471	6.55E+02	4.88	5.32E-02	1.193E+01	4.1317	4.6975
Exp. Sym.	0.5-50	0.01	-3.1150	6.55E+02	4.88	1.05E-01	1.057E+01	4.1317	4.6975
Exp. Sym.	0.5-50	0.05	-0.4581	6.55E+02	4.88	4.99E-01	7.386E+00	4.1317	4.6975
Exp. Sym.	0.5-50	0.1	-0.1934	6.55E+02	4.88	9.61E-01	6.006E+00	4.1317	4.6975
Exp. Sym.	0.5-50	0.5	-0.0210	6.55E+02	4.88	4.12E+00	2.799E+00	4.1317	4.6975
Exp. Sym.	0.5-50	1	-0.0059	6.55E+02	4.88	7.49E+00	1.416E+00	4.1317	4.6975
Exp. Sym.	1-100	0.0001	-543.3634	2.62E+03	4.88	1.09E-03	4.783E+00	8.2635	9.3950
Exp. Sym.	1-100	0.0005	-93.6126	2.62E+03	4.88	5.42E-03	4.099E+00	8.2635	9.3950
Exp. Sym.	1-100	0.001	-43.2455	2.62E+03	4.88	1.08E-02	3.774E+00	8.2635	9.3950
Exp. Sym.	1-100	0.005	-6.9622	2.62E+03	4.88	5.32E-02	2.990E+00	8.2635	9.3950
Exp. Sym.	1-100	0.01	-3.1192	2.62E+03	4.88	1.05E-01	2.647E+00	8.2635	9.3950
Exp. Sym.	1-100	0.05	-0.4583	2.62E+03	4.88	4.99E-01	1.847E+00	8.2635	9.3950
Exp. Sym.	1-100	0.1	-0.1935	2.62E+03	4.88	9.61E-01	1.502E+00	8.2635	9.3950
Exp. Sym.	1-100	0.5	-0.0210	2.62E+03	4.88	4.12E+00	6.997E-01	8.2635	9.3950
Exp. Sym.	1-100	1	-0.0059	2.62E+03	4.88	7.49E+00	3.541E-01	8.2635	9.3950
Exp. Sym.	5-500	0.0001	-558.2680	6.55E+04	4.88	1.09E-03	1.966E-01	41.3174	46.9751
Exp. Sym.	5-500	0.0005	-94.4397	6.55E+04	4.88	5.42E-03	1.654E-01	41.3174	46.9751
Exp. Sym.	5-500	0.001	-43.4797	6.55E+04	4.88	1.08E-02	1.518E-01	41.3174	46.9751
Exp. Sym.	5-500	0.005	-6.9744	6.55E+04	4.88	5.32E-02	1.198E-01	41.3174	46.9751
Exp. Sym.	5-500	0.01	-3.1226	6.55E+04	4.88	1.05E-01	1.060E-01	41.3174	46.9751
Exp. Sym.	5-500	0.05	-0.4585	6.55E+04	4.88	4.99E-01	7.392E-02	41.3174	46.9751
Exp. Sym.	5-500	0.1	-0.1935	6.55E+04	4.88	9.61E-01	6.010E-02	41.3174	46.9751
Exp. Sym.	5-500	0.5	-0.0210	6.55E+04	4.88	4.12E+00	2.799E-02	41.3174	46.9751
Exp. Sym.	5-500	1	-0.0059	6.55E+04	4.88	7.49E+00	1.417E-02	41.3174	46.9751
Exp. Sym.	10-1000	0.0001	-560.1807	2.62E+05	4.88	1.09E-03	4.931E-02	82.6347	93.9501
Exp. Sym.	10-1000	0.0005	-94.5439	2.62E+05	4.88	5.42E-03	4.140E-02	82.6347	93.9501
Exp. Sym.	10-1000	0.001	-43.5092	2.62E+05	4.88	1.08E-02	3.797E-02	82.6347	93.9501
Exp. Sym.	10-1000	0.005	-6.9759	2.62E+05	4.88	5.32E-02	2.996E-02	82.6347	93.9501
Exp. Sym.	10-1000	0.01	-3.1230	2.62E+05	4.88	1.05E-01	2.650E-02	82.6347	93.9501
Exp. Sym.	10-1000	0.05	-0.4585	2.62E+05	4.88	4.99E-01	1.848E-02	82.6347	93.9501
Exp. Sym.	10-1000	0.1	-0.1935	2.62E+05	4.88	9.61E-01	1.502E-02	82.6347	93.9501
Exp. Sym.	10-1000	0.5	-0.0210	2.62E+05	4.88	4.12E+00	6.998E-03	82.6347	93.9501
Exp. Sym.	10-1000	1	-0.0059	2.62E+05	4.88	7.49E+00	3.541E-03	82.6347	93.9501
Log.	0.1-10	0.0001	-410.0958	2.88E+01	4.51	1.09E-03	3.554E+02	0.7898	0.9386
Log.	0.1-10	0.0005	-84.7976	2.88E+01	4.51	5.42E-03	3.656E+02	0.7898	0.9386
Log.	0.1-10	0.001	-40.6616	2.88E+01	4.51	1.08E-02	3.493E+02	0.7898	0.9386
Log.	0.1-10	0.005	-6.8234	2.88E+01	4.51	5.32E-02	2.885E+02	0.7898	0.9386
Log.	0.1-10	0.01	-3.0807	2.88E+01	4.51	1.05E-01	2.574E+02	0.7898	0.9386
Log.	0.1-10	0.05	-0.4564	2.88E+01	4.51	4.99E-01	1.811E+02	0.7898	0.9386
Log.	0.1-10	0.1	-0.1930	2.88E+01	4.51	9.61E-01	1.475E+02	0.7898	0.9386
Log.	0.1-10	0.5	-0.0210	2.88E+01	4.51	4.12E+00	6.883E+01	0.7898	0.9386
Log.	0.1-10	1	-0.0058	2.88E+01	4.51	7.49E+00	3.484E+01	0.7898	0.9386

Log.	0.5-50	0.0001	-524.7114	7.20E+02	4.51	1.09E-03	1.819E+01	3.9488	4.6930
Log.	0.5-50	0.0005	-92.5376	7.20E+02	4.51	5.42E-03	1.596E+01	3.9488	4.6930
Log.	0.5-50	0.001	-42.9390	7.20E+02	4.51	1.08E-02	1.476E+01	3.9488	4.6930
Log.	0.5-50	0.005	-6.9462	7.20E+02	4.51	5.32E-02	1.175E+01	3.9488	4.6930
Log.	0.5-50	0.01	-3.1148	7.20E+02	4.51	1.05E-01	1.041E+01	3.9488	4.6930
Log.	0.5-50	0.05	-0.4581	7.20E+02	4.51	4.99E-01	7.272E+00	3.9488	4.6930
Log.	0.5-50	0.1	-0.1934	7.20E+02	4.51	9.61E-01	5.914E+00	3.9488	4.6930
Log.	0.5-50	0.5	-0.0210	7.20E+02	4.51	4.12E+00	2.755E+00	3.9488	4.6930
Log.	0.5-50	1	-0.0059	7.20E+02	4.51	7.49E+00	1.394E+00	3.9488	4.6930
Log.	1-100	0.0001	-542.8505	2.88E+03	4.51	1.09E-03	4.704E+00	7.8977	9.3860
Log.	1-100	0.0005	-93.5834	2.88E+03	4.51	5.42E-03	4.035E+00	7.8977	9.3860
Log.	1-100	0.001	-43.2372	2.88E+03	4.51	1.08E-02	3.715E+00	7.8977	9.3860
Log.	1-100	0.005	-6.9618	2.88E+03	4.51	5.32E-02	2.944E+00	7.8977	9.3860
Log.	1-100	0.01	-3.1191	2.88E+03	4.51	1.05E-01	2.606E+00	7.8977	9.3860
Log.	1-100	0.05	-0.4583	2.88E+03	4.51	4.99E-01	1.819E+00	7.8977	9.3860
Log.	1-100	0.1	-0.1935	2.88E+03	4.51	9.61E-01	1.479E+00	7.8977	9.3860
Log.	1-100	0.5	-0.0210	2.88E+03	4.51	4.12E+00	6.889E-01	7.8977	9.3860
Log.	1-100	1	-0.0059	2.88E+03	4.51	7.49E+00	3.486E-01	7.8977	9.3860
Log.	5-500	0.0001	-558.1596	7.20E+04	4.51	1.09E-03	1.935E-01	39.4883	46.9301
Log.	5-500	0.0005	-94.4338	7.20E+04	4.51	5.42E-03	1.629E-01	39.4883	46.9301
Log.	5-500	0.001	-43.4781	7.20E+04	4.51	1.08E-02	1.494E-01	39.4883	46.9301
Log.	5-500	0.005	-6.9743	7.20E+04	4.51	5.32E-02	1.180E-01	39.4883	46.9301
Log.	5-500	0.01	-3.1225	7.20E+04	4.51	1.05E-01	1.044E-01	39.4883	46.9301
Log.	5-500	0.05	-0.4585	7.20E+04	4.51	4.99E-01	7.278E-02	39.4883	46.9301
Log.	5-500	0.1	-0.1935	7.20E+04	4.51	9.61E-01	5.917E-02	39.4883	46.9301
Log.	5-500	0.5	-0.0210	7.20E+04	4.51	4.12E+00	2.756E-02	39.4883	46.9301
Log.	5-500	1	-0.0059	7.20E+04	4.51	7.49E+00	1.395E-02	39.4883	46.9301
Log.	10-1000	0.0001	-560.1261	2.88E+05	4.51	1.09E-03	4.854E-02	78.9766	93.8603
Log.	10-1000	0.0005	-94.5410	2.88E+05	4.51	5.42E-03	4.076E-02	78.9766	93.8603
Log.	10-1000	0.001	-43.5083	2.88E+05	4.51	1.08E-02	3.738E-02	78.9766	93.8603
Log.	10-1000	0.005	-6.9758	2.88E+05	4.51	5.32E-02	2.949E-02	78.9766	93.8603
Log.	10-1000	0.01	-3.1230	2.88E+05	4.51	1.05E-01	2.609E-02	78.9766	93.8603
Log.	10-1000	0.05	-0.4585	2.88E+05	4.51	4.99E-01	1.819E-02	78.9766	93.8603
Log.	10-1000	0.1	-0.1935	2.88E+05	4.51	9.61E-01	1.479E-02	78.9766	93.8603
Log.	10-1000	0.5	-0.0210	2.88E+05	4.51	4.12E+00	6.890E-03	78.9766	93.8603
Log.	10-1000	1	-0.0059	2.88E+05	4.51	7.49E+00	3.487E-03	78.9766	93.8603
Dbl. Log.	0.1-10	0.0001	-294.0487	5.96E+00	17.22	1.09E-03	3.223E+02	0.3398	0.6179
Dbl. Log.	0.1-10	0.0005	-74.1977	5.96E+00	17.22	5.42E-03	4.046E+02	0.3398	0.6179
Dbl. Log.	0.1-10	0.001	-37.3259	5.96E+00	17.22	1.08E-02	4.056E+02	0.3398	0.6179
Dbl. Log.	0.1-10	0.005	-6.6296	5.96E+00	17.22	5.32E-02	3.545E+02	0.3398	0.6179
Dbl. Log.	0.1-10	0.01	-3.0261	5.96E+00	17.22	1.05E-01	3.198E+02	0.3398	0.6179
Dbl. Log.	0.1-10	0.05	-0.4537	5.96E+00	17.22	4.99E-01	2.277E+02	0.3398	0.6179
Dbl. Log.	0.1-10	0.1	-0.1923	5.96E+00	17.22	9.61E-01	1.859E+02	0.3398	0.6179
Dbl. Log.	0.1-10	0.5	-0.0210	5.96E+00	17.22	4.12E+00	8.693E+01	0.3398	0.6179
Dbl. Log.	0.1-10	1	-0.0058	5.96E+00	17.22	7.49E+00	4.403E+01	0.3398	0.6179
Dbl. Log.	0.5-50	0.0001	-482.0907	1.49E+02	17.22	1.09E-03	2.114E+01	1.6989	3.0893
Dbl. Log.	0.5-50	0.0005	-89.9010	1.49E+02	17.22	5.42E-03	1.961E+01	1.6989	3.0893
Dbl. Log.	0.5-50	0.001	-42.1772	1.49E+02	17.22	1.08E-02	1.833E+01	1.6989	3.0893
Dbl. Log.	0.5-50	0.005	-6.9060	1.49E+02	17.22	5.32E-02	1.477E+01	1.6989	3.0893
Dbl. Log.	0.5-50	0.01	-3.1036	1.49E+02	17.22	1.05E-01	1.312E+01	1.6989	3.0893
Dbl. Log.	0.5-50	0.05	-0.4576	1.49E+02	17.22	4.99E-01	9.187E+00	1.6989	3.0893
Dbl. Log.	0.5-50	0.1	-0.1933	1.49E+02	17.22	9.61E-01	7.474E+00	1.6989	3.0893
Dbl. Log.	0.5-50	0.5	-0.0210	1.49E+02	17.22	4.12E+00	3.484E+00	1.6989	3.0893

Dbl. Log.	0.5-50	1	-0.0059	1.49E+02	17.22	7.49E+00	1.763E+00	1.6989	3.0893
Dbl. Log.	1-100	0.0001	-519.4521	5.96E+02	17.22	1.09E-03	5.694E+00	3.3978	6.1785
Dbl. Log.	1-100	0.0005	-92.2258	5.96E+02	17.22	5.42E-03	5.029E+00	3.3978	6.1785
Dbl. Log.	1-100	0.001	-42.8496	5.96E+02	17.22	1.08E-02	4.656E+00	3.3978	6.1785
Dbl. Log.	1-100	0.005	-6.9416	5.96E+02	17.22	5.32E-02	3.712E+00	3.3978	6.1785
Dbl. Log.	1-100	0.01	-3.1135	5.96E+02	17.22	1.05E-01	3.291E+00	3.3978	6.1785
Dbl. Log.	1-100	0.05	-0.4581	5.96E+02	17.22	4.99E-01	2.299E+00	3.3978	6.1785
Dbl. Log.	1-100	0.1	-0.1934	5.96E+02	17.22	9.61E-01	1.870E+00	3.3978	6.1785
Dbl. Log.	1-100	0.5	-0.0210	5.96E+02	17.22	4.12E+00	8.713E-01	3.3978	6.1785
Dbl. Log.	1-100	1	-0.0059	5.96E+02	17.22	7.49E+00	4.409E-01	3.3978	6.1785
Dbl. Log.	5-500	0.0001	-553.0960	1.49E+04	17.22	1.09E-03	2.425E-01	16.9892	30.8926
Dbl. Log.	5-500	0.0005	-94.1557	1.49E+04	17.22	5.42E-03	2.054E-01	16.9892	30.8926
Dbl. Log.	5-500	0.001	-43.3994	1.49E+04	17.22	1.08E-02	1.886E-01	16.9892	30.8926
Dbl. Log.	5-500	0.005	-6.9702	1.49E+04	17.22	5.32E-02	1.491E-01	16.9892	30.8926
Dbl. Log.	5-500	0.01	-3.1214	1.49E+04	17.22	1.05E-01	1.320E-01	16.9892	30.8926
Dbl. Log.	5-500	0.05	-0.4584	1.49E+04	17.22	4.99E-01	9.204E-02	16.9892	30.8926
Dbl. Log.	5-500	0.1	-0.1935	1.49E+04	17.22	9.61E-01	7.483E-02	16.9892	30.8926
Dbl. Log.	5-500	0.5	-0.0210	1.49E+04	17.22	4.12E+00	3.486E-02	16.9892	30.8926
Dbl. Log.	5-500	1	-0.0059	1.49E+04	17.22	7.49E+00	1.764E-02	16.9892	30.8926
Dbl. Log.	10-1000	0.0001	-557.5685	5.96E+04	17.22	1.09E-03	6.111E-02	33.9784	61.7852
Dbl. Log.	10-1000	0.0005	-94.4015	5.96E+04	17.22	5.42E-03	5.148E-02	33.9784	61.7852
Dbl. Log.	10-1000	0.001	-43.4689	5.96E+04	17.22	1.08E-02	4.724E-02	33.9784	61.7852
Dbl. Log.	10-1000	0.005	-6.9738	5.96E+04	17.22	5.32E-02	3.730E-02	33.9784	61.7852
Dbl. Log.	10-1000	0.01	-3.1224	5.96E+04	17.22	1.05E-01	3.300E-02	33.9784	61.7852
Dbl. Log.	10-1000	0.05	-0.4585	5.96E+04	17.22	4.99E-01	2.301E-02	33.9784	61.7852
Dbl. Log.	10-1000	0.1	-0.1935	5.96E+04	17.22	9.61E-01	1.871E-02	33.9784	61.7852
Dbl. Log.	10-1000	0.5	-0.0210	5.96E+04	17.22	4.12E+00	8.715E-03	33.9784	61.7852
Dbl. Log.	10-1000	1	-0.0059	5.96E+04	17.22	7.49E+00	4.410E-03	33.9784	61.7852

Acknowledgments

All the data obtained from the pore network simulations and used in this paper are available in Appendix C. The authors strongly thank the financial support of ANR EXCITING (Grant No ANR-17-CE06-0012) for this work and for the PhD thesis funding of A. Mendieta. A. Maineult also acknowledges the support of the Russian Science Foundation (Grant No. 17-17-668 01160 'Physical-chemical models of Induced Polarization and Self-Potential with application to pumping test experiments'). The authors strongly thank the editor, Hugh Daigle, and an anonymous referee for their help improving the paper through a very thorough and detailed review process.

References

Bernabé, Y. (1998), Streaming potential in heterogeneous networks, *Journal of Geophysical Research: Solid Earth*, *103*(B9), 20,827–20,841.

Bernabé, Y., and A. Revil (1995), Pore-scale heterogeneity, energy dissipation and the transport properties of rocks, *Geophysical Research Letters*, *22*(12), 1529–1532.

Bolève, A., J. Vandemeulebrouck, and J. Grangeon (2012), Dyke leakage localization and hydraulic permeability estimation through self-potential and hydro-acoustic measurements: Self-potential 'abacus' diagram for hydraulic permeability estimation and uncertainty computation, *Journal of Applied Geophysics*, *86*, 17–28.

Brovelli, A., and G. Cassiani (2010), Sensitivity of intrinsic permeability to electrokinetic coupling in shaly and clayey porous media, *Transport in Porous Media*, *83*(3), 681–697.

Bryant, S., and M. Blunt (1992), Prediction of relative permeability in simple porous media, *Physical review A*, *46*(4), 2004.

Cherubini, A., B. Garcia, A. Cerepi, and A. Revil. (2018), Streaming potential coupling coefficient and transport properties of unsaturated carbonate rocks, *Vadose Zone Journal*, *17*(180030), –, doi: 10.2136/vzj2018.02.0030.

Darcy, H. (1856), *Les fontaines publiques de la ville de Dijon: exposition et application...*, Victor Dalmont.

Dullien, F. A. (2012), *Porous media: fluid transport and pore structure*, Academic press.

Fox, R. W. (1830), On the electromagnetic properties of metalliferous veins in the mines of cornwall., *Philosophical Transactions of the Royal Society*, *120*, 399–414.

Glover, P. W., and N. Déry (2010), Streaming potential coupling coefficient of quartz glass bead packs: Dependence on grain diameter, pore size, and pore throat radius, *Geophysics*, *75*(6), F225–F241.

Gonçalvès, J., P. Rousseau-Gueutin, and A. Revil (2007), Introducing interacting diffuse layers in tlm calculations: A reappraisal of the influence of the pore size on the swelling pressure and the osmotic efficiency of compacted bentonites, *Journal of colloid and interface science*, *316*(1), 92–99.

Guarracino, L., and D. Jougnot (2018), A physically based analytical model to describe effective excess charge for streaming potential generation in water saturated porous media, *Journal of Geophysical Research: Solid Earth*, *123*(1), 52–65.

Guarracino, L., T. Rötting, and J. Carrera (2014), A fractal model to describe the evolution of multiphase flow properties during mineral dissolution, *Advances in Water Resources*, *67*, 78–86.

Helmholtz, H. V. (1879), Studien über electrische grenzschichten, *Annalen der Physik*, *243*(7), 337–382.

Hiemstra, T., and W. H. Van Riemsdijk (2006), On the relationship between charge distribution, surface hydration, and the structure of the interface of metal hydroxides, *Journal of Colloid and Interface Science*, *301*(1), 1–18.

Hunter, R. (1981), *Zeta Potential in Colloid Science: Principles and Applications*, Colloid Science Series, Academic Press.

Jaafar, M. Z., J. Vinogradov, and M. D. Jackson (2009), Measurement of streaming potential coupling coefficient in sandstones saturated with high salinity nacl brine, *Geophysical Research Letters*, *36*(21), n/a–n/a, doi:10.1029/2009GL040549, l21306.

Jackson, M. D. (2008), Characterization of multiphase electrokinetic coupling using a bundle of capillary tubes model, *Journal of Geophysical Research*, *113*(B4).

Jackson, M. D. (2010), Multiphase electrokinetic coupling: Insights into the impact of fluid and charge distribution at the pore scale from a bundle of capillary tubes model, *Journal of Geophysical Research*, *115*, doi:10.1029/2009JB007092.

Jardani, A., and A. Revil (2009), Stochastic joint inversion of temperature and self-potential data, *Geophysical Journal International*, *179*(1), 640–654.

Jardani, A., A. Revil, A. Bolève, A. Crespy, J. Dupont, W. Barrash, and B. Malama (2007), Tomography of the darcy velocity from self-potential measurements, *Geophysical Research Letters*, *34*(24), L24,403.

Jougnot, D., N. Linde, A. Revil, and C. Doussan (2012), Derivation of soil-specific streaming potential electrical parameters from hydrodynamic characteristics of partially saturated soils, *Vadose Zone Journal*, *11*(1).

Jougnot, D., J. G. Rubino, M. Rosas-Carbajal, N. Linde, and K. Holliger (2013), Seismoelectric effects due to mesoscopic heterogeneities, *Geophysical Research Letters*, *40*(10), 2033–2037, doi:10.1002/grl.50472.

Jougnot, D., N. Linde, E. Haarder, and M. Looms (2015), Monitoring of saline tracer movement with vertically distributed self-potential measurements at the HOBE agricultural test site, voulund, denmark, *Journal of Hydrology*, *521*(0), 314 – 327, doi:http://dx.doi.org/10.1016/j.jhydrol.2014.11.041.

Jouniaux, L., and J. Pozzi (1995a), Streaming potential and permeability of saturated sandstones under triaxial stress: Consequences for electrotelluric anomalies prior to earthquakes, *Journal of Geophysical Research: Solid Earth*, *100*(B6), 10,197–10.

Jouniaux, L., and J. Pozzi (1995b), Permeability dependence of streaming potential in rocks for various fluid conductivities, *Geophysical Research Letters*, *22*(4), 485–488.

Jouniaux, L., A. Maineult, V. Naudet, M. Pessel, and P. Sailhac (2009), Review of self-potential methods in hydrogeophysics, *Comptes Rendus Geosciences*, *341*(10-11), 928–936.

Kirchhoff, S. (1845), Ueber den durchgang eines elektrischen stromes durch eine ebene, insbesondere durch eine kreisförmige, *Annalen der Physik*, *140*(4), 497–514.

Kormiltsev, V. V., A. N. Ratushnyak, and V. A. Shapiro (1998), Three-dimensional modeling of electric and magnetic fields induced by the fluid flow movement in porous media, *Physics of the earth and planetary interiors*, *105*(3), 109–118.

Leroy, P., and A. Maineult (2018), Exploring the electrical potential inside cylinders beyond the debye–hückel approximation: a computer code to solve the poisson–boltzmann equation for multivalent electrolytes, *Geophysical Journal International*, *214*(1), 58–69.

Leroy, P., and A. Revil (2004), A triple-layer model of the surface electrochemical properties of clay minerals, *Journal of Colloid and Interface Science*, *270*(2), 371–380.

Leroy, P., D. Jougnot, A. Revil, A. Lassin, and M. Azaroual (2012), A double layer model of the gas bubble/water interface, *Journal of Colloid and Interface Science*, *388*(1), 243–256.

Leroy, P., N. Devau, A. Revil, and M. Bizi (2013), Influence of surface conductivity on the apparent zeta potential of amorphous silica nanoparticles, *Journal of Colloid and Interface Science*, *410*, 81–93.

Leroy, P., C. Tournassat, O. Bernard, N. Devau, and M. Azaroual (2015), The electrophoretic mobility of montmorillonite. zeta potential and surface conductivity effects, *Journal of colloid and interface science*, *451*, 21–39.

Li, S., P. Leroy, F. Heberling, N. Devau, D. Jougnot, and C. Chiaberge (2016), Influence of surface conductivity on the apparent zeta potential of calcite, *Journal of colloid and interface science*, *468*, 262–275.

Linde, N. (2009), Comment on "characterization of multiphase electrokinetic coupling using a bundle of capillary tubes model" by mathew d. jackson, *Journal of Geophysical Research*, *114*(B6), B06,209.

Linde, N., A. Revil, A. Boleve, C. Dagès, J. Castermant, B. Suski, and M. Voltz (2007), Estimation of the water table throughout a catchment using self-potential and piezometric data in a bayesian framework, *Journal of Hydrology*, *334*(1), 88–98.

Linde, N., J. Doetsch, D. Jougnot, O. Genoni, Y. Dürst, B. Minsley, T. Vogt, N. Pasquale, and J. Luster (2011), Self-potential investigations of a gravel bar in a restored river corridor, *Hydrology and Earth System Sciences*, *15*(3), 729–742.

Maineult, A., A. Revil, C. Camerlynck, N. Florsch, and K. Titov (2017), Upscaling of spectral induced polarization response using random tube networks, *Geophysical Journal International*, *209*(2), 948–960.

Maineult, A., D. Jougnot, and A. Revil (2018), Variations of petrophysical properties and spectral induced polarization in response to drainage and imbibition: a study on a correlated random tube network, *Geophysical Journal International*, *212*(2), 1398–1411.

McCleskey, R. B. (2011), Electrical conductivity of electrolytes found in natural waters from (5 to 90) c, *Journal of Chemical & Engineering Data*, *56*(2), 317–327.

Monachesi, L. B., J. G. Rubino, M. Rosas-Carbajal, D. Jougnot, N. Linde, B. Quintal, and K. Holliger (2015), An analytical study of seismoelectric signals produced by 1-d mesoscopic heterogeneities, *Geophysical Journal International*, *201*(1), 329–342.

Morgan, F., E. Williams, and T. Madden (1989), Streaming potential properties of westerly granite with applications, *Journal of Geophysical Research: Solid Earth*, *94*(B9), 12,449–12,461.

Nourbehecht, B. (1963), Irreversible thermodynamic effects in inhomogeneous media and their applications in certain geoelectric problems, Ph.D. thesis, Massachusetts Institute of Technology.

Obliger, A., M. Jardat, D. Coelho, S. Bekri, and B. Rotenberg (2014), Pore network model of electrokinetic transport through charged porous media, *Physical Review E*, *89*(4), 043,013.

Pengra, D. B., S. Xi Li, and P.-z. Wong (1999), Determination of rock properties by low-frequency ac electrokinetics, *Journal of Geophysical Research: Solid Earth*, *104*(B12), 29,485–29,508.

Pride, S. R., and F. Morgan (1991), Electrokinetic dissipation induced by seismic waves, *Geophysics*, *56*(7), 914–925.

Quincke, G. (1859), Ueber eine neue art elektrischer ströme, *Annalen der Physik*, *183*(5), 1–47.

Revil, A. (2017), Comment on dependence of shear wave seismoelectrics on soil textures: a numerical study in the vadose zone by f.i. zyserman, l.b. monachesi and l. jouniaux, *Geophysical Journal International*, *209*(2), 1095, doi:10.1093/gji/ggx078.

Revil, A., and L. Cathles (1999), Permeability of shaly sands, *Water Resources Research*, *35*(3), 651–662.

Revil, A., and A. Jardani (2013), *The Self-Potential Method: Theory and Applications in Environmental Geosciences*, Cambridge University Press.

Revil, A., and P. Leroy (2004), Constitutive equations for ionic transport in porous shales, *Journal of Geophysical Research*, *109*(B3), B03,208.

Revil, A., P. Pezard, and P. Glover (1999a), Streaming potential in porous media: 1. theory of the zeta potential, *Journal of Geophysical Research: Solid Earth*, *104*(B9), 20,021–20,031.

Revil, A., H. Schwaeger, L. Cathles, and P. Manhardt (1999b), Streaming potential in porous media: 2. theory and application to geothermal systems, *Journal of Geophysical Research: Solid Earth*, *104*(B9), 20,033–20,048.

Revil, A., N. Linde, A. Cerepi, D. Jougnot, S. Matthäi, and S. Finsterle (2007), Electrokinetic coupling in unsaturated porous media, *Journal of Colloid and Interface Science*, *313*(1), 315–327.

Revil, A., A. Jardani, P. Sava, and A. Haas (2015), *The Seismoelectric Method: Theory and Application*, John Wiley & Sons.

Roubinet, D., N. Linde, D. Jougnot, and J. Irving (2016), Streaming potential modeling in fractured rock: Insights into the identification of hydraulically active fractures, *Geophysical Research Letters*, *43*(10), 4937–4944.

Schwartz, L. M., P. N. Sen, and D. L. Johnson (1989), Influence of rough surfaces on electrolytic conduction in porous media, *Physical Review B*, *40*(4), 2450.

Sen, P. N., and P. A. Goode (1992), Influence of temperature on electrical conductivity on shaly sands, *Geophysics*, *57*(1), 89–96.

Sill, W. R. (1983), Self-potential modeling from primary flows, *Geophysics*, *48*(1), 76–86.

Soldi, M., D. Jougnot, and L. Guarracino (2019), An analytical effective excess charge density model to predict the streaming potential generated by unsaturated flow, *Geophysical Journal International*, *216*(1), 380–394.

Soueid Ahmed, A., A. Jardani, A. Revil, and J. Dupont (2014), Hydraulic conductivity field characterization from the joint inversion of hydraulic heads and self-potential data, *Water Resources Research*, *50*(4), 3502–3522.

Sverjensky, D. A. (2006), Prediction of the speciation of alkaline earths adsorbed on mineral surfaces in salt solutions, *Geochimica et Cosmochimica Acta*, *70*(10), 2427–2453.

Thanh, L. D. (2018), Effective excess charge density in water saturated porous media, *VNU Journal of Science: Mathematics - Physics*, *34*(4), doi:10.25073/2588-1124/vnumap.4294.

Titov, K., Y. Ilyin, P. Konosavski, and A. Levitski (2002), Electrokinetic spontaneous polarization in porous media: petrophysics and numerical modelling, *Journal of Hydrology*, *267*(3–4), 207 – 216, doi: http://dx.doi.org/10.1016/S0022-1694(02)00151-8.

Tyler, S. W., and S. W. Wheatcraft (1990), Fractal processes in soil water retention, *Water Resources Research*, *26*(5), 1047–1054.

von Smoluchowski, M. (1903), Contribution to the theory of electro-osmosis and related phenomena, *Bull Int Acad Sci Cracovie*, *3*, 184–199.

Winsauer, W. O., H. Shearin Jr, P. Masson, and M. Williams (1952), Resistivity of brine-saturated sands in relation to pore geometry, *AAPG bulletin*, *36*(2), 253–277.

Yu, B., J. Li, Z. Li, and M. Zou (2003), Permeabilities of unsaturated fractal porous media, *International journal of multiphase flow*, *29*(10), 1625–1642.

Zhang, W., J. Yao, Y. Gao, Q. Zhang, and H. Sun (2015), Analysis of electrokinetic coupling of fluid flow in porous media using a 3-d pore network, *Journal of Petroleum Science and Engineering*, *134*, 150–157.

Bibliography

Archie, G.E. (1942). "The electrical resistivity log as an aid in determining some reservoir characteristics". In: *Transactions of the American Institute of mining and metallurgical engineers* 146, pp. 54–62. DOI: 10.2118/942054-G.

Bairlein, K., M. Bücker, A. Hördt, and B. Hinze (2016). "Temperature dependence of spectral induced polarization data: experimental results and membrane polarization theory". In: *Geophysical Journal International* 205, pp. 440–453. ISSN: 1365246X. DOI: 10.1093/gji/ggw027.

Bergaya, F. and G. Lagaly (2006). "General introduction: clays, clay minerals, and clay science". In: *Handbook of Clay Science*. Ed. by Bergaya F., Theng B.K.G., and Lagaly G. 1st ed. Vol. 1. Elsevier Ltd. Chap. 1, pp. 1–18. DOI: 10.1016/S1572-4352(05)01001-9.

Bergaya, F., G. Lagaly, and M. Vayer (2013). "Cation and anion exchange". In: *Developments in Clay Science*. Ed. by Faïza Bergaya and G. Lagaly. Vol. 5. Elsevier. Chap. 2.11, pp. 333–359. DOI: 10.1016/B978-0-08-098259-5.00013-5. URL: http://dx.doi.org/10.1016/B978-0-08-098259-5.00013-5.

Bernabe, Y. (1995). "The transport properties of networks of cracks and pores". In: *Journal of Geophysical Research* 100, pp. 4231–4241. DOI: 10.1029/94JB02986.

Blaschek, R. and A. Hördt (2009). "Numerical modelling of the IP effect at the pore scale". In: *Near Surface Geophysics* 7, pp. 579–588. DOI: 10.3997/1873-0604.2009030.

Börner, F.D. (1992). "Complex conductivity measurements of reservoir properties". In: *Advances in core evaluation: Reservoir management: Reviewed Proceedings of the Society for Core Analysis Third European Core Analysis Symposium*. Ed. by P.F. Worthington and C. Chardaire-Rivière. Hardwood Academic, pp. 359–386.

Breede, K., A. Kemna, O. Esser, E. Zimmermann, H. Vereecken, and J.A. Huisman (2012). "Spectral induced polarization measurements on variably saturated sand-clay mixtures". In: *Near Surface Geophysics* 10, pp. 479–489. DOI: 10.3997/1873-0604.2012048.

Brigatti, M.F., E. Galan, and B.K.G. Theng (2006). “Structures and mineralogy of clay minerals”. In: *Handbook of Clay Science*. Ed. by Bergaya F., Theng B.K.G., and Lagaly G. Vol. 1. Elsevier Ltd. Chap. 2, pp. 19–86. DOI: 10.1016/S1572-4352(05)01002-0.

Bruggeman, D.A.G. (1935). “Berechnung verschiedener physikalischer Konstanten von heterogenen Substanzen. I. Dielektrizitätskonstanten und Leitfähigkeiten der Mischkörper aus isotropen Substanzen”. In: *Annalen der Physik* 416, pp. 636–664. DOI: 10.1002/andp.19354160705..

Bücker, M., A. Flores Orozco, A. Hördt, and A. Kemna (2017). “An analytical membrane-polarization model to predict the complex conductivity signature of immiscible liquid hydrocarbon contaminants”. In: *Near Surface Geophysics* 15, pp. 547–562. DOI: 10.3997/1873-0604.2017051.

Bücker, M., A. Flores Orozco, S. Undorf, and A. Kemna (2019). “On the role of Stern- and diffuse-layer polarization mechanisms in porous media”. In: *Journal of Geophysical Research: Solid Earth* 124, pp. 5656–5677. DOI: 10.1029/2019JB017679.

Bücker, M. and A. Hördt (2013a). “Analytical modelling of membrane polarization with explicit parametrization of pore radii and the electrical double layer”. In: *Geophysical Journal International* 194, pp. 804–813. DOI: 10.1093/gji/ggt136.

— (2013b). “Long and short narrow pore models for membrane polarization”. In: *Geophysics* 78, E299–E314. DOI: 10.1190/GEO2012-0548.1.

Chelidze, T.L. and Y. Gueguen (1999). “Electrical spectroscopy of porous rocks: A review-I. Theoretical models”. In: *Geophysical Journal International* 137, pp. 1–15. DOI: 10.1046/j.1365-246X.1999.00799.x.

Chen, Y. and D. Or (2006). “Effects of Maxwell-Wagner polarization on soil complex dielectric permittivity under variable temperature and electrical conductivity”. In: *Water Resources Research* 42, pp. 1–14. DOI: 10.1029/2005WR004590.

Chorover, J., R. Kretzschmar, F. Garica-Pichel, and D.L. Sparks (2007). “Soil biogeochemicial processes within the critical zone”. In: *Elements* 3, pp. 321–326. DOI: 10.2113/gselements.3.5.321.

Cole, K.S. and R.H. Cole (1941). “Dispersion and absorption in dielectrics”. In: *Journal of Chemical Physics* 9, pp. 341–351. DOI: 10.1063/1.1750906.

Comparon, L. (2005). “Étude expérimentale des propriétés électriques et diélectriques des matériaux argileux consolidés”. PhD thesis. Institut de Physique du Globe de Paris.

Corrado, S., L. Aldega, A.S. Celano, A.A. De Benedetti, and G. Giordano (2014). “Cap rock efficiency and fluid circulation of natural hydrothermal systems by means of XRD on clay minerals (Sutri, Northern Latium, Italy)”. In: *Geothermics* 50, pp. 180–188. DOI: 10.1016/j.geothermics.2013.09.011.

Cosenza, P., A. Ghorbani, A. Revil, M. Zamora, M. Schmutz, D. Jougnot, and N. Florsch (2008). "A physical model of the low-frequency electrical polarization of clay rocks". In: *Journal of Geophysical Research* 113, pp. 1–9. DOI: 10.1029/2007JB005539.

Cumming, W. and R. Mackie (2010). "Resistivity imaging of geothermal resources using 1D , 2D and 3D MT inversion and TDEM static shift correction illustrated by a Glass Mountain case history". In: *Proceedings World Geothermal Congress 2010* April, pp. 1–10.

Debye, P. (1929). *Polar Molecules*. New York: The Chemical Catalog Company.

Florsch, N., C. Camerlynck, and A. Revil (2012). "Direct estimation of the distribution of relaxation times from induced-polarization spectra using a Fourier transform analysis". In: *Near Surface Geophysics* 10.6, pp. 517–531. DOI: 10.3997/1873-0604.2012004.

Ghorbani, A., P. Cosenza, A. Revil, M. Zamora, M. Schmutz, N. Florsch, and D. Jougnot (2009). "Non-invasive monitoring of water content and textural changes in clay-rocks using spectral induced polarization: A laboratory investigation". In: *Applied Clay Science* 43, pp. 493–502. DOI: 10.1016/j.clay.2008.12.007.

Guarracino, L. and D. Jougnot (2018). "A physically based analytical model to describe effective excess charge for streaming potential generation in water saturated porous media". In: *Journal of Geophysical Research: Solid Earth* 123, pp. 52–65. ISSN: 21699356. DOI: 10.1002/2017JB014873.

Günther, T., T. Martin, and C. Rücker (2016). "Spectral Inversion of SIP field data using pyGIMLi/BERT". In: *Proceedings of the 4th International Workshop on Induced Polarization*. Aarhus.

Hall, B.D. (2015). "Evaluating the measurement uncertainty of complex quantities: A selective review". In: *Metrologia* 53, S25–S31. DOI: 10.1088/0026-1394/53/1/S25.

Hanai, T. (1960). "Theory of the dielectric dispersion due to the interfacial polarization and its application to emulsions". In: *Kolloid-Zeitschrift* 171.1, pp. 23–31.

Hillier, S. (2003). "Clay mineralogy". In: *Encyclopedia of sediments and sedimentary rocks*. Ed. by G.V. Middleton, M.J. Church, M. Coniglio, L.A. Hardie, and F.J. Longstaffe. Dordrecht: Kluwer Academic Publishers. Chap. Clay miner, pp. 139–142.

Hördt, A., K. Bairlein, A. Bielefeld, M. Bücker, E. Kuhn, S. Nordsiek, and H. Stebner (2016). "The dependence of induced polarization on fluid salinity and pH, studied with an extended model of membrane polarization". In: *Journal of Applied Geophysics* 135, pp. 408–417. DOI: 10.1016/j.jappgeo.2016.02.007.

Huisman, J.A., E. Zimmermann, O. Esser, F.H. Haegel, A. Treichel, and H. Vereecken (2016). "Evaluation of a novel correction procedure to remove electrode impedance effects from broadband SIP measurements". In: *Journal of Applied Geophysics* 135, pp. 466–473. DOI: 10.1016/j.jappgeo.2015.11.008.

Ishida, T., T. Makino, and C. Wang (2000). "Dielectric-relaxation spectroscopy of kaolinite, montmorillonite, allophane, and imogolite under moist conditions". In: *Clays and Clay Minerals* 48.1, pp. 75–84. ISSN: 00098604. DOI: 10.1346/CCMN.2000.0480110.

Islam, M.T., B.C.S. Chittoori, and M. Burbank (2020). "Evaluating the applicability of biostimulated calcium carbonate precipitation to stabilize clayey soils". In: *Journal of Materials in Civil Engineering* 32, pp. 1–11. DOI: 10.1061/(ASCE)MT.1943-5533.0003036.

Izumoto, S., J.A. Huisman, Y. Wu, and H. Vereecken (2020). "Effect of solute concentration on the spectral induced polarization response of calcite precipitation". In: *Geophysical Journal International* 220, pp. 1187–1196. ISSN: 1365246X. DOI: 10.1093/gji/ggz515.

Jougnot, D. (2009). "Étude géophysique des phénomènes de transfert dans les argilites du Callovo-Oxfordien partiellement saturées en eau : application à l'EDZ du site de Bure". PhD thesis. Université de Savoie.

Jougnot, D., A. Ghorbani, A. Revil, P. Leroy, and P. Cosenza (2010). "Spectral induced polarization of partially saturated clay-rocks : a mechanistic approach". In: *Geophysical Journal International* 180, pp. 210–224. DOI: 10.1111/j.1365-246X.2009.04426.x.

Jougnot, D. and N. Linde (2013). "Self-potentials in partially saturated media : the importance of explicit modeling of electrode effects". In: *Vadose Zone Journal* 12.2, pp. 1–49. DOI: 10.2136/vzj2012.0169.1.

Jougnot, D., A. Mendieta, P. Leroy, and A. Maineult (2019). "Exploring the effect of the pore size distribution on the streaming potential generation in saturated porous media, insight from pore network simulations". In: *Journal of Geophysical Research: Solid Earth* 124, pp. 5315–5335. DOI: 10.1029/2018JB017240.

Jougnot, D. and A. Revil (2010). "Thermal conductivity of unsaturated clay-rocks". In: *Hydrology and Earth System Sciences*, pp. 91–98.

Karaoulis, M., P. Tsourlos, J.H. Kim, and A. Revill (2014). "4D time-lapse ERT inversion: Introducing combined time and space constraints". In: *Near Surface Geophysics* 12, pp. 25–34. DOI: 10.3997/1873-0604.2013004.

Kemna, A., A. Binley, G. Cassiani, E. Niederleithinger, A. Revil, L. Slater, K.H. Williams, A. Flores Orozco, F.H. Haegel, A. Hördt, S. Kruschwitz, V. Leroux, K. Titov, and E. Zimmermann (2012). "An overview of the spectral induced polarization method for near-surface applications". In: *Near Surface Geophysics* 10, pp. 453–468. DOI: 10.3997/1873-0604.2012027.

Knight, R.J. and A.L. Endres (2005). "An introduction to rock physics principles for near-surface geophysics". In: *Near-Surface Geophysics*. Ed. by Dwain K. Butler. Tulsa, Oklahoma: Society of Exploration Geophysicists. Chap. 3, pp. 31–65. ISBN: 0-931830-46-X. DOI: 10.1190/1.9781560801719.ch3.

Kremer, T. (2015). “Utilisation des méthodes électriques pour la détection et suivi de transferts de CO_2 dans la subsurface”. PhD thesis. Institut de Physique du Globe de Paris.

Kremer, T., M. Schmutz, A. Maineult, and P. Agrinier (2016). “Laboratory monitoring of CO2 injection in saturated silica and carbonate sands using spectral induced polarization”. In: *Geophysical Journal International* 207, pp. 1258–1272. DOI: 10.1093/gji/ggw333.

Kruschwitz, S. and U. Yaramanci (2004). “Detection and characterization of the disturbed rock zone in claystone with the complex resistivity method”. In: *Journal of Applied Geophysics* 57, pp. 63–79. ISSN: 09269851. DOI: 10.1016/j.jappgeo.2004.09.003.

Kuila, U. and M. Prasad (2013). “Specific surface area and pore-size distribution in clays and shales”. In: *Geophysical Prospecting* 61, pp. 341–362. DOI: 10.1111/1365-2478.12028.

Leroy, P. (2005). “Transport ionique dans les argiles. Influence de la microstructure et des effets d’interface. Application aux argilites du site de Bure (Meuse/Haute Marne)”. PhD thesis. Université de Droit, d’Economie et des Sciences d’Aix-Marseille III.

Leroy, P. and A. Maineult (2018). “Exploring the electrical potential inside cylinders beyond the Debye – Huckel approximation : a computer code to solve the Poisson – Boltzmann equation for multivalent electrolytes”. In: *Geophysical Journal International* 214, pp. 58–69. DOI: 10.1093/gji/ggy124.

Leroy, P. and A. Revil (2004). “A triple-layer model of the surface electrochemical properties of clay minerals”. In: *Journal of Colloid and Interface Science* 270, pp. 371–380. DOI: 10.1016/j.jcis.2003.08.007.

— (2009). “A mechanistic model for the spectral induced polarization of clay materials”. In: *Journal of Geophysical Research* 114.B10202, pp. 1–21. DOI: 10.1029/2008JB006114.

Leroy, P., A. Revil, S. Altmann, and C. Tournassat (2007). “Modeling the composition of the pore water in a clay-rock geological formation (Callovo-Oxfordian, France)”. In: *Geochimica et Cosmochimica Acta* 71, pp. 1087–1097. ISSN: 00167037. DOI: 10.1016/j.gca.2006.11.009.

Leroy, P., C. Tournassat, O. Bernard, N. Devau, and M. Azaroual (2015). “The electrophoretic mobility of montmorillonite. Zeta potential and surface conductivity effects”. In: *Journal of Colloid and Interface Science* 451, pp. 21–39. DOI: 10.1016/j.jcis.2015.03.047.

Leroy, P., M. Weigand, G. Mériguet, E. Zimmermann, C. Tournassat, F. Fagerlund, A. Kemna, and J.A. Huisman (2017). “Spectral induced polarization of Na-montmorillonite dispersions”. In: *Journal of Colloid And Interface Science* 505, pp. 1093–1110. DOI: 10.1016/j.jcis.2017.06.071.

Lévy, L., B. Gibert, F. Sigmundsson, O.G. Flóvenz, G.P. Hersir, P. Briole, and P.A. Pezard (2018). “The role of smectites in the electrical conductivity of active hydrothermal systems: Electrical prop-

erties of core samples from Krafla volcano, Iceland". In: *Geophysical Journal International* 215, pp. 1558–1582. DOI: 10.1093/gji/ggy342.

Lévy, L., P.K. Maurya, S. Byrdina, J. Vandemeulebrouck, F. Sigmundsson, K. Árnason, T. Ricci, D. Deldicque, M. Roger, B. Gibert, and P. Labazuy (2019a). "Electrical resistivity tomography and time-domain induced polarization field investigations of geothermal areas at Krafla, Iceland: Comparison to borehole and laboratory frequency-domain electrical observations". In: *Geophysical Journal International* 218, pp. 1469–1489. DOI: 10.1093/gji/ggz240.

Lévy, L., A. Weller, and B. Gibert (2019b). "Influence of smectite and salinity on the imaginary and surface conductivity of volcanic rocks". In: *Near Surface Geophysics* 17, pp. 653–673. DOI: 10.1002/nsg.12069.

Loewer, M., T. Günther, J. Igel, S. Kruschwitz, T. Martin, and N. Wagner (2017). "Ultra-broad-band electrical spectroscopy of soils and sediments-a combined permittivity and conductivity model". In: *Geophysical Journal International* 210.3, pp. 1360–1373. ISSN: 1365246X. DOI: 10.1093/gji/ggx242.

Lyklema, J., S.S. Dukhin, and V.N. Shilov (1983). "The relaxation of the double layer around colloidal particles and the low-frequency dielectric dispersion: Part I. Theoretical considerations". In: *Journal of Electroanalytical Chemistry and Interfacial Electrochemistry* 143, pp. 1–21. DOI: 10.1016/S0022-0728(83)80251-4.

Maineult, A. (2018). "Corrigendum to "Upscaling of spectral induced polarization response using random tube networks", by Maineult et al. (2017, Geophysical Journal International, 209, pp. 948–960)." In: *Geophysical Journal International* 213, pp. 1296–1296. DOI: 10.1093/gji/ggy052.

Maineult, A., Y. Bernabé, and P. Ackerer (2004). "Electrical response of flow, diffusion, and advection in a laboratory sand box". In: *Vadose Zone Journal* 3, pp. 1180–1192. DOI: 10.2136/vzj2004.1180.

Maineult, A., A. Revil, C. Camerlynck, N. Florsch, and K. Titov (2017). "Upscaling of spectral induced polarization response using random tube networks". In: *Geophysical Journal International* 209, pp. 948–960. DOI: 10.1093/gji/ggx066.

Marshall, D.J. and T.R. Madden (1959). "Induced polarization, a study of its causes". In: *Geophysics* 24, pp. 790–816. DOI: 10.1190/1.1438659.

Maxwell, J.C. (1865). "A dynamical theory of the electromagnetic field". In: *Philosophical transactions of the Royal Society of London*, pp. 459–512.

Mendieta, A., D. Jougnot, P. Leroy, and A. Maineult (2021). "Spectral induced polarization characterization of non-consolidated clays for varying salinities - an experimental study". In: *Journal of Geophysical Research: Solid Earth* 126. DOI: 10.1029/2020jb021125.

Mitchell, J.K. and K. Soga (2005). *Fundamentals of Soil Behavior*. 3rd ed. John Wiley and Sons, p. 558. DOI: 10.1097/00010694-199407000-00009.

Morgan, F.D. and D.P. Lesmes (1994). "Inversion for dielectric relaxation spectra". In: *J. Chem. Phys.* 100, pp. 671–681. ISSN: 00219606. DOI: 10.1063/1.466932.

Morsy, S. and J.J. Sheng (2014). "Effect of water salinity on shale reservoir productivity". In: *Advances in Petroleum Exploration and Development* 8, pp. 9–14. DOI: 10.3968/5604.

Okay, G., P. Cosenza, A. Ghorbani, C. Camerlynck, J. Cabrera, N. Florsch, and A. Revil (2013). "Localization and characterization of cracks in clay-rocks using frequency and time-domain induced polarization". In: *Geophysical Prospecting* 61, pp. 134–152. DOI: 10.1111/j.1365-2478.2012.01054.x.

Okay, G., P. Leroy, A. Ghorbani, P. Cosenza, C. Camerlynck, J. Cabrera, N. Florsch, and A. Revil (2014). "Spectral induced polarization of clay-sand mixtures : Experiments and modeling". In: *Geophysics* 79, pp. 353–375. DOI: 10.1190/GEO2013-0347.1.

Ortiz, L., G. Volckaert, and D. Mallants (2002). "Gas generation and migration in Boom Clay, a potential host rock formation for nuclear waste storage". In: *Engineering Geology* 64, pp. 287–296. DOI: 10.1016/S0013-7952(01)00107-7.

Parker, B.L., S.W. Chapman, and M.A. Guilbeault (2008). "Plume persistence caused by back diffusion from thin clay layers in a sand aquifer following TCE source-zone hydraulic isolation". In: *Journal of Contaminant Hydrology* 102, pp. 86–104. DOI: 10.1016/j.jconhyd.2008.07.003.

Pelton, W.H., S.H. Ward, P.G. Hallof, W.R. Sill, and P.H. Nelson (1978). "Mineral discrimination and removal of inductive coupling with multifrequency IP". In: *Geophyics* 43, pp. 588–609. DOI: 10.1190/1.1440839.

Rasmusson, M., W. Rowlands, R.W. O'Brien, and R.J. Hunter (1997). "The dynamic mobility and dielectric response of sodium bentonite". In: *Journal of Colloid and Interface Science* 189, pp. 92–100. DOI: 10.1006/jcis.1997.4793.

Revil, A. (2012). "Spectral induced polarization of shaly sands: Influence of the electrical double layer". In: *Water Resources Research* 48.2, pp. 1–23. DOI: 10.1029/2011WR011260.

Revil, A., V. Naudet, J. Nouzaret, and M. Pessel (2003). "Principles of electrography applied to self-potential electrokinetic sources and hydrogeological applications". In: *Water Resources Research* 39.5, pp. 1–15. DOI: 10.1029/2001WR000916.

Robinson, D.A., A. Binley, N. Crook, F.D. Day-Lewis, T.P.A. Ferré, V.J.S. Grauch, R.J. Knight, M.D. Knoll, V. Lakshmi, R. Miller, J. Nyquist, L. Pellerin, K. Singha, and L. Slater (2008). "Advancing process-based watershed hydrological research using near-surface geophysics: a vision for,

and review of, electrical and magnetic geophysical methods". In: *Hydrological Processes*, pp. 3604–3636. DOI: 10.1002/hyp.6963.

Schlumberger, C. (1920). *Étude sur la prospection électrique du sous-sol*. Paris: Gauthier-Villars.

Schroeder, P. (2018). *Clays in the Critical Zone*. Cambridge University Press. ISBN: 978-1-107-13667-0. DOI: 10.1017/9781316480083.

Schwartz, N. and A. Furman (2015). "On the spectral induced polarization signature of soil organic matter". In: *Geophysical Journal International* 200, pp. 589–595. DOI: 10.1093/gji/ggu410.

Schwarz, G. (1962). "A theory of the low-frequency dielectric dispersion of colloidal particles in electrolyte solution". In: *Journal of Physical Chemistry* 66, pp. 2636–2642. DOI: 10.1021/j100818a067.

Seigel, H.O. (1959). "Mathematical formulation and type curves for induced polarization". In: *Geophysics* 24.3, pp. 547–565. DOI: 10.1190/1.1438625.

Sen, P.N., C. Scala, and M.H. Cohenf (1981). "A self-similar model for sedimentary rocks with application to the dielectric constant of fused glass beads". In: *Geophysics* 46.5, pp. 781–795.

Soldi, M., D. Jougnot, and L. Guarracino (2019). "An analytical effective excess charge density model to predict the streaming potential generated by unsaturated flow". In: *Geophysical Journal International* 216, pp. 380–394. ISSN: 1365246X. DOI: 10.1093/gji/ggy391.

Sondi, I., J. Biscan, and V. Pravdic (1996). "Electrokinetics of pure clay minerals revisited". In: *Journal of Colloid And Interface Science* 178, pp. 514–522. DOI: 10.1006/jcis.1996.0403.

Tarasov, A. and K. Titov (2013). "On the use of the Cole-Cole equations in spectral induced polarization". In: *Geophysical Journal International* 195, pp. 352–356. DOI: 10.1093/gji/ggt251.

Titov, K., V. Komarov, V. Tarasov, and A. Levitski (2002). "Theoretical and experimental study of time domain-induced polarization in water-saturated sands". In: *Journal of Applied Geophysics* 50.4, pp. 417–433. DOI: 10.1016/S0926-9851(02)00168-4..

Tournassat, C., I.C. Bourg, C.I. Steefel, and F. Bergaya (2015). "Surface Properties of Clay Minerals". In: *Developments in Clay Science*. Ed. by C. Tournassat, I.C. Bourg, C.I. Steefel, and F. Bergaya. Vol. 6. Elsevier. Chap. 1, pp. 5–31. DOI: 10.1016/B978-0-08-100027-4.00001-2.

Tournassat, C. and C.I. Steefel (2015). "Ionic transport in nano-porous clays with consideration of electrostatic effects". In: *Reviews in Mineralogy and Geochemistry* 80, pp. 287–329. DOI: 10.2138/rmg.2015.80.09.

Vanhala, H. and H. Soininen (1995). "Laboratory technique for measurement of spectral induced polarization response of soil sampies". In: *Geophysical Prospecting* 43.5, pp. 655–676. DOI: 10.1111/j.1365-2478.1995.tb00273.x.

Volkmann, J. and N. Klitzsch (2010). "Frequency-dependent electric properties of microscale rock models for frequencies from one millihertz to ten kilohertz". In: *Vadose Zone Journal* 9, pp. 858–870. DOI: 10.2136/vzj2009.0162.

Voytek, E.B., H.R. Barnard, D. Jougnot, and K. Singha (2019). “Transpiration- and precipitation-induced subsurface water flow observed using the self-potential method”. In: *Hydrological Processes* 33.13, pp. 1784–1801. DOI: 10.1002/hyp.13453.

Wagner, J.F. (2013). “Mechanical properties of clays and clay minerals”. In: *Handbook of Clay Science*. Ed. by F. Bergaya and G. Lagaly. 2nd ed. Vol. 5A. Elsevier Inc. Chap. 9, pp. 347–381. DOI: 10.1016/B978-0-08-098258-8.00011-0.

Wang, C. and L.D. Slater (2019). “Extending accurate spectral induced polarization measurements into the kHz range: Modelling and removal of errors from interactions between the parasitic capacitive coupling and the sample holder”. In: *Geophysical Journal International* 218, pp. 895–912. DOI: 10.1093/gji/ggz199.

Warburg, E. (1899). “Über das Verhalten sogenannter unpolarisiebarer Elek- troden gegen Wechelstrom (About the behaviour of so-called “impolarizable electrodes” in the present of alternating current)”. In: *Ann. Phys. Chem.* 67, pp. 493–499.

Ward, S.H. (1988). “The resistivity and induced polarization methods”. In: *Symposium on the Application of Geophysics to Engineering and Environmental Problems*, pp. 109–250. DOI: 10.1190/1.9781560802785.ch6.

Waxman, M.H. and L.J.M. Smits (1968). “Electrical conductivities in oil-bearing shaly sands”. In: *Society of Petroleum Engineers Journal* 243, pp. 107–122. DOI: 10.2118/1863-A.

Weigand, M. and A. Kemna (2016). “Relationship between Cole-Cole model parameters and spectral decomposition parameters derived from SIP data”. In: *Geophysical Journal International* 205, pp. 1414–1419. DOI: 10.1093/gji/ggw099.

Weller, A., L. Slater, J.A. Huisman, O. Esser, and F.H. Haegel (2015a). “On the specific polarizability of sands and sand-clay mixtures”. In: *Geophysics* 80, A57–A61. ISSN: 19422156. DOI: 10.1190/GEO2014-0509.1.

Weller, A., L. Slater, and S. Nordsiek (2013). “On the relationship between induced polarization and surface conductivity: Implications for petrophysical interpretation of electrical measurements”. In: *Geophysics* 78, pp. D315–D325. DOI: 10.1190/GEO2013-0076.1.

Weller, A., Z. Zhang, and L. Slater (2015b). “High-salinity polarization of sandstones”. In: *Geophysics* 3, pp. D309–D318. ISSN: 19422156. DOI: 10.1190/GEO2014-0483.1.

Wenk, H.R., M. Voltolini, M. Mazurek, L.R. Van Loon, and A. Vinsot (2008). “Preferred orientations and anisotropy in shales: Callovo-oxfordian shale (France) and opalinus clay (Switzerland)”. In: *Clays and Clay Minerals* 56, pp. 285–306. DOI: 10.1346/CCMN.2008.0560301.

Zisser, N. and G. Nover (2009). “Anisotropy of permeability and complex resistivity of tight sandstones subjected to hydrostatic pressure”. In: *Journal of Applied Geophysics* 68, pp. 356–370. DOI: 10.1016/j.jappgeo.2009.02.010.

Zonge, K., J. Wynn, and S. Urquhart (2005). “Resistivity, induced polarization, and complex resistivity”. In: *Near Surface Geophysics*. Ed. by Dwain K. Butler. Society of Exploration Geophysicists. Chap. 9, pp. 265–300. DOI: 10.1190/1.9781560801719.ch9.

Abstract

Clays are ubiquitously present in the Earth's near surface and they have a high impact on the permeability of a system. Due to this property, clay formations are used in a variety of geology related applications (oil and gas, geothermal, nuclear waste storage, critical zone research, among others). Clays have a high surface charge and a high specific surface area, this property gives clays a particularly strong electrical double layer (EDL). Spectral induced polarization (SIP) is an active geo-electrical method that measures in a non-invasive manner the frequency-dependent complex conductivity of a geo-material from the mHz to the kHz. The complex conductivity informs about the ability the probed material has to conduct an electrical current and the ability to polarize (to reversibly store electrical charges). This thesis presents a detailed laboratory protocol to obtain SIP measurements of different types of clay at varying salinities, as well as an artificial heterogeneous mixture of illite and red montmorillonite with a salinity of around 10^{-2} mol L^{-1}. The results of the first study show that the real part of the electrical conductivity increases with salinity, but the imaginary part increases until a maxima and then decreases. An interpretation of the decrease can come from the fact that clays coagulate at high salinities. The potential coagulation of clays would alter the pore space and then alter the polarization mechanisms in play. Furthermore, when comparing the ratio of the surface conductivity (imaginary versus real) of these results with other data in the literature, we notice that this ratio decreases with clay content. For the second study, we observe that red montmorillonite dominates the polarization with respect to illite. However, both clays effect the conduction of the mixtures. Mixing laws are an effective approach to model the complex conductivity of these heterogeneous mixtures. Complex conductance network models are better at predicting the shape of the polarization spectra. The results of this thesis work open new opportunities for clay characterization using SIP.

Key-words

spectral induced polarization, clays, variation with salinity, heterogeneous mixtures, mixing laws, complex conductance networks